A Quantitative Study of the Feasibility of Oxygen Laser Induced Fluorescence for Engineering Gas Temperature Measurements

by

İsmail Ceyhan

B. S., with Distinction, Mechanical Engineering, Stanford University, 1988
M. S., Mechanical Engineering, Stanford University, 1989

Submitted to the Department of Mechanical Engineering
in partial fulfillment of the requirements for the Degree of

Doctor of Philosophy

at the

MASSACHUSETTS INSTITUTE OF TECHNOLOGY

February 1997

Author: _____
Department of Mechanical Engineering
September 27, 1996

Certified by: _____
C. Forbes Dewey, Jr.
Professor of Mechanical Engineering
Chairman

Certified by: _____
Alan H. Epstein
Professor of Aeronautics and Astronautics
Director, Gas Turbine Laboratory
Supervisor

Certified by: _____
Edward M. Greitzer
H. Nelson Slater Professor of Aeronautics and Astronautics
Associate Head, Department of Aeronautics and Astronautics

Accepted by: _____
Ain A. Sonin
Professor of Mechanical Engineering
Chairman, Departmental Graduate Committee

A Quantitative Study of the Feasibility of Oxygen Laser Induced Fluorescence for Engineering Gas Temperature Measurements

by

İsmail Ceyhan

Submitted to the Department of Mechanical Engineering
on September 27, 1996, in partial fulfillment of the
requirements for the Degree of
Doctor of Philosophy

Abstract

The feasibility of using laser induced fluorescence of oxygen (O_2 LIF) as a temperature diagnostic for engineering gas temperature measurements in general and turbomachinery rigs in particular has been investigated through experiments and analysis. A comprehensive, quantitative error analysis has been performed for the regime of 300–550 K and 1–6 atm. Oxygen ion fluorescence (O_2^+ LIF), saturation, collisional quenching and vibrational relaxation have been identified as the significant error sources, whereas quantum and detector noise are the significant uncertainty sources.

The technique precision is limited by quantum and detector noise, and its accuracy is limited by higher-order O_2^+ LIF and saturation processes. For a single-shot measurement, increasing laser fluence reduces uncertainty but increases error. At optimum fluence, the measurement accuracy is equal to the measurement error. The measurement precision may be increased by integrating fluorescence signal from multiple laser shots; the improvement scales as $N^{1/3}$.

Collisional quenching has been found to be small but not negligible. At 300 K and 1 atm, the measured quenching rate is 5.3×10^9 s^{-1}. The quenching rate scales as $P/T^{0.7}$, and neglegting collisional quenching leads to an error of 3 K/atm over the 300–530 K temperature range.

The most severe limitation is associated with the vibrational relaxation time. For temperatures above 300 K, the oxygen LIF technique relies on vibrational excitation for temperature sensitivity and may not be used in high-speed flows due to the long vibrational relaxation time of oxygen molecules. For a Mach 1 flow at 500 K and 1 atm, for example, the vibrational relaxation distance is of the order of 1 m. For a Mach 1 flow at 500 K and 1 atm, for example, the vibrational relaxation distance is of the order of 1 m. For temperatures below 250 K, the technique may be used even with high-speed flows as the technique relies on rotational distributions.

In conclusion, the oxygen LIF technique is not suitable for use on turbomachinery or other high-speed flows above 300 K because of the long vibrational relaxation time of oxygen.

Thesis Supervisor:	Alan H. Epstein
Supervisor Title:	Professor of Aeronautics and Astronautics
	Director, Gas Turbine Laboratory

Acknowledgments

First of all, I would like to thank my advisor, Professor Alan H. Epstein, for giving me the opportunity to work on such a challenging project as well as for all his help and advice during my four years at MIT.

In addition, I thank Professors C. Forbes Dewey and Edward M. Greitzer, my committee members, for taking the time from their busy schedules to advise me and review my thesis.

I gratefully acknowledge the assistance of Dr. Kurt Annen of Aerodyne Research, Inc., with spectroscopy. At the Gas Turbine Laboratory, I would like to thank Dr. Gerald R. Guenette for his help with instrumentation; Messrs. Bill Ames and Jimmy Letendre for their technical assistance in the laboratory; Mr. Viktor Dubrowski for his assistance in the shop; and Mr. Mariano Hellwig for his assistance with electronic equipment. Also, I would like to thank Ms. Holly E. Anderson for her help with purchasing orders and financial affairs.

This project was supported by the National Aeronautics and Space Administration (NASA) through the Lewis Research Center, with Dr. Anthony J. Strazisar as technical monitor. Additional funding was provided by ABB.

Finally, I would like to thank my father, Mr. Argun Ceyhan, my mother, Mrs. Ayşe Ceyhan, and my sister, Ms. Pınar Ceyhan, for their support throughout this project.

Contents

List of Figures

List of Tables

Chapter 1
Introduction

1.1 Motivation

As gas turbine engine technology matures, increasing engine performance in terms of either specific thrust (or power) or efficiency requires detailed understanding of the internal flows in turbomachinery. One tool necessary for studying internal flow phenomena in compressors and turbines is a new, nonintrusive, high-resolution and high-speed temperature measurement technique. Conventional temperature measurement methods are too intrusive, too coarse and too slow for use with turbomachinery bladerows.

In addition, the drastic increase in computational capacity over the past 10–20 years have led to the development of many computational codes for analyzing turbomachinery flows and designing turbomachinery components. However, the development of these tools have outstripped the ability of experimentalists to verify the validity of these computer codes.

Three sample applications illustrate the need for and the potential utility of a nonintrusive technique for intrarotor temperature measurements in turbomachinery:

1. **Turbine Heat Transfer:** For a given thrust, the turbine inlet temperature determines the size and weight of an aircraft engine. Higher turbine inlet temperatures result in smaller and lighter engines. However, turbine inlet temperature is limited by the metal temperature of the turbine blades, which are heated by the hot combustion gases. Numerous cooling schemes have been used in jet engines to increase the turbine inlet temperature.

   Unfortunately, the heat transfer process from the combustion gases to the turbine blades is not well understood, and the design of turbine blade cooling schemes is art rather than science. Although heat transfer rates calculated by computer codes agree with the rates measured in experiments using stationary cascades, the actual heat transfer rates in real engines are up to twice as high. Underestimation of the heat transfer rates has a severe impact on engine life. For example, in a typical military aircraft turbine, a 5% underestimation in the heat transfer rate leads to a 33 K higher metal temperature with a subsequent 50% reduction in turbine life [25]. Therefore, designers are forced to use substantial safety margins with a resulting penaly in cost and performance.

   Several studies at MIT Gas Turbine Laboratory (GTL) have used a fully-scaled, blowdown model [6, 7, 11, 12] of a high-work aircraft engine turbine to study turbine heat

transfer. Specially manufactured heat flux and temperature sensors were used to measure heat flux into and metal temperature on turbine blades [1,2,8]. If a nonintrusive technique is used to measure the intrarotor gas temperature driving the heat transfer in this turbine, the local Nusselt (or Stanton) number may be computed along the blade. The Nusselt (or Stanton) number data will then lead to a more fundamental understanding of the heat transfer processes in a gas turbine.

The temperature measurement accuracy required for heat transfer measurements is 5–10% of the temperature difference driving the heat transfer. At full-scale temperatures, this is approximately 18–36 K. At the scaled temperatures of the MIT Blowdown Turbine facility, the accuracy requirement is 5–10 K.

2. **Compressor Aerodynamics:** The understanding of turbomachinery aerodynamics is important to prevent compressor unstabilities such as stalls and surges, which restrict the operating envelope of an aircraft engine and pose safety hazards to the aircraft.

   Optical velocity measurement techniques, such as laser doppler anemometry (LDA) and particle image velocimetry (PIV), have been and are being implemented on turbomachines to measure intrarotor velocity fields [13,28,29]. However, since internal turbomachinery flows are transonic, they are governed by the nondimensional Mach number. As the speed of sound in a gas is a function of temperature, local velocity measurements are not enough and complementary temperature measurements are necessary to compute the Mach number.

   The temperature measurement accuracy required for 0.5–1% accuracy in Mach number is 1–2%. At 300 K, this translates to 3–6 K.

3. **Efficiency Measurements:** The fuel consumption of a gas turbine engine is determined by the efficiency of the turbomachinery. Therefore, engine designers are pushing towards higher efficiencies and accurate measurement of such efficiencies is essential.

   The efficiency of a compressor stage is calculated from the inlet and outlet temperatures and pressures. If a nonintrusive technique is used to measure the temperatures, these measurements may be combined with complementary pressure measurements to calculate the stage efficiency.

   For a compresssor stage pressure ratio of 1.7, the required temperature measurement accuracy for 1% accuracy in calculated efficiency is 0.14% overall, or 0.07% for each temperature measurement. At 300 K, this corresponds to an absolute temperature measurement accuracy of 0.2 K.

Laser induced fluorescence (LIF) of oxygen has been touted as a high-accuracy temperature measurement technique. It is indeed very attractive for turbomachinery measurements. Specifically, this tehcnique uses high-energy ultraviolet (UV) photons, which are easier to detect than visible or infrared (IR) radiation. As it uses oxygen molecules in air, it requires no seeding or cleanup, an important consideration for large turbomachinery rigs. Furthermore, this technique provides a wavelength shift which allows the apparatus to distinguish

the temperature-sensitive signals from reflected laser light. Finally, this technique uses commercially available equipment (e. g. laser, spectrometer, detector) allowing the engineers to concentrate on the measurement rather than on the apparatus development.

1.2 Literature Review

The oxygen LIF temperature measurement technique has been feasible since about 1984, when the first argon fluoride (ArF) excimer laser, which is used to excite the oxygen molecules, was developed. The following survey describes the research in this field since 1984:

- In 1984, Massey and Lemon [21] used a custom-built excimer laser to study oxygen LIF in room-temperature air. Although these researchers calculated that a ± 1 K temperature, $\pm 1\%$ density, 1 mm^3 spatial and 1 μs temporal resolution could be achieved simultaneously, they did not achieve these results in their experiments. This was the first reported study using oxygen LIF.

- In 1986, Lee and Hanson [19] developed a spectral model for the oxygen LIF process. These authors also calculated and published theoretical data for line strenghts, spectral absorption coefficients, relative fluorescence spectra, total fluorescence and integrated absorption coefficients for oxygen transitions excited by a broadband ArF excimer laser at 300 K, 500 K, 1000 K, 1500 K and 2000 K.

- Also in 1986, Lee, Paul and Hanson [20] used planar oxygen LIF to qualitatively study the real-time evolution of discrete flame structures in high-temperature ($\sim$2000 K) methane-air flames.

- In 1987, Cohen, Lee, Paul and Hanson [5] published several two-dimensional images taken across a slightly underexpanded supersonic free jet using oxygen LIF.

- In 1988, Laufer, McKenzie and Huo [18] used experiments and theoretical calculations to determine conditions under which oxygen LIF could be used for temperature measurements in aerodynamic flows. The researchers identified and discussed various external features present in the LIF spectrum, but did not present any data on accuracy and resolution.

- Also in 1988, Miles, Connors, Howard, Markovitz and Roth [23] proposed a combination of simultaneous oxygen LIF and Rayleigh scattering measurements for two-dimensional measurements of temperature and density. They developed models for both mechanisms and experimentally studied the LIF emission spectrum between 100 K and 1600 K.

- Between 1988 and 1990, Laufer, Fletcher and McKenzie [15–17] investigated low-pressure ($\sim$ 0.01 atm) and low-temperature ($\sim$ 60 K) measurements in hypersonic wind tunnel flows using oxygen LIF. They concluded that the uncertainty in temperature measurements could be less than 2% if it were limited by the photon-statistical noise.

- In 1989, Miles, Connors, Markovitz, Howard and Roth [22,24] used oxygen LIF plus oxygen Raman excitation to examine statistics and structure of velocity profiles across the free shear layer of an underexpanded, supersonic free jet.

- In 1990, Annen [3] studied the feasibility of various optical temperature diagnostics and concluded that the oxygen LIF was the best method for temperature measurements in turbomachinery. Annen also showed the feasiblity of oxygen LIF for temperature measurements by performing qualitative proof-of-concept experiments.

- In 1991, Fletcher and McKenzie [9,10] used narrowband oxygen LIF measurements with Raman normalization to measure density, temperature and their fluctuations is a Mach 2 wind tunnel.

- In 1992, working at the MIT Gas Turbine Laboratory, Kolczak [14] built a benchtop apparatus and attempted to measure temperature in low-speed flow in a controlled-temperature test cell using oxygen LIF. Although this author investigated the effect of various experimental parameters and identified several problems with his components and setup, he was unable to reduce his data to achieve the desired precision. The current project uses the components (i. e. laser, spectrometer and detector) from Kolczak's research.

- Also in 1992, Annen and Nelson [4] conducted experiments on Kolczak's apparatus to demonstrate quantitatively the feasibility of simultaneous oxygen LIF and Raman measurements as a temperature diagnostic. These researchers claimed to demonstrate a better than 2 K temperature measurement precision.

- In 1992 and 1993, Smith, Price and Williams [26,27] evaluated the feasibility of a two-line exicitation method using oxygen LIF for measurements in the 300–500 K temperature range. Based on low-speed measurements, these authors claimed that errors less than $\pm 5\%$ were achievable.

As this survey shows, although oxygen LIF has been proposed and used as a temperature diagnostic, the experiments have been run on clean, well-understood, laboratory-type flows with almost unlimited optical access. The objective of these studies have been either to demostrate temperature sensitivity or to obtain qualitative data to study flow structures. Furthermore, only a few of these studies were on high-speed, compressible flows. Finally, no comprehensive data analysis for the oxygen LIF technique has been published.

1.3 Objectives and Approach

The main objective of this study is to evaluate the feasiblity of using the oxygen LIF temperature measurement technique for high-accuracy intrarotor measurements in turbomachines. In addition, a comprehensive, quantitative error analysis will be performed for temperature measurements in both low-speed and high-speed flows.

The turbomachinery environment imposes severe constraints on the experimental apparatus. The most important constraint is the limited optical access to the flow path.

Consequently, the experimental apparatus will be designed for the turbomachinery environment in general and the MIT Blowdown Turbine facility in particular. This facility, which is described by Guenette [12], and Epstein, Guenette and Norton [7], is representative of the many turbomachinery research rigs. The engineering requirements for the experimental apparatus are listed in Table 1.1.

To be of engineering utility, a measurement technique must have an NIST-traceable calibration as well as a robust error analysis. The experimental apparatus will be used to perform a comprehensive, quantitative error analysis in a controlled-temperature, controlled-pressure test cell. The error analysis will then be extended to high-speed, compressible flows by studying the flow issuing from a converging nozzle.

Although the turbomachinery environment provides the main motivation for this project, the error analysis will, of course, be applicable to other situations.

1.4 Thesis Organization

The LIF temperature measurement theory is discussed in Chapter 2. The theory is used in the identification of the potential error sources as well as the preliminary evaluation of various measurement and normalization methods.

Chapter 3 describes the experimental apparatus. This chapter points out the constraints imposed by the turbomachinery environment and their influence on the apparatus design. The performance of the apparatus components (e. g. laser, detector), as well as their impact on the measurement technique, are discussed.

Chapter 4 details the data reduction technique.

The error analysis for low-speed flows is discussed in Chapter 5. The impact of various error and noise sources on the measurement accuracy and precision is described and supported by experimental data where necessary. Various techniques for improving technique precision and accuracy, as well as their limitations, are outlined.

Chapter 6 extends the error analysis to compressible, high-speed flows. Vibrational relaxation rate, which limits the applicability of the technique in high-speed flow, is discussed. Spectroscopic and experimental data are used to support the discussion. The data from the literature involving compressible flows are re-examined in light of the discussion of this chapter.

A final summary and conclusions are provided in Chapter 7. The contribution of the thesis are outlined in that chapter.

Finally, Appendix A describes the calibration apparatus used in this project.

References

[1] Abhari, R. S., and Epstein, A. H. An Experimental Study of Film Cooling in a Rotating Transonic Turbine. *Journal of Turbomachinery 116*, 1 (January 1994), 63–70.

[2] Abhari, R. S., Guenette, G. R., Epstein, A. H., and Giles, M. B. Comparison of Time-Resolved Turbine Rotor Blade Heat Transfer Measurements and Numerical Calculations. *Journal of Turbomachinery 114*, 4 (October 1992), 818–827.

[3] ANNEN, K. State Variable Diagnostic Studies. Tech. Rep. ARI-RR-766, Aerodyne Research, Inc., 45 Manning Road, Billerica, MA 01821, February 1990.

[4] ANNEN, K., AND NELSON, D. Turbomachinery Tempearture Measurements Using an O_2 LIF Flowfield Diagnostic. Tech. Rep. ARI-RR-954, Aerodyne Research, Inc., 45 Manning Road, Billerica, MA 01821, September 1992.

[5] COHEN, L. M., LEE, M. P., PAUL, P. H., AND HANSON, R. K. Two-Dimensional Imaging Measurements in Supersonic Flows Using Laser-Induced Fluorescence of Oxygen. *AIAA Paper AIAA-87-1527* (1987).

[6] EPSTEIN, A. H., GUENETTE, G. R., AND NORTON, R. J. G. The MIT Blowdown Turbine Facility. *ASME Paper 84-GT-116* (1984).

[7] EPSTEIN, A. H., GUENETTE, G. R., AND NORTON, R. J. G. The Design of the MIT Blowdown Turbine Facility. Tech. Rep. 183, Massachusetts Institute of Technology, Cambridge, Massachusetts, April 1985.

[8] EPSTEIN, A. H., GUENETTE, G. R., NORTON, R. J. G., AND YUZHANG, C. High-Frequency Response Heat-Flux Gauge. *Review of Scientific Instruments 57*, 4 (April 1986), 639–649.

[9] FLETCHER, D., AND MCKENZIE, R. Measurements of Density, Temperature, and Their Fluctuations in Turbulent, Supersonic Flow Using UV Laser Spectroscopy. *Sixth International Symposium on Applications of Laser Techniques to Fluid Mechanics* (July 1992).

[10] FLETCHER, D., AND MCKENZIE, R. Single-Pulse Measurement of Density and Temperature in a Turbulent, Supersonic Flow Using UV Laser Spectroscopy. *Optics Letters 17*, 22 (November 1992), 1614–1616.

[11] GUENETTE, G. R., EPSTEIN, A. H., GILES, M. B., HAIMES, R., AND NORTON, R. J. G. Fully scaled transonic turbine rotor heat transfer measurements. *ASME Paper 88-GT-171* (1988).

[12] GUENETTE, JR., G. R. *A Fully Scaled Short Duration Turbine Experiment.* PhD thesis, Massachusetts Institute of Technology, Cambridge, MA, 1985.

[13] HATHAWAY, M. D., CHRISS, R. M., WOOD, J. R., AND STRAZISAR, A. J. Experimental and Computational Investigation of the NASA low-speed centrifugal compressor flow field. *Journal of Turbomachinery 115*, 3 (July 1993), 527–542.

[14] KOLCZAK, F. Temperature Measurements in a Flow Using Laser Induced Fluorescence of Oxygen. Master's thesis, Massachusetts Insitititue of Technology, Cambridge, MA 02139, September 1992.

[15] LAUFER, G., FLETCHER, D., AND MCKENZIE, R. A Method for Measuring Temperatures and Densities in Hypersonic Wind Tunnel Air Flows Using Laser Induced O_2 Fluorescence. *AIAA Paper AIAA-90-0626* (1990).

[16] LAUFER, G., MCKENZIE, R., AND FLETCHER, D. Method for Measuring Temperatures and Densities in Hypersonic Wind Tunnel Air Flows Using Laser Induced O_2 Fluorescence. *Applied Optics 29*, 33 (November 1990), 4873–4883.

[17] LAUFER, G., AND MCKENZIE, R. L. Temperature Measurements in Hypersonic Air Flows Using Laser-Induced O_2 Fluorescence. *AIAA Paper AIAA-88-4679-CP* (1988).

[18] LAUFER, G., MCKENZIE, R. L., AND HUO, W. M. Radiative Processes in Air Excited by an ArF Laser. *Optics Letters 13*, 2 (February 1988), 99–101.

[19] LEE, M. P., AND HANSON, R. K. Calculations of O_2 Absorption and Fluorescence at Elevated Temperatures for A Broadband Argon-Fluoride Laser Source at 193 nm. *Journal of Quantitative Spectroscopy and Radiative Transfer 36*, 5 (1986), 425–440.

[20] LEE, M. P., PAUL, P. H., AND HANSON, R. K. Laser-fluorescence imaging of O_2 in combustion flows using an ArF laser. *Optics Letters 11*, 1 (January 1986), 7–9.

[21] MASSEY, G., AND LEMON, C. Feasibility of Measuring Temperature and Density Fluctuations in Air Using Laser-Induced O_2 Fluorescence. *IEEE Journal of Quantum Electronics QE20* (May 1984), 454–457.

[22] MILES, R. B., CONNORS, J., MARKOVITZ, E., HOWARD, P., AND ROTH, G. Instantaneous Supersonic Velocity Profiles in An Underexpanded Sonic Air Jet by Oxygen Flow Tagging. *Physics of Fluids: A. Fluid Dynamics 1*, 2 (February 1989), 389–393.

[23] MILES, R. B., CONNORS, J. J., HOWARD, P. J., MARKOVITZ, E. C., AND ROTH, G. J. Proposed Single-Pulse Two-Dimensional Temperature and Density Measurements of Oxygen and Air. *Optics Letters 13*, 3 (March 1988), 195–197.

[24] MILES, R. B., CONNORS, J. J., MARKOVITZ, E. C., HOWARD, P. J., AND ROTH, G. J. Instantaneous Profiles and Turbulence Statistics of Supersonic Free Shear Layers by Raman Excitation plus Laser-Induced Electronic Fluorescence (RELIEF) Velocity Tagging of Oxygen. *Experiments in Fluids 8* (1989), 17–27.

[25] SHANG, T. *Influence of Inlet Temperature Distortion on Turbine Heat Transfer.* PhD thesis, Massachusetts Institute of Technology, Cambridge, Massachusetts, 1995.

[26] SMITH, M., PRICE, L., AND WILLIAMS, W. Laser-Induced Fluorescence Diagnostics Using a Two-Line Excitation Method. *AIAA Journal 31*, 3 (March 1993), 478–482.

[27] SMITH, M. S., PRICE, L. L., AND WILLIAMS, W. D. Laser-Induced Fluorescence Diagnostics Using a Two-Line Excitation Method. *AIAA Paper AIAA-92-0512* (1992).

[28] STRAZISAR, A. J. Laser Fringe Anemometry for Aero Engine Components. In *AGARD Conference Proceedings* (1986), vol. 399, pp. 6–1 to 6–32.

[29] WOOD, J. R., STRAZISAR, A. J., AND SIMONYI, P. S. Shock Structure Measured in a Transonic Fan Using Laser Anemometry. In *AGARD Conference Proceedings* (1987), vol. 401.

Table 1.1: Engineering Requirements

Temperature Range	300–500 K	BDT rig range
Temperature Accuracy	5–10 K	for heat transfer
	3–6 K	for Mach number
	0.2 K	for efficiency
Pressure Range	1–6 atm	BDT rig range
Spatial Resolution	$\leq$ 1mm	$\leq$3.6% of blade pitch
		$\leq$2.8% of blade chord
		$\leq$2.2–2.9% of blade span
Temporal Resolution	$\leq 4\mu$sec	$\leq$ 2% of blade passing

Chapter 2
Oxygen LIF Temperature Measurement Theory

2.1 General Description

During an oxygen LIF temperature measurement experiment, ultraviolet light at 193 nm from a pulsed argon-fluoride (ArF) excimer laser is focussed onto the point where the temperature is to be measured. The spectrum of the ArF laser overlaps a number of rovibrionic[1] transitions in the $B^3\Sigma_u^- \leftarrow X^3\Sigma_g^-$ Schumann-Runge band system of oxygen molecules. Consequently, some of the molecules occupying the lower quantum states of the overlapped transitions are promoted to the upper electronic state, with each promoted molecule absorbing a single photon from the laser beam.

The upper B electronic state of oxygen is highly unstable. Molecules promoted to this state undergo one of three processes. Most of the molecules predissociate into two oxygen molecules with no radiative release; the remaining molecules either spontaneously decay (fluoresce) back to the ground X electronic state or are moved out of the B state as a result of collisions with other molecules (collisional quenching). Each fluorescing molecule releases a single photon, whose wavenumber (inverse wavelength) is proportional to the energy difference between the upper and lower states of the fluorescence transitions.

Only those molecules occupying the ground quantum states of the absorption transitions overlapped by the laser may be promoted to the B electronic state, and may later fluoresce. Consequently, the fluorescence signal is proportional to the number of molecules in these quantum states. However, the distribution of molecules among quantum states is given by the Boltzmann distribution, which is a strong function of temperature (see Figure 2.1). Therefore, the fluorescence signal is a strong function of temperature. The LIF temperature measurement technique uses this temperature dependence of the fluorescence signal to determine the gas temperature.

2.2 LIF Model

In order to assist with the design of the experimental apparatus, as well as the evaluation of the subsequent results, a theoretical model of the LIF process was developed. Since all of the data and formulae in the model were obtained from literature, they are not re-listed here in the interest of brevity and accuracy.

The basic LIF model uses the equations given in Lee and Hanson [15]. The quantum level energies (term values) are computed using formulae given by Bergaman and Wofsy [2]

[1] In rovibrionic transitions, both the vibrational quantum number v and the rotational quantum number J change as the molecule transitions between two electronic states.

with the spectroscopic constants given by Creek and Nichols [7]. The partition function is computed using the formulae and data given by Vincenti and Kruger [24]. The absorption oscillator strengths are computed from Einstein coefficients listed in Allison, Dalgarno and Pasachoff [1] using formulae from Hollas [9]; the former source is also used for the fluroescence rates. Hönl-London factors (rotational line strenghts) are computed using the equations of Tatum [22], and Tatum and Watson [23]. Predissociation rates and line widths are calculated using the empirical model and data of Lewis et. al. [16]. Pressure broadening line widths are obtained from Cann et. al. [5,6][2].

The laser spectrum $E(\nu)$ was modeled as follows:

$$E(\nu) = E\left\{\underbrace{\frac{\eta_{\mathrm{LE}}}{\sigma_{\mathrm{NB}}\sqrt{\pi}}\exp\left[-\left(\frac{\nu-\nu_{\mathrm{NB}}}{\sigma_{\mathrm{NB}}}\right)^2\right]}_{\text{NARROWBAND COMPONENT}} + \underbrace{\frac{1-\eta_{\mathrm{LE}}}{\sigma_{\mathrm{BB}}\sqrt{\pi}}\exp\left[-\left(\frac{\nu-\nu_{\mathrm{BB}}}{\sigma_{\mathrm{BB}}}\right)^2\right]}_{\text{BROADBAND COMPONENT}}\right\} \tag{2.1}$$

In equation (2.1), E is the laser energy (J), η_{LE} is the laser locking efficiency[3] ($0 \leq \eta_{\mathrm{LE}} \leq 1$), and ν is the wavenumber. The central wavenumber ν_{BB} of the broadband component is 51714 cm^{-1} (193.37 nm); the central location ν_{NB} of the narrowband component is specified by the user. The characteristics widths σ_{NB} and σ_{BB} of the narrowband and broadband components are 2.67 cm^{-1} (0.01 nm) and 77.1 cm^{-1} (0.288 nm) respectively.

In addition, the model accounts for saturation (section 2.6), collisional quenching (section 2.7), and beam path absorption (section 2.8). The details of the model and data for these phenomena are discussed in the indicated sections.

The model was verified by comparing the spectral absorption coefficients at 300 K and 500 K calculated by the model to the data published by Lee and Hanson [15].

The relative strengths of the LIF signals, computed using LIF model, are shown in Figure 2.2. This figure demonstrates that in the temperature range of interest, the temperature sensitivity of the LIF signals originates from the upper vibrational levels ($v'' = 1$ and 2) being populated.

2.3 Normalization Methods

The measured fluorescence signal, in addition to being a function of temperature, also depends on laser energy, gas pressure (through density), measurement volume, collection solid angle, collection efficiency and detection efficiency. To determine the temperature, all of these extraneous quantities must be accounted for; any error or lack of precision in one or more of these parameters will result in a corresponding error or lack of precision in the determined temperature.

For turbomachinery applications, it is very difficult—even impossible—to determine all of these parameters to the required precision and accuracy. For example, measuring intrarotor pressure distribution in a turbomachine requires the implementation of another optical

[2]In the 1979 paper by Cann et. al. [5], the power -0.7 in equation (10) is incorrect. The correct power is $+0.7$. The formula appears correctly in the authors' 1984 paper [6].

[3]See section 2.5 for definition of laser locking efficiency.

technique which at best doubles the complexity of the overall measurement and at worst interferes with temperature measurement. Limited optical access prevents the placement of an intensity standard, such as a mercury lamp, necessary to determine collection efficiency and collection solid angle. Likewise, determining measurement volume, defined by the intersection of the laser beam with the imaged area, to the desired precision is impossible.

However, the ratio $\mathcal{R} = S_N/S_D$ of two signals which have a different temperature dependence but the same dependence on all of the other quantities is a function of temperature only, and is independent of other quantities. In this report, S_N and S_D are called numerator and denumerator signals, and $\mathcal{R}$ is called the temperature diagnostic ratio.

There are four ways of choosing the two signals S_N and S_D. Each of these normalization methods are described below.

2.3.1 Rayleigh Normalization

In this method, the total LIF signal is normalized by the Rayleigh signal generated by elastic scattering from oxygen and nitrogen molecules in air. The Rayleigh scattering is linearly dependent on density and is otherwise independent of temperature. It depends linearly on all of the other extraneous quantities listed above. Rayleigh normalization is discussed by Miles et. al. [19].

Unfortunately, the Rayleigh signal is at the same wavelength as the incident laser radiation. Consequently, the Rayleigh signal is contaminated by the reflection of laser light from casing window as well as flow surfaces.

In conclusion, Rayleigh normalization is not a feasible method for this application, and is not considered further.

2.3.2 Raman Normalization

In addition to LIF and Rayleigh signals, there are three signals originating from the vibrational Raman effect. One signal, centered near 202.5 nm, is due to nitrogen molecules, and the other two signals, centered near 199.4 nm and 205.7 nm, are due to oxygen molecules[4]. All Raman signals have the same spectral shape and width as the incident laser light. They depend linearly on density, but are otherwise independent of temperature. They depend lineary on all extraneous parameters.

Raman scattering coefficients for nitrogen and oxygen molecules are given by Bischel and Black [4] for the fundamental signals ($\Delta\nu = 1$). The strength of the second-order oxygen Raman signal is 16% of the fundamental signal [14].

The fundamental oxygen Raman signal at 199.5 nm is blocked by the spectral filter used to eliminate reflected laser light. The weaker second-order oxygen Raman signal is not blocked; however, for temperatures above 300 K, this Raman signal is swamped by a stronger LIF signal at the same wavelength.

[4]The 205.7 nm signal is due to second-order Raman effect ($\Delta\nu = 2$). Although prohibited by classical spectroscopic principles, the second-order Raman signal is produced by the ArF laser because of the closeness of the laser wavelength to the resonance regions of the Schumann-Runge bands [14].

The spectral filter also reduces the nitrogen Raman signal 36% relative to the LIF signals. As a result, the nitrogen Raman signal level ranges from 10% of the LIF signal level at 300 K to 1.3% of the LIF signal level at 500 K. If Raman normalization is used, the precision of the ratio $\mathcal{R}$, and as a result, the precision of the measurement, will depend almost entirely on the uncertainty in the Raman signal. The strength of the Raman signal is compared with the LIF signal in Figure 2.3.

Although it is not attractive compared to the spectral normalization in the temperature range of interest, normalization by nitrogen Raman signals is feasible, and will be examined further in this chapter. For narrowband measurements, as well as for measurements below 300 K, Raman normalization is the only possibility.

2.3.3 Two-Line Normalization

In this technique, two narrowband pulses tuned to different absorption transitions are used, and the total fluorescence from each transition is recorded separately. The ratio of the two signals is used as the temperature diagnostic [20,21].

The advantage of this technique is that each pulse can be tuned to the optimal transitions such that the temperature measurement precision is maximized. For example, Smith, Price and Williams [20,21] suggest the use of $P(15)$ ($v'' = 0$) and $P(23)$ ($v'' = 1$) transitions for temperature measurement in the 297–500 K range.

However, this advantage is more than offset by the requirement for two expensive ArF lasers. Furthermore, this technique requires either two sets of focusing optics (e. g. turning mirrors and focusing lenses) to bring each pulse into the measurement volume or a mechanical apparatus for switching between the two laser beams. Consquently, both the cost and complexity of the experiment is increased significantly.

Therefore, two-line normalization is not feasible for this application and will not be considered further.

2.3.4 Spectral Normalization

The fluorescence spectrum induced by the ArF laser is shown in Figure 2.4 for three different temperatures. The fluorescence appears in spectral regions. As this figure shows, each spectral region has a different dependence on temperature. For example, the peaks at 205 nm and 212 nm increase significantly with temperature, and the peaks at 235 nm, 242 nm, 250 nm and 257 nm show a shift slightly to lower wavelengths with increasing temperature.

In spectral normalization, the total fluorescence signal is computed for each spectral region in the spectrum. These signals are then assigned to the numerator and denumerator signals S_N and S_D to form the temperature diagnostic ratio $\mathcal{R}$. Since all LIF signals exhibit the same dependence on extraneous parameters, the temperature diagnostic ratio is ideally a function of temperature only.

The assignment of regional signals to the numerator and denumerator signals is made using experimental data in such a way that the measurement precision is maximized. Details of these assignments are given in Chapter 4.

The spectral dependence of the LIF signals may be explained from LIF theory. The ArF laser spectrum overlaps transitions originating from $v'' = 0, 1$ and 2 vibrational levels of the ground electronic state. The transitions from each vibrational level fills a different vibrational level in the upper electronic state ($v'' = 0$ fills $v' = 4$, $v'' = 1$ fills $v' = 7$, and $v'' = 2$ fills $v' = 10$). The fluorescence from each upper vibrational level is concentrated in several spectral peaks, with each peak corresponding to a different vibrational level in the ground electronic state. The relative distribution of the fluorescence from a given upper vibrational level among these peaks is different for each vibrational level and is given by the ratio $A_{v'v''} / \sum_{v''} A_{v'v''}$, which can be computed from the data given by Allison, Dalgarno and Pasachoff [1]. As temperature increases, the fluorescence resulting from $v'' = 1$ and $v'' = 2$ absorption transitions become stronger, and the fluorescence spectrum shifts from the $v' = 4$ emission spectrum to $v' = 7$ and $v' = 10$ emission spectra.

Figure 2.5 shows the distribution of the fluorescence spectrum among vibrational bands for each of the upper vibrational states. The bar heights represent the fraction of total fluorescence in in each vibrational band. Because of bands outside the 200-270 nm spectrum considered here, the total does not sum to unity. However, 80%, 88% and 64% of the total emission from $v' = 4, 7$ and 10 levels are in this wavelength range.

Since spectral normalization depends on the relative strength of LIF signals originating from different vibrational levels, it cannot be used for temperatures below 300 K as the $v'' = 1$ and 2 transitions are very weak below this temperature. Futhermore, it cannot be used for narrowband measurements where only a single absorption transition from one vibrational level is excited. Raman normalization is the only feasible alternative for such measurements.

Although a spectrometer is needed to obtain the best precision from spectral normalization, this method may also be used with a less-complicated and less-expensive non-spectroscopic apparatus. In such a setup, two detectors are used to measure LIF signals. One detector, with a low pass filter, measures the total LIF signal in the $\lambda < \lambda_c$ region; the other detector, with a high-pass filter, measures the signal in the $\lambda > \lambda_c$ region. The two signals then form the temperature diagnostic ratio. The optimum cutoff wavelength λ_c has been determined to be 229 nm; details of this calculation are also given in Chapter 4.

The nitrogen Raman signal, marked in Figure 2.4, has the same linear dependence on extraneous parameters as LIF signals, and can be used as part of the denumerator signal S_D.

In conclusion, the spectral normalization offers the best performance in the temperature range for this application.

2.4 Theoretical Precision

The temperature diagnostic ratio is defined as

$$\mathcal{R} = \frac{S_N}{S_D} \tag{2.2}$$

where S_N and S_D are measured simultaneously but independently. Each measurement is accompanied by an uncertainty σ_{S_N} or σ_{S_D}. The resulting uncertainty in $\mathcal{R}$ is then given

by [3]

$$\sigma_{\mathcal{R}} = \mathcal{R}\left[\left(\frac{\sigma_{S_N}}{S_N}\right)^2 + \left(\frac{\sigma_{S_D}}{S_D}\right)^2\right]^{1/2} \tag{2.3}$$

and the temperature uncertainty is

$$\sigma_{\mathcal{R}} = \frac{\sigma_{\mathcal{R}}}{|d\mathcal{R}/dT|} = \frac{\mathcal{R}}{|d\mathcal{R}/dT|}\left[\left(\frac{\sigma_{S_N}}{S_N}\right)^2 + \left(\frac{\sigma_{S_D}}{S_D}\right)^2\right]^{1/2} \tag{2.4}$$

With the regional boundaries and assignments given in Chapter 4, the LIF model may be used to determine the theoretical $\mathcal{R}(T)$ curve for spectral and N_2 Raman normalization. These curves are plotted in Figure 2.6 and 2.7.

There are various sources of noise which contribute to the uncertainty in S_N and S_D. However, the fundamental noise in the signal originates from the quantum nature of radiation, and is therefore called quantum noise. Quantum noise, which cannot be eliminated, scales with the square root of the signal [17]

$$\sigma_{S_N} = K_Q\sqrt{S_N} \tag{2.5a}$$

$$\sigma_{S_D} = K_Q\sqrt{S_D} \tag{2.5b}$$

where $K_Q \geq 1$. For quantum-noise limited measurements, the temperature uncertainty may now be written

$$\sigma_T = \frac{K_Q\mathcal{R}/\sqrt{S_N}}{|d\mathcal{R}/dT|}(1+\mathcal{R})^{1/2} \tag{2.6}$$

Note from equation (2.6) that the temperature uncertainty depends on the square-root of the signal level. Increasing the signal level by a factor of four will cut the temperature uncertainty in half. Futhermore, these equations demonstrate that if one signal, say S_D, is much smaller than the other, the measurement uncertainty will be dominated by the noise in that signal.

Figure 2.8 plots the theoretical uncertainty for spectral and N_2 Raman normalizations as a function of temperature. As this figure shows, spectral normalization is better than N_2 Raman normalization for the 300-550 K temperature range of interest.

The values from Figure 2.8 may be converted to absolute uncertainties upon the specification of experimental parameters. For example, assuming a laser beam energy of 100 mJ, a measurement volume length of 1 mm, collection solid angle of 0.095 sr, transmission efficiency of 0.5% and pressure of 1 atm, the corresponding temperature uncertainties are 1.3 K for spectral normalization and 3.0 K for N_2 Raman normalization.

2.5 Narrowband and Broadband Measurements

The ArF laser used in this project can be operated in either narrowband or broadband mode. In broadband mode, the laser spectrum overlaps 58 absorption transitions in seven vibrational bands. In the narrowband mode, the laser spectrum can be tuned across the 192.9–193.8 nm range to one of these 58 transitions. The spectral width of the narrowband emission, which is 0.005 nm, is comparable with the line widths of the overlapped transitions.

The main advantage of narrowband measurement is that the laser can be tuned to the absorption transition which gives the best precision. Furthermore, this transition can be different depending on the temperature.

Spectral normalization uses the different emission spectra of the absorption transitions originating from different vibrational levels of the ground electronic state. As narrowband measurements excite a single transition from one quantum state, spectral normalization cannot be used with narrowband measurements. Consequently, nitrogen Raman is the only feasible normalization method.

Even when the laser is operated in narrowband mode, the laser spectrum contains some broadband component. The fraction of the total laser power in the narrowband component is known as the locking efficiency. The fluorescence spectrum also consists of broadband and narrowband components and depends strongly on locking efficiency. Consequently, for narrowband measurements, the locking efficiency must be precisely known. Also, in order to maximize the benefits of the narrowband measurement, the locking efficiency should be as close to unity as possible.

Figure 2.9 shows the temperature diagnostic ratio for narrowband measurements using the $P(19)$ transition from the $v'' = 1$ vibrational level. Five $\mathcal{R}$ curves are shown at different laser locking efficiencies.

The theoretical precision of the narrowband measurement technique is compared to the broadband measurement techniques in Figure 2.10. Except for temperatures below 350 K, the narrowband measurement precision is worse than broadband measurement using spectral normalization. This is because the measurement precision is determined by the uncertainties in the nitrogen Raman signal.

Figure 2.11 demonstrates the error resulting from the laser locking efficiency. This figure shows that the narrowband measurement is highly sensitive to the laser locking efficiency. At high temperature, the temperature error is almost 1 K for each 1% deviation in locking efficiency.

As will be discussed in Chapter 3, the maximum locking efficiency obtained from the particular ArF laser used in this project was less than 25%. Furthermore, the locking efficiency varied drastically with number of shots, going as low as 2% during a given experiment.

In conclusion, narrowband measurement is not feasible as a high-accuracy, high-precision technique for this application, and it is not considered further.

2.6 Saturation

Saturation is the loss in the expected fluorescence signal due to the depletion of the ground quantum states by the absorption transitions. The laser pump moves molecules

from the ground states to the upper electronic level. The ground states are then replenished by collisions with other molecules. These processes are shown schematically in Figure 2.12.

For transitions excited by the ArF laser, the laser pulse duration (approximately 10^{-8} s) is much longer than the response time of the oxygen molecules (approximately 10^{-11} s) [11]. Consequently, the system may be considered to be in steady state for the duration of the laser pulse. In steady state, the laser pump rate will equal the collisional replenishment rate. In this case, the formula for LIF signals become

$$S = \frac{1}{1 + (W_{12}/W_1^C)} S_o \tag{2.7}$$

where S_o is the LIF signal without saturation.

The collisional replenishment rate may be obtained from the pressure (collisional) broadening linewidth given by Cann et. al. [5,6] using the following formula given by Hollas [9]:

$$W_1^C = \pi c \Gamma(T, P) \tag{2.8}$$

In this equation, Γ is the pressure broadening linewidth (cm^{-1}).

In general, the collision rate scales with $P/T^{1/2}$. Consequently, saturation will be more important at low pressures and high temperatures. Futhermore, transitions originating from $v'' = 1$ and 2 vibrational levels are much stronger than those from $v'' = 0$ vibrational level. Since these transitions become stronger with increasing temperature, saturation will be more important at high temperatures.

Figure 2.13 shows the effect of saturation on the temperature diagnostic ratio $\mathcal{R}$, and Figure 2.14 shows the resulting temperature error ΔT. The theory indicates that saturation may indeed be a problem. Therefore, saturation will be examined using experimental data.

2.7 Collisional Quenching

Once an oxygen molecule is promoted to the upper electronic state by the laser pump, it may be moved out of this state before fluorescing as a result of collisions with other molecules. Consequently, the total LIF signal is reduced. This is known as collisional quenching. Furthermore, since the collision rate is a linear function of pressure, this introduces an additional, nonlinear pressure dependence to the temperature diagnostic ratio $\mathcal{R}$.

Most discussions of the oxygen LIF neglect collisional quenching by arguing that the predissociation rate is much higher than the collisional quenching rate [8, 12, 13, 15, 18]. However, if the collisional rate for the upper state is assumed to be equal to the collision rate for the lower state, which may be computed from the pressure broadening data given by Cann et. al. [5,6], the collision and predissociation rates seem to be of equal order in the pressure and temperature range of interest.

The only LIF study to mention collisional quenching is the paper by Miles et. al. [19]. For lines with low predissociation rates (i. e. $v'' = 1$ and $v'' = 2$ transitions), the measurements of these authors yield much less fluorescence than predicted, and the inclusion of a collisional

quenching rate of 1.0×10^{11} s^{-1} at 500 K and 1 atm is necessary to match the LIF theory to their experiments. This rate is about five times the rate predicted by the Cann data.

Figure 2.12 shows the dynamic processes which populate and deplete the energy level. In steady states, the population rate will equal the depletion rate. This yields the following expression for the LIF signal with collisional quenching:

$$S = \frac{1}{1 + \left(W_2^C / W_2^P\right)} S_o \tag{2.9}$$

In equation (2.9), S_o is the LIF signal without collisional quenching.

Since collision rate increases with increasing pressure, collisional quenching becomes more important at higher pressures. Furthermore, as temperature increases, transitions originating from $v'' = 1$ and $v'' = 2$ levels become stronger. Because these signals have lower predissociation rates than $v'' = 0$ signals, they are subject to stronger influence by collisional quenching. As a result, collisional quenching effects increase with temperature, even though the collision rate decreases with temperature ($\sim 1/T^{1/2}$).

Figures 2.15 and 2.16 shows the effect of collisional quenching on the temperature diagnostic ratio $\mathcal{R}$. If the pressure is known perfectly, the temperature may be determined from a $\mathcal{R}(T)$ curve calibrated at that pressure, but any error or uncertainty in the pressure will result in a corresponding error or uncertainty in the determined temperature. This error is shown in Figure 2.17.

The effect of collisional quenching on $\mathcal{R}$ may be written as follows:

$$\mathcal{R} \approx \mathcal{R}_{\text{ref}} + C\left(P - P_{\text{ref}}\right) \tag{2.10}$$

where $P_{\text{ref}} = 3.77$ atm. Figure 2.18 shows the quantity $C/\mathcal{R}_{\text{ref}}$ as a function of temperature. This data will be used in Chapter 5 to evaluate the influence of collisional quenching.

In conclusion, even though most LIF studies neglect collisional quenching because of the high predissociation rate of oxygen, the small amount of data in the literature suggest that this approximation may not be valid. This will be examined further using experimental data.

2.8 Beam Path Absorption

The beam has to travel some distance before it gets to the measurement volume. In this path, the beam will excite the same processes which produce the radiative signals of interest in the measurement volume. These processes will absorb photons from the laser beam and will not only reduce the beam fluence at the measurement volume but also modify its spectral distribution. This section studies the impact of these beam effects on the temperature measurement accuracy.

The impact of beam path absorption on the laser spectrum may be modeled using the following equation:

$$E(\nu) = E_o(\nu) \int_0^{L_p} k_\nu\left(\nu; T_p(x)\right) P_p(x) X_{O_2} dx \tag{2.11}$$

In equation (2.11), $E_o(\nu)$ is the original laser spectrum, $0 \leq x \leq L_p$ is the beam path, $T_p(x)$ and $P_p(x)$ are the beam path temperature and pressure distributions, and X_{O_2} is the mole fraction of oxygen ($X_{O_2} = 0.2$ for air). The quantity $k_\nu(\nu;T)$ is the spectral absorption coefficient, which may be computed using the formulae given by Lee and Hanson [15].

As equation (2.11) indicates, the impact of the beam path absorption on the LIF signals from the measurement volume depends on not only the beam path length but also the beam path temperature distribution. Figure 2.19 shows the temperature error resulting from beam path absorption effects when the path temperature is equal to the measurement point temperature. Figures 2.20 through 2.22 are corresponding plots for fixed measurement point temperatures of 300 K, 425 K and 550 K respectively.

For a fixed path length, beam path absorption effects appear as pressure effects. The impact of beam path absorption effects may be approximated with the formula

$$\begin{aligned} \mathcal{R} &\approx \mathcal{R}_{\text{ref}} + C' \left[(P_p X_{O_2} L_p) - (P_p X_{O_2} L_p)_{\text{ref}} \right] \\ &\approx \mathcal{R} + C \left[P_p - (P_p)_{\text{ref}} \right] \end{aligned} \tag{2.12}$$

where $(P_p)_{\text{ref}} = 3.77$ atm. Figure 2.23 plots the quantity $C/\mathcal{R}_{\text{ref}}$ as a function of temperature. In Chapter 5, this quantity is used to determine whether the observed pressure effects originate from collisional quenching or beam path absorption.

Because beam path absorption effects depend on the path temperature, a thorough verification of the simple model presented here requires the independent variation of the path and measurement point temperatures.

2.9 Contaminating Signals

According to Laufer et. al. [14], the ArF laser signal radiation produces additional signals which interfere with the use of oxygen fluorescence in temperature measurement. Apart from the Raman signals discussed earlier (see section 2.3.2), the authors identify two signals, one due to carbon atom fluorescence (C-LIF) and the other due to oxygen ion fluorescence (O_2^+ LIF).

Both of these signals are generated by fluorescence transitions resulting from multiphoton absorption transitions and show a nonlinear dependence on laser fluence. Therefore, in the presence of these signals, the spectral normalization method is not able to remove the laser fluence dependence. Furthermore, since these transitions do not necessarily originate from highly predissociated states with short lifetimes, they may be subject to strong collisional quenching. Consequently, it is necessary to understand the behavior of these signals so that they can be either eliminated during the experiment or accounted for during data reduction.

Figure 2.24 presents three experimental spectra taken at (a) high fluence and high pressure, (b) high fluence and low pressure, and (c) low fluence and high pressure. The O_2 LIF and N_2 Raman peaks are marked. The remaining signals are due to the two contaminating processes discussed here.

According to Laufer et. al. [14] ,the peak at 248 nm is due to carbon atom fluorescence (C LIF). According to the model presented by the authors, this signal shows a cubic dependence

on laser fluence. Since the C LIF peak is localized to a small region around 248 nm, it can be omitted from the S_N and S_D signals.

The remaining contaminating signals are due to O_2^+ fluorescence. Although the O_2^+ LIF spectrum consists of a number of emission lines, the separation of these lines are too small to be resolved by the apparatus[5]. The resulting "smeared" O_2^+ spectrum appears as a series of localized peaks on a slowly varying background. Note that the O_2^+ LIF spectrum is also present under O_2 LIF signals and therefore cannot be spectrally isolated.

Figure 2.25 replots the high fluence, low pressure spectrum of Figure 2.24. Superimposed on the spectra are the band head locations of the $A^2\Pi_u \rightarrow X^2\Sigma_g$ system of O_2^+ computed using the data given by Krupenie [10]. The experimental data is consistent with O_2^+ fluorescence from this system. First, the increasing separation of band heads with increasing wavelength explains the decrease in the background. Second, this band system is "red-shifted," which means that the actual peak centers will fall slightly to the longer wavelength side of the band head; this is indeed the case in Figure 2.25.

Yang et. al. [25] suggest the following two-step, three-photon process for the production of fluorescing O_2^+ ions: an O_2 molecule in the X ground electronic state absorbs three photons from the ArF spectrum exciting it to an energy above the energy of the A state of O_2^+. Subsequently, the electron is ejected from this excited O_2 molecule to leave the O_2^+ ion at the fluorescing A electronic state[6]. Since the production of the fluorescing ions is a three-photon process, the O_2^+ LIF spectrum should exhibit a cubic dependence on laser fluence[7].

As the electrons ejected during the three-photon ionization process may have continuous distribution of translational energy, the ionization process does not take between specific quantum states. Therefore, all O_2 molecules may be ionized, and, except of a $1/T$ dependence introduced through density effects, O_2^+ LIF signal should be independent of temperature.

2.10 Summary

The oxygen laser induced fluorescence (LIF) technique measures gas temperature by probing the lower quantum states of electronic transitions overlapped by the argon fluoride (ArF) laser. Since the distribution of molecules among quantum states is a strong function of temperature, the LIF signals produced by the ArF laser depend on temperature, and the gas temperature may be inferred from the strength of LIF signals.

A model for the LIF process has been constructed from formulae and data in literature.

[5]The experimental apparatus cannot resolve the rotational lines of O_2 LIF spectrum either. See section 4.6.

[6]The emission wavelengths given in Yang et. al. [25] are incorrect. The emission for the $A \rightarrow X$ band is over 194–653 nm, and the emission for the $b \rightarrow a$ band is over 499–853 nm [10].

[7]The model presented by Laufer et. al. is not clear. Their paper implies that the fluoresence *originates* from the X ground electronic state of O_2^+, but does not identify the lower electronic state. Moreover, the source of the data used to mark the O_2^+ LIF wavelenghts is also not given. Finally, the O_2^+ flourescence locations in their experimental spectrum do not agree with the O_2^+ locations given. Although the authors suggest that this is due to poor signal-to-noise ratio, their O_2 LIF peaks, which are of similar strength, are in their correct location. Consequently, their model cannot be trusted.

This model may be used to understand the behavior and evaluate the theoretical precision of the technique.

LIF signals also depend on extraneous quantities such as laser fluence and gas pressure. Since these quantities cannot be measured simultaneously during turbomachinery experiments, a normalization method must be used. Four normalization methods are described, but only two, namely N_2 Raman normalization and spectral normalization, are feasible for turbomachinery measurements. LIF model indicates that the theoretical precision of the spectral normalization method is better than that of the N_2 Raman normalization.

Although narrowband measurements, where the laser wavelength is tuned to the optimum transition, allow the measurement precision to be maximized, any variation in the laser locking efficiency introduces a substantial error into the measured temperature. Since the locking efficiency of the ArF laser used in this project is neither high nor stable, narrowband measurements are not feasible.

Extraenous processes, specifically collisional quenching, saturation, beam path absorption and O_2^+ LIF signals may affect the accuracy of the temperature measurements obtained using O_2 LIF techinique. These processes will be studied further using experimental data.

References

[1] ALLISON, A. C., DALGARNO, A., AND PASACHOFF, N. W. Absorption by Vibrationally Excited Molecular Oxygen in the Schumann-Runge Continuum. *Planetary and Space Science 19* (1971), 1463–1473.

[2] BERGEMAN, T. H., AND WOFSY, S. C. The Fine Structure of O_2 ($B^3\Sigma_u^-$). *Chemical Physics Letters 15*, 1 (July 1972), 104–107.

[3] BEVINGTON, P. R., AND ROBINSON, D. K. *Data Reduction and Error Analysis for the Physical Sciences*, second ed. McGraw-Hill, Inc., New York, NY, 1992.

[4] BISCHEL, W., AND BLACK, G. Wavelength Dependence of Raman Scattering Cross Sections From 200-600 nm. *AIP Conference Proceedings 100* (1983), 181–187.

[5] CANN, M. W. P., NICHOLLS, R. W., EVANS, W. F. J., KOHL, J. L., ET AL. High Resolution Atmospheric Transmission Calculations Down to 28.7 km in the 200-243-nm Spectral Range. *Applied Optics 18*, 7 (April 1979), 964–977.

[6] CANN, M. W. P., SHIN, J. B., AND NICHOLS, R. W. Oxygen absorption in the spectral range 180-300 nm for temperatures to 3000K and pressures to 50 atm. *Canadian Journal of Physics 62* (1984), 1738–1751.

[7] CREEK, D. M., AND NICHOLS, R. W. A comprehensive re-analysis of the O_2 ($B^3\Sigma_u^- - X^3\Sigma_g^-$) Schumann-Runge band system. *Proceedings of the Royal Society of London; Series A 341* (1975), 517–536.

[8] FLETCHER, D., AND MCKENZIE, R. Single-Pulse Measurement of Density and Temperature in a Turbulent, Supersonic Flow Using UV Laser Spectroscopy. *Optics Letters 17*, 22 (November 1992), 1614–1616.

[9] HOLLAS, J. M. *Modern Spectroscopy*, second ed. John Wiley & Sons, Chichester, England, 1992.

[10] KRUPENIE, P. H. The Spectrum of Molecular Oxygen. *Journal of Physical and Chemical Reference Data 1*, 2 (1972), 423–534.

[11] LAUFER, G., FLETCHER, D., AND MCKENZIE, R. A Method for Measuring Temperatures and Densities in Hypersonic Wind Tunnel Air Flows Using Laser Induced O_2 Fluorescence. *AIAA Paper AIAA-90-0626* (1990).

[12] LAUFER, G., MCKENZIE, R., AND FLETCHER, D. Method for Measuring Temperatures and Densities in Hypersonic Wind Tunnel Air Flows Using Laser Induced O_2 Fluorescence. *Applied Optics 29*, 33 (November 1990), 4873–4883.

[13] LAUFER, G., AND MCKENZIE, R. L. Temperature Measurements in Hypersonic Air Flows Using Laser-Induced O_2 Fluorescence. *AIAA Paper AIAA-88-4679-CP* (1988).

[14] LAUFER, G., MCKENZIE, R. L., AND HUO, W. M. Radiative Processes in Air Excited by an ArF Laser. *Optics Letters 13*, 2 (February 1988), 99–101.

[15] LEE, M. P., AND HANSON, R. K. Calculations of O_2 Absorption and Fluorescence at Elevated Temperatures for A Broadband Argon-Fluoride Laser Source at 193 nm. *Journal of Quantitative Spectroscopy and Radiative Transfer 36*, 5 (1986), 425–440.

[16] LEWIS, B. R., BERZINS, L., CARVER, J. H., AND GIBSON, S. T. Rotational Variation of Predissociation Linewidth in the Schumann-Runge Bands of O_2. *Journal of Quantitative Spectroscopy and Radiative Transfer 36*, 3 (1986), 187–207.

[17] MARCUSE, D. *Principles of Quantum Electronics.* Academic Press, New York, NY, 1980.

[18] MASSEY, G., AND LEMON, C. Feasibility of Measuring Temperature and Density Fluctuations in Air Using Laser-Induced O_2 Fluorescence. *IEEE Journal of Quantum Electronics QE20* (May 1984), 454–457.

[19] MILES, R. B., CONNORS, J. J., HOWARD, P. J., MARKOVITZ, E. C., AND ROTH, G. J. Proposed Single-Pulse Two-Dimensional Temperature and Density Measurements of Oxygen and Air. *Optics Letters 13*, 3 (March 1988), 195–197.

[20] SMITH, M., PRICE, L., AND WILLIAMS, W. Laser-Induced Fluorescence Diagnostics Using a Two-Line Excitation Method. *AIAA Journal 31*, 3 (March 1993), 478–482.

[21] SMITH, M. S., PRICE, L. L., AND WILLIAMS, W. D. Laser-Induced Fluorescence Diagnostics Using a Two-Line Excitation Method. *AIAA Paper AIAA-92-0512* (1992).

[22] TATUM, J. B. Hönl-London Factors for $^3\Sigma^{\pm} - {}^3\Sigma^{\pm}$ Transitions. *Canadian Journal of Physics 44* (1966), 2944–2946.

[23] TATUM, J. B., AND WATSON, J. K. G. Rotational Line Strengths in $^3\Sigma^{\pm} - {}^3\Sigma^{\pm}$ Transitions with Intermediate Coupling. *Canadian Journal of Physics 49* (1971), 2693–2703.

[24] VINCENTI, W. G., AND KRUGER, JR., C. H. *Introduction to Physical Gas Dynamics.* Robert E. Krieger Publishing Company, Malabar, FL, 1965.

[25] YANG, S., HILL, W. T., AND DIXIT, S. N. Multiphoton dissociative ionization of O_2: Competition between dissociation and ionization in excited states. *Journal of Chemical Physics 100*, 9 (May 1994), 6434–6444.

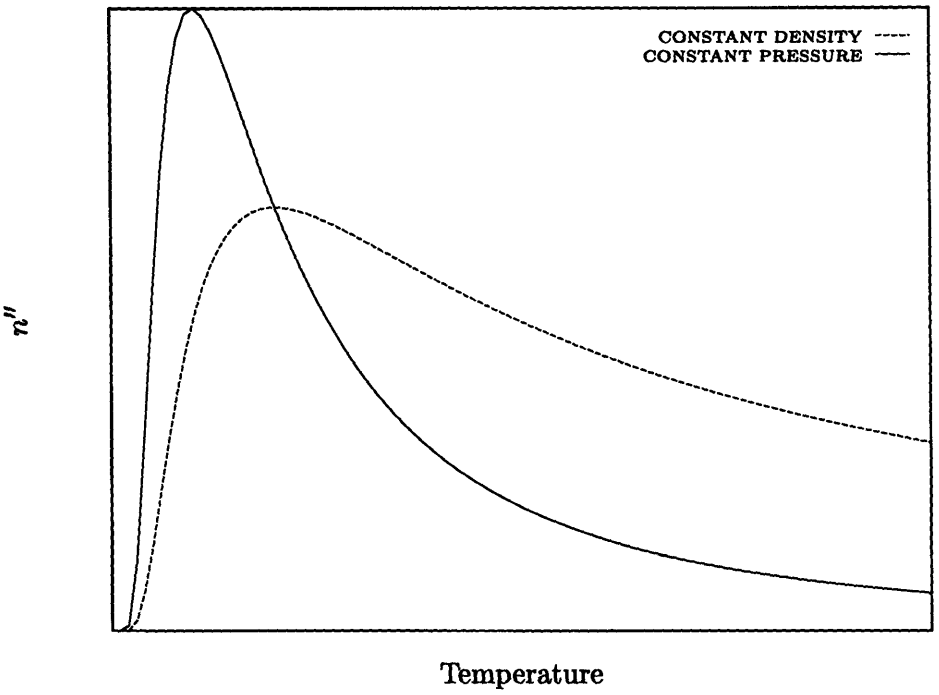

Figure 2.1: Temperature Dependence of Quantum State Populations

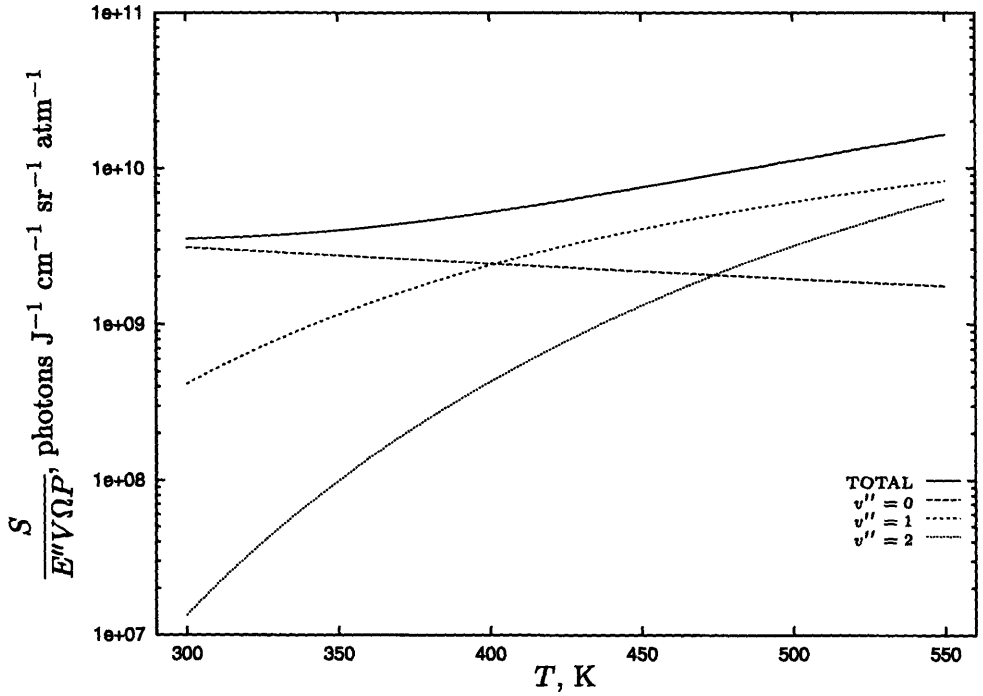

Figure 2.2: Temperature Dependence of LIF Signals

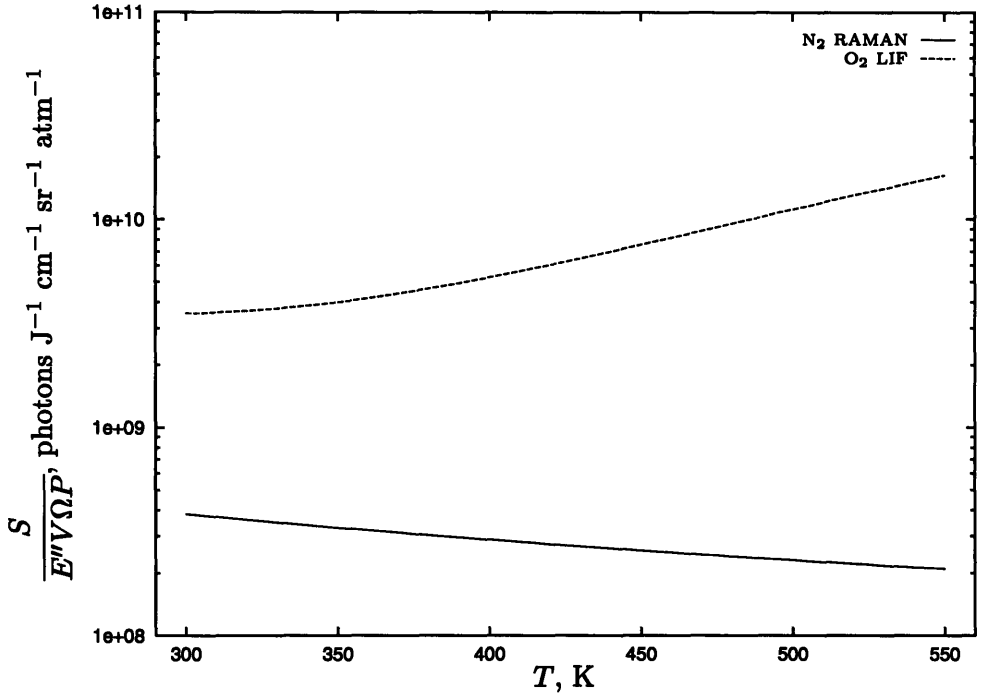

NOTE: The N_2 Raman signal has been scaled by the relative tranmission of the spectral filter, which is 36% compared to the O_2 LIF signals.

Figure 2.3: Temperature Dependence of N_2 Raman Signal compared with O_2 LIF Signal

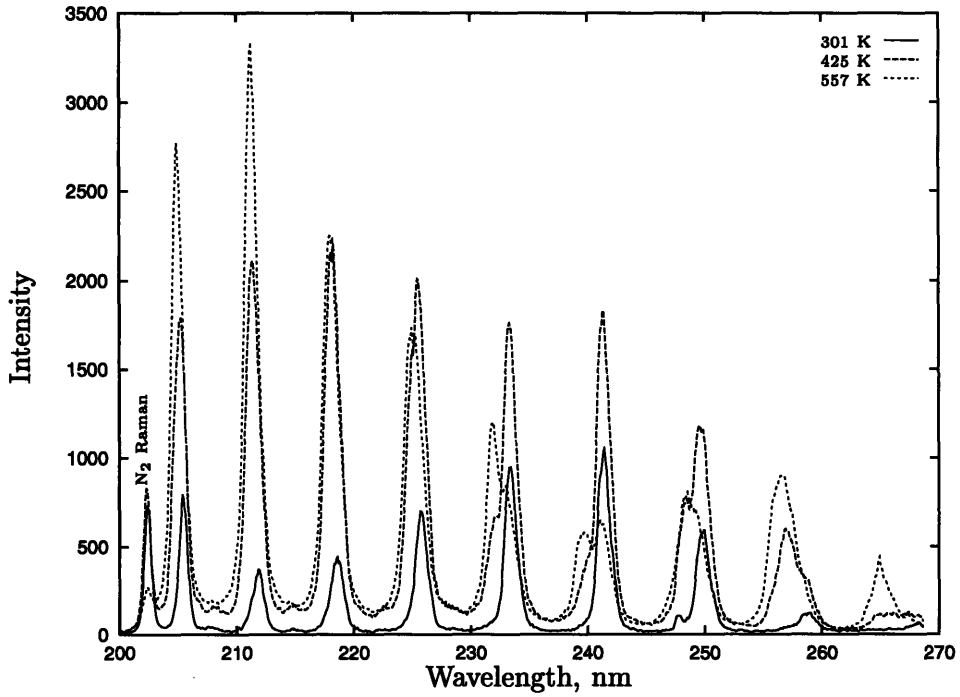

Figure 2.4: Measured Temperature Dependence of Typical LIF Spectra

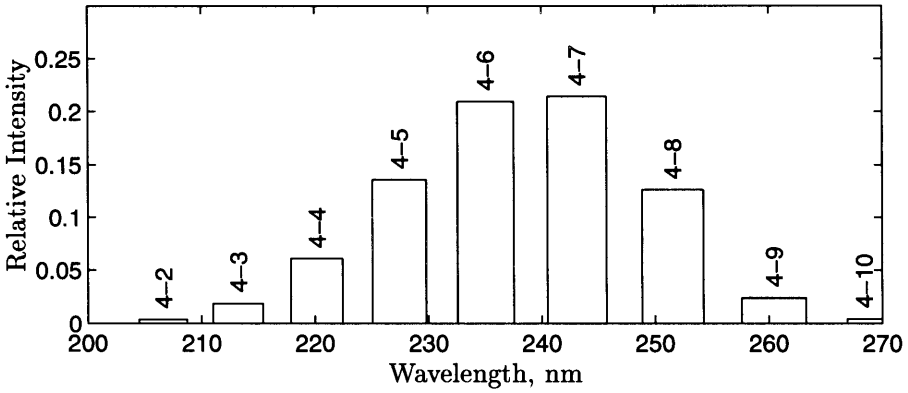

(a) $v' = 4$ (filled from $v'' = 0$)

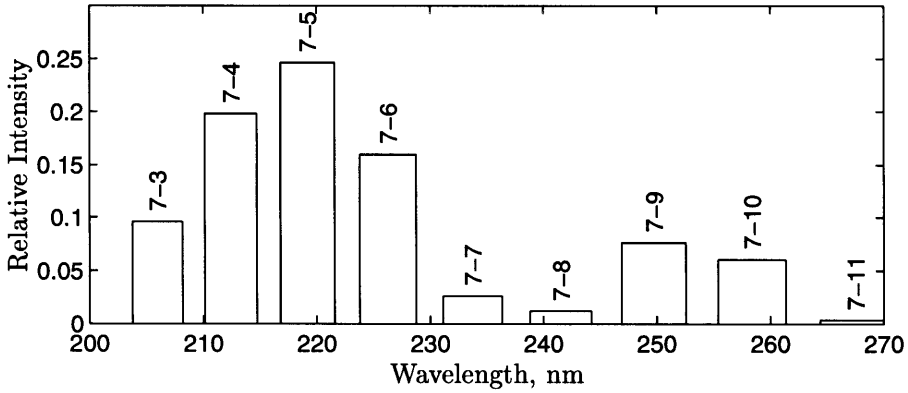

(b) $v' = 7$ (filled from $v'' = 1$)

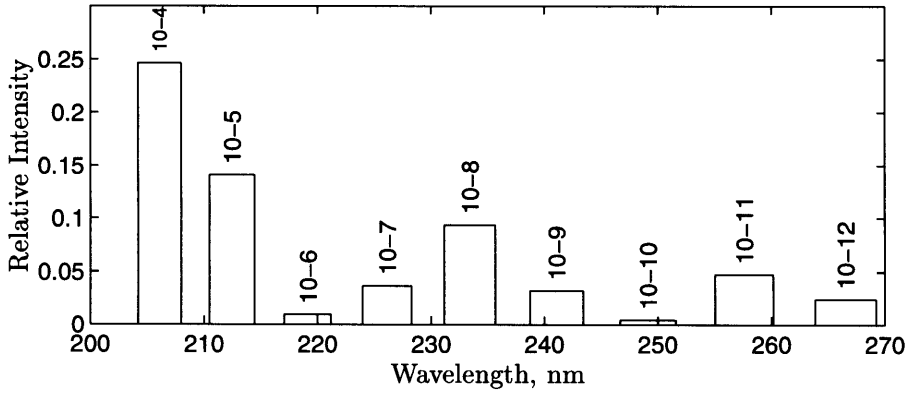

(c) $v' = 10$ (filled from $v'' = 2$)

Figure 2.5: Relative Strengths of Vibrational Emission Bands

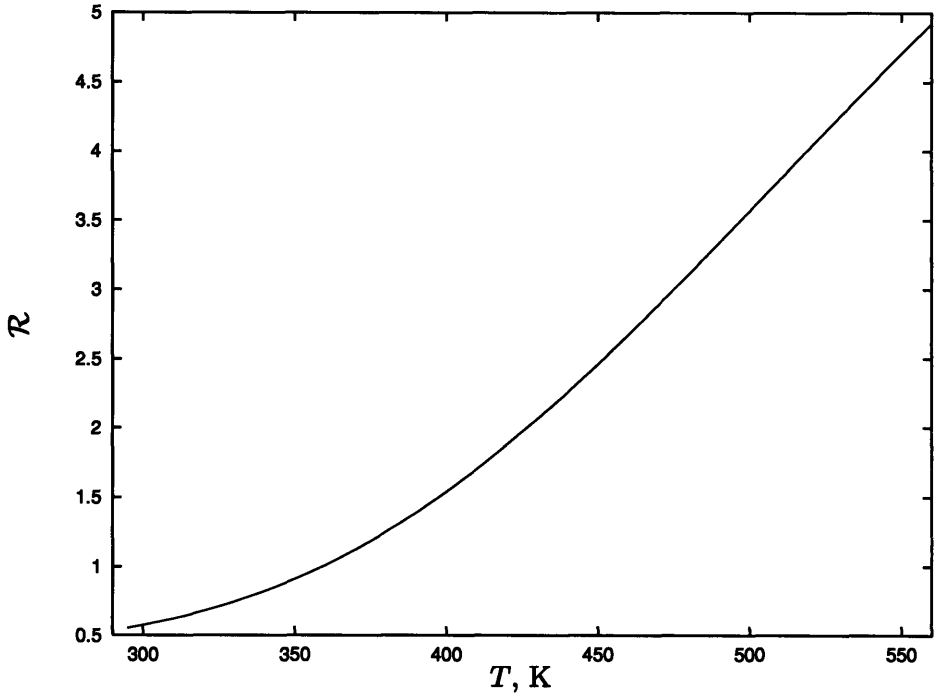

Figure 2.6: Theoretical Temperature Dependence of Diagnostic Ratio for Spectral Normalization

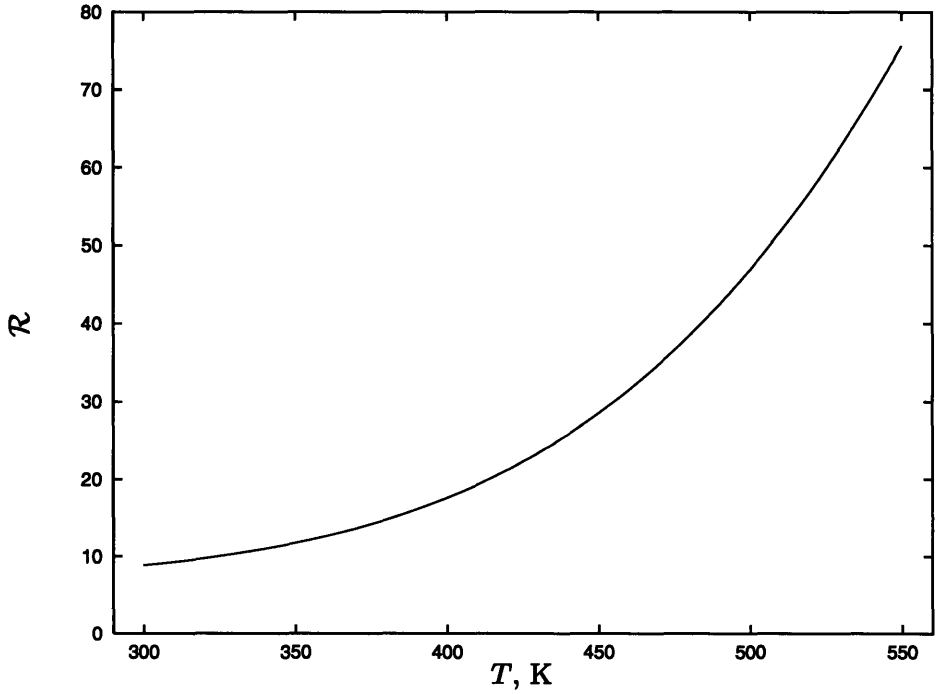

Figure 2.7: Theoretical Temperature Dependence of Diagnostic Ratio for N_2 Raman Normalization

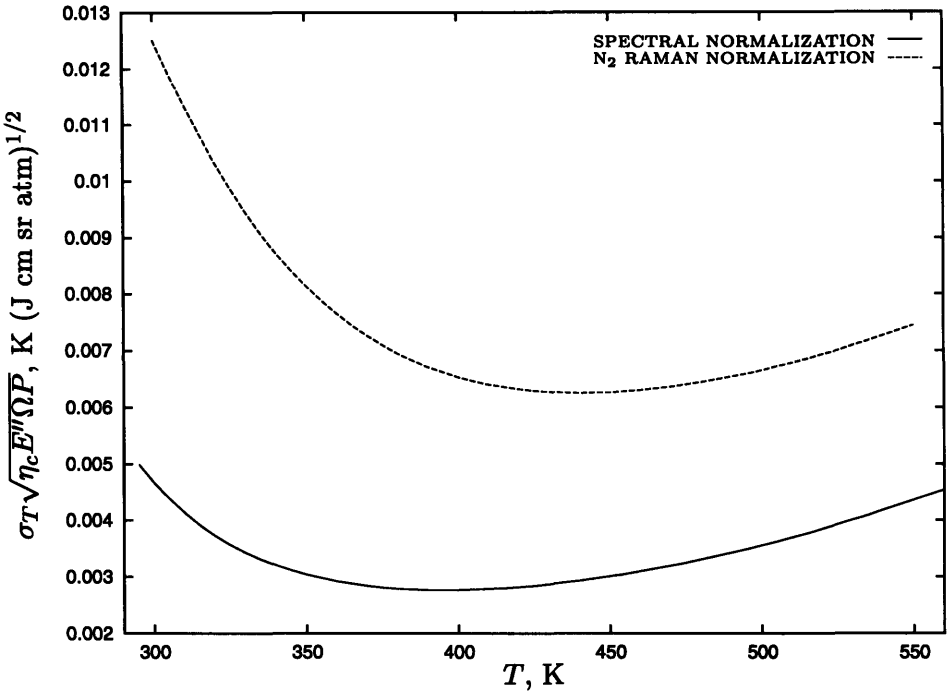

Figure 2.8: Theoretical Temperature Uncertainty for Spectral and N_2 Raman Normalizations

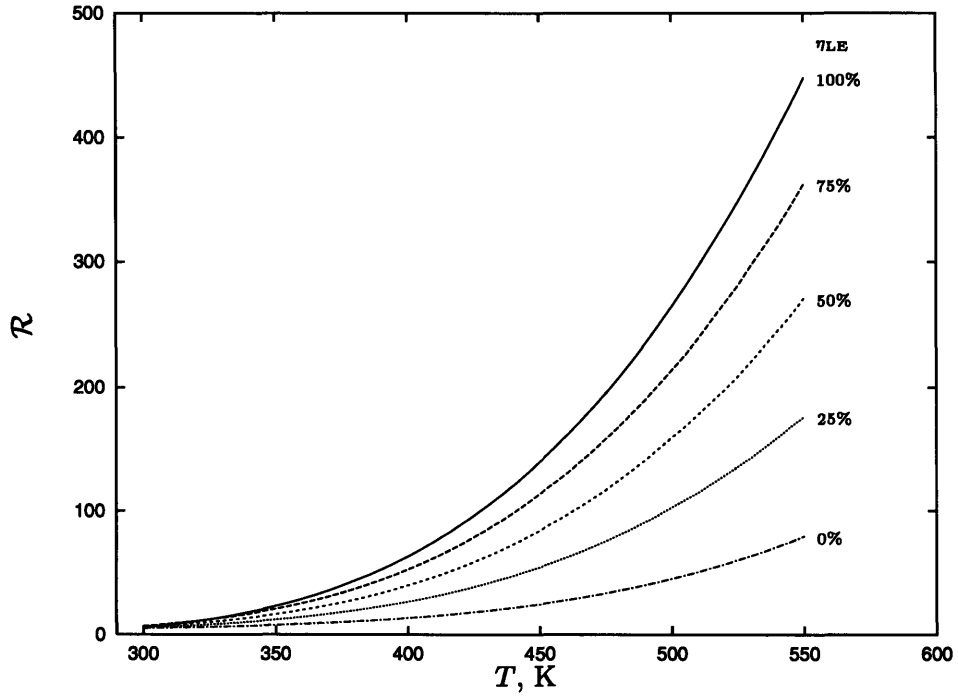

Figure 2.9: Temperature Diagnostic Ratio for Narrowband Measurements as a Function of Temperature and Laser Locking Efficiency

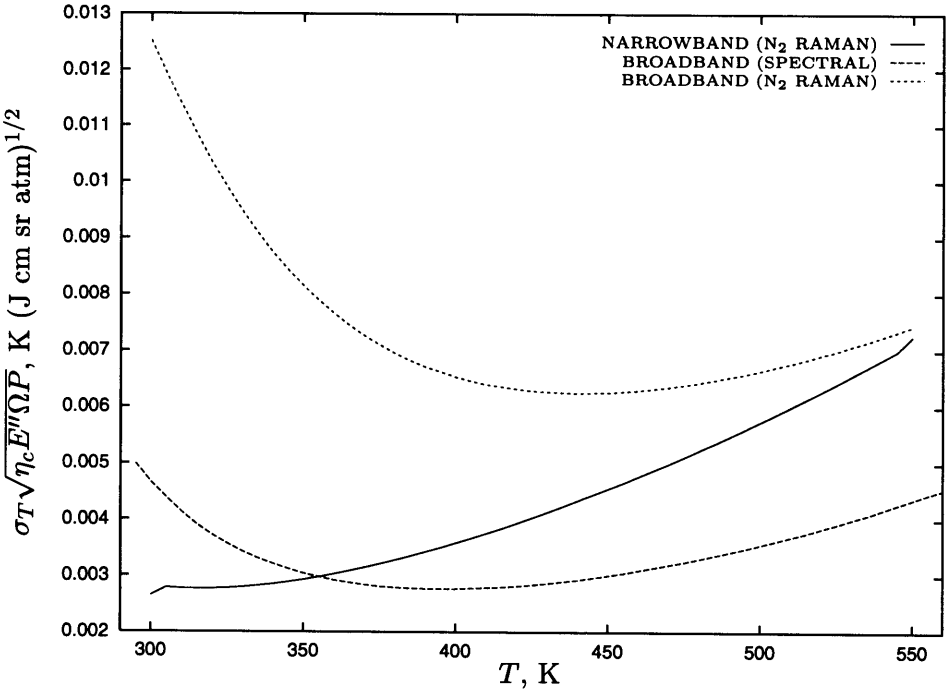

Figure 2.10: Measurement Uncertainty for Narrowband Measurements Compared to Broadband Measurements

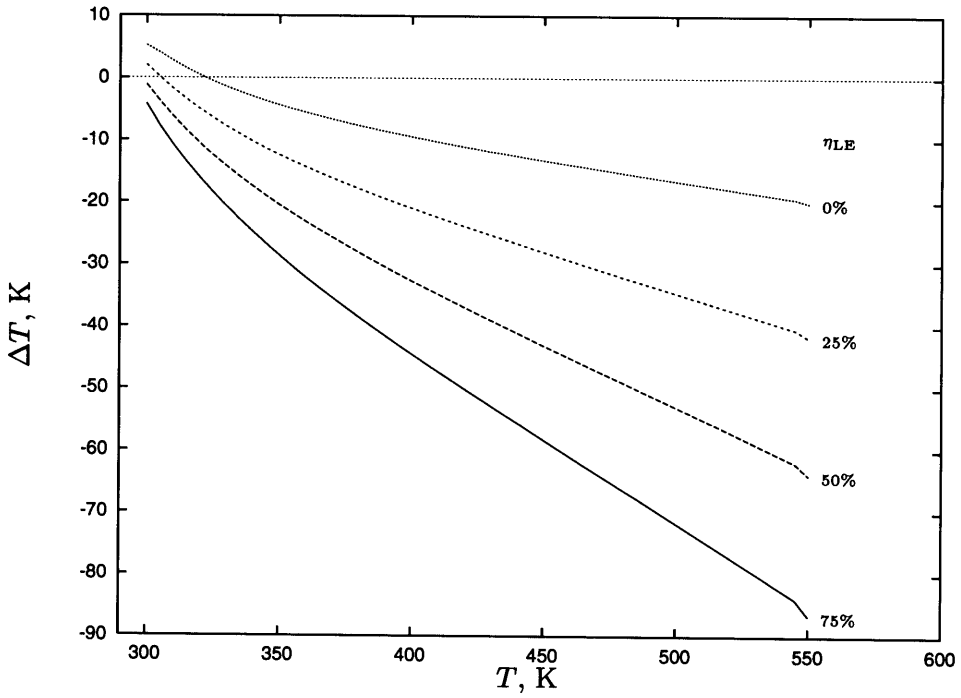

Figure 2.11: Temperature Measurement Error Resulting from Laser Locking Efficiency Variations for Narrowband Measurements

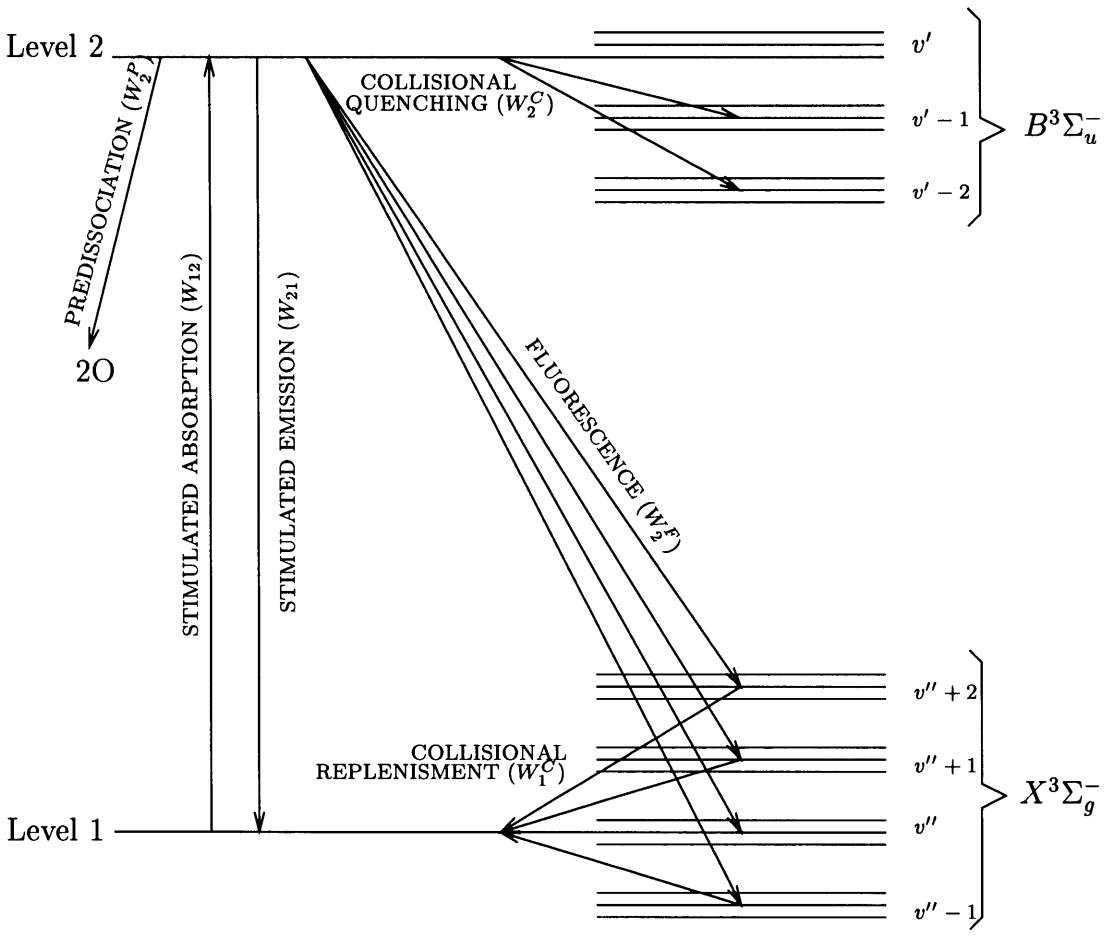

Figure 2.12: Dynamic Processes Excited During LIF Temperature Measurement

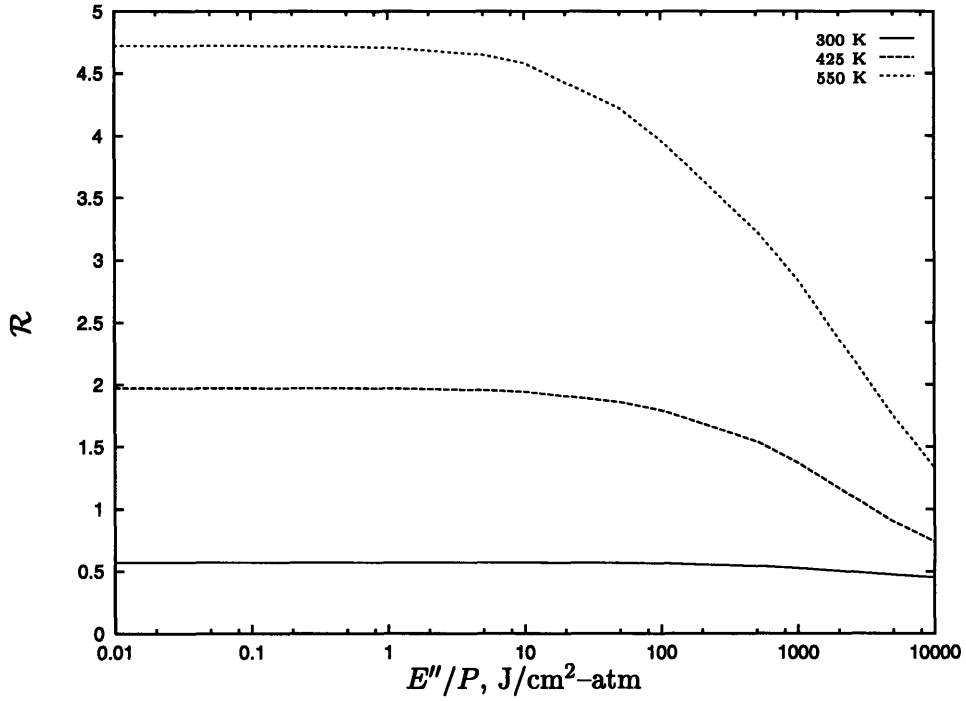

Figure 2.13: Effect of Saturation on Temperature Diagnostic Ratio

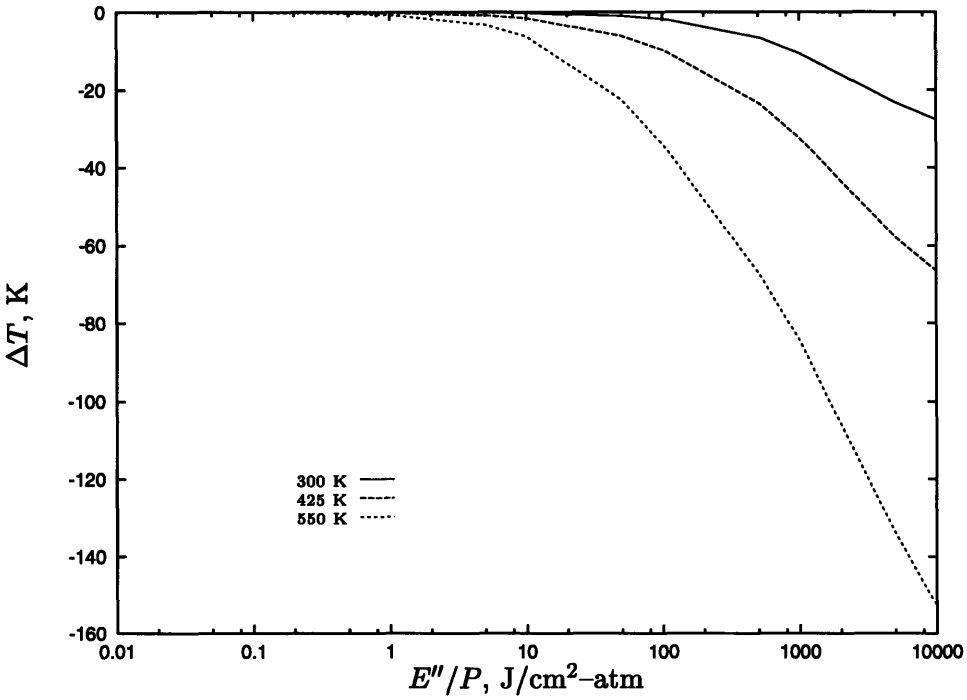

Figure 2.14: Temperature Error Resulting from Saturation Effects

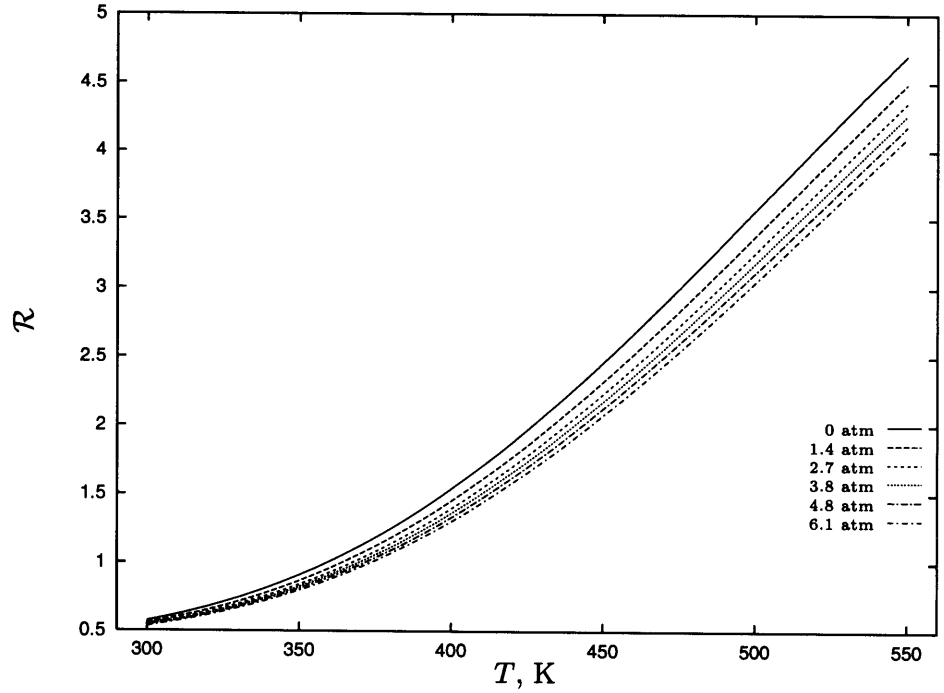

Figure 2.15: Effect of Collisional Quenching on Temperature Diagnostic Ratio (Cann data)

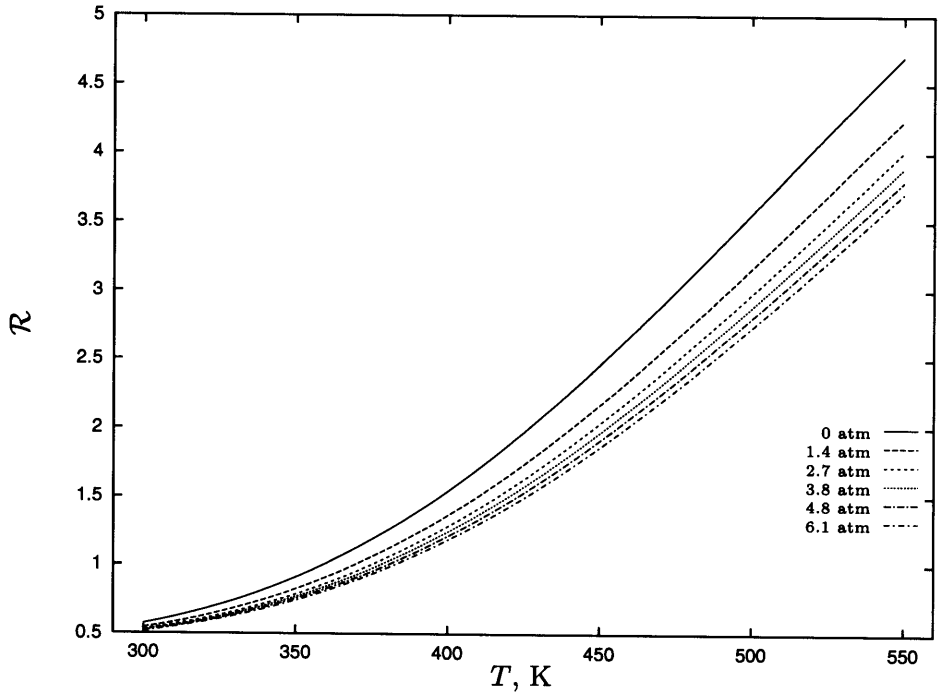

Figure 2.16: Effect of Collisional Quenching on Temperature Diagnostic Ratio (Miles data)

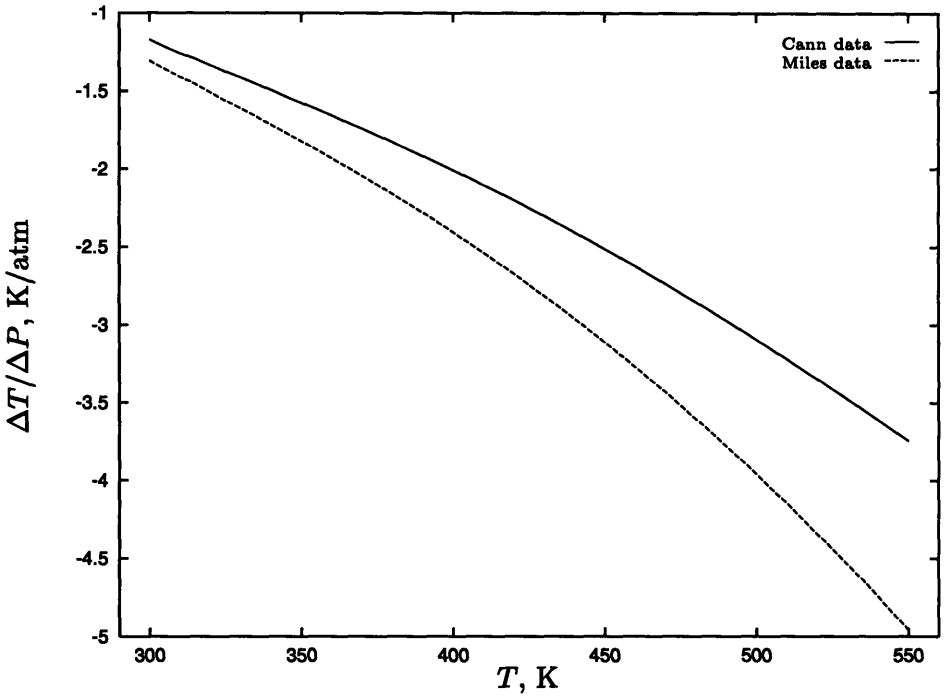

Figure 2.17: Temperature Error Resulting from Collisional Quenching

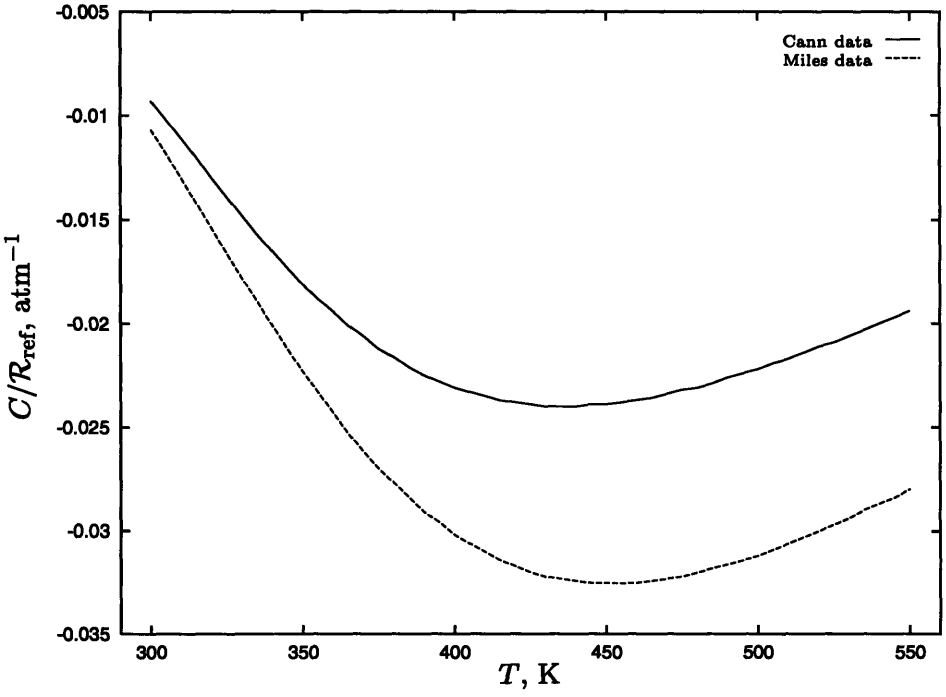

Figure 2.18: Temperature Dependence of the $C/\mathcal{R}_{\text{ref}}$ Parameter

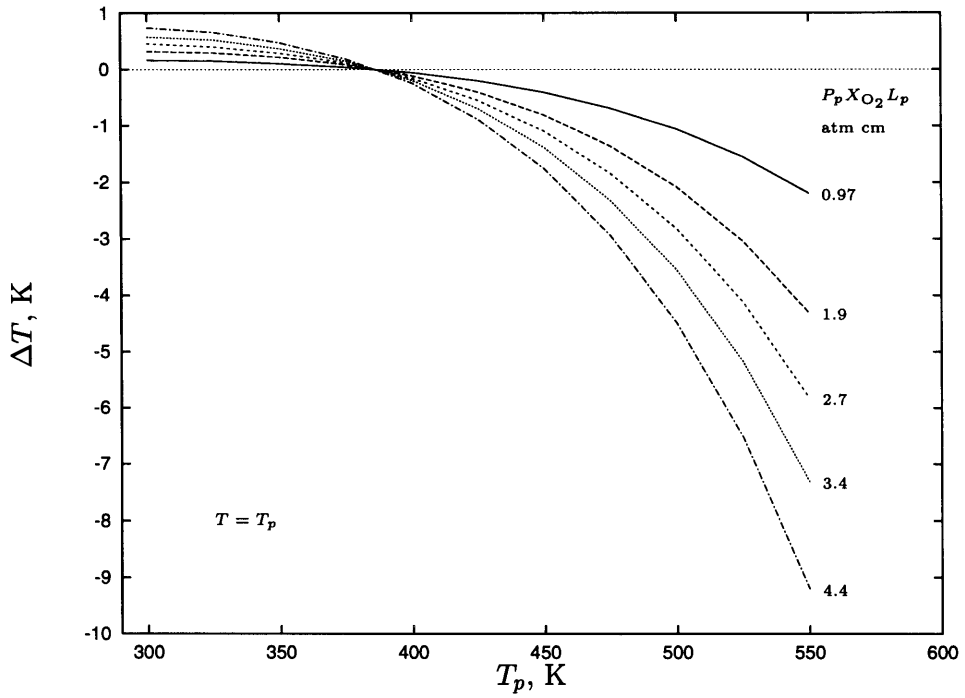

Figure 2.19: Temperature Measurement Error Resulting from Beam Path Absorption Effects, $T = T_p$

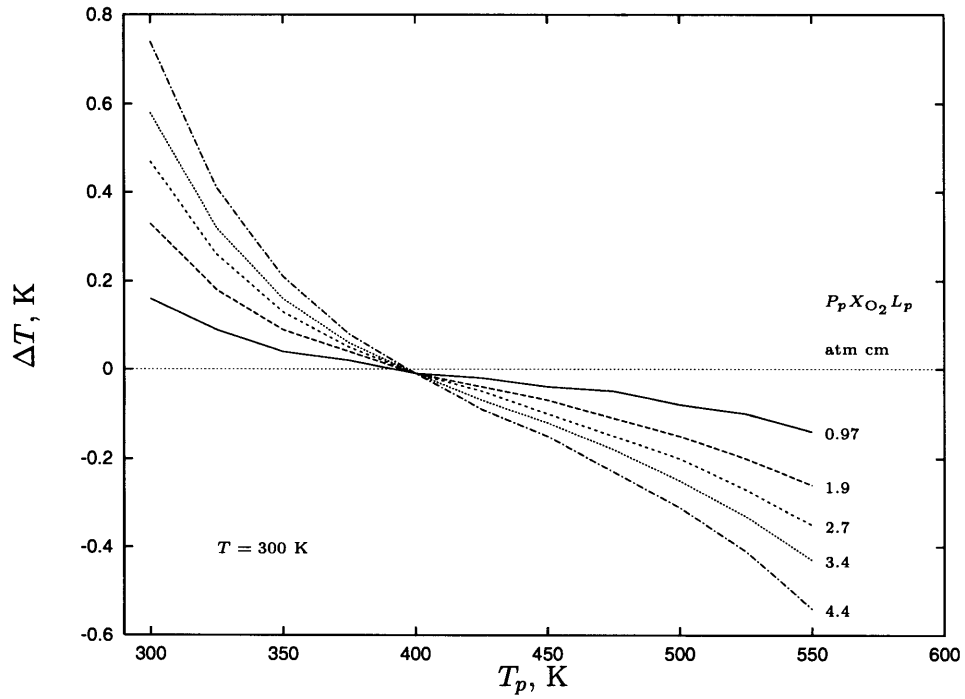

Figure 2.20: Temperature Measurement Error Resulting from Beam Path Absorption Effects, $T = 300$ K

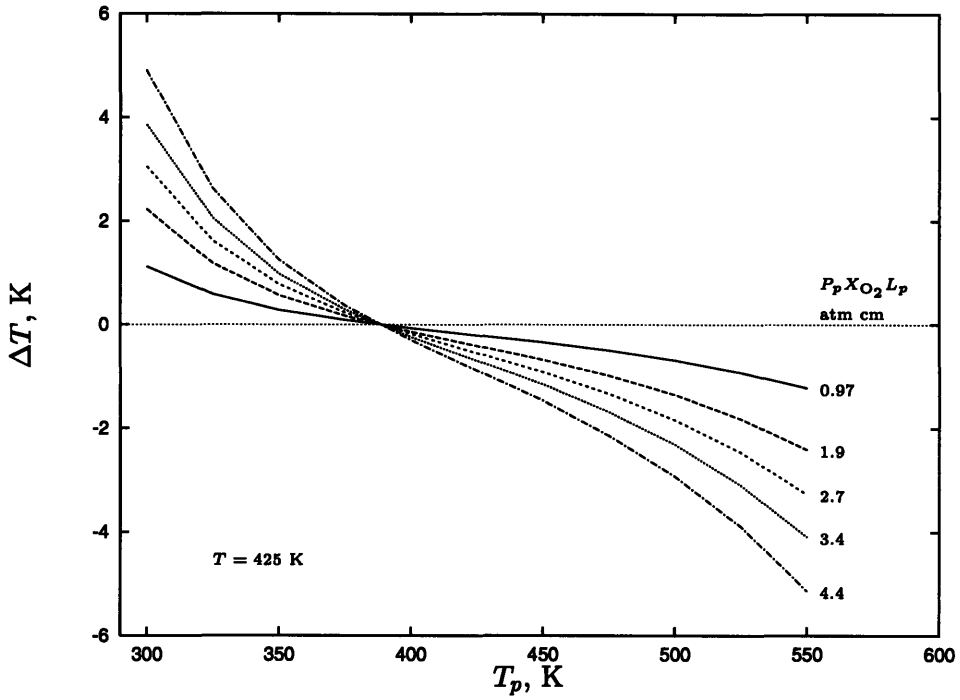

Figure 2.21: Temperature Measurement Error Resulting from Beam Path Absorption Effects, $T = 425$ K

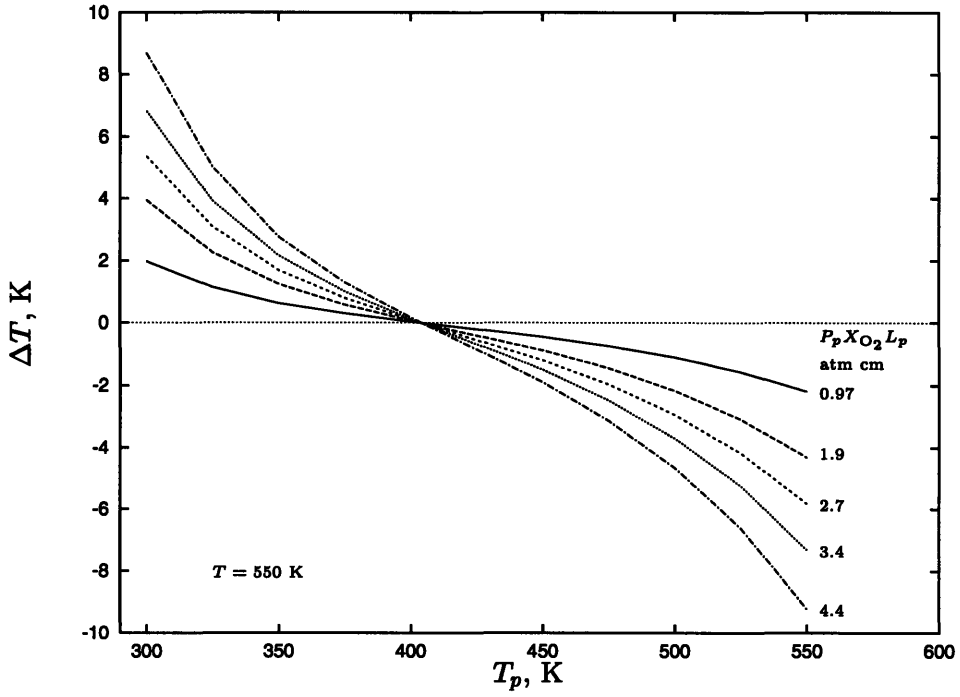

Figure 2.22: Temperature Measurement Error Resulting from Beam Path Absorption Effects, $T = 550$ K

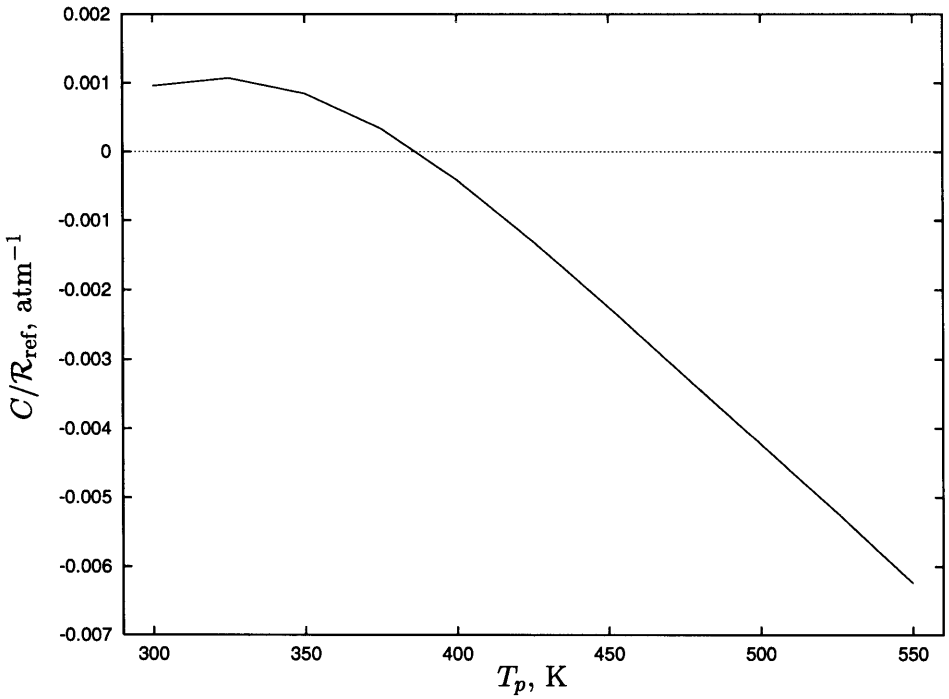

Figure 2.23: Apparent Pressure Dependence Resulting from Beam Path Absorption Effects, $L_p = 3.6$ cm

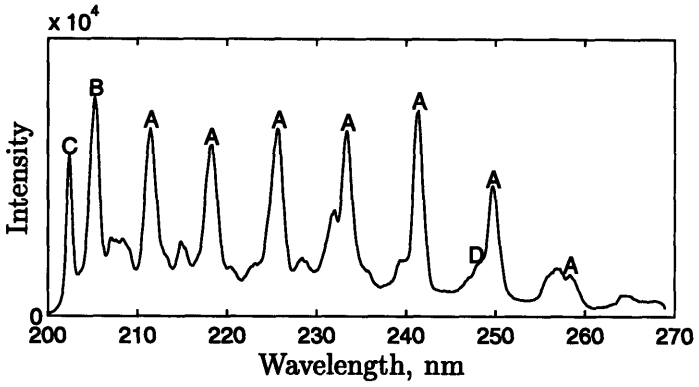

(a) High E, High P

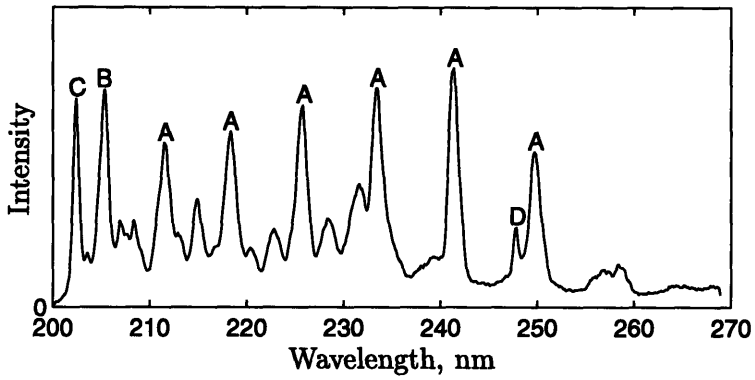

(b) High E, Low P

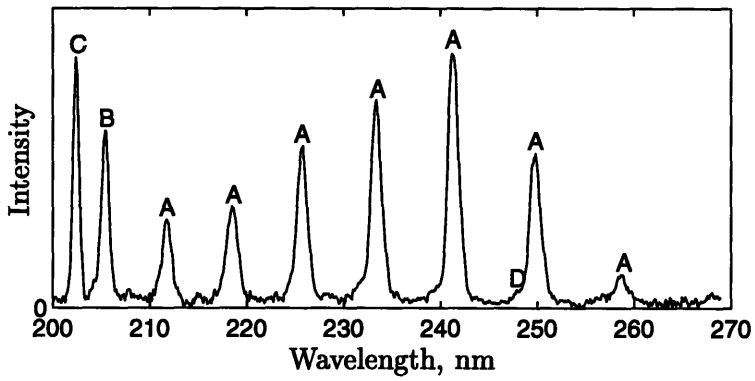

(c) Low E, High P

Features are identified as follows: (A) O_2 LIF, (B) O_2 LIF plus O_2 Raman (2nd Order), (C) N_2 Raman, (D) C-LIF. All other peaks are attributed to O_2^+ LIF.

Figure 2.24: Contaminating Signals

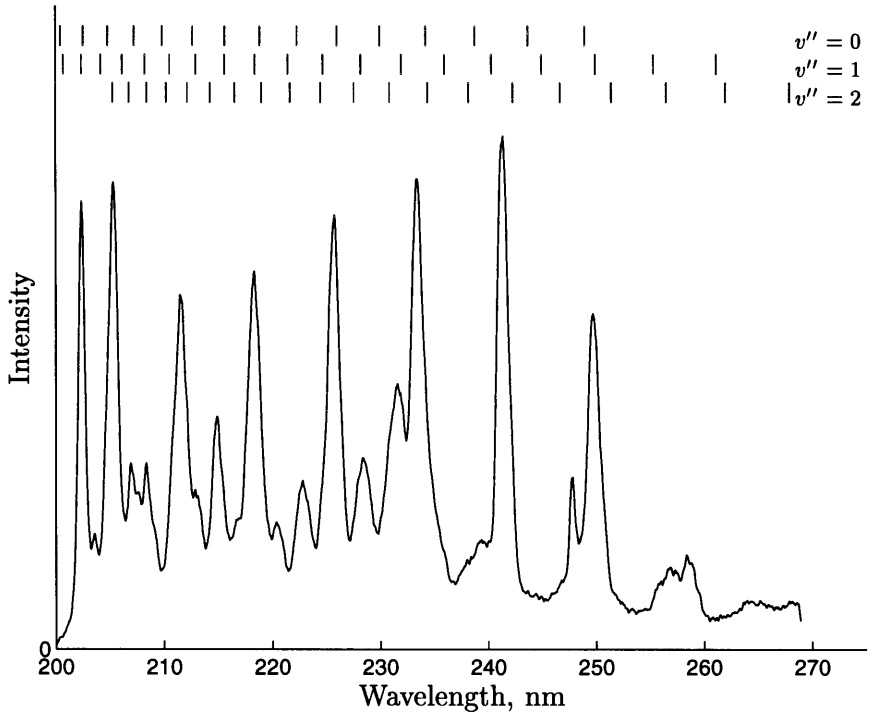

Figure 2.25: Experimental Spectrum with O_2^+ Fluorescence Band Heads

Chapter 3
Experimental Apparatus

Turbomachinery environment presents severe challenges for optical experiments. For example, typical experimental optical configurations cannot be used in turbomachinery because of the limited access to the flow path. The experimental apparatus used in this project was designed to address these challenges. This chapter describes the experimental apparatus.

Section 3.1 presents a general description of the experimental apparatus. The oblique-scatter configuration used in this project is compared with the side-scatter configurations typical of optical experiments in section 3.2. The characteristics of apparatus components are discussed in section 3.3. Finally, section 3.4 compares the measurement volume dimensions with the spatial resolution requirements, and section 3.5 compares the recorded signal levels to theoretical signal levels.

3.1 General Description

The schematic of the experimental apparatus is shown in Figure 3.1. The light from an argon-fluoride (ArF) laser is steered through six turning mirrors and directed by the focusing lens to the volume where temperature is to be determined. As discussed in Chapter 2, the laser light excites oxygen molecules in the measurement volume to an upper electronic state, and these molecules produce fluorescence signals as they decay back to the ground electronic state.

The fluorescence signal is collected by an imaging lens. After passing the collected light through a spectral filter to eliminate extremely strong reflection and Rayleigh scattering signals at 193 nm, the imaging lens delivers the fluorescence signals to the entrance slit of a spectrometer.

The spectrometer uses a diffraction grating to disperse the fluorescence signal into its component wavelengths, and this spectral distribution is measured and recorded by a multichannel optical detector placed at the exit plane of the spectrometer.

The entire apparatus is placed in an acrylic box, which is purged with nitrogen gas to eliminate absorption of the laser light by oxygen molecules in the atmosphere. A casing window separates the flow field being examined from the apparatus volume purged with nitrogen.

Figures 3.2 through 3.6 are various views of the experimental apparatus. In these figures, the experimental apparatus have been set up for temperature measurements in a supersonic free jet (see Chapter 6 for details of these measurements).

3.2 Optical Configurations

Most LIF setups utilize the side-scatter configuration shown in Figure 3.7. In this configuration, the focusing and imaging axis are oriented perpendicular to each other. The flow to be examined is along the third axis.

The main advantage of the side-scatter configuration is that the windows the laser beam passes through are isolated from the imaging optics. Consequently, the imaging optics does not collect any signals due to reflections or window fluorescence. In addition, the laser energy or power may be monitored simultaneously by placing an energy or power meter on the other side of the measurement volume. The additional measurement may then be used to normalize the LIF data for laser energy variations. In some setups of this type, the optics are fixed; different points in the flow field are measured by moving the flow apparatus relative to the optics.

The most severe constraint for optical measurements is limited optical access to the flow path. For almost all turbomachines, the only optical access is through a window on the casing. The side-scatter configuration is incompatible with this constraint; consequently, an oblique-scatter configuration, as shown in Figure 3.1, must be used.

In addition, the large and heavy turbomachinery rigs may not be easily moved. Therefore, in order to measure different points, the optics must be moved relative to the rig.

3.3 Component Characteristics

The performance of the overall experimental apparatus is determined partially by the characteristics of the components, which are discussed in this section.

3.3.1 Optical Materials

The optical material used for both the focusing optics and the casing window must be transparent to ultraviolet radiation at 193 nm. In addition, for turbomachinery applications, the material used for the casing window must be mechanically strong. Only two materials, namely fused silica and calcium fluoride (CaF_2), meet these requirements, with the latter material being 2–5 times as expensive as the former.

In addition, these materials must have a high damage threshold at 193 nm [1]. Excimer laser radiation at 193 nm damages optical materials in two ways: color center formation and pitting. Color center formation occurs after a large number ($\sim 10^6$) of medium fluence (~ 100 mJ/cm^2) shots, whereas pitting is caused by a single shot of high fluence ($\gtrsim 1$ J/cm^2) shot. Although calcium fluoride has a higher threshold against color center formation, both materials have about the same resistance against pitting.

For this project, fused silica is used for both the focusing optics and the casing window because of its lower cost and wider availability.

Another important consideration is fluorescence. The casing window fluorescences in response to the laser shots, and this fluorescence, if at the same wavelength as LIF signals,

[1] Material presented in this section was obtained during private communications with Marty Rothschild, Ph. D. , MIT Lincoln Laboratories, Lexington, Massachusetts.

will contaminate the LIF readings. Each of the several commercially available fused silica types, and even each lot of a given type, may exhibit different fluorescence properties. Therefore, it is important to obtain and test a sample from a lot before manufacturing complicated and expensive casing windows.

Figure 3.8 shows the index of refraction of fused silica as a function of wavelength. Because of its high dispersion, fused silica cannot be used for the imaging lens which must operate over a relatively wide wavelength region. In addition, because of the variations in index of refraction, a visible light source, such as a HeNe laser, cannot be used in aligning the focusing optics.

At 193 nm, the surface losses are approximately 5% per surface. In addition, at this wavelength, fused silica exhibits some absorption, with the absorption losses ranging from 1% cm^{-1} to 4% cm^{-1} depending on the type and batch.

3.3.2 Laser

The particular laser used in this project is Lambda-Physik EMG160MSC excimer laser operating with an argon-fluoride (ArF) gas mix at 193 nm. This laser has two resonating tubes and may be configured in either narrowband or broadband mode. The important performance parameters for the laser are the beam shape, beam divergence, beam energy, repetition rate, short-term (shot-to-shot) and long-term stability of beam energy, and, for narrowband mode, locking efficiency level and stability.

Table 3.1 compares the observed values of these parameters with the values specified by the manufacturer. As this table shows, neither the beam energy nor the locking efficiency levels observed during these experiments reached the manufacturer specifications.

Figure 3.9 plots the beam energy (E) as a function of repetition rate and laser discharge voltage, both of which may be set by the user. For a constant discharge voltage, energy decreases roughly linearly with increasing repetition rate.

The short-term, shot-to-shot stability of the beam energy are shown in Figures 3.10 and 3.11. The former figure shows a histogram of energy distributions for 501 shots at 100 Hz. The distribution can be approximated with a normal (Gaussian) distribution. The latter figure plots the standard deviation (σ_E) of the beam energy distributions as a function of repetition rate. Note that the shot-to-shot variation increases slightly with increasing repetition rate.

The laser output spectrum is shown in Figures 3.12 and 3.13 for narrowband and broadband configurations respectively. In the narrowband configuration, the output consists of a narrowband component superimposed in a broadband component. The location of the narrowband component may be adjusted by the user, but the location of the broadband component remains fixed. In Figure 3.12, the narrowband component is broadened by the recording instrument; the actual width of the narrowband component is approximately 0.005 nm (FWHM).

The fraction of total beam energy contained in the narrowband component is refered to as *locking efficiency*. The locking efficiency for the spectrum shown in Figure 3.12 is approximately 21%.

The broadband emission spectrum may be modeled with a Gaussian function. The three slight dips are due to absorption by ambient oxygen molecules, and the contributing 4–0 transition lines are marked on Figure 3.13. The absorption dips are also visible in the narrowband emission spectrum of Figure 3.12.

For narrowband temperature measurement, stability of locking efficiency is more important than the absolute level. Figures 3.14 and 3.15 plot the time history of the locking efficiency for two different experiments. The locking efficiency decreases significantly for both of these experiments with increasing number of shots.

Finally, Figure 3.16 plots the beam energy as a function of number of shots. Without cryogenic purification to eliminate chemical products of the lasing reaction, the gas half-life is approximately 150,000 shots. Cryogenic purification extends the gas half-life approximately 70% to 256,000 shots.

3.3.3 Focusing Lens

The focusing lens must direct the laser beam to the measurement volume as efficiently as possible. The focusing lens is a fused silica, plano-convex lens with a focal length of 127 mm (5 in) at 587 nm. At the ArF laser wavelength of 193 nm, the focal length is 104.3 nm. The lens is oriented with the convex side towards the laser (see Figure 3.17). The important performance parameter for the focusing optics is the spot size at the measurement volume.

The spot size may be limited by either diffraction or geometric effects. For diffraction-limited performance, the spot size is given by [5]

$$l_s = f\theta \tag{3.1}$$

where f is the focal length of the lens and θ is the full-angle divergence. For values given in Table 3.1, the minimum spot size is less than 21 μm.

Geometric aberrations may be computed using conventional optical formulae or an optical design program. For this configuration, geometric calculations yield a root-mean-square spot which is 20 μm high and 34 μm wide. The overall spot size can then be estimated as 28 μm high by 48 μm wide.

Based on these values, the focusing lens is limited by geometric aberrations. Although the diffraction-limited performance may be approached by designing a special focusing lens just for this application, values presented above suggest that the gain in performance is probably not worth the cost of such a lens.

The transmission of the focusing systems, including beam steering optics, was measured experimentally. Without beam path purging, the tranmission efficiency was measured to be 8%. Since beam path purging increases the signal level by a factor of 2, the transmission efficiency with beam path purging is estimated[2] to be 15%.

[2]The beam path includes six turning mirrors with a specified reflectivity of 94–95% each, four surfaces (two for the lens and two for the casing window) with a transmission of 95%, and the 2-cm-thick casing window with a transmission of 92–98%. In addition, elastic (Rayleigh) scattering by N_2 molecules along the beam path leads to a 10% reduction in signal level. Consequently, the total transmission of the purged ideal system should be 47–53%. The measured transmission is lower by a factor of about 3. This reduction is probably due to several sources including damaged or dirty coatings on the turning mirrors, and the

3.3.4 Casing Window

The casing window separates the flow being studied from the optical apparatus. The thickness of the casing window must be designed for mechanical strength.

For this project, a casing window thickness of 19 mm (.750 in) was chosen. This thickness, with a safety factor of 10, is appropriate for the Blowdown Turbine Rig at the MIT Gas Turbine Laboratory, and is probably typical of the window thicknesses which would be appropriate for other turbomachinery rigs. A relatively large safety factor is used because the failure of the window would result in expensive damage to the rig. As mentioned above, the material for the casing window is fused silica.

The total transmittance of the window, including both reflection and absorption loses, is between 82% and 88%. Since the outgoing fluorescence signals must also pass through the same casing window, a narrowband antireflection coating, which would block these signals, cannot be used. Although a single-layer, broadband coating does reduce reflection losses slightly at 193 nm, it also increases reflection losses at other fluorescence wavelengths. In addition, coatings may exhibit lower resistance to laser damage and are expensive. Therefore, the casing window used in this project is not coated.

3.3.5 Imaging Optics

The imaging optics collects the fluorescence signals from the measurement volume and delivers these signals to the entrance slit of the spectrometer. The particular lens used in this project was a Lyman-Alpha I lens manufactured by the NYE Optical Company. Figure 3.18 shows a cross-section of the imaging optics.

The performance of the imaging lens was investigated using ZEMAX-SE Optical Design Program written by Focusoft, Inc., of Tucson, Arizona. The optical parameters used in the model was determined by physical and photographic inspection of the lens.

Because of the high dispersion of the few optical materials transparent to ultraviolet radiation in the wavelength range of interest, an all-reflective lens is attractive. The Lyman-Alpha I lens is an all-reflective lens of Cassegrain telescope configuration. Important specifications are given in Table 3.2.

The imaging lens may be used at different conjugate ratios, each with its own object-to-image distance (see Figure 3.19). For most turbomachinery applications, the smallest possible object-to-image distance is determined by geometric factors such as casing shape. For this project, a minimum object-to-image distance of 500 mm was chosen. This distance is appropriate for the Blowdown Turbine Rig at MIT Gas Turbine Laboratory, which is geometrically representative of many turbomachinery rigs. This point is marked in Figures 3.19–3.21.

Figure 3.20 shows the spot size (in root-mean-square sense) produced by the imaging optics. For the point measurements performed during this study, only the performance at the single measurement point is important, and the only contributing aberration source

spreading laser beam being truncated by the turning mirrors and focusing lenses. As will be discussed in Chapter 5, even with this low transmission efficiency, the fluence at the measurement volume is limited by non-linear process errors; consequently, the improvement in the transmission efficiency of the beam steering optics was not pursued.

is spherical aberration (third and higher orders). However, the Lyman-Alpha lens used is designed for photography, and the aberrations are balanced over the entire object field, which is 45 mm by 30 mm at the chosen conjugate ratio. If it were possible to design and manufacture a dedicated imaging lens for this project, the optics may be optimized to yield diffraction-limited performance at the measurement point.

Figure 3.21 plots the image-space f-number, which measures the angle of convergence of the light rays towards the image plane, as a function of conjugate ratio. The operating point is also indicated on this figure. Ideally, the f-number of the imaging lens will be equal to or greater than the spectrometer f-number of 3.8, for a smaller f-number will result in some of the rays not being accepted by the spectrometer optics. Unfortunately, because the imaging lens was designed for photography, its f-number at all conjugates is larger than 3.8. The resulting transmission efficiency of the imaging lens, including reflections losses and obscuration in the lens, is approximately 23%. Again, if a dedicated imaging lens were designed, that lens would be designed so that its f-number matches the spectrometer f-number with a resulting transmission efficiency of approximately 70%.

The casing window introduces some chromatic aberrations into the system. Figure 3.22 shows the focal shift as a function of wavelength. This figure assumes that the system is aligned at 193 nm; because of lack of suitable light sources, it is not possible to align the system for a middle wavelength to minimize the effect of chromatic aberrations on the system. The chromatic aberrations are smaller than the measurement volume depth of 1 mm.

3.3.6 Spectral Filter

Since the fluorescence signal produced in the measurement volume is only 10^{-9} of the number of photons in the laser beam, the imaging lens collects an intense signal at the laser wavelength in addition to the fluorescence signals. This signal originates from surface and window reflections, as well as elastic Rayleigh scattering from the air. If this intense signal is not physically eliminated, it will contaminate the fluroescence signals and reduce the measurement precision.

The radiation collected by the imaging lens is passed through a 2-mm-thick potassium bromide (KBr) disk placed in front of the spectrometer slit. This material has a sharp cutoff at approximately 202 nm, and absorbs all of the radiation contaminating the fluorescence signals. Unfortunately, the fundamental oxygen Raman peak at 199.4 nm is completely eliminated and the strength of the nitrogen Raman peak at 202.5 nm is significantly reduced. Figure 3.23 and 3.24 compare the fluorescence spectra without and with the KBr disk.

McKenzie [4] suggests the use of a weak acetone-water solution as the spectral filter. Figure 3.25 and 3.26 show spectra resulting from the use of 0.5% and 1.0% spectroscopic-grade acetone solutions in spectroscopic-grade distilled water. Although, both concentrations pass the nitrogen peak unchanged, they also absorb radiation at wavelengths greater than 230 nm. Consequently, the 2-mm-thick KBr disk is chosen as the best spectral filter for this project.

The transmission of the spectral filter, estimated from Figures 3.23 and 3.24, is approximately 50–60% over the LIF peaks and about 20% for the nitrogen Raman peak.

3.3.7 Spectrometer

The light collected by the imaging optics is dispersed into its component wavelength by a spectrometer. The particular spectrometer used in this project is SpectraPro^{TM}275, manufactured by the Acton Research Corporation. The specifications of the spectrometer is given in Table 3.3. Table 3.4 lists the specifications of the three gratings mounted in the spectrometer.

The important performance parameters for the spectrometer are the f-number, range, resolution and transmission efficiency. These parameters are listed in Tables 3.3 and 3.4. The grating efficiencies are obtained from theoretical plots provided by Loewen, Nevière and Maystre [3].

Figure 3.27 shows the resolution, in FWHM, of the spectrograph, which consists of the spectrometer and the detector. For small slit widths, the resolution is limited by the detector spread function, whereas for large slit widths, the resolution is determined by the slit width. For all experiments in this project, the slit width is set to 140μm to achieve the required spatial resolution. This point, shown in Figure 3.27, corresponds to a FWHM of approximately 10 diodes.

Unless otherwise noted, all LIF spectra presented in this report are taken with the 1200 mm^{-1} grating set at 234 nm. Corresponding spectrograph range and resolution are 200–270 nm and 0.68 nm (FWHM) respectively.

3.3.8 Detector

The light dispersed by the spectrometer is monitored and recorded by a multi-channel detector. The particular detector used in this project was a Princeton Instruments IPDA-1024 intensified photodiode array with variable gain, controlled by a Princeton Instruments ST-1000 detector controller. The detector contains 1024 diodes, each of which is 25 μm wide and 25 mm high.

The important performance parameters for the detector are detector quantum efficiency, detector gain, and baseline level and noise.

The quantum efficiency (η_{QE}) is plotted as a function of wavelength on Figure 3.28. Over the 200–300 nm range of interest, the quantum efficiency is approximately 24%.

Figure 3.29 plots the detector gain (K_D) as a function of detector gain switch setting. For this project, where the light levels are extremely low, the detector is operated at the highest gain where $K_D = 1.8$. In other words, each photoelectron produced at the phosphor results, on average, 1.8 counts on the photodiode array. When the quantum efficiency is taken into account, each photon arriving at the detector produces, on average, 0.43 counts on the photodiode array. Of course, the larger-than-unity detector gain cannot compensate for the loss in precision due to lower-than-unity quantum efficiency.

Because the fluorescence signal is relatively weak and the collection efficiency is low, the most important performance parameter for this project is the baseline level and baseline noise. The baseline signal consists of two components. First, there is a constant offset of about 160 counts per diode. Second, there is also a build-up of dark charge, which is an extraneous signal that collects on the photodiode as a result of random thermal processes

even when there is no light incident on the photodiode. This thermal effect increases linearly with increasing exposure. Figure 3.30 shows both the offset and dark charge as a function of exposure.

This detector is thermoelectrically cooled to -20 °C to reduce dark charge. The excess heat is rejected into cold tap water flowing through the detector. The temperature is controlled by a user-adjusted thermostat. Although the dark charge may be reduced further by reducing the detector temperature, this requires special equipment and coolant.

The variation in baseline level is known as baseline noise. If the baseline level was perfectly stable and precisely known, it could always be subtracted from the spectral data with no loss in precision. However, the noise (uncertainty) in the baseline level will add to the uncertainty in the data.

The baseline noise (σ_B) is shown in Figure 3.31 as a function of exposure. The baseline noise consists of two components. First, there is a constant readout noise of approximately 1.4 counts per diode. Second, there is thermal noise associated with the dark charge discussed earlier. Thermal noise increases with square root of exposure (i. e. $\sim \sqrt{X}$).

The IPDA-1024 detector may be interfaced with a Princeton Instruments PG-10 pulse generator, which acts as a shutter control. The detector is shielded except during a very short gate pulse. Although gating is useful for extracting short-duration signals from long duration or continuous background signals (e. g. ambient light), it is not beneficial for this experiment. Since the LIF signals occupy the 200–270 nm ultraviolet range, they are already isolated from the continous signals such as ambient light. Gating has no effect on either baseline level or baseline noise.

3.3.9 Positioning Mechanism and Alignment

The optics are mounted on two tables as shown in Figure 3.1. The bottom table is stationary. The middle table moves in one (indicated) direction relative to the bottom table, and the top table, which is mounted on the middle table, moves in a perpendicular direction (also indicated) relative to the middle table.

For turbomachinery, these directions would be the radial and axial directions, respectively. Positioning along the third (circumferential) direction would be achieved by synchronizing the laser pulse to the blade passing.

The measurement location is obtained from two 50-mm micrometers which measure the displacement of the middle table with respect to the bottom table (radial location) and the displacement of the top table with respect to the bottom table (axial location). The resolution of the micrometers is 0.01 mm.

The beam is steered through three sets of 45° turning mirrors as shown in Figure 3.1. Each set contains two turning mirrors. Each pair of turning mirrors is located as shown on the schematic. The advantage of the configuration chosen is that the optical system does not need realignment at every measurement point. If combined with a motorized positioning system, this configuration allows for rapid acquisition of data at a large number of points.

3.3.10 Beam Path Purging

In order to avoid absorption of laser light by oxygen molecules in the ambient atmosphere, the experimental apparatus is enclosed in an acrylic box and purged with nitrogen. The beam path length is approximately 8 m. Purging increases LIF signal strengths by 200% to 250%. This corresponds to an absorption coefficient of 0.004–0.005 cm^{-1} atm^{-1}, which agrees with the values plotted by Lee and Hanson [2].

3.4 Measurement Volume

The measurement volume is determined by the intersection of the laser beam with the area imaged by the imaging lens (see Figure 3.32).

The measurement volume length along the axial direction is determined by the spectrometer slit width, which acts as a field stop. The spectrometer slit width was 140 μm, and the magnification of the imaging optics was 0.8. Consequently, the measurement volume dimension in the axial direction is 175 μm.

In the circumferential direction, the field is determined by the beam height, which is estimated as <100 μm. A 1-mm slit placed in front of the spectrometer ensures that the measurement volume dimension in this direction is no larger than 1.25 mm.

In the radial direction, the field is defined by the intersection of the imaged region and laser beam. If the laser beam is 50 μm wide (geometric calculations of section 3.3.3 yield an RMS spot size of 34 μm), the measurement volume depth is 846 μm. However, the effective path length, which should be used in the spectroscopic formulae, is 653 μm.

Based on these calculations, the spatial resolution of the experimental apparatus does indeed satisfy the requirements discussed in Chapter 1.

3.5 Signal Levels

The data given in this chapter may be used to compare the expected signal level with the actual signal level.

Assume a measurement volume pressure of 1 atm and temperature of 300 K, and a laser beam energy of 50 mJ (in front of the laser). From equation (5.2), the detector counts for the N_2 Raman signal (region 1 signal) is 11.

The beam steering and focusing optics have a tranmission efficiency of 15% (see section 3.3.3). Therefore, the beam energy at the measurement volume is 7.5 mJ. The Raman scattering cross section computed from formulae given in Bischel and Black [1] yields a N_2 Raman signal of 4.8×10^5 photons per unit solid angle (sr). The collection angle for the imaging optics is 0.095 sr ($\Omega = \pi(\mathrm{NA})^2$, NA = 0.174), so the imaging lens collects 4.6×10^4 photons.

The transmission of the imaging and detection optics may be estimated as follows: The casing window has a transmission of 90% due to reflection losses from two surfaces. The transmission of the imaging lens is approximately 23%. For N_2 Raman signal, the transmission of the spectral filter is estimated around 20%. The theoretical efficiency of the

grating is 10%. The quantum efficiency of the detector at 200 nm is 22%, and the detector gain is 1.8. Therefore, the total transmission is 0.16%.

Therefore, the expected signal level at the detector is 73 counts. The observed signal is lower by a factor of about 6.7.

The same calculation may be repeated for the LIF signals, specifically the denumerator signal S_D. According to equation (5.4a), the detector counts is 324 counts. In the measurement volume, a laser energy of 7.5 mJ produces 1.3×10^7 photons, and the imaging lens collects 1.0×10^5 photons. The tranmission efficiency of the collection and detection optics is 0.5%, so the expected signal at the detector is 500 counts. The observed signal is lower by a factor of about 1.5.

Considering the approximate nature of the transmission estimates, as well as the relative magnitudes of the numbers involved, the agreement for LIF signal level is excellent. The agreement for N_2 Raman signal is lower, but is still within an order of magnitude.

3.6 Summary

The experimental apparatus described in this chapter was designed for the turbomachinery environment, which place severe constraints on the geometry of the apparatus. In particular, the traditional side-scatter optical configuration is not compatible with the limited optical access offered by turbomachinery rigs, and a oblique-scatter configuration must be used. An oblique-scatter configuration does not allow simultaneous measurement of laser energy, and necessitates the use of a spectral filter to remove intense light due to reflections.

The experimental apparatus was designed for the MIT Blowdown Turbine facility, the geometry of which is typical of other turbomachinery rigs. The important performance parameters of the components are discussed in the chapter.

The measurement volume, which is limited by the intersection of the laser beam and imaged volume, is shown to be within the spatial resolution requirements of Chapter 1.

Finally, the signal levels for O_2 LIF and N_2 Raman signals have been shown to be roughly equal to the values predicted by theoretical formulas.

References

[1] BISCHEL, W., AND BLACK, G. Wavelength Dependence of Raman Scattering Cross Sections From 200-600 nm. *AIP Conference Proceedings 100* (1983), 181–187.

[2] LEE, M. P., AND HANSON, R. K. Calculations of O_2 Absorption and Fluorescence at Elevated Temperatures for A Broadband Argon-Fluoride Laser Source at 193 nm. *Journal of Quantitative Spectroscopy and Radiative Transfer 36*, 5 (1986), 425–440.

[3] LOEWEN, E. G., NEVIÈRE, M., AND MAYSTRE, D. Grating efficiency theory as it applies to blazed and holographic gratings. *Applied Optics 16*, 10 (October 1977), 2711–2721.

[4] MCKENZIE, R. Progress in Laser Spectroscopic Techniques for Aerodynamic Measurements: An Overview. *AIAA Journal 31*, 3 (March 1993), 465–477.

[5] QUESTEK INC. 100 Common Questions about Excimer Lasers.

Table 3.1: Performance of Lambda-Physik EMG160MSC Laser

	Narrowband Mode		Broadband Mode	
	Specified	Observed	Specified	Observed
Max. Discharge Voltage, kV	N/S	26.2	N/S	26.2
Max. Repetion Rate, Hz	250	250	250	250
Max. Pulse Energy, mJ	100	N/M	240	120
Divergence, full-angle, 50% energy, mrad	0.2	N/M	<0.2	N/M
Beam Height, mm	21	21	21	21
Beam Width, mm	4	4	4	4
Pulse Width, FWHM, ns	N/S	N/M	13	N/M
Bandwidth, FWHM, nm	0.005	N/M	N/S	0.35
Locking Efficiency, %	50%	$\leq$22%	N/A	N/A

N/A - not applicable
N/M - not measured
N/S - not specified
FWHM - full width at half maximum

Table 3.2: Specifications for the Imaging Lens

Manufacturer	NYE Optical Company
Model	Lyman-Alpha I
Configuration	Cassegrain
Length	5 in
Focal Length	275 mm
f-number	2.8
Operating Point	
Object-to-Lens Distance	332 mm
Back Focal Length	43 mm
Magnification	0.8
Image-space f-number	2.332
Object-space Numerical Aperture	0.174
Spot size (RMS)	31.3 μm
Transmission efficiency	23%

Table 3.3: Specifications for the ARC SpectraPro 275 Spectrometer

Configuration	Czerny-Turner	
Focal Length	275 mm	
Focal Plane Width	25 mm	
F-number	3.8	
Slit Width	10–3000 μm	adjustable
Wavelength Accuracy	±0.2 nm/500 nm	with 1200 mm^{-1} grating
Wavelength Reproducibility	±0.05 nm	with 1200 mm^{-1} grating

Table 3.4: Specifications for the Spectrometer Gratings

Type	Blazed	Holographic	Blazed
Pitch, grooves/mm	300	1200	3600
Blaze Wavelength, nm	300	N/A	240
Optimum Range, nm	200–450	190–800	160–320
Range, nm	256	64	21.3
Dispersion, nm/mm	10.24	2.56	0.852
Max. Resolution, nm	2.6	0.64	0.21
Max. Wavelength, nm	6000	1500	500
Efficiency @ 235 nm [3]	0.6	0.1	0.7

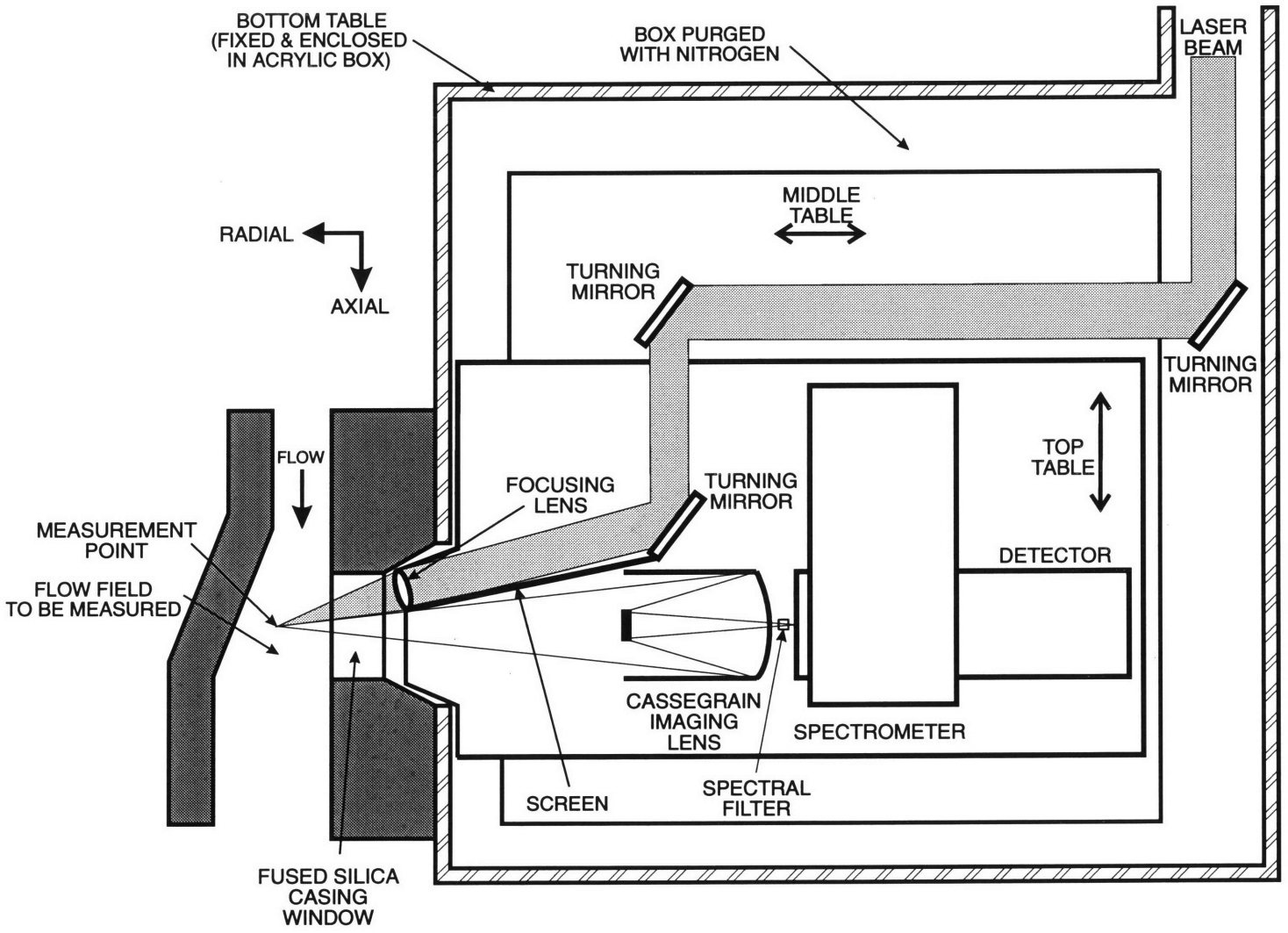

Figure 3.1: Experimental Apparatus Schematic

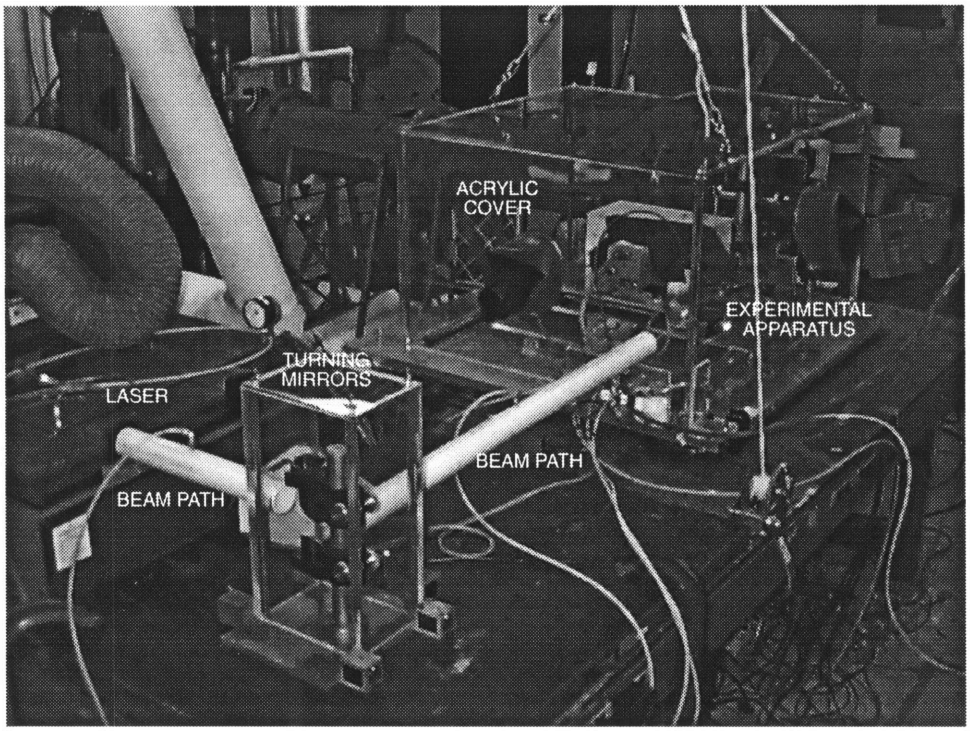

Figure 3.2: Experimental Apparatus, Rear View

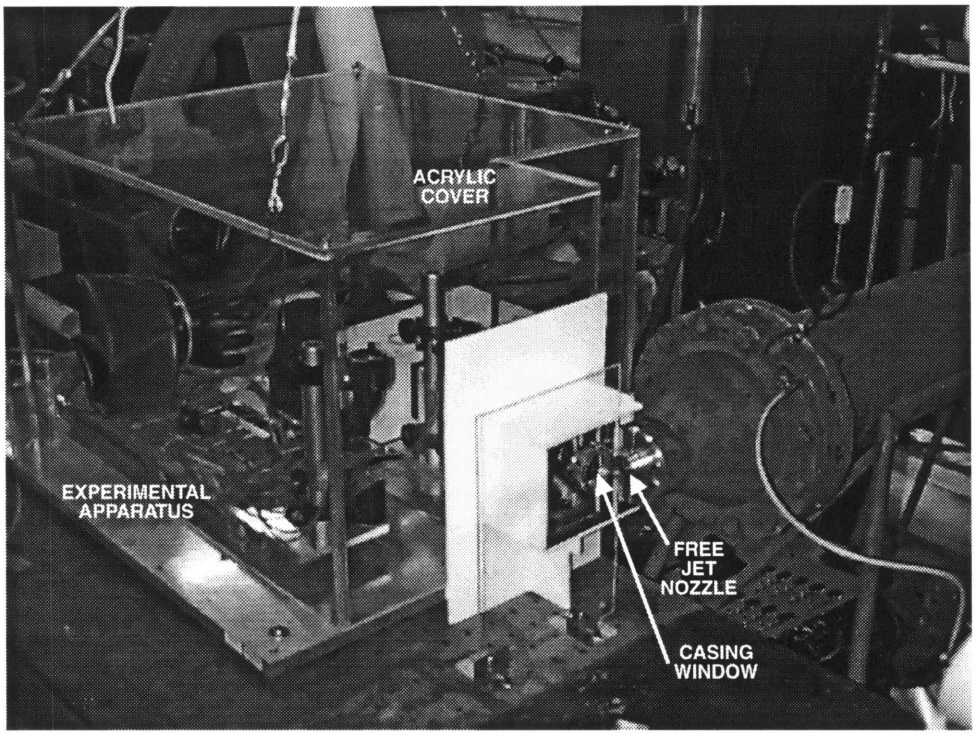

Figure 3.3: Experimental Apparatus, Front View

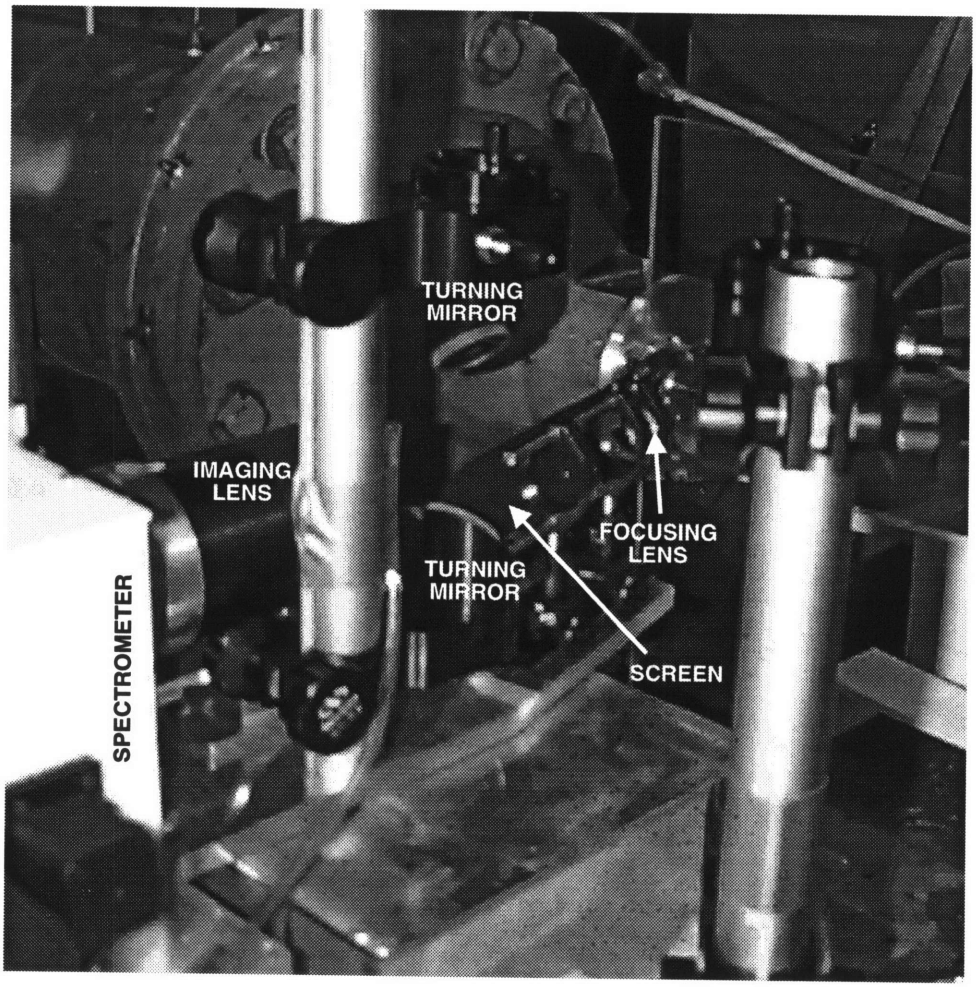

Figure 3.4: Focusing Optics

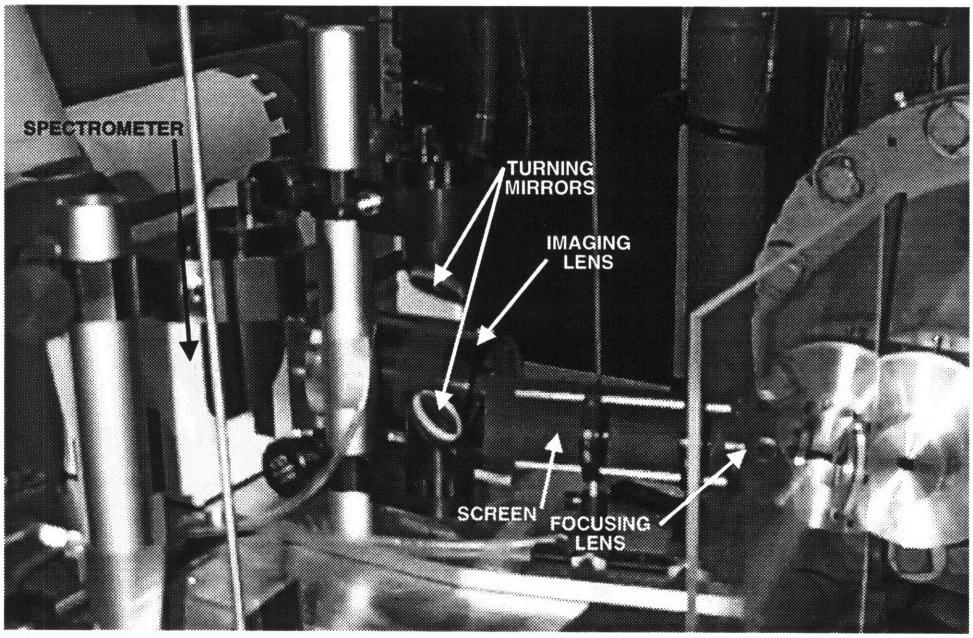

Figure 3.5: Imaging and Focusing Optics

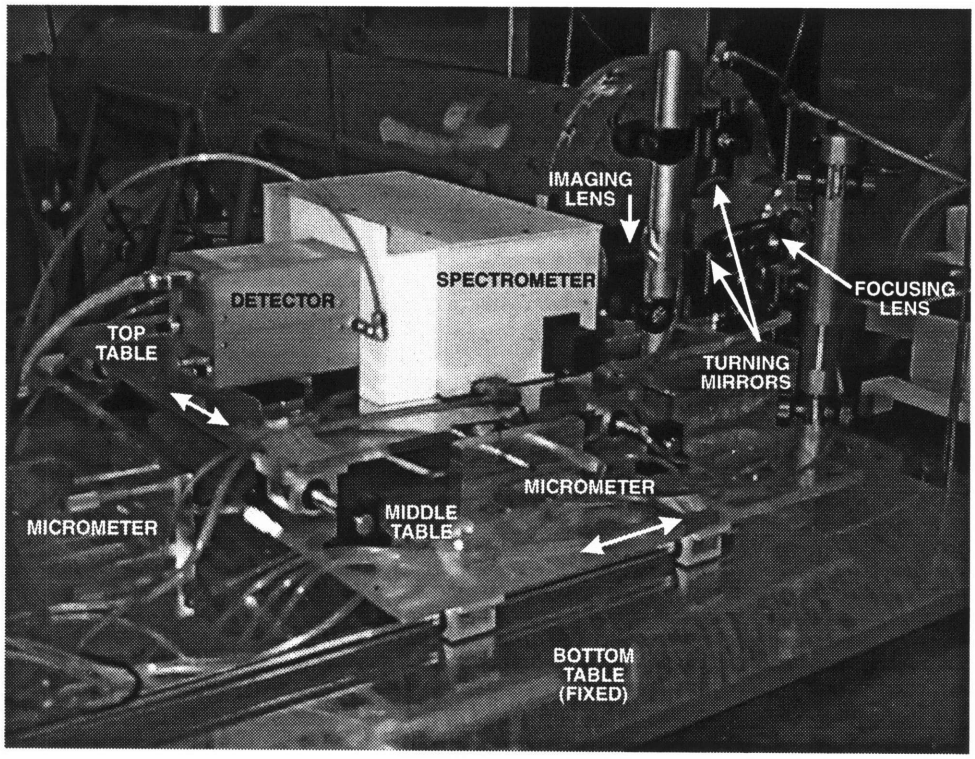

Figure 3.6: Tables and Positioning Mechanisms

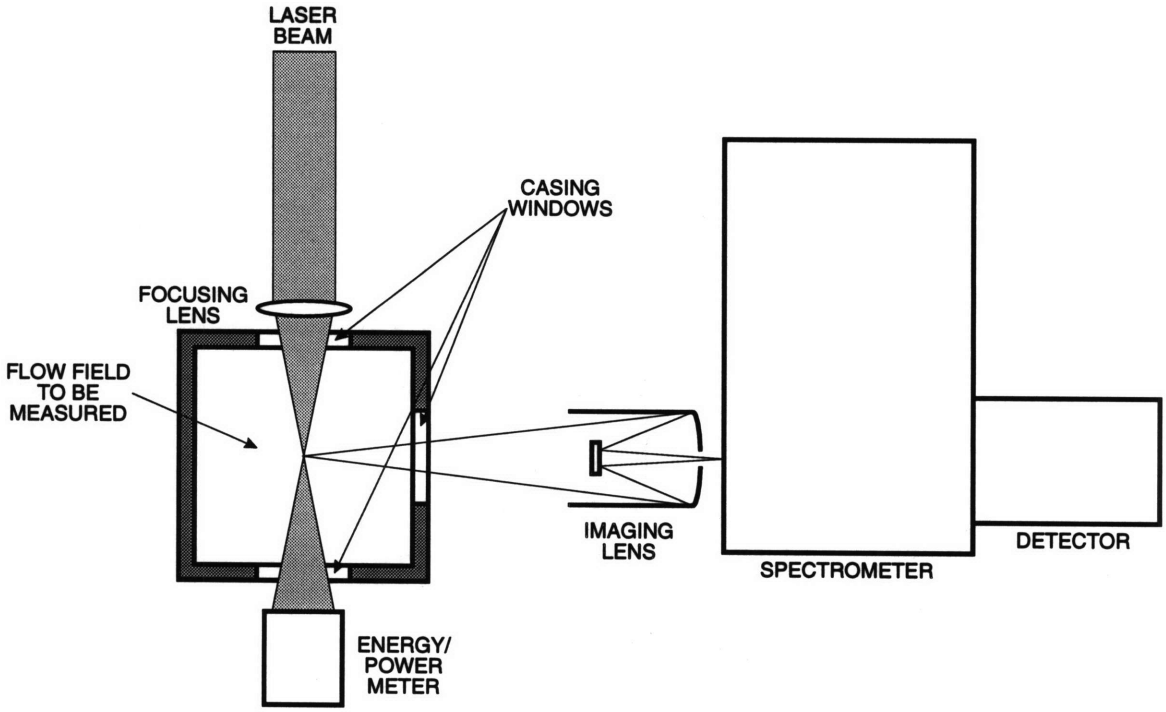

Figure 3.7: Side-Scatter Optical Configuration

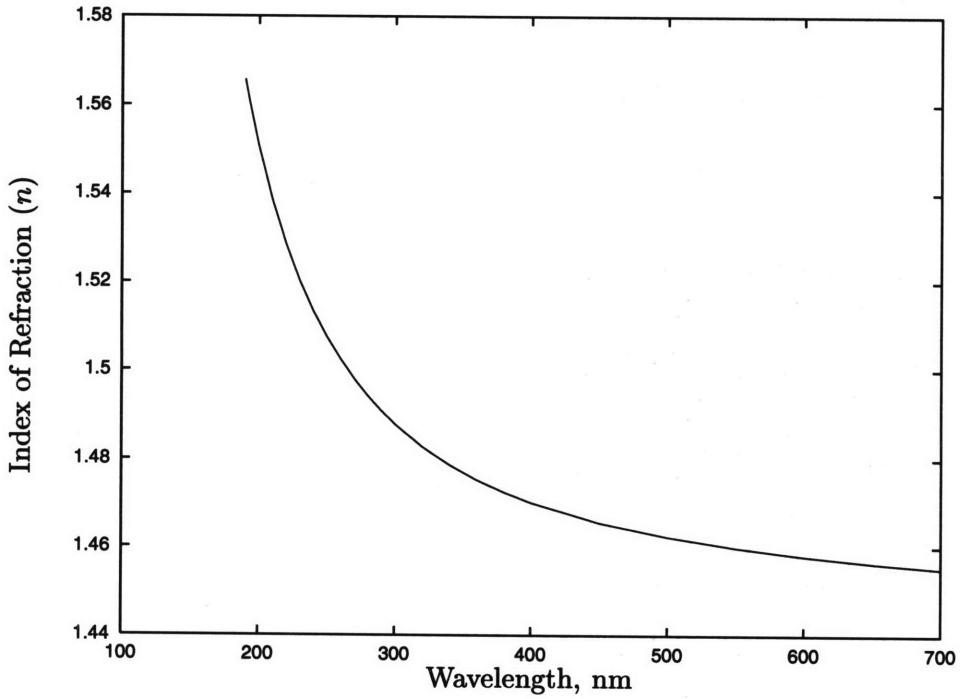

Figure 3.8: Index of Refraction of Fused Silica

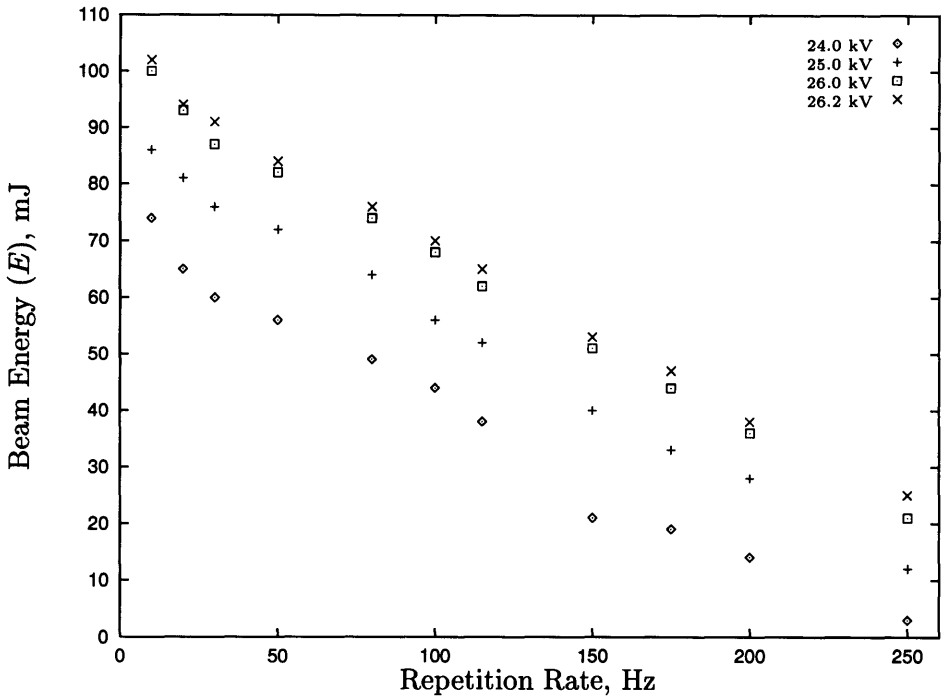

Figure 3.9: Laser Beam Energy as a Function of Laser Repetition Rate

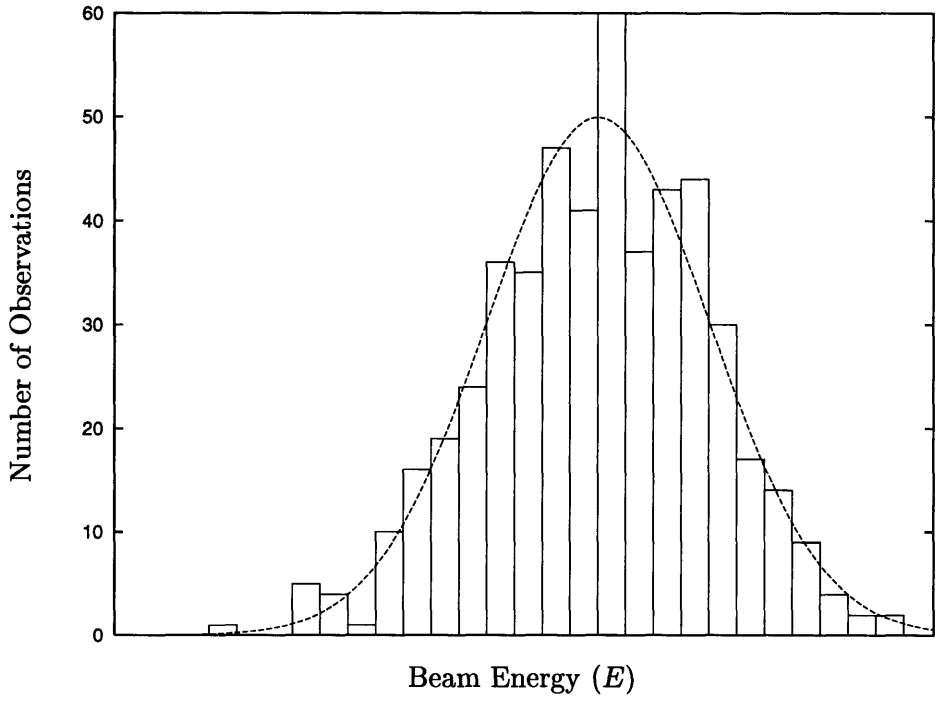

Figure 3.10: Distribution of Laser Beam Energy Level at 100 Hz

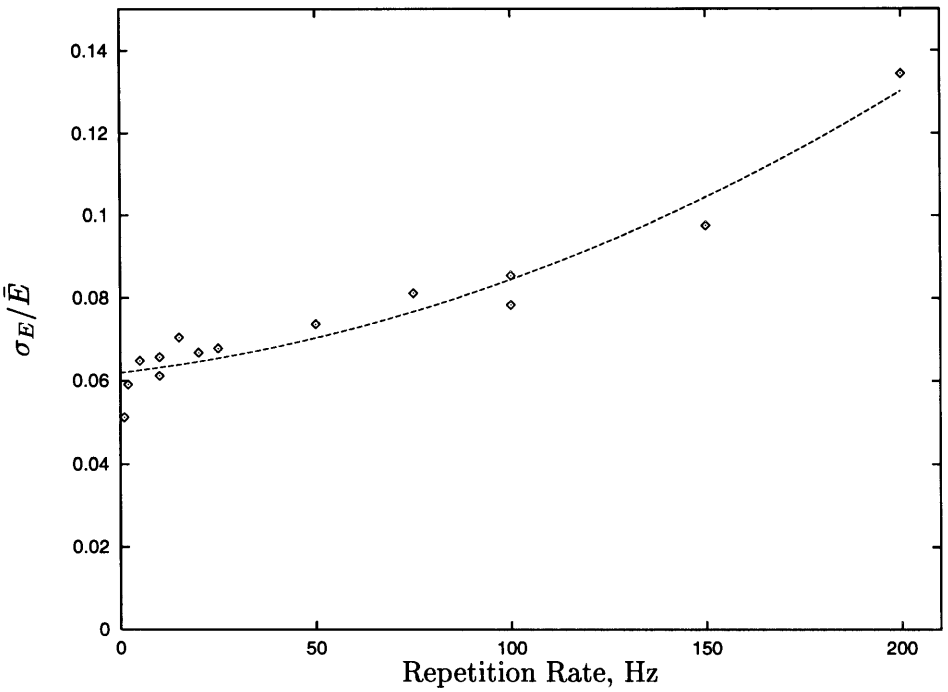

Figure 3.11: Shot-to-shot Laser Beam Energy Stability

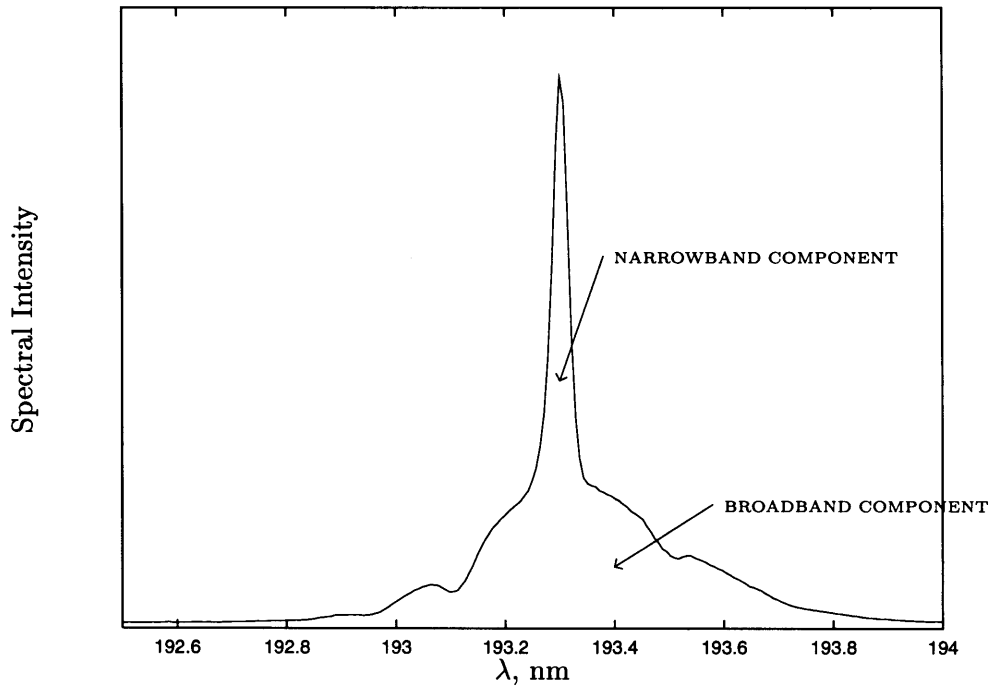

Figure 3.12: Laser Emission Spectrum in Narrowband Mode

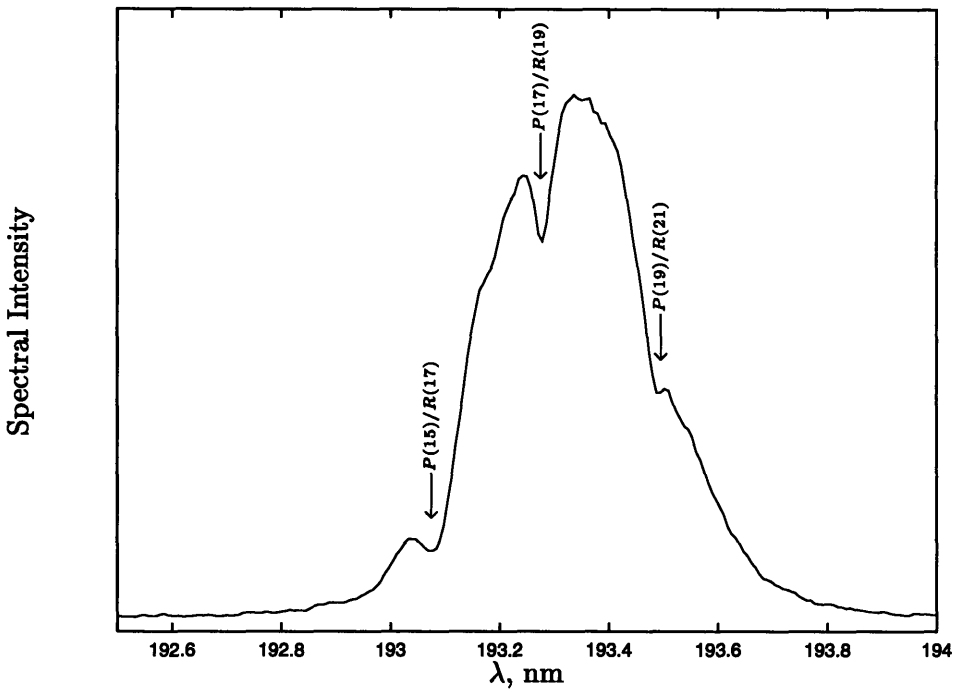

Figure 3.13: Laser Emission Spectrum in Broadband Mode

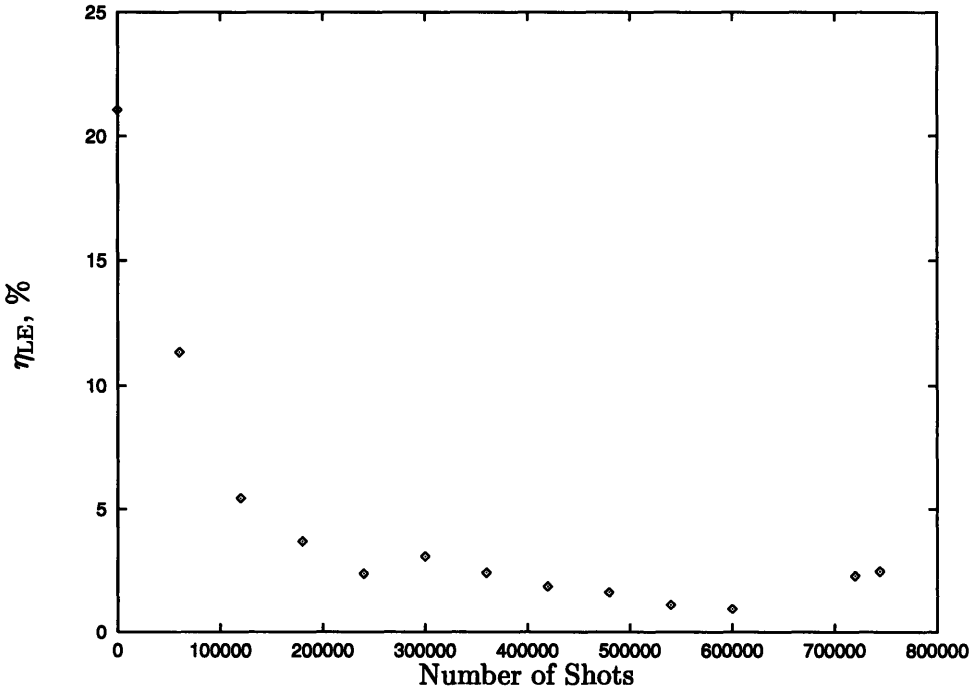

Figure 3.14: Stability of Laser Locking Efficiency

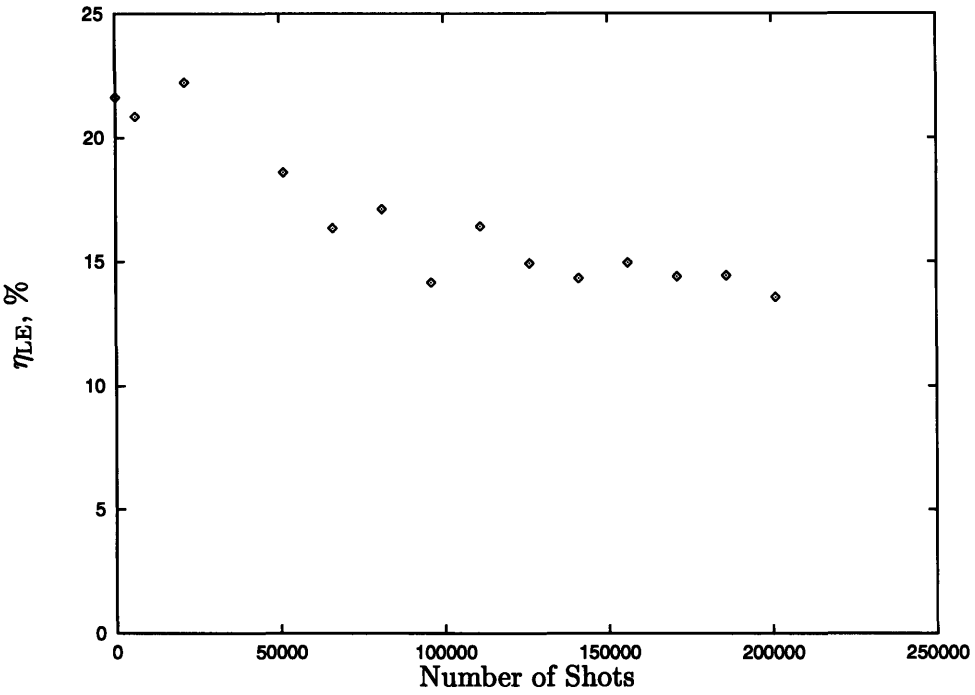

Figure 3.15: Stability of Laser Locking Efficiency

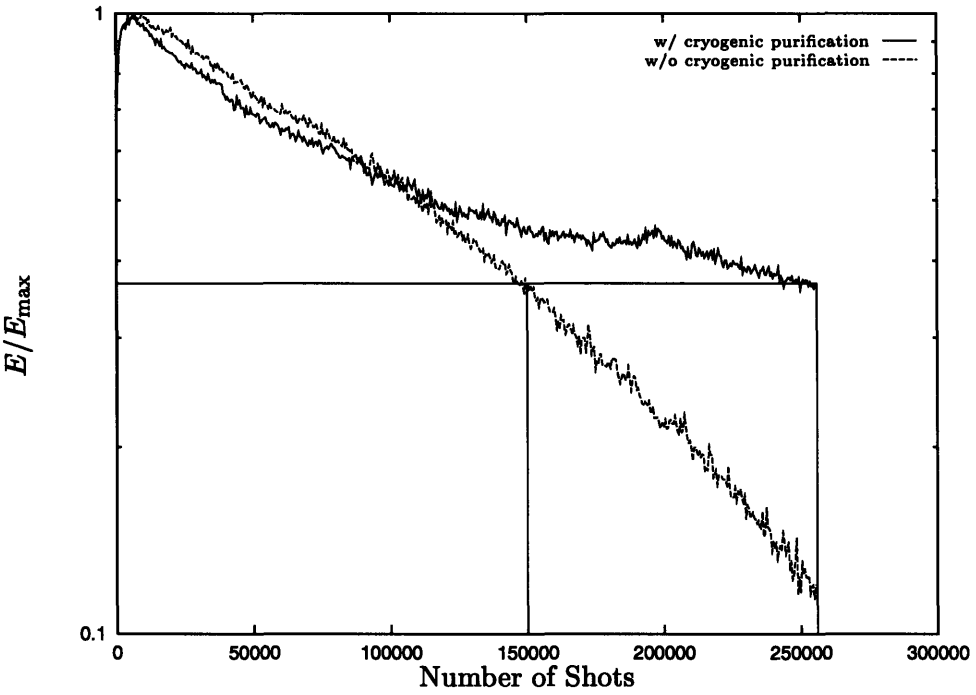

Figure 3.16: Long Term Stability of Laser Beam Energy

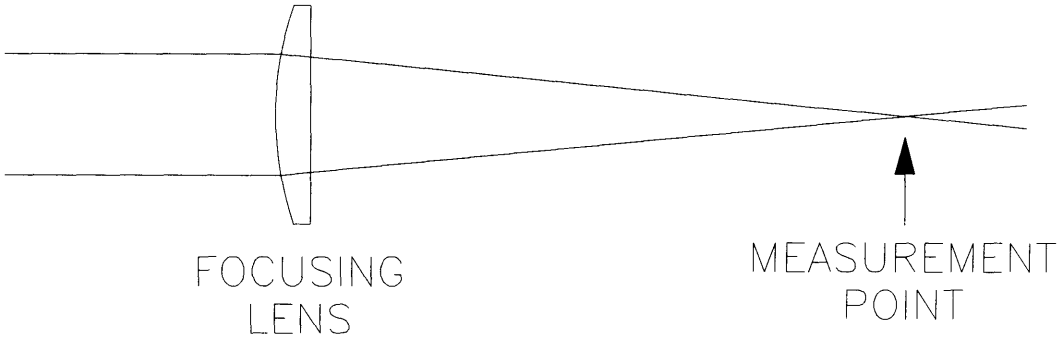

Figure 3.17: Configuration of the Focusing Lens

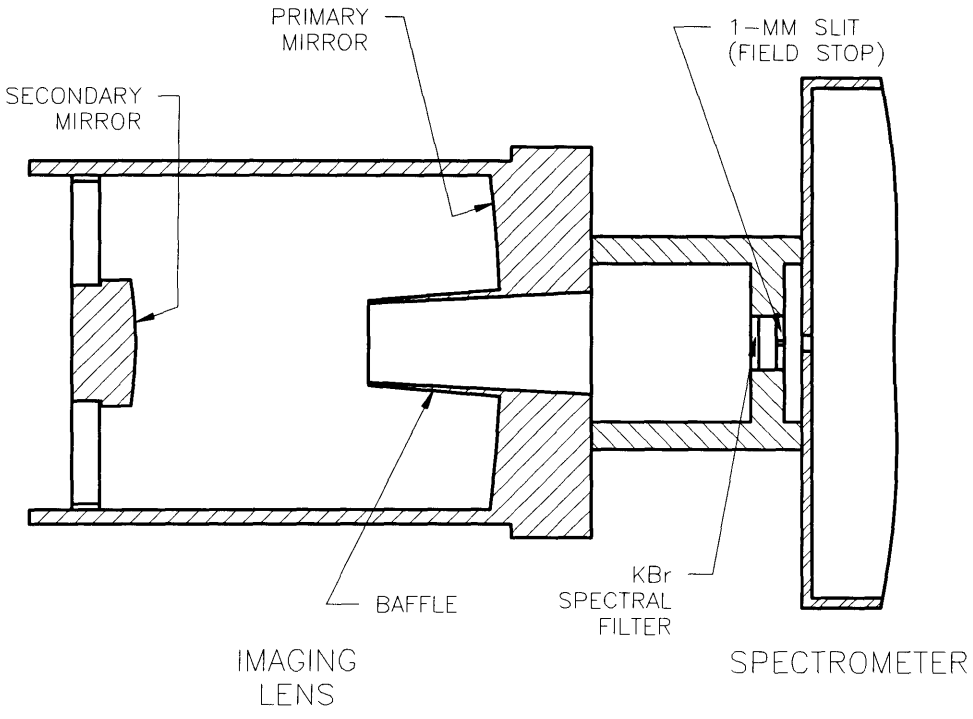

Figure 3.18: Imaging Lens

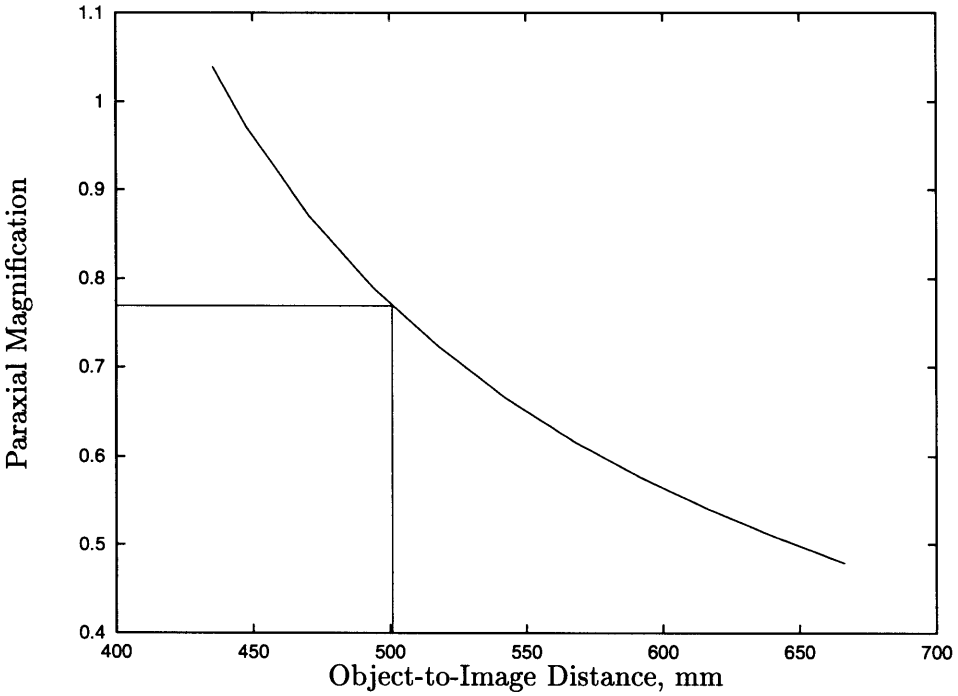

Figure 3.19: Conjugate Ratios for the Imaging Lens

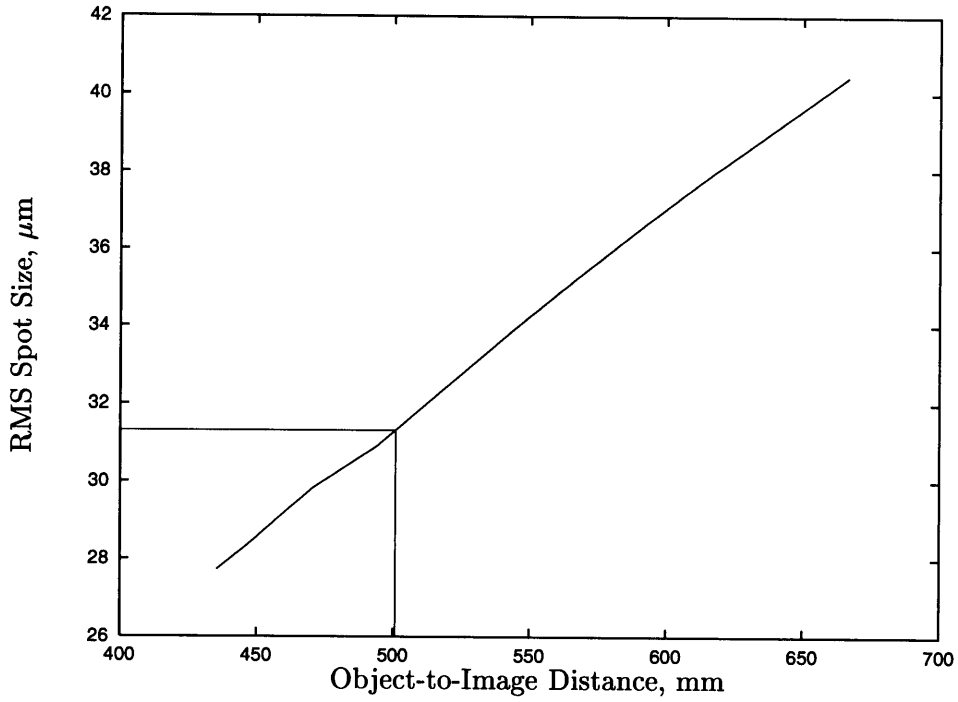

Figure 3.20: Spot Size

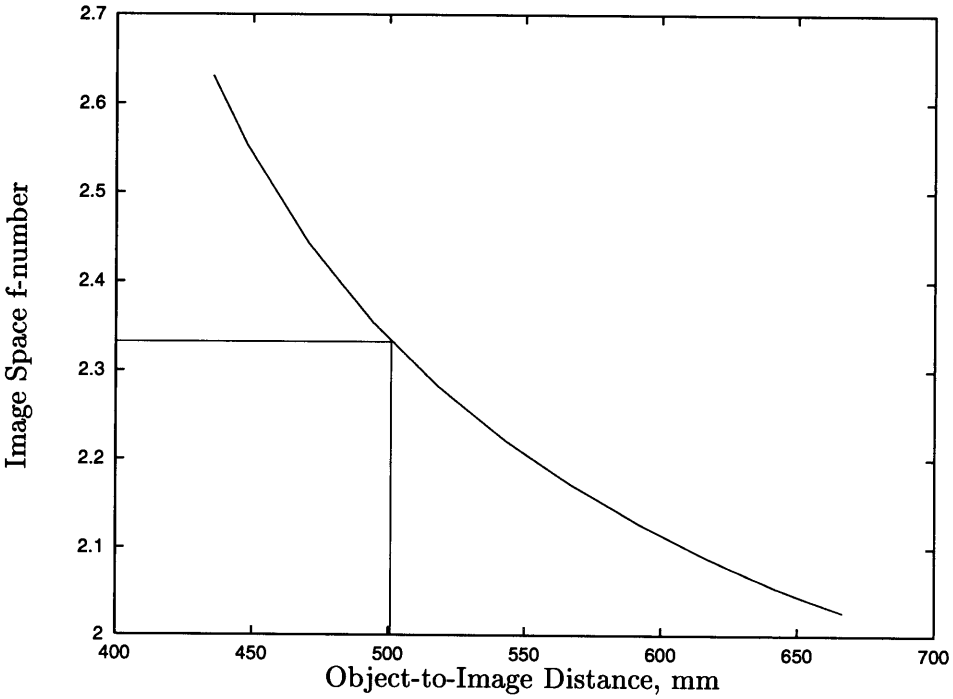

Figure 3.21: Image Space f-number

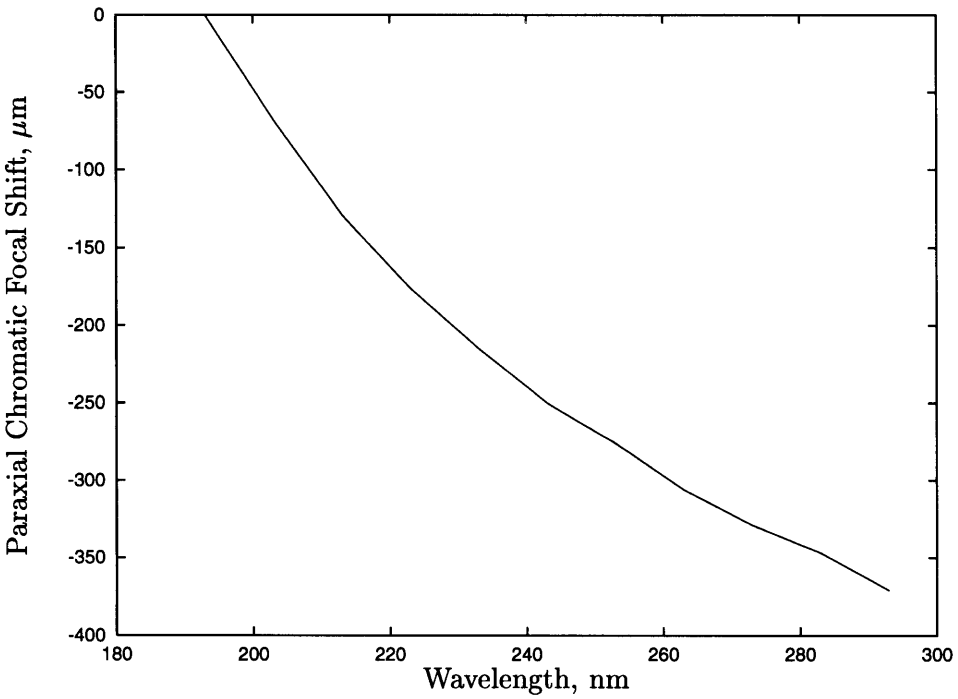

Figure 3.22: Chromatic Aberrations

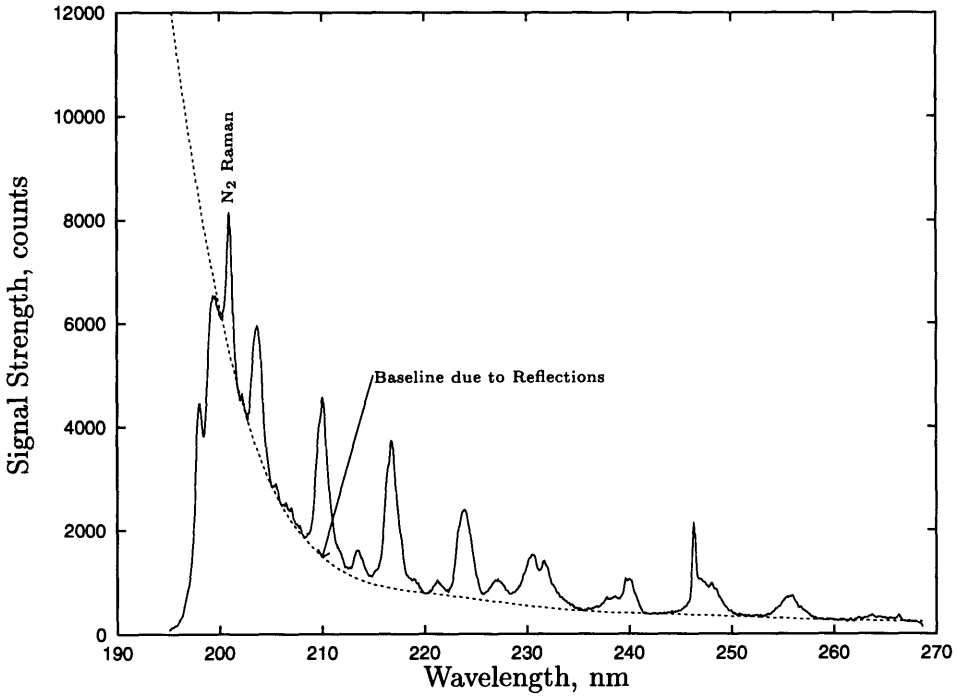

Figure 3.23: LIF Spectrum with No Spectral Filter

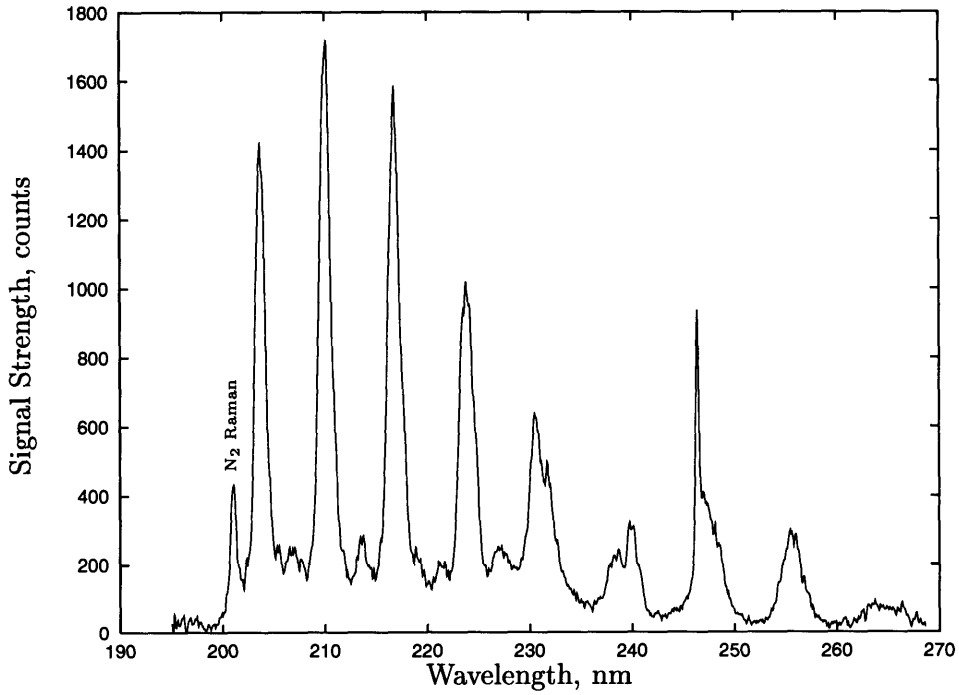

Figure 3.24: LIF Spectrum with 2-mm-thick KBr Disk

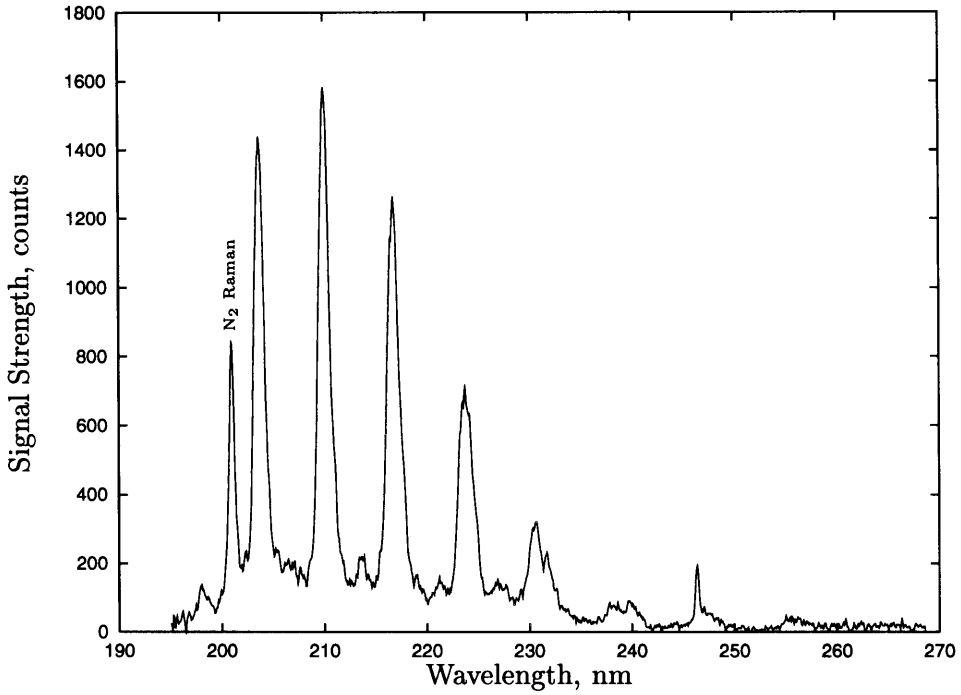

Figure 3.25: LIF Spectrum with 0.5% Acetone Solution

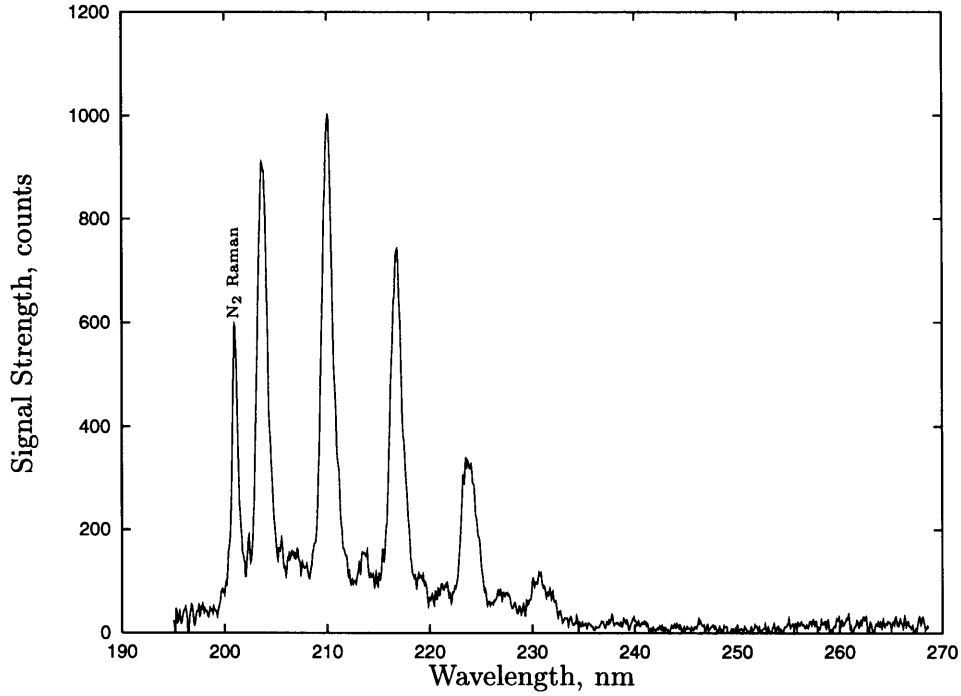

Figure 3.26: LIF Spectrum with 1.0% Acetone Solution

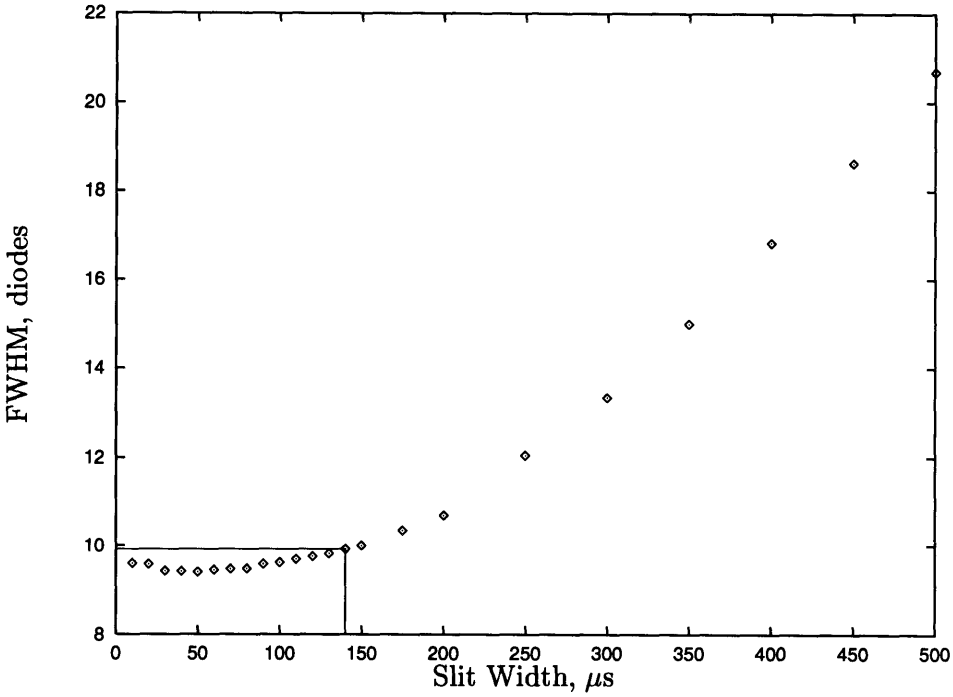

Figure 3.27: Spectrograph Resolution

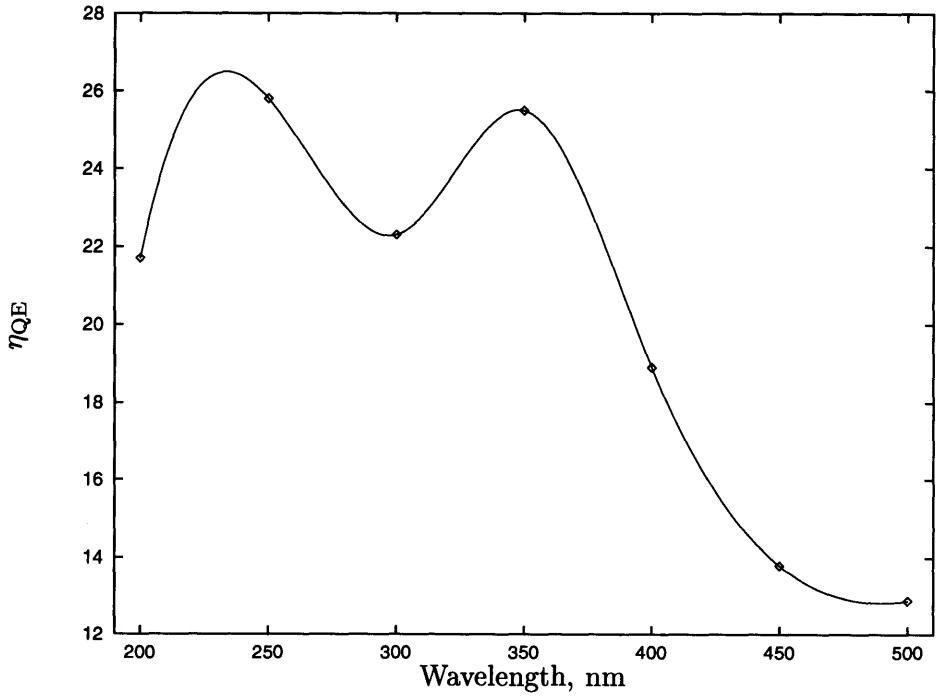

Figure 3.28: Detector Quantum Efficiency

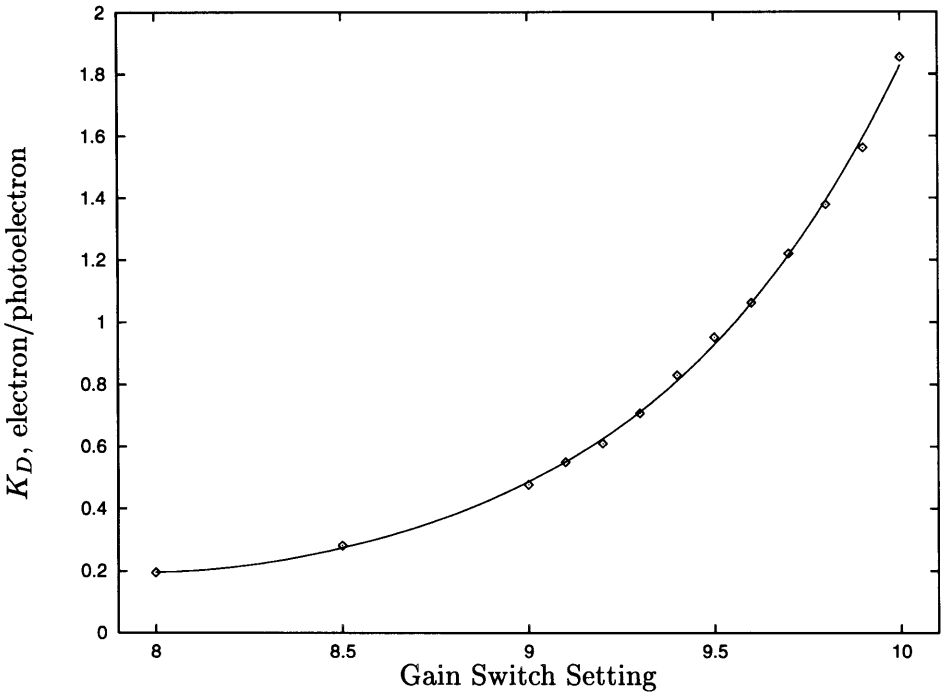

Figure 3.29: Detector Gain

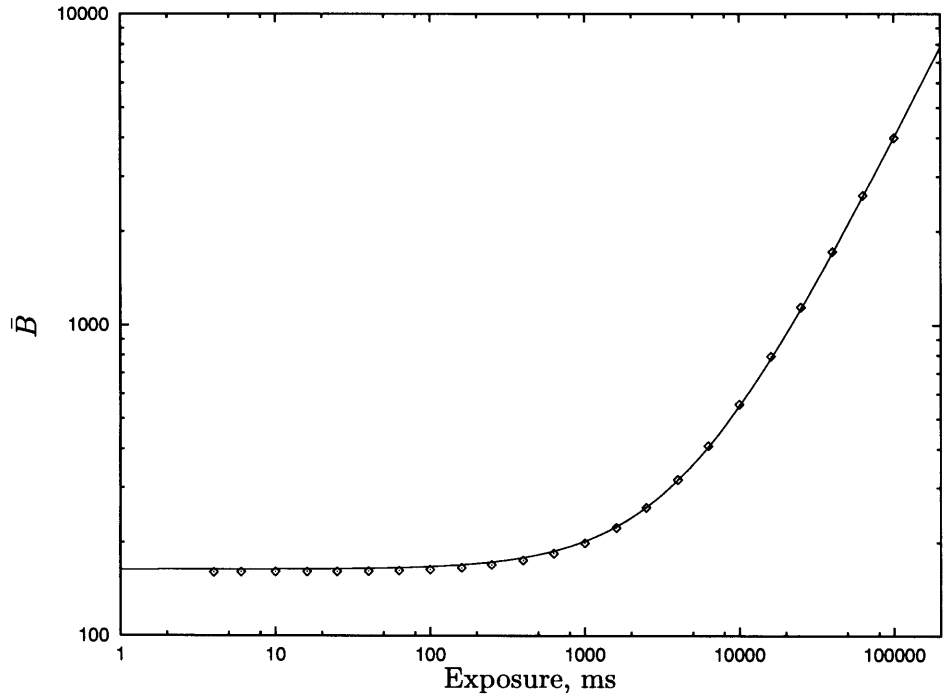

Figure 3.30: Detector Baseline Level

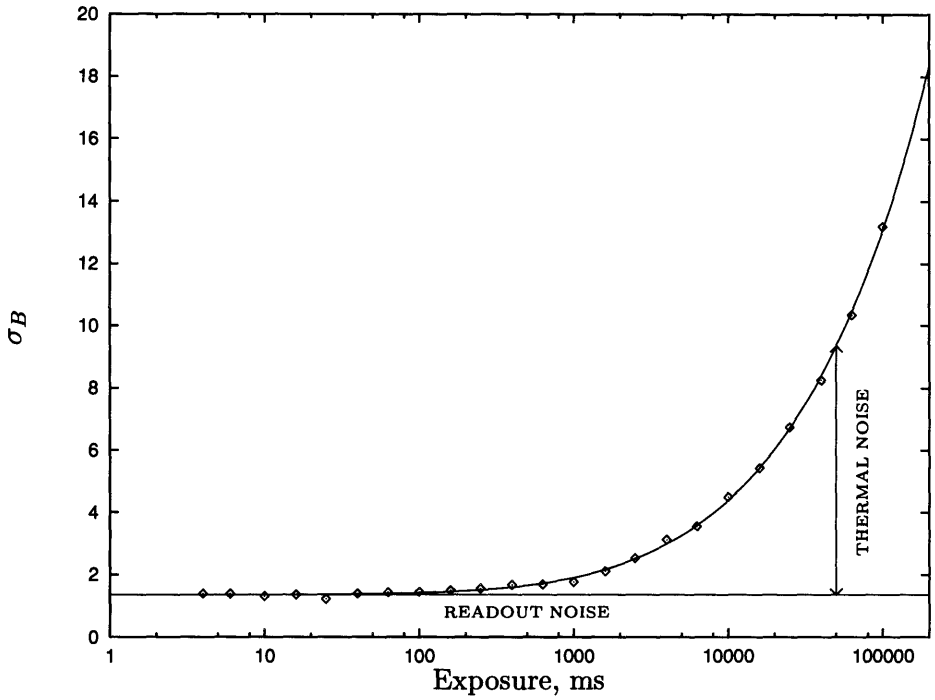

Figure 3.31: Detector Baseline Noise

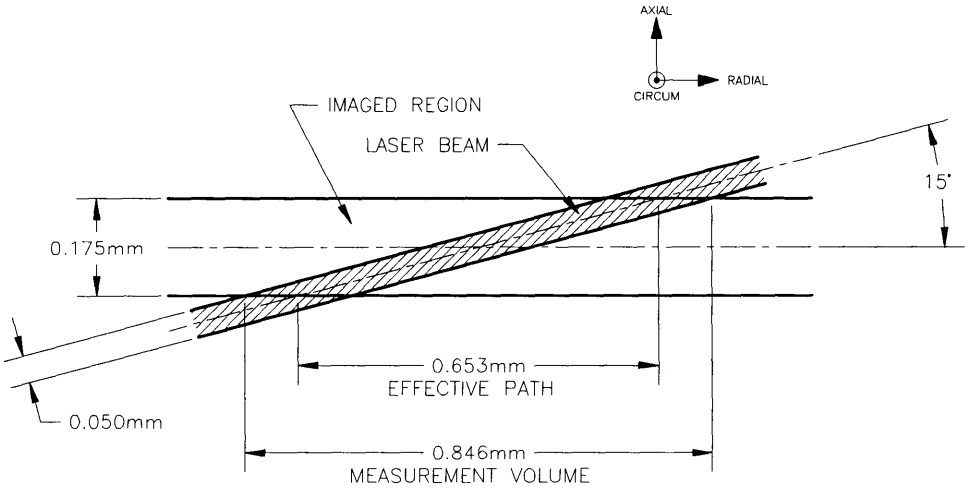

Figure 3.32: Measurement Volume Dimensions

Chapter 4
Data Reduction Technique and Calibration

Figure 4.1 shows typical spectra collected by the experimental apparatus at 301 K, 425 K and 557 K. The temperature dependence of the LIF signals can be clearly seen in these spectra. The objective of the data reduction procedure is to determine the gas temperature from a spectrum as precisely and accurately as possible.

The data reduction procedure uses the following steps in determining the temperature:

1. Elimination of Anomalous Spectra (see section 4.1)
2. Subtraction of Baseline (see section 4.2)
3. Grouping of Channels into Regional Signals (see section 4.3)
4. Calculation of Temperature Diagnostic Ratio ($\mathcal{R}$) (see section 4.4)
5. Determination of Gas Temperature (see section 4.5)

Each step is discussed in detail in the sections indicated.

In addition, the data reduction procedure estimates the uncertainty in the temperature measurement. This calculation is discussed in Chapter 5.

The data reduction method used in this project is relatively unsophisticated. Section 4.6 discusses the advantage of this technique over more sophisticated methods such as curve fitting.

The discussion in this chapter concentrates on data collected by a spectroscopic apparatus, where the LIF signals are dispersed by a spectrograph and the entire LIF spectrum is recorded. Section 4.7 discusses how the data reduction technique may be adapted for a non-spectroscopic apparatus such as one which would be used in a PLIF experiment.

4.1 Elimination of Anomalous Spectra

Occassionally, a spectrum recorded by the detector is contaminated by an anamolous pattern. Two types of anomalous patterns, designated A and B, and shown in Figure 4.3, are observed. Both types are observed even when the laser is not firing, so these anomalies are not caused by radiative processes excited by the laser.

Type A anomaly is a broad, skewed distribution. The peak of this distribution occurs at channel 50 (198.6 nm) and the distribution has a HWHM[1] of apprimately 100 channels

[1]HWHM: Half-width at half-maximum.

(3.6 nm). Average observed peak count is about 1000, although peak counts as high as 1500 are possible. This type of anomaly is observed approximately once every 500 spectra (6.25-s exposure). The source of this anomaly is not known.

In contrast, type B anomaly is a sharp and localized peak. Typical amplitude is about 500 counts, although amplitudes as high as 1000 counts have been observed. The anomaly has a FWHM of approximately 1 channel (0.07 nm). This type of anomaly may occur at any channel, and is observed approximately once every 100 spectra (6.25-s exposure). According to Princeton Instruments, Inc., the detector manufacturer, this anomaly is caused by cosmic rays hitting the detector.

Either type of anomaly contaminates the LIF spectrum and introduces an error to the temperature determination. Therefore, during the data reduction procedure, the recorded spectra are first examined for these anomalies, and the spectra with anomalies are not processed further.

4.2 Subtraction of Baseline

As discussed in Chapter 3, each spectrum recorded by the detector contains a baseline distribution. The baseline distribution consists of two components: a constant offset introduced by the detector, and a exposure-dependent component caused by buildup of thermal charge.

To determine the baseline to be subtracted, two additional experiments are run just before and just after each LIF experiment. The experimental conditions for these additional experiments are identical to the main experiment except that the laser is turned off. Several (typically 10) spectra are recorded during each experiment. Each spectra is examined for anomalies described earlier. The mean of the non-anomalous spectra is then subtracted as the baseline from each of the spectra in the main LIF experiment.

The variation in the spectra recorded during the two baseline experiments is then taken as an estimate of the baseline uncertainty (thermal and readout noise) during the main LIF experiment.

4.3 Grouping of Channels into Regional Signals

One spectrum recorded by the detector contains 1024 numbers, each number being the count recorded by one channel in the detector. After baseline subtraction, these 1024 counts are grouped into 13 regional signals. The main objectives in this grouping are to extract oxygen LIF signals from regions with no LIF signals, to isolate regions containing contaminating signals (e. g. C-atom LIF at 248 nm), and to separate oxygen LIF signals with high temperature sensitivity from those with low temperature sensitivity.

The boundaries of the thirteen regions are listed in Table 4.1. They are also shown in Figure 4.2 for the three spectra at 301 K, 425 K and 557 K. Note that the region at 248 nm is not included in any signal because of contamination due to C-atom fluorescence.

The boundaries of each region must be chosen to maximize the signal-to-noise ratio of the regional signal. This involves a trade off between shot noise and baseline noise. Since

the shot noise of a signal scales as $\sqrt{S}$, the shot-noise-limited signal-to-noise ratio ($\sim \sqrt{S}$) increases with increasing signal level. If shot noise were the only noise source, all of the 1024 counts in a spectrum would be assigned to a region, for each additional count, no matter how small, would improve the signal-to-noise ratio.

However, each channel reading also has baseline noise associated with it. Compared to a channel near the center of an LIF peak, a channel in the tails has the same amount of baseline noise but a much weaker LIF signal. Therefore, inclusion of such a count in the regional signal would decrease the signal-to-noise ratio, as the improvement in shot-noise due to the small increase in signal would not be enough the compensate for the additional baseline noise.

4.4 Calculation of Temperature Diagnostic Ratio ($\mathcal{R}$)

The data reduction procedure now calculates a temperature diagnostic ratio ($\mathcal{R}$) from the thirteen regional signals ($S_1, \ldots, S_{13}$) as follows:

$$\mathcal{R} = \frac{S_N}{S_D} = \frac{S_2 + S_3 + S_4 + S_5 + S_6 + S_8 + S_{11}}{S_1 + S_7 + S_9 + S_{10} + S_{12} + S_{13}} \tag{4.1}$$

Theoretically, each regional signal is not only a function of temperature but also linearly dependent on gas pressure and laser energy. The temperature diagnostic ratio, however, is independent of gas pressure and laser energy, and is a function of temperature alone.

The regional signal must be grouped into the numerator (S_N) and denumerator (S_D) signals in such a way that the temperature measurement precision is maximized.

4.4.1 Theoretical Development

The temperature diagnostic ratio is given by

$$\mathcal{R} = \frac{S_N}{S_D} \tag{4.2}$$

with

$$S_N = S_1^n + \ldots + S_M^n \tag{4.3}$$
$$S_D = S_1^d + \ldots + S_N^d \tag{4.4}$$

The shot noise in each signal scales as $\sqrt{S}$. The shot noise of S_N and S_D is then given by

$$\sigma_{S_N} = \sqrt{\sigma_{S_1^n}^2 + \ldots + \sigma_{S_M^n}^2} = \sqrt{S_1^n + \ldots + S_M^n} = \sqrt{S_N} \tag{4.5}$$
$$\sigma_{S_D} = \sqrt{\sigma_{S_1^d}^2 + \ldots + \sigma_{S_N^d}^2} = \sqrt{S_1^d + \ldots + S_N^d} = \sqrt{S_D} \tag{4.6}$$

The resulting uncertainty in $\mathcal{R}$ can be computed using

$$\sigma_{\mathcal{R}} = \mathcal{R}\sqrt{\left(\frac{\sigma_{S_N}}{S_N}\right)^2 + \left(\frac{\sigma_{S_D}}{S_D}\right)^2} = \mathcal{R}\sqrt{\frac{1}{S_N} + \frac{1}{S_D}} \tag{4.7}$$

The temperature dependence of $\mathcal{R}$ is given by

$$\begin{aligned}
\frac{d\mathcal{R}}{dT} &= \frac{1}{S_D}\frac{dS_N}{dT} - \frac{S_N}{S_D^2}\frac{dS_D}{dT} \\
&= \mathcal{R}\left[\frac{dS_N/dT}{S_N} - \frac{dS_D/dT}{S_D}\right] \\
&= \mathcal{R}\left[\frac{dS_1^n/dT + \ldots + dS_M^n/dT}{S_1^n + \ldots + S_M^n} - \frac{dS_1^d/dT + \ldots + dS_M^d/dT}{S_1^d + \ldots + S_N^d}\right]
\end{aligned} \tag{4.8}$$

Finally, the uncertainty in the temperature determined from $\mathcal{R}$ may be computed using

$$\sigma_T = \frac{\sigma_{\mathcal{R}}}{d\mathcal{R}/dT} = \frac{\sqrt{\dfrac{1}{S_1^n + \ldots + S_M^n} + \dfrac{1}{S_1^d + \ldots + S_N^d}}}{\dfrac{dS_1^n/dT + \ldots + dS_M^n/dT}{S_1^n + \ldots + S_M^n} - \dfrac{dS_1^d/dT + \ldots + dS_M^d/dT}{S_1^d + \ldots + S_N^d}} \tag{4.9}$$

To maximize precision, temperature uncertainty σ_T should be minimized. From equation (4.9), following general rules may be formulated for grouping the regional signals into numerator and denumerator signals:

1. Signals with higher temperature sensitivity should be placed in the numerator and signals with lower temperature sensitivity should be placed in the denumerator.
2. Both the numerator and the denumerator should have approximately the same magnitude. If one component is much smaller than the other, the temperature uncertainty would be dominated by the uncertainty in that signal.
3. The numerator and the denumerator signals should be as large as possible. This means that all regional signals should be assigned to either the numerator or the denumerator.

4.4.2 Analysis of LIF Data

In order to determine the temperature dependence of the regional signals, LIF data was collected at eleven temperatures using the calibration apparatus[2]. The pressure during these experiments were 3.73 ± 0.07 atm. Ten spectra were recorded during each experiment. Regional signals were computed for each spectra after elimination of anomalous spectra and baseline subtraction as described above.

[2]For a description of the calibration apparatus, see Appendix A.

For each experiment, the regional signals from the ten recorded spectra were averaged. In order to account for laser energy and gas pressure variations, the mean signals were scaled so that region 1 signal, which is the nitrogen Raman signal, was equal to

$$S_1 = \frac{1000}{T/273.2\ \mathrm{K}} \tag{4.10}$$

Nitrogen Raman signal was chosen for normalization, because it depends on temperature only through density (e. g. $\sim 1/T$). The 1000 counts on the numerator of equation (4.10) is arbitrary.

The normalized data for these signals are plotted in Figures 4.4 through 4.16. The error bars shown are the standard deviation of the ten spectra (minus any anomalous spectra rejected) recorded during each experiment (scaled with the spectra).

All regional signals, except for Region 1, contain O_2 LIF signals which increase with temperature. The purpose of this procedure is to separate the regions with high temperature dependence from those with low temperature dependence. The former will be assigned to the numerator signal (S_N) and the latter will be part of the denumerator signal (S_D).

A function of form

$$S = \exp\left[A_0 + A_1\left(\frac{T}{T_{\mathrm{ref}}}\right) + A_2\left(\frac{T}{T_{\mathrm{ref}}}\right)^2\right], \tag{4.11}$$

where $T_{\mathrm{ref}} = 425$ K, was next fitted to each regional signal. The purpose of this function is to provide a smooth approximation to the temperature derivative of the regional signals. The coefficients for these fits are listed in Table 4.2. Although not perfect, the fits are adequate for the evaluation of various data reduction schemes. Most of the variations in the signals originate from laser energy and gas temperature variations which the simple normalization described above cannot completely account for. The slope of the regional signals with respect to temperature can be computed using

$$\frac{dS}{dT} = \left(\frac{S}{T_{\mathrm{ref}}}\right)\left[A_1 + 2A_2\left(\frac{T}{T_{\mathrm{ref}}}\right)\right] \tag{4.12}$$

The slopes (dS/dT) were then computed at 425 K, and the signals were then ranked from high dS/dT to low dS/dT. The signals were assigned to numerator and denumerator in various ways, with the signals with high dS/dT always going to the numerator and signals with low dS/dT always going to the denumerator. The temperature uncertainty σ_T was computed for each assignment. The results of these calculations are shown in Tables 4.3 and 4.4[3].

The same calculation was repeated at 325 K and 525 K. Results of these calculations are listed in Tables 4.5 through 4.8[4].

[3]Each line in Table 4.4 is a way of assigning the thirteen regions of Table 4.3 to the numerator and denumerator signals. This table attempts to determine the assignment with the highest precision (lowest σ_T).

[4]It should be noted that the absolute value of the temperature uncertainty (σ_T) shown in Tables 4.4 through 4.8 is arbitrary. The σ_T values should be only used to compare various assignments to each other. The absolute precision of the temperature measurement technique is discussed in Chapter 5.

After examining the data in Tables 4.3 through 4.8, the following assignment was chosen as giving the optimum precision across the temperature range:

S_N	$S_2, S_3, S_4, S_5, S_6, S_8, S_{11}$
S_D	$S_1, S_7, S_9, S_{10}, S_{12}, S_{13}$

4.5 Determination of Gas Temperature

Once the temperature diagnostic ratio $\mathcal{R}$ is calculated, the temperature may be determined from a $T(\mathcal{R})$ calibration curve.

Calibration data was obtained using the calibration apparatus. A full factorial set of experiments at 11 temperatures, 5 pressures and 5 laser pulse energy levels were run for a total of 275 experiments. Ten spectra were recorded during each experiment. These spectra were processed as described in sections 4.1 through 4.4.

The mean and standard deviation for $\mathcal{R}$ were computed for the spectra in each experiment. For a given temperature and pressure level, the mean $\mathcal{R}$ values for the five energy level experiments were averaged using the reciprocal of standard deviations in $\mathcal{R}$ as weighting factors. The resulting data is listed in Table 4.9.

The last column in Table 4.9 lists the average of $\mathcal{R}$ for the five pressure levels. Once again, the reciprocal of the standard deviation was used as the weighting factor in the averaging process.

An equation of the following form was then fitted to the data in each column:

$$\mathcal{R} = \frac{1 + A_1(T/T_{\text{ref}}) + A_2(T/T_{\text{ref}})^2}{A_3 + A_4(T/T_{\text{ref}}) + A_5(T/T_{\text{ref}})^2} \tag{4.13}$$

Again, $T_{\text{ref}} = 425$ K. The coefficients for the fits are listed in Table 4.10.

The calibration curves are plotted in Figures 4.17 and 4.18. Note that the calibration curves are monotonic in the 300–560 K interval.

The sensitivity of the temperature diagnostic ratio $\mathcal{R}$ can be computed using the following equation:

$$\frac{d\mathcal{R}}{dT} = \frac{\mathcal{R}}{T_{\text{ref}}}\left[\frac{A_1 + 2A_2\,(T/T_{\text{ref}})}{1 + A_1\,(T/T_{\text{ref}}) + A_2\,(T/T_{\text{ref}})^2} - \frac{A_4 + 2A_5\,(T/T_{\text{ref}})}{A_3 + A_4\,(T/T_{\text{ref}}) + A_5\,(T/T_{\text{ref}})^2}\right] \tag{4.14}$$

The temperature derivative of the calibration curves are plotted in Figures 4.19 and 4.20.

Using quadratic formula, equation (4.14) can be written explicitly for T given $\mathcal{R}$:

$$T = T_{\text{ref}}\left[\frac{A_1 - RA_4 - \sqrt{(A_1 - RA_4)^2 - 4\,(RA_5 - A_2)\,(RA_3 - 1)}}{2\,(RA_5 - A_2)}\right] \tag{4.15}$$

For the 300-550 K temperature range, the indicated root of the quadratic formula should be used.

4.6 Curve Fitting Techniques

The traditional data reduction method in spectroscopy is curve fitting. In this technique, the spectrum is modeled with an analytical function containing a number of different peak functions such as Lorentzian or Gaussian, and least-squares techniques are used to determine the set of peak amplitudes, locations and widths which best agree with the experimental data. Because the analytical function depends nonlinearly on peak locations and widths, nonlinear optimization techniques must be used. ROBFIT [2, 3] is an example program which implements this procedure.

If such a technique is used in this project, the total power for each peak would be computed by integrating the analytical function over all wavelenghts, and this number would be assigned to either the numerator or denominator signal depending on the location of the peak.

Unfortunately, the parameters determined by nonlinear minimization techniques are extremely sensitive to fluctuations in the experimental data. Therefore, the data fluctuations may be amplified by the curve fitting method, and the resulting uncertainty in the diagnostic ratio may reduce the measurement precision.

Each spectrum consists of 1024 channels, only 445 of which have relevant O_2 LIF data. The uncertainty in the composite signals S_N and S_D is then given by simple error propagation formulae [1]. The data reduction method cannot improve the uncertainty unless it brings in new information.

The curve fitting techniques used in traditional spectroscopy do bring in additional information, namely the analytical shape of the peak. However, in this experiment, each LIF peak consists of a large number of superimposed peaks, which are not resolved by the spectrograph at operating conditions. For example, Figure 4.21 shows two views of one LIF peak. The top spectrum was recorded using the 1200 mm^{-1} grating used in all LIF experiments. The bottom spectrum shows the same LIF peak recorded using the 3600 mm^{-1} grating which has a higher resolving power. Comparison of the two spectra shows that the LIF peak is indeed made up of a number of narrow peaks, which are not resolved at the operating conditions.

Because an analytical function for the composite LIF peaks does not exist, curve fitting does not bring in any additional information. Therefore, the simple summation technique presented earlier offers the best precision for this technique and is used for this project.

4.7 Non-Spectroscopic Apparatus

The data reduction technique discussed above relies on the spectrograph to disperse the LIF signals into component wavelengths. Since the entire spectrum is known, regional signals may be assigned to the numerator and denumerator in such a way that the temperature measurement precision is maximized.

However, a non-spectroscopic apparatus, such as one which may be used for a PLIF experiment, cannot record the entire spectrum. Instead, two detectors may be used. The first detector, with a low-pass spectral filter, will record $\lambda < \lambda_c$, and the second detector,

with a high-pass spectral filter, will record $\lambda > \lambda_c$. The signals from the two detectors will then be used to form the temperature diagnostic ratio.

The data presented in section 4.3 can be used to determine the optimum value of cutoff wavelength λ_c. Tables 4.11–4.13 show the precision for various λ_c at 325 K, 425 K and 525 K. Based on this data, the best λ_c is chosen as 229.3 nm. The temperature precision of the non-spectroscopic apparatus, for identical experimental conditions, is about 50% of that of spectroscopic apparatus at 425 K.

4.8 Summary

The main points of this chapter are highlighted below:

- The first step in the data reduction method used in this project is the elimination of two types of anomalous spectra which contaminate the LIF data.
- The baseline signal, which is determined from baseline spectra taken immediately before and after the LIF experiment, is then subtracted from the LIF spectrum.
- The remaining LIF signals are divided into spectral regions, and the total signal for each region is computed by summing the data from individual channels in the region.
- The regional signals are grouped into a numerator and a denumerator signal. This grouping is chosen to maximize temperature measurement precision. The ratio of the two signals, called the temperature diagnostic ratio, is then computed.
- Temperature is then determined from an empirical temperature versus temperature diagnostic ratio function.
- The simple summation technique used for this project is the most precise data reduction method. More sophisticated curve fitting routines, which are tradionally used in spectroscopy, do not provide any advantage because the LIF peak shapes cannot be be expressed with analytical functions.
- The data reduction technique presented in this chapter for a spectroscopic apparatus may be easily extended to a non-spectroscopic apparatus. The appropriate wavelength boundary is 229.3 nm. The precision of the non-spectroscopic apparatus is only 50% of the precision of the spectroscopic apparatus.

References

[1] BEVINGTON, P. R., AND ROBINSON, D. K. *Data Reduction and Error Analysis for the Physical Sciences*, second ed. McGraw-Hill, Inc., New York, NY, 1992.

[2] COLDWELL, R. L. Iterative Codes for Fitting Complete Spectra. *Nuclear Instruments and Methods In Physics Research A242* (1986), 455–461.

[3] COLDWELL, R. L., AND BAMFORD, G. J. *The theory and operation of spectral analysis using ROBFIT.* American Institute of Physics, New York, NY, 1991.

Table 4.1: Region Boundaries

Region	Channel Index[a]		Number of Channels	Wavelength, nm		Comment
	Low	High		Low	High	
1	95	108	14	201.76	202.77	N_2 Raman
2	122	154	33	203.70	206.08	
3	208	242	35	209.89	212.41	
4	298	342	45	216.36	219.60	
5	390	450	61	222.98	227.37	
6	505	525	21	231.25	232.76	
7	526	550	25	232.76	234.56	
8	598	632	35	237.94	240.46	
9	633	663	31	240.46	242.69	
10	753	773	21	249.09	250.60	
11	820	869	50	253.91	257.51	
12	870	908	39	257.51	260.31	
13	953	987	35	263.48	265.99	

[a]Assumes 1200 mm^{-1} grating centered at 234 nm

Table 4.2: Fitted Coefficients for Temperature Dependence Function (see equation (4.11))

Region	χ^2	A_0	A_1	A_2
1	0.011	8.008	−2.063	0.520
2	67.784	8.303	−4.354	3.798
3	62.705	2.405	6.426	−0.844
4	50.129	3.025	6.478	−1.336
5	55.231	5.510	2.455	0.248
6	63.638	4.397	0.905	1.579
7	32.000	8.058	−1.425	0.964
8	55.963	5.122	−0.991	2.387
9	31.533	7.609	0.276	−0.091
10	33.475	7.522	−1.242	−0.961
11	59.512	−1.803	11.657	−2.900
12	60.284	−1.749	−1.749	2.113
13	88.667	−7.329	−7.329	6.149

Table 4.3: Regional Signal Levels at 425 K

Region	S	dS/dT
3	2943	32.8
4	3524	31.6
5	3690	25.6
2	2316	17.7
11	1047	14.4
6	974	9.31
8	678	6.03
12	668	3.89
13	251	2.93
7	1993	2.36
10	1395	2.23
9	2425	0.531
1	642	−1.55

Table 4.4: Regional Assignments at 425 K

Numerator Regions	Denumerator Regions	S_N	S_D	dS_N/dT	dS_D/dT	σ_T
3	1–2, 4–13	2943	19602	32.8	115	0.0741
3–4	1–2, 5–13	6467	16078	64.4	83.5	0.0455
3–5	1–2, 6–13	10156	12388	90.0	57.8	0.0428
2–5	1, 6–13	12472	10072	108	40.2	0.0387
2–5, 11	1, 6–10, 12–13	13519	9026	122	25.7	0.0299
2–6, 11	1, 7–10, 12–13	14492	8052	131	16.4	0.0275
2–6, 8, 11	1, 7, 9–10, 12–13	15169	7374	137	10.4	0.0264
2–6, 8, 11–12	1, 7, 9–10, 13	15838	6707	141	6.51	0.0267
2–6, 8, 11–13	1, 7, 9–10	16089	6456	144	3.58	0.0258
2–8, 11–13	1, 9–10	18082	4462	147	1.22	0.0357
2–8, 10–13	1, 9	19477	3067	149	−1.01	0.0473
2–13	1	21902	642.3	149	−1.55	0.1737

Table 4.5: Regional Signal Levels at 325 K

Region	S	dS/dT
4	1336	13.9
5	1868	12.5
3	921	11.1
2	1332	4.56
11	225	3.82
6	408	3.19
8	318	1.99
12	419	1.46
9	2360	0.756
10	1254	0.672
13	110	0.535
7	1868	0.219
1	841	−2.509

Table 4.6: Regional Assignments at 325 K

Numerator Regions	Denumerator Regions	S_N	S_D	dS_N/dT	dS_D/dT	σ_T
4	1–3, 5–13	1336	11924	13.9	38.3	0.1152
4–5	1–3, 6–13	3204	10056	26.4	25.8	0.0726
3–5	1–2, 6–13	4126	9135	37.5	14.7	0.0470
2–5	1, 6–13	5458	7802	42.1	10.1	0.0485
2–5, 11	1, 6–10, 12–13	5683	7577	45.9	6.31	0.0425
2–6, 11	1, 7–10, 12–13	6091	7169	49.1	3.12	0.0398
2–6, 8, 11	1, 7, 9–10, 12–13	6409	6851	51.1	1.13	0.0387
2–6, 8, 11–12	1, 7, 9–10, 13	6828	6432	52.6	–0.327	0.0390
2–6, 8–9, 11–12	1, 7, 10, 13	9188	4072	53.3	–1.08	0.0584
2–6, 8–12	1, 7, 13	10442	2818	54.0	–1.75	0.0778
2–6, 8–13	1, 7	10552	2709	54.5	–2.29	0.0772
2–13	1	12419	841	54.7	–2.51	0.1718

Table 4.7: Regional Signal Levels at 525 K

Region	S	dS/dT
3	8559	87.4
2	3129	72.5
4	8016	59.9
5	7490	54.1
11	3537	37.4
6	2765	31.3
8	1884	21.8
13	1135	21.0
12	1344	11.0
7	2367	5.33
10	1727	4.60
9	2466	0.291
1	520	−0.952

Table 4.8: Regional Assignments at 525 K

Numerator Regions	Denumerator Regions	S_N	S_D	dS_N/dT	dS_D/dT	σ_T
3	1–2, 4–13	8559	39380	87.4	318	0.0668
2–3	1, 4–13	14688	33251	160	246	0.0280
2–4	1, 5–13	22704	25235	220	186	0.0360
2–5	1, 6–13	30194	17745	274	132	0.0541
2–5, 11	1, 6–10, 12–13	33731	14208	311	94.3	0.0386
2–6, 11	1, 7–10, 12–13	36496	11444	343	63.0	0.0296
2–6, 8, 11	1, 7, 9–10, 12–13	38380	9559	364	41.3	0.0252
2–6, 8, 11, 13	1, 7, 9–10, 12	39515	8424	385	20.3	0.0196
2–6, 8, 11–13	1, 7, 9–10	40859	7080	396	9.27	0.0198
2–8, 11–13	1, 9–10	43226	4713	402	3.94	0.0278
2–8, 10–13	1, 9	44953	2986	406	−0.661	0.0386
2–13	1	47419	520	407	−0.952	0.1870

Table 4.9: Calibration Data

			P_{set}, psia	20	40	55	70	90	
T_{set}	$\bar{T}$	σ_T	$\bar{P}$, atm	1.38	2.74	3.77	4.75	6.14	
°C	K	K	σ_P, atm	0.003	0.016	0.022	0.027	0.033	MEAN[a]
25	301.1	0.10	$\bar{\mathcal{R}}$	0.8879	0.8665	0.8592	0.8391	0.8497	0.8604
			$\sigma_{\mathcal{R}}$	0.0562	0.0988	0.0570	0.0962	0.0456	
50	322.4	0.18	$\bar{\mathcal{R}}$	1.0234	0.9923	0.9868	0.9748	0.9793	0.9912
			$\sigma_{\mathcal{R}}$	0.0541	0.0418	0.0435	0.0383	0.0307	
75	348.4	0.23	$\bar{\mathcal{R}}$	1.1394	1.0881	1.0840	1.0742	1.0760	1.092
			$\sigma_{\mathcal{R}}$	0.0456	0.0352	0.0331	0.0267	0.0255	
100	374.9	0.89	$\bar{\mathcal{R}}$	1.3638	1.3263	1.3101	1.2979	1.3032	1.320
			$\sigma_{\mathcal{R}}$	0.0470	0.0366	0.0318	0.0367	0.0294	
125	400.8	1.10	$\bar{\mathcal{R}}$	1.7123	1.6395	1.6336	1.6108	1.6175	1.642
			$\sigma_{\mathcal{R}}$	0.0644	0.0448	0.0458	0.0505	0.0345	
150	425.8	0.63	$\bar{\mathcal{R}}$	2.0314	2.0302	2.0134	2.0070	1.9950	2.015
			$\sigma_{\mathcal{R}}$	0.0690	0.0688	0.0680	0.0602	0.0538	
175	452.7	1.38	$\bar{\mathcal{R}}$	2.6685	2.5825	2.5507	2.5128	2.5298	2.568
			$\sigma_{\mathcal{R}}$	0.1042	0.0706	0.0896	0.0747	0.0517	
200	477.8	0.55	$\bar{\mathcal{R}}$	3.2540	3.1766	3.1543	3.1030	3.0674	3.151
			$\sigma_{\mathcal{R}}$	0.2347	0.0922	0.1133	0.1504	0.2495	
225	505.0	1.20	$\bar{\mathcal{R}}$	3.9963	3.8582	3.8268	3.8824	3.7637	3.865
			$\sigma_{\mathcal{R}}$	0.1464	0.1047	0.1023	0.1020	0.1078	
250	531.4	1.67	$\bar{\mathcal{R}}$	4.3990	4.3299	4.2794	4.2558	4.2385	4.300
			$\sigma_{\mathcal{R}}$	0.1941	0.1368	0.1330	0.1050	0.1038	
275	556.9	0.84	$\bar{\mathcal{R}}$	4.6575	4.5723	4.5437	4.5412	4.4904	4.561
			$\sigma_{\mathcal{R}}$	0.1693	0.1582	0.1238	0.1478	0.1713	

[a]See Section 5.2.5.1 for how data in this column were obtained.

Table 4.10: Fitted Coefficients for Calibration Function (see equation (4.13))

P_{set}, psia	20	40	55	70	90	MEAN
A_1	−1.798	−1.823	−1.842	−1.811	−1.823	−1.798
A_2	1.027	1.061	1.079	1.043	1.071	1.041
A_3	1.167	1.181	1.156	1.215	1.201	1.222
A_4	−1.805	−1.817	−1.778	−1.873	−1.835	−1.876
A_5	0.749	0.754	0.740	0.775	0.759	0.775

Table 4.11: Cutoff Wavelength at 325 K

λ_c nm	Numerator Regions	Denumerator Regions	S_N	S_D	dS_N/dT	dS_D/dT	σ_T
203.2	1	2–13	841	129069	−2.51	59.7	−0.1664
208.0	1–2	3–13	2173	115736	2.05	55.2	−0.1430
214.4	1–3	4–13	3095	106521	13.2	44.0	3.3123
221.3	1–4	5–13	4431	93162	27.1	30.1	0.1151
229.3	1–5	6–13	6299	74483	39.6	17.6	0.0748
236.3	1–7	8–13	8575	51725	43.0	14.2	0.1369
245.9	1–9	10–13	11253	24944	45.7	11.5	−0.9100
252.3	1–10	11–13	13218	528	55.2	2.00	4.91
261.9	1–12	13	13637	110	56.7	0.535	> 10

Table 4.12: Cutoff Wavelength at 425 K

λ_c nm	Numerator Regions	Denumerator Regions	S_N	S_D	dS_N/dT	dS_D/dT	σ_T
203.2	1	2–13	642	23153	−1.55	160	0.1716
208.0	1–2	3–13	2958	20837	16.1	142	0.2782
214.4	1–3	4–13	5901	17815	48.9	110	0.1043
221.3	1–4	5–13	9425	14371	80.5	78.1	0.0566
229.3	1–5	6–13	13114	10681	106	52.5	0.0535
236.3	1–7	8–13	16081	7714	118	40.8	0.0945
245.9	1–9	10–13	19183	4612	124	34.3	0.2833
252.3	1–10	11–13	22877	919	152	6.82	1.4240
261.9	1–12	13	23554	251	156	2.93	0.7928

Table 4.13: Cutoff Wavelength at 525 K

λ_c nm	Numerator Regions	Denumerator Regions	S_N	S_D	dS_N/dT	dS_D/dT	σ_T
203.2	1	2–13	520	50151	−0.952	424	−0.1884
208.0	1–2	3–13	6648	44022	71.6	353	0.0630
214.4	1–3	4–13	15208	35462	159	266	0.0317
221.3	1–4	5–13	23224	27447	219	206	0.0412
229.3	1–5	6–13	30714	19956	273	152	0.0643
236.3	1–7	8–13	35846	14825	310	115	0.1093
245.9	1–9	10–13	40196	10475	332	93.0	−0.1901
252.3	1–10	11–13	48191	2480	393	32.0	−0.0893
261.9	1–12	13	49535	1135	404	21.0	−0.0870

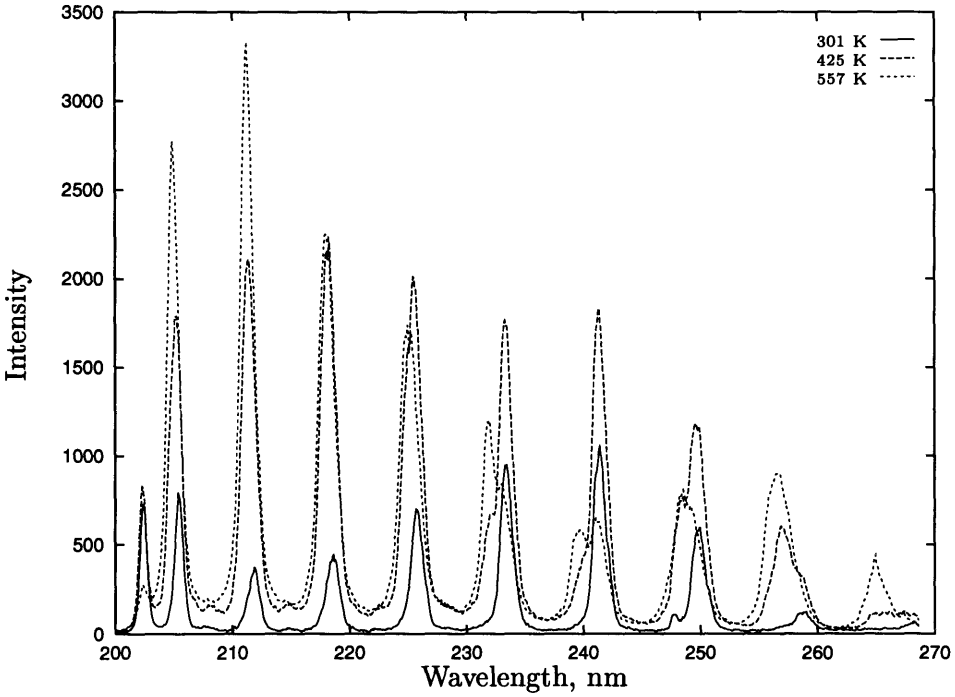

Figure 4.1: Temperature Dependence of Typical Spectra

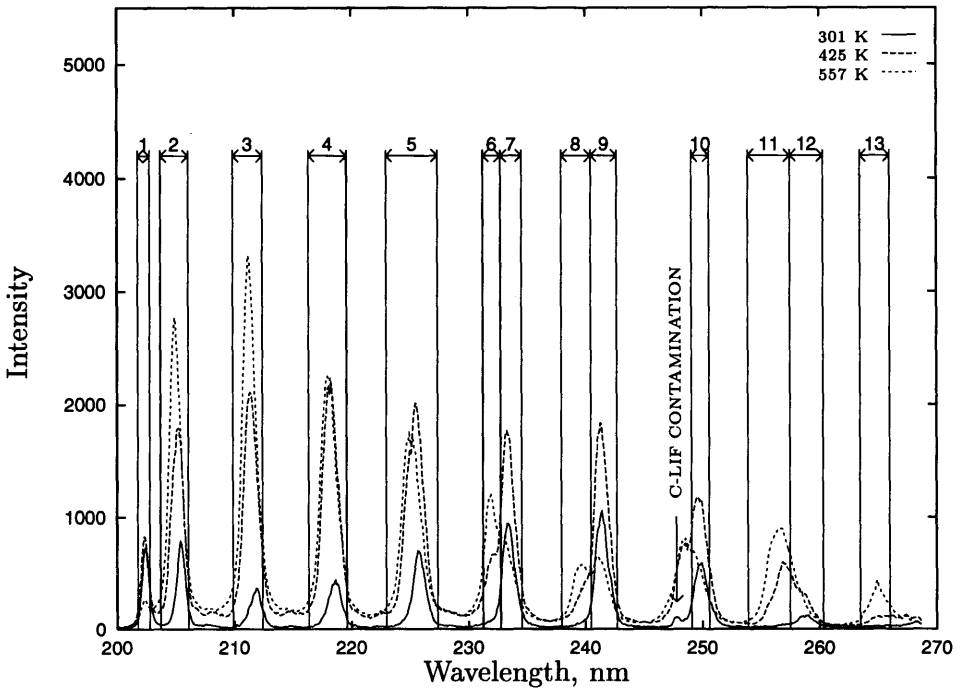

Figure 4.2: Regional Boundaries

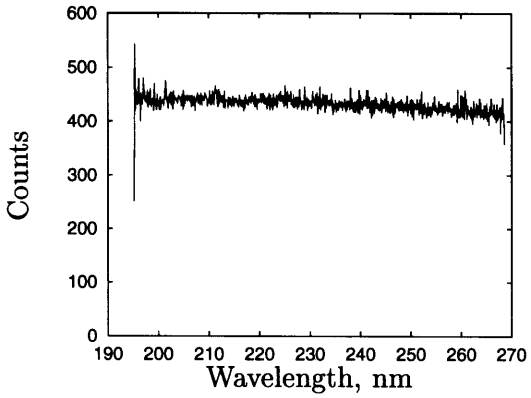

(a) Nominal Background Spectrum

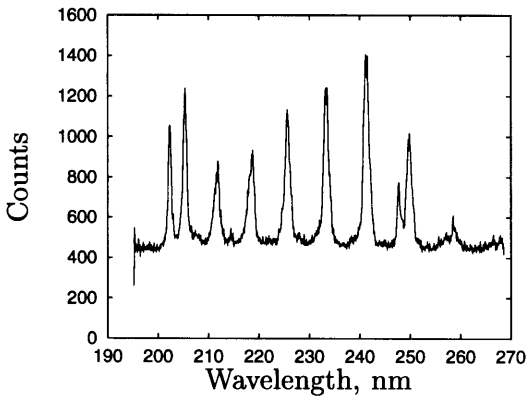

(b) Nominal LIF Spectrum

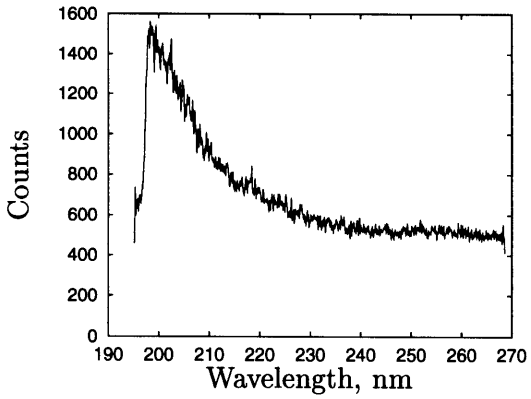

(c) Background Spectrum with Type A Anomaly

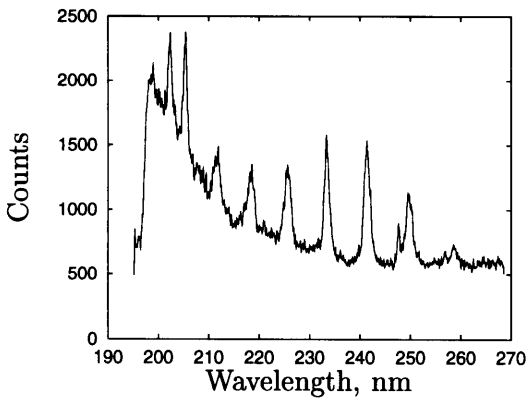

(d) LIF Spectrum with Type A Anomaly

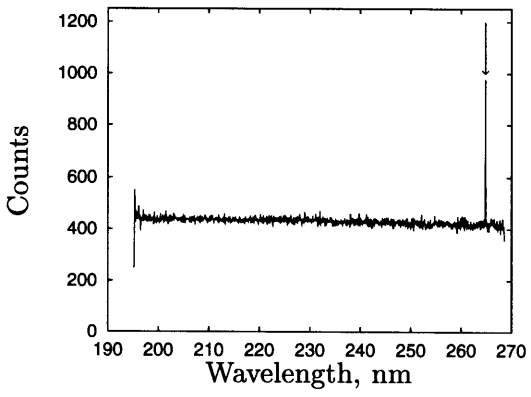

(e) Background Spectrum with Type B Anomaly

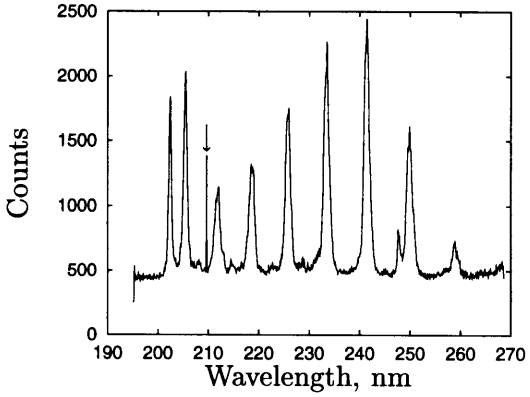

(f) LIF Spectrum with Type B Anomaly

Figure 4.3: Anomalous Spectra

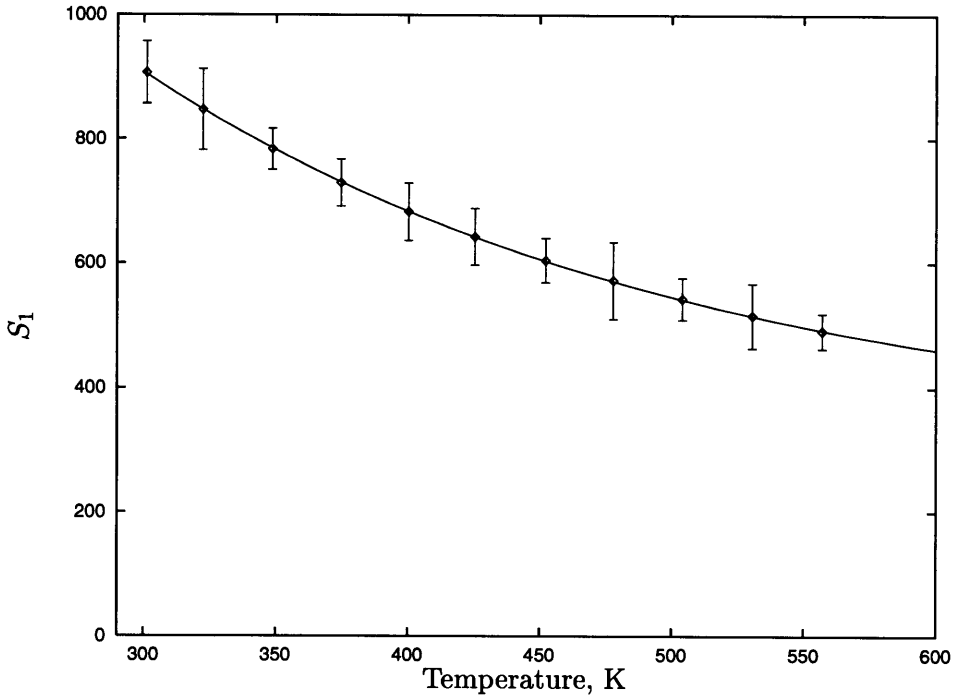

Figure 4.4: Temperature Dependence of Region 1 Signal (201.76–202.77 nm)

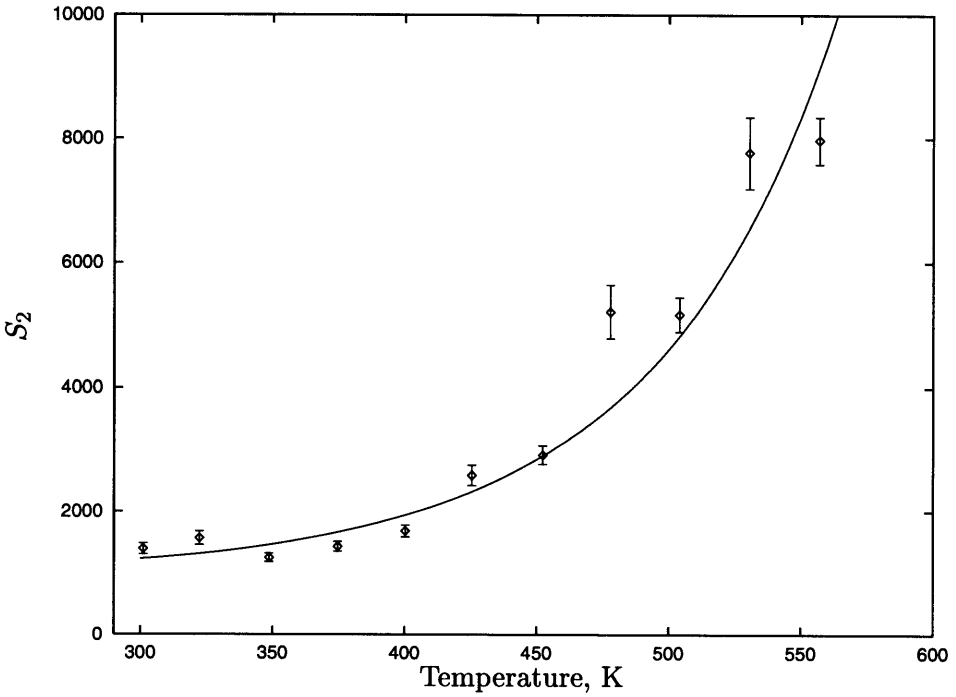

Figure 4.5: Temperature Dependence of Region 2 Signal (203.70–206.08 nm)

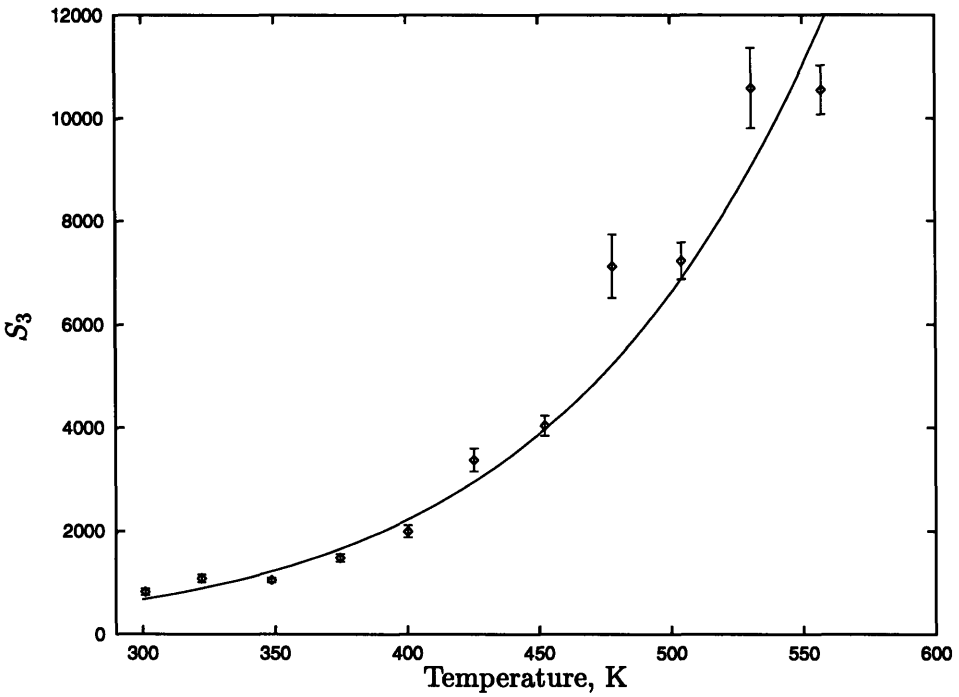

Figure 4.6: Temperature Dependence of Region 3 Signal (209.89–212.41 nm)

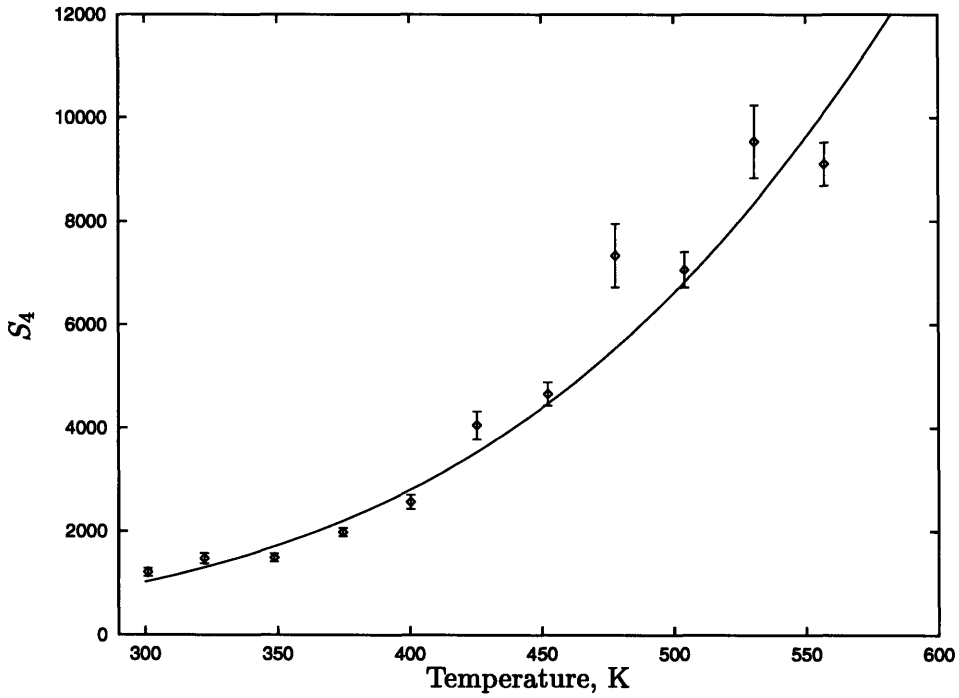

Figure 4.7: Temperature Dependence of Region 4 Signal (216.36–219.60 nm)

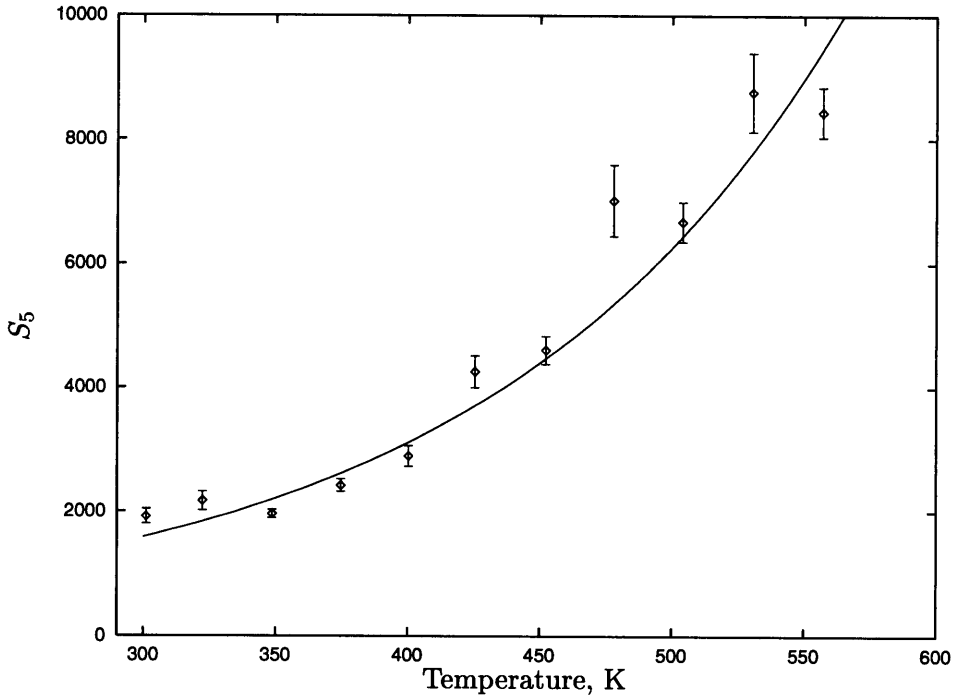

Figure 4.8: Temperature Dependence of Region 5 Signal (222.98–227.37 nm)

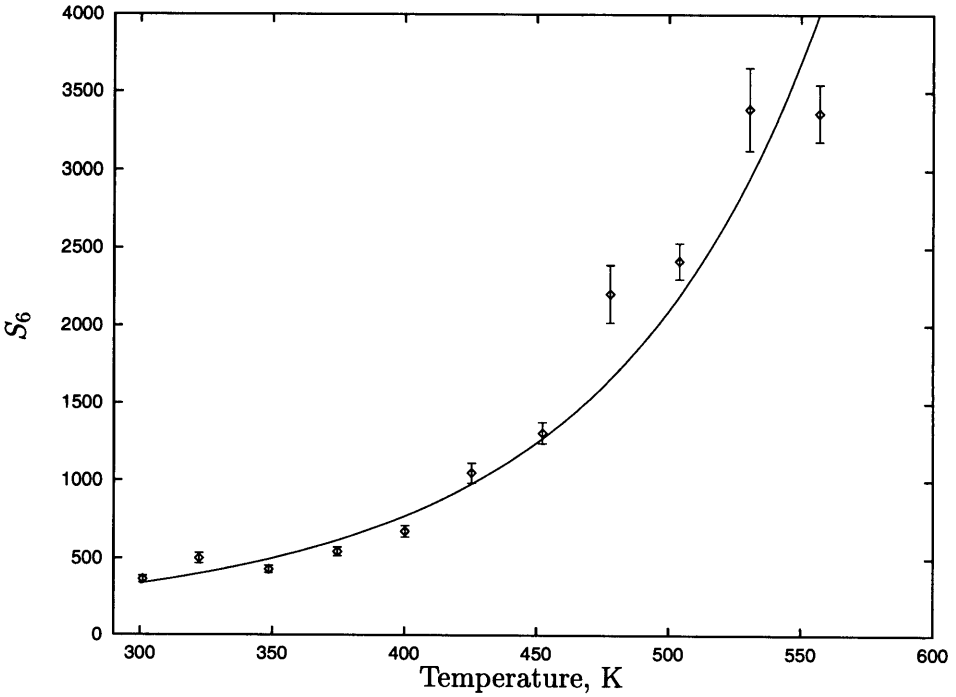

Figure 4.9: Temperature Dependence of Region 6 Signal (231.25–232.76 nm)

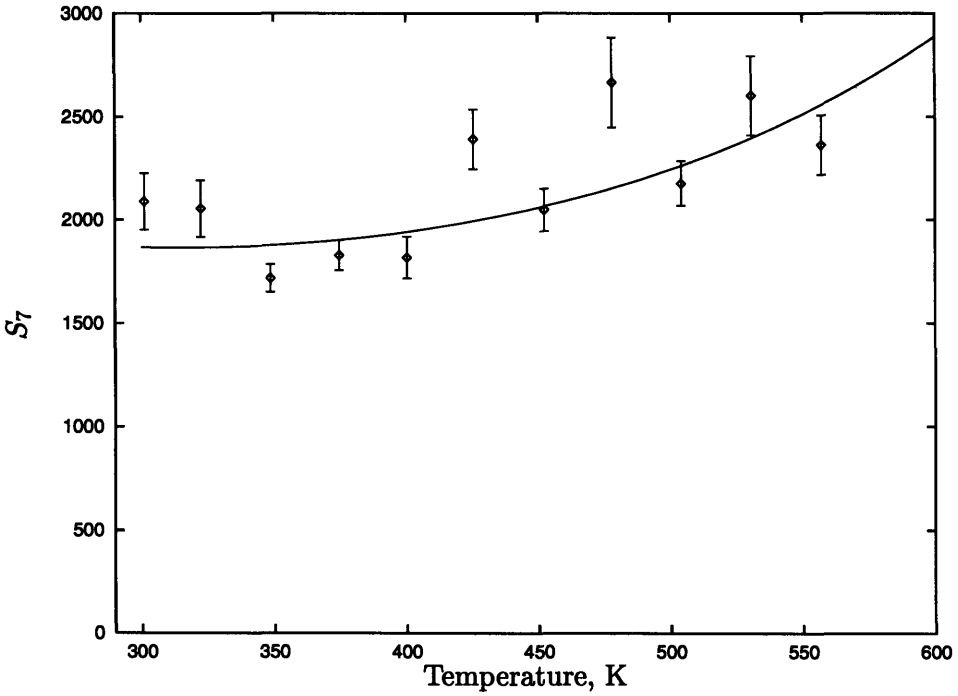

Figure 4.10: Temperature Dependence of Region 7 Signal (232.76–234.56 nm)

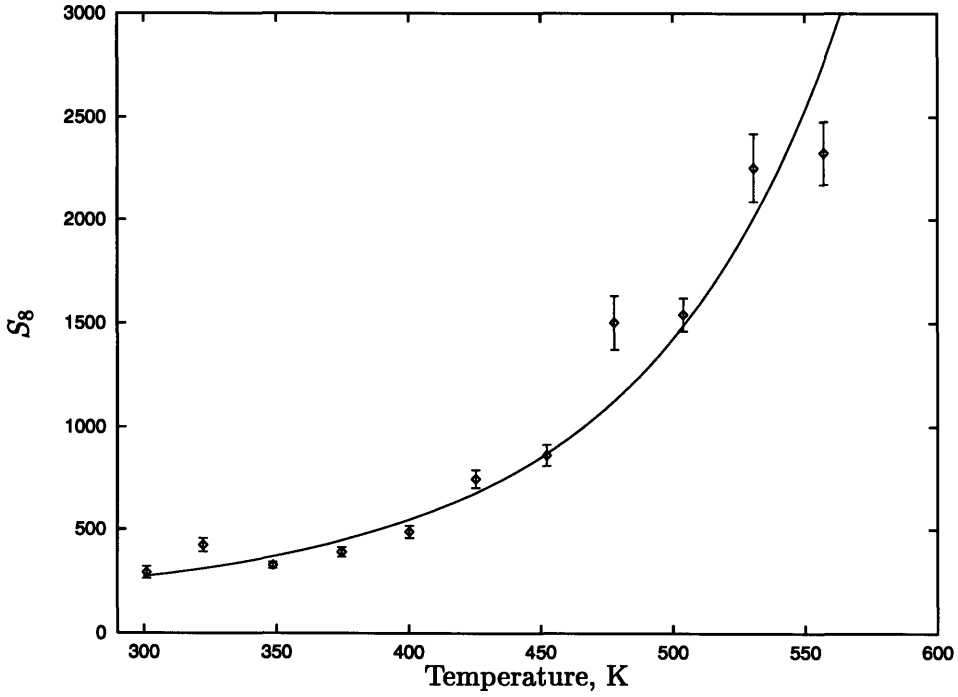

Figure 4.11: Temperature Dependence of Region 8 Signal (237.94–240.46 nm)

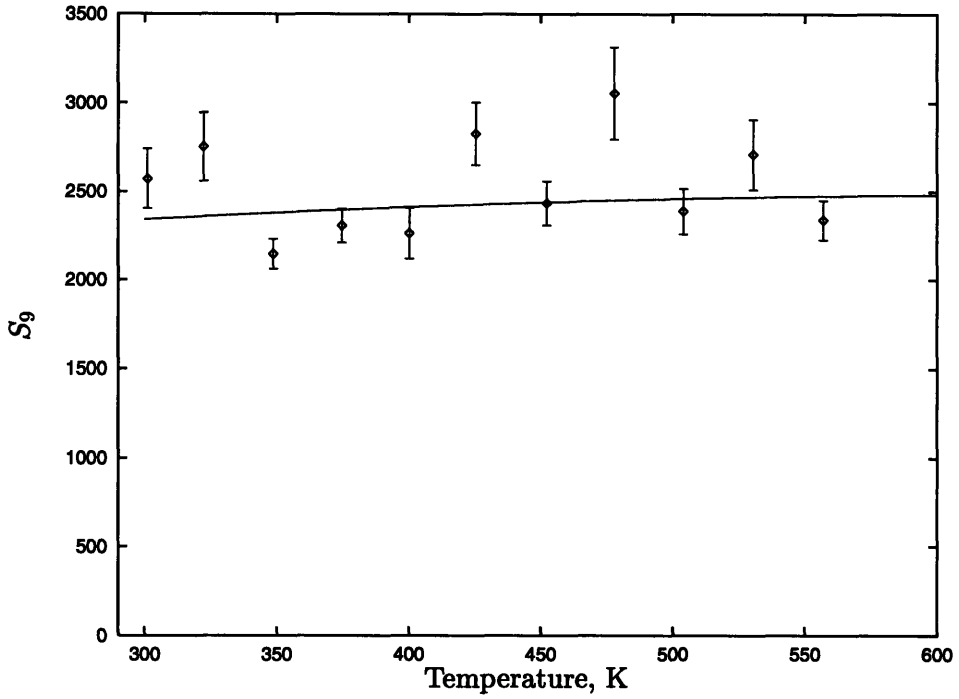

Figure 4.12: Temperature Dependence of Region 9 Signal (240.46–242.69 nm)

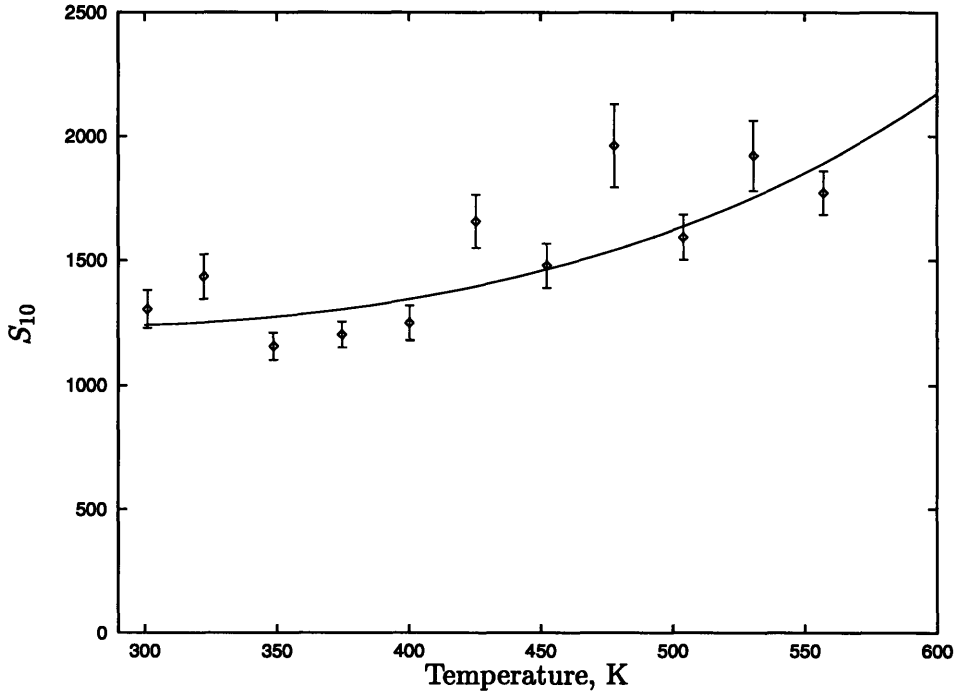

Figure 4.13: Temperature Dependence of Region 10 Signal (249.09–250.60 nm)

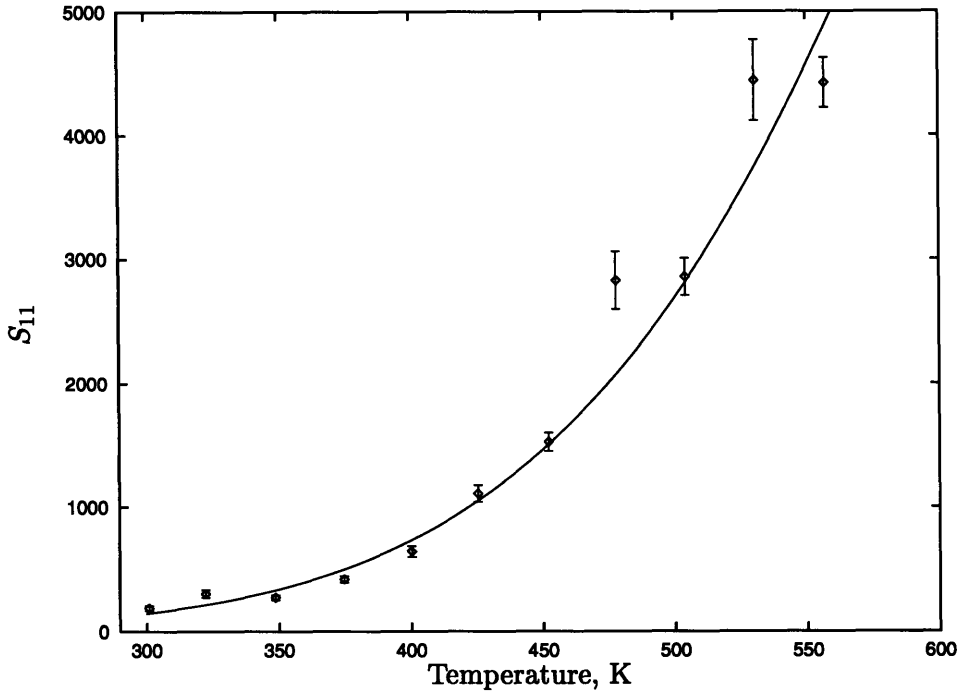

Figure 4.14: Temperature Dependence of Region 11 Signal (253.91–257.51 nm)

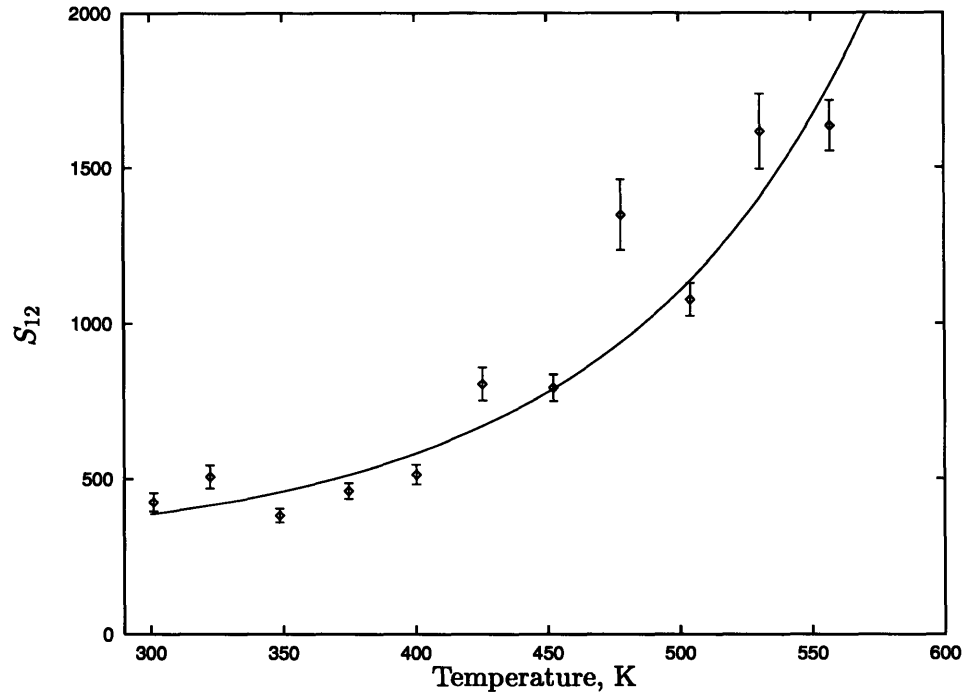

Figure 4.15: Temperature Dependence of Region 12 Signal (257.51–260.31 nm)

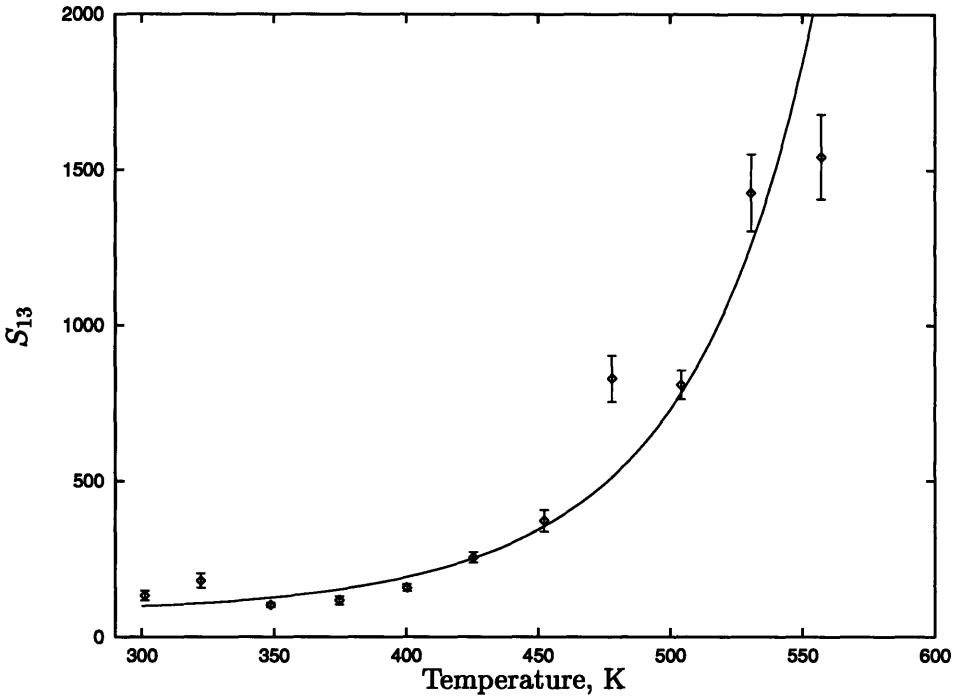

Figure 4.16: Temperature Dependence of Region 13 Signal (263.48–265.99 nm)

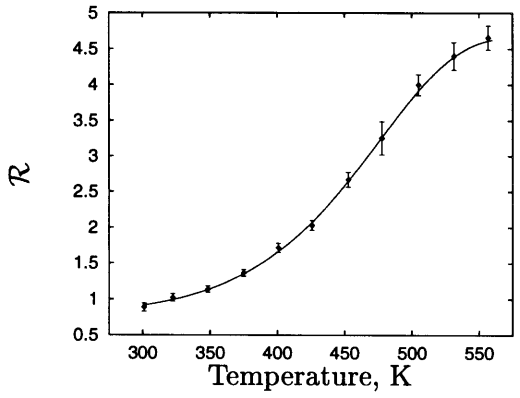

(a) $P = 1.38$ atm

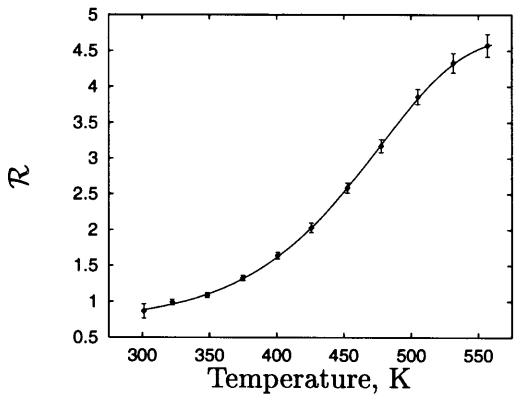

(b) $P = 2.74$ atm

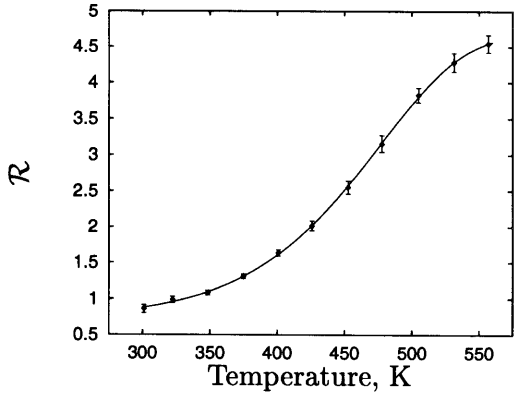

(c) $P = 3.77$ atm

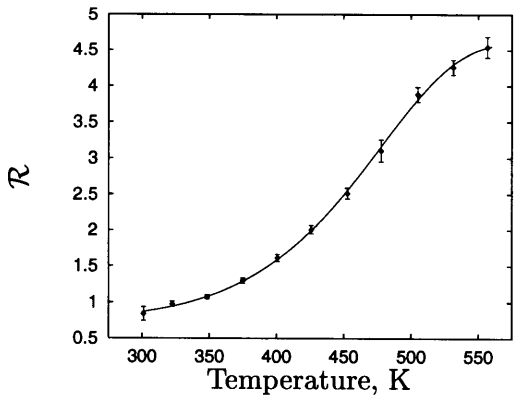

(d) $P = 4.75$ atm

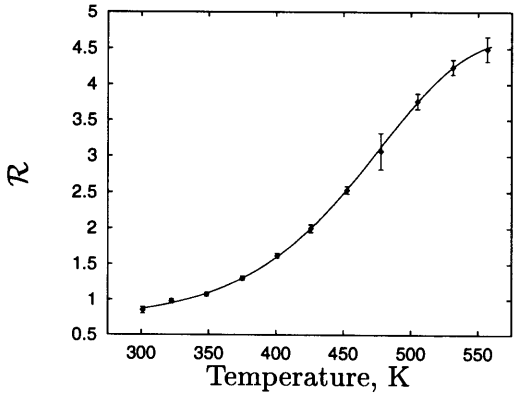

(e) $P = 6.14$ atm

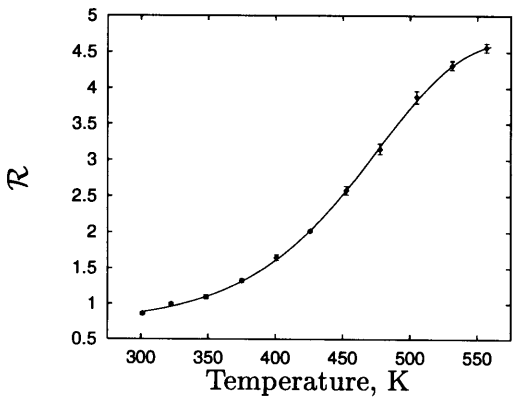

(f) Mean Data

Figure 4.17: Calibration Curves

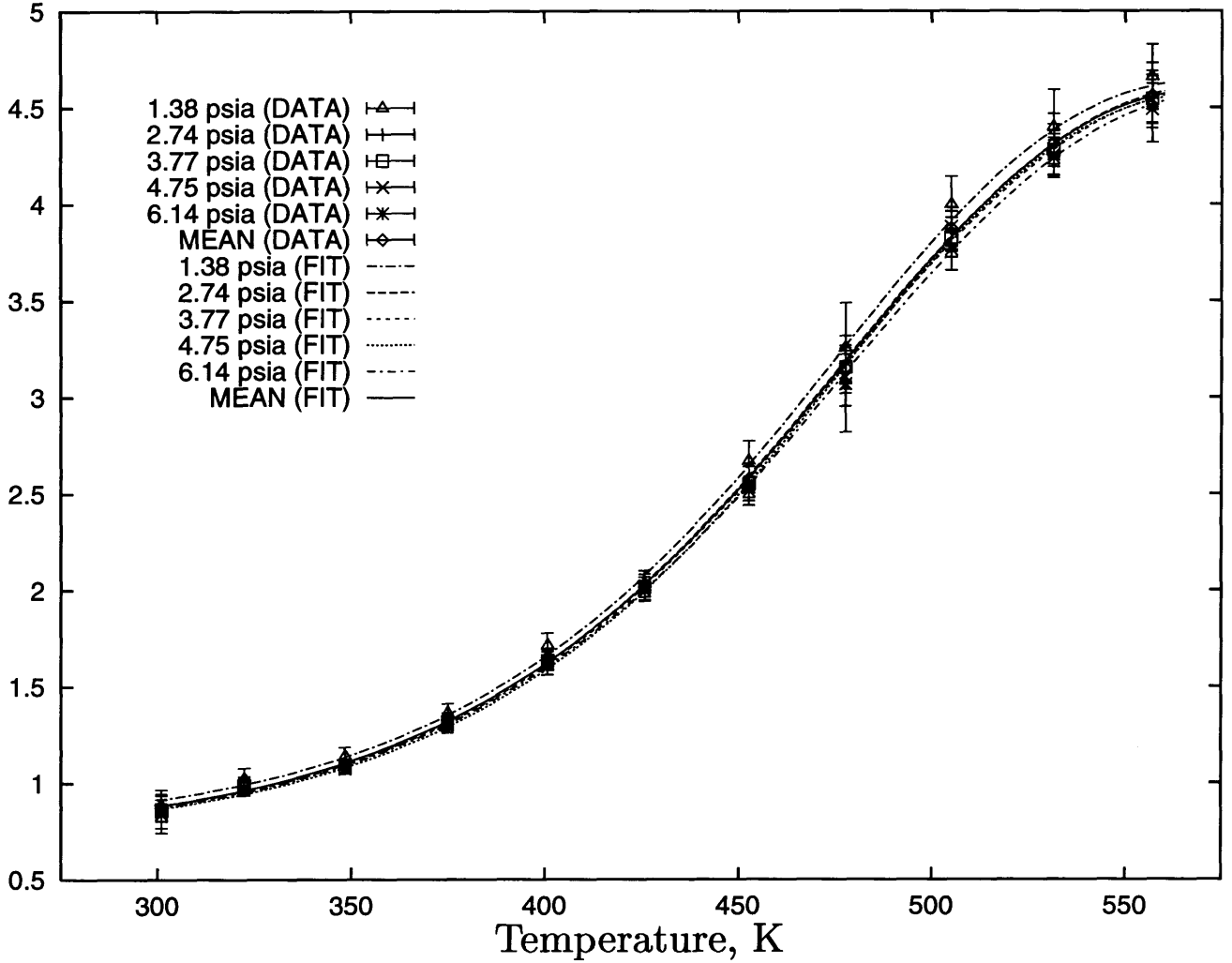

Figure 4.18: Calibration Curves

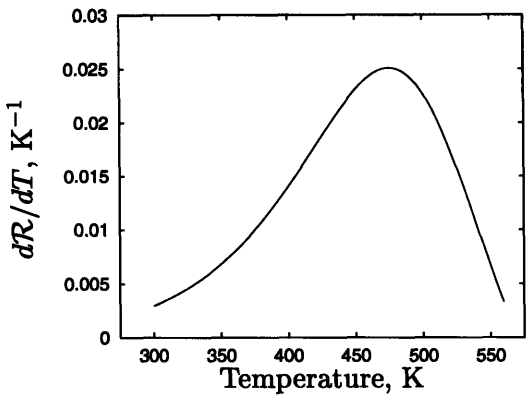

(a) $P = 1.38$ atm

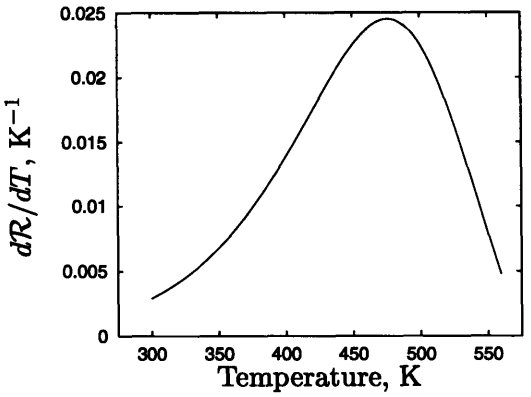

(b) $P = 2.74$ atm

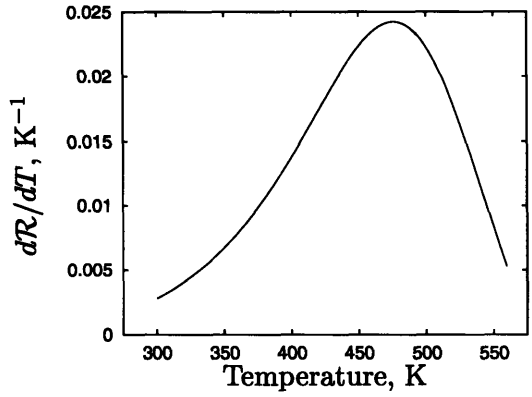

(c) $P = 3.77$ atm

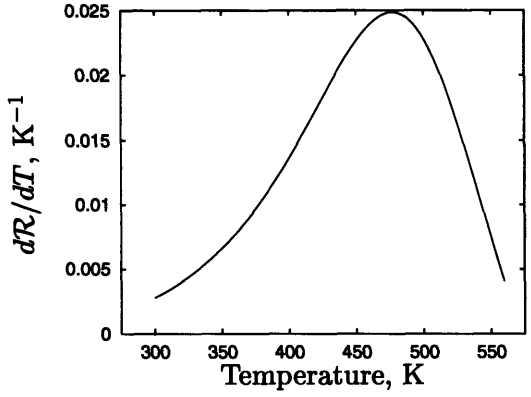

(d) $P = 4.75$ atm

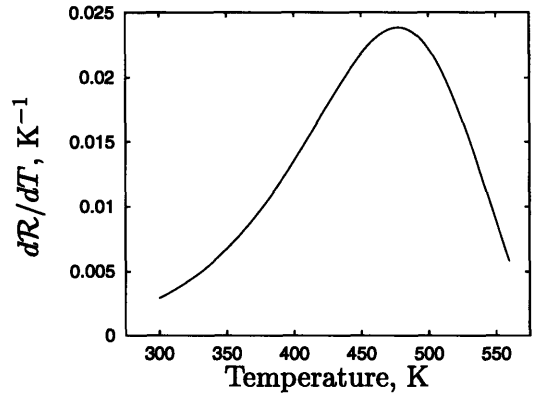

(e) $P = 6.14$ atm

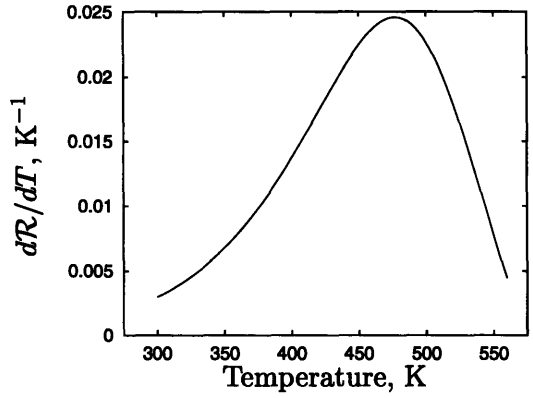

(f) Mean Data

Figure 4.19: Sensitivity of Calibration Curves to Temperature

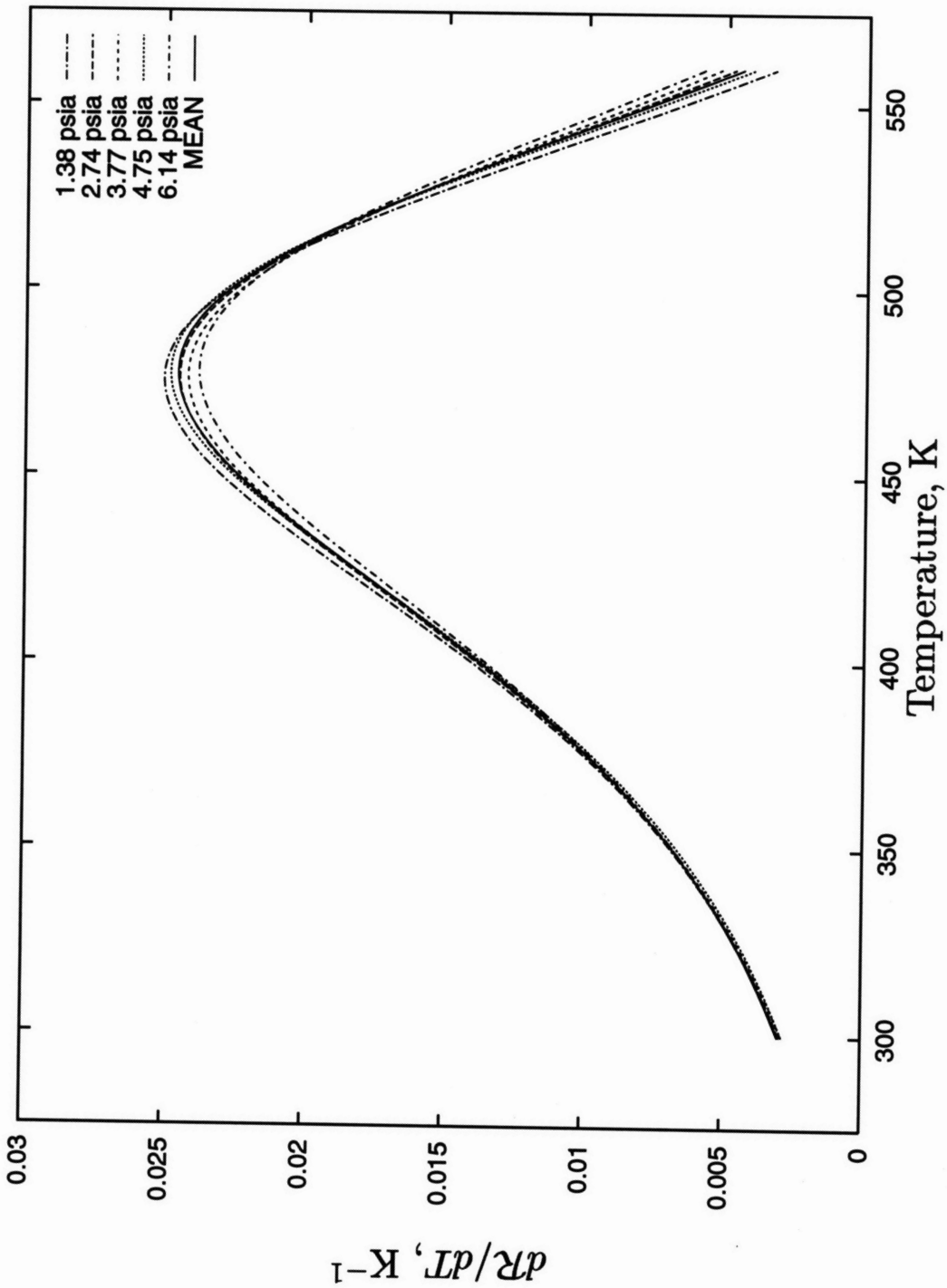

Figure 4.20: Sensitivity of Calibration Curves to Temeprature

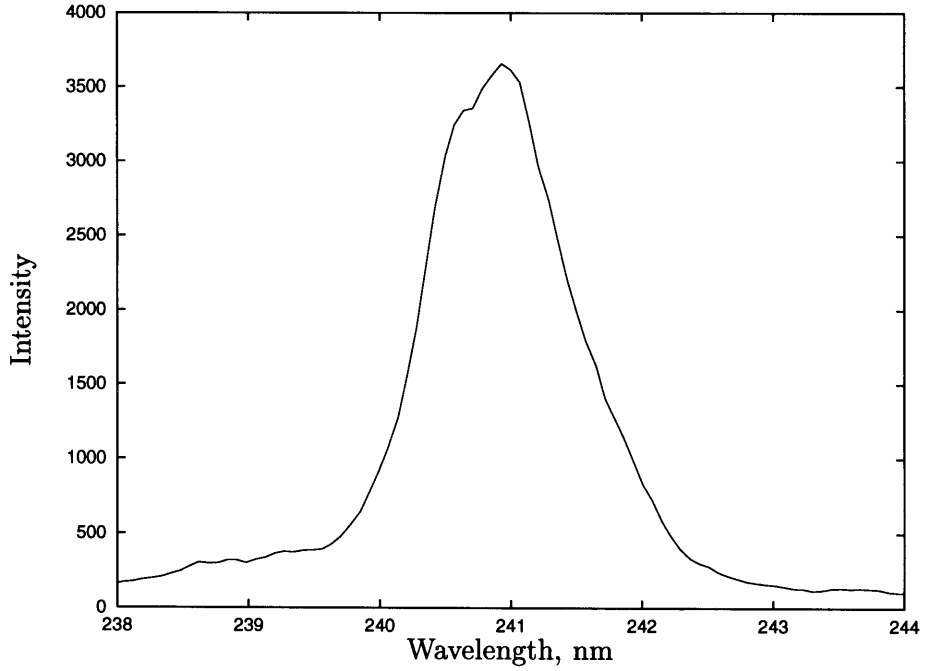

(a) 1200 mm^{-1} grating

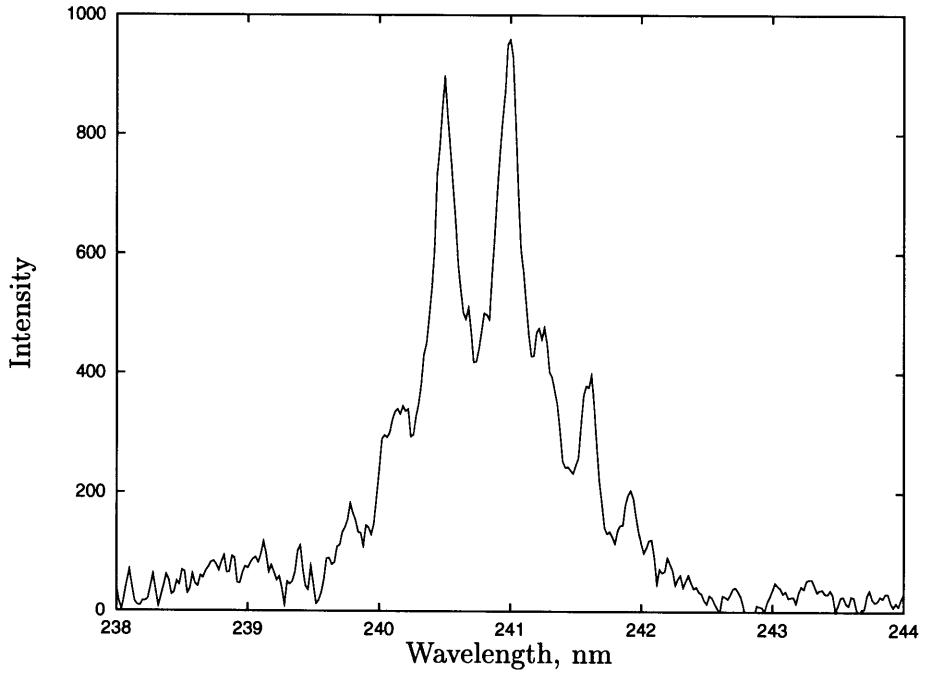

(b) 3600 mm^{-1} grating

Figure 4.21: Component Peaks of an LIF Region

Chapter 5
Error and Uncertainty Analysis

In order to be of engineering utility, the O_2 LIF temperature measurement technique, in addition to giving an estimate of the gas temperature, must also provide an estimate of the accuracy and precision of the measurement. This chapter discusses sources of error and uncertainty affecting the technique for low-speed flows. Error analysis for high-speed flows is presented in Chapter 6. This is the first ever detailed and quantitative error and uncertainty analysis for the O_2 LIF temperature measurement technique.

The following sources of error and uncertainty are considered:

1. Quantum noise
2. Laser noise
3. Detector noise
    - Thermal noise
    - Readout noise
4. Nonlinear Processes
    - O_2^+ LIF Signal Contamination
    - Saturation
5. Pressure Effects
    - Collisional Quenching
    - Beam Path Absorption
6. Flow Rate Effects
7. Temperature Variations
8. Calibration Uncertainty

The discussion first develops an approximate relation between the laser energy, flow temperature, flow pressure, and number of shots and the recorded signals. Each error or uncertainty source is then discussed separately. Next, three methods for improving measurement precision and their limits are presented, and the optimum accuracy and precision is calculated for various conditions. The chapter concludes by outlining the benefits and disadvantages of a fluence measurement and correction technique, and by briefly discussing considerations for practical measurents.

5.1 Signal Levels

As discussed in Chapter 3, the experimental apparatus does not allow simultaneous measurement of laser fluence (or laser pulse energy) and LIF signals. Consequently, the data reduction method described in Chapter 4 is independent of laser fluence.

The accuracy and precision of the technique, however, does depend on the absolute signal level. Therefore, we now develop several approximate formulae for predicting the signal levels from the laser fluence, gas pressure and temperature, and number of shots averaged.

Before each set of calibration experiments at a given temperature level, the laser power was measured just in front of the laser using a laser power meter. The laser pulse energy was then obtained by dividing the power (in W) with the laser repetition rate (in Hz).

Laser fluence E'' (J/cm^2) at the measurement volume is related to the laser pulse energy E (J) in front of the laser as follows:

$$E'' = \frac{\eta_f E}{A_b} \tag{5.1}$$

In equation 5.1, η_f is the transmission efficiency of the beam steering and focusing optics (approximately 15%, see Chapter 3), and A_b is the cross-sectional area of the laser beam at the measurement volume (for 28 μm by 48 μm beam, $A_b = 1.3 \times 10^{-5}$ cm^2, see Chapter 3).

The time interval between the laser power measurement and the first experiment of the set was approximately 20 minutes, during which the experimental apparatus was purged with nitrogen. Since the cryogenic purification system was being operated during this interval, the laser energy might have deviated from that obtained during power measurement. A complex data analysis method was used to relate the LIF signal level to the beam energy.

First, the denominator signal S_D and region 1 signal S_1, which is the nitrogen Raman signal, were computed for each experiment. The ratio of the two signals was approximated with the formula

$$\frac{S_D}{S_1} = 8.3 + 1400 \exp(-2600\text{K}/T) \tag{5.2}$$

The parameters in this equation were determined by a fit to the S_D/S_1 data. The characteristic temperature 2600 K compares well with the 2230 K separation between the $v'' = 0$ and $v'' = 1$ vibrational levels; the value in equation (5.2) is probably slightly higher due to the presence of small amount of signals originating from $v'' = 2$ absorption transitions.

Next, the Raman signal was approximated by he following equation:

$$S_1 = \frac{KPE''}{(T/273.2\text{ K})} \tag{5.3}$$

The constant K was calculated for each experiment, for which T, P, E'' and S_1 were known. The mean value for K was then calculated as 0.025 cm^2 atm^{-1} J^{-1}.

In conclusion, the denumerator and numerator signal levels may be approximated by the following formulae:

$$S_D = \frac{0.025PE}{(T/273.2)}[8.3 + 1400\exp(-2600\text{K}/T)] \tag{5.4a}$$

$$S_N = \mathcal{R}S_D \tag{5.4b}$$

$\mathcal{R}$ is calculated using equation (4.13).

5.2 Error and Uncertainty Sources

Various error and uncertainty sources described below affect the signals S_N and S_D recorded by the detector. These signals are combined into a temperature diagnostic ratio $\mathcal{R}$ using following equation:

$$\mathcal{R} = \frac{S_N}{S_D} \tag{5.5}$$

The temperature dependence of $\mathcal{R}$ is given by equation (4.13), and the temperature may be estimated using equation (4.15).

If a noise source i causes an uncertainty in $\sigma_{\mathcal{R}_i}$ in $\mathcal{R}$, the resulting uncertainty σ_T in the determined temperature is given by [2]

$$\sigma_T = \frac{\sqrt{\sum_i \sigma_{\mathcal{R}_i}^2}}{|d\mathcal{R}/dT|} \tag{5.6}$$

provided the noise sources are independent.

Similarly, if an error source j causes an error $\Delta\mathcal{R}_j$ in $\mathcal{R}$, the corresponding error ΔT in the determined temperature is given by

$$\Delta T = \frac{\sum_j \Delta\mathcal{R}_j}{d\mathcal{R}/dT} \tag{5.7}$$

The temperature derivative of $\mathcal{R}$ may be computed using equation (4.14).

5.2.1 Quantum Noise

Quantum noise is the statistical variation introduced to the radiative signals due to the quantum (discrete) nature of light. Any interaction between light and matter is a source of quantum noise. In this technique, such interactions include the production of laser light, the absorption of laser light by O_2 molecules, the fluorescence by O_2 molecules, and the detection of light.

Quantum noise is governed by Poisson distribution [9], which may be modeled as a normal distribution with variance σ_S^2 equal to the mean S. Therefore, the quantum uncertainty in the signals S_N and S_D is given by

$$\sigma_{S_N}^Q = K_Q\sqrt{S_N} \tag{5.8a}$$

$$\sigma_{S_D}^Q = K_Q\sqrt{S_D} \tag{5.8b}$$

For this apparatus, K_Q has been empirically determined to be about 3.

The resulting uncertainty in $\mathcal{R}$ is given by

$$\sigma_{\mathcal{R}}^Q = \mathcal{R}\left[\left(\frac{\sigma_{S_N}}{S_N}\right)^2 + \left(\frac{\sigma_{S_D}}{S_D}\right)^2\right]^{1/2} = K_Q\mathcal{R}\left[\frac{1}{S_N} + \frac{1}{S_D}\right]^{1/2} \tag{5.9}$$

For measurements limited by quantum noise, equation (5.9) suggests that the numerator signal and denumerator signal should ideally have the same magnitude (i. e. $\mathcal{R} \sim 1$). This is indeed the case. If one signal is much smaller than the other, the measurement precision will be limited by the quantum noise in that signal.

5.2.2 Laser Noise

The beam energy of the laser fluctuates shot-to-shot. As described in section 3.3.2, the distribution of laser energies may be modeled with a normal distribution. At 100 Hz, the standard deviation is $0.084\bar{E}$.

Let S_N and S_D exhibit the following dependence on laser energy E:

$$S_N = k_1^N E + k_2^N E^2 + \ldots \tag{5.10a}$$

$$S_D = k_1^D E + k_2^D E^2 + \ldots \tag{5.10b}$$

In equations 5.10, the quadratic terms have been included in anticipation of the discussion of nonlinear processes later this chapter.

The temperature diagnostic ratio may then be written as

$$\mathcal{R} = \frac{S_N}{S_D} = \frac{k_1^N + k_2^N E}{k_1^D + k_2^D E} = \frac{k_1^N}{k_1^D} + \frac{k_1^N}{k_1^D}\left(\frac{k_2^N}{k_1^N} - \frac{k_2^D}{k_2^N}\right) + \ldots = \mathcal{R} + \mathcal{R}\left(\frac{k_2^N}{k_1^N} - \frac{k_2^D}{k_2^N}\right) + \ldots \tag{5.11}$$

and the uncertainty in $\mathcal{R}$ due to laser noise is given by

$$\sigma_{\mathcal{R}}^L = \frac{\partial\mathcal{R}}{\partial E}\sigma_E = \mathcal{R}\left(\frac{k_2^N}{k_1^N} - \frac{k_2^D}{k_2^N}\right)\sigma_E + \ldots \tag{5.12}$$

If the numerator and denumerator signals exhibit purely linear dependence on beam energy (i. e. $k_2^N = k_2^D = 0$), the laser noise does not affect the temperature diagnostic ratio. Quadratic—and higher order—terms do, however, transmit the laser noise to the temperature diagnostic ratio.

5.2.3 Detector Noise

The detector noise consists of two components: thermal noise and readout noise. Each source is independent of the other.

Even when no signals are incident on the detector, there is a buildup of charge on the photodiodes of the detector as a result of thermal processes. The thermal charge increases linearly with exposure as discussed in section 3.3.8. Although the mean value of the thermal charge is subtracted from the recorded data as describe in section 4.2, the uncertainty in the thermal charge, called thermal noise, does affect the uncertainty in S_N and S_D. For this detector, the thermal noise is given by

$$\sigma_{S_N}^T = 2.27\sqrt{X} \tag{5.13a}$$

$$\sigma_{S_D}^T = 0.986\sqrt{X} \tag{5.13b}$$

where X is the exposure in milliseconds.

Readout noise originates from the electronics which measure the charge collected on the photodiodes, as well as from the digitization of these measurements. Readout noise is independent of exposure and is given by

$$\sigma_{S_N}^R = 33.8 \tag{5.14a}$$

$$\sigma_{S_D}^R = 22.4 \tag{5.14b}$$

The detector noise is shown in Figure 5.1 for the numerator and denumerator signals. The constant portion of the curves is the readout noise; the linearly increasing portion, which has a slope of 1/2 is the thermal noise. For $X < 100$ ms, the detector noise is dominated by readout noise, whereas thermal noise is the dominant factor for $X > 1000$ ms.

Thermal charge, and therefore thermal noise, may be reduced by cooling the detector. The particular detector used in this project is electrostatically cooled to $-20°C$ rejecting heat to cold tap water. Further cooling requires special coolant and equipment.

The uncertainty in $\mathcal{R}$ due to detector noise is given by

$$\sigma_{\mathcal{R}}^D = \mathcal{R}\left[\underbrace{\left(\frac{\sigma_{S_N}^T}{S_N}\right)^2 + \left(\frac{\sigma_{S_D}^T}{S_D}\right)^2}_{\text{THERMAL NOISE}} + \underbrace{\left(\frac{\sigma_{S_N}^R}{S_N}\right)^2 + \left(\frac{\sigma_{S_D}^R}{S_D}\right)^2}_{\text{READOUT NOISE}}\right]^{1/2} \tag{5.15}$$

5.2.4 Nonlinear Phenomena

At low laser pulse energy levels, both the S_N and S_D signals depend linearly on laser energy E. However, at high E, the laser signals deviate from the linear dependence due to two nonlinear processes: O_2^+ LIF and saturation.

5.2.4.1 O_2^+ LIF

Figure 5.2 shows two spectra taken at 301 K (28°C) at low and high laser pulse energy levels. The O_2 LIF and N_2 Raman signals of interest are marked on both spectra. In addition, the higher energy spectrum shows additional signals which are attributed to the O_2^+ fluorescence excited by the laser.

A theoretical discussion of the O_2^+ LIF process appears in Chapter 2. That discussion and examination of Figure 5.2 show the following:

1. O_2^+ LIF spectrum originates from a three-photon absorption process excited by the ArF laser radiation. Consequently, it should exhibit a cubic dependence on laser energy.

2. Unlike the absorption processes which produce O_2 LIF signals, the absorption processes which produce O_2^+ LIF signals need not take place between two energy levels whose energy difference matches the laser wavelength. Since the electron ejected during the $O_2 \rightarrow O_2^+ + e^-$ ionization process may have any translational energy, all O_2 molecules in the ground electronic state may be ionized. Consequently, O_2^+ LIF shows only a $1/T$ dependence on temperature through density; there is no additional temperature dependence.

3. Unlike the upper electronic state of O_2, the fluorescing electronic state of O_2^+ is not known to be predissociated. This means that O_2^+ LIF signals are subject to strong collisional quenching. If there were no collisional quenching, O_2^+ LIF signals would be linearly dependent on pressure (i. e. $\sim P$); however, because of collisional quenching, the pressure dependence may be weaker (i. e. $\sim P^n, n < 1$).

4. O_2^+ LIF spectrum is stronger at lower wavelengths. Most of the regional O_2 LIF signals at lower wavelengths are assigned to the numerator signal because of their high sensitivity. Consequently, the temperature diagnostic ratio $\mathcal{R}$ increases with increasing laser energy. In other words, if S_N versus S_D curve is concave upward (i. e. $S_N''(S_D) > 0$).

5. O_2^+ LIF signals overlap almost all of the O_2 LIF signals which have higher temperature sensitivity. Consequently, it is not possible to spectrally isolate and neglect O_2^+ LIF signals[1].

6. O_2^+ LIF signal is not known a priori. Furthermore, because O_2^+ LIF signals are in turn contaminated by O_2 LIF signals, this spectrum cannot be accurately determined for background subtraction.

5.2.4.2 Saturation Effects

The other nonlinear dependence is saturation. Without saturation, O_2 LIF signals exhibit a linear dependence on energy. However, as laser energy increases, the laser pump depletes the ground states of absorption transitions faster than they are replenished by

[1]The C-LIF signal at 248 nm, which also shows a cubic dependence on laser energy [8], is spectrally isolated. This involves the loss of a small portion of O_2 LIF signal.

collisions with other molecules. A detailed discussion of saturation is given in Chapter 2. Saturation results in a reduction of LIF signal.

Saturation is more important at higher temperatures for two reasons. First, the absorption transitions originating from $v'' = 1$ and 2 vibrational levels of the ground electronic state have much higher transition probabilities than $v'' = 0$ transitions. Consequently, it is easier for the laser pump to deplete these levels. Since transitions originating from $v'' = 1$ and 2 levels become stronger with increasing temperatures, so do the effects of saturation.

In addition, the collision rate, which replenishes the ground levels, scales[2] as $1/\sqrt{T}$. Therefore, the replenishment rate decreases with increasing temperature, and saturation effects become stronger at higher temperatures.

Since LIF signals produced by $v'' = 1$ and 2 absorption transitions have higher temperature sensitivity, they are mostly assigned to the numerator signal S_N. Consequently, as saturation effects become stronger with increasing laser energy, $\mathcal{R}$ decreases. In other words, S_N versus S_D is concave downward (i. e. $S_N''(S_D) < 0$). This is the opposite effect of O_2^+ LIF signals.

5.2.4.3 Data Analysis

In order to analyze the effect of these nonlinear phenomena, data was taken at nine different temperatures. The laser energy was varied by adjusting the laser discharge voltage. The resulting data is shown in Figures 5.3 and 5.4. A function of form

$$S_N = A_1 S_D + A_2 S_D^2 + A_3 S_D^3, \tag{5.16}$$

where both S_D and S_N are per shot and per atmosphere, was fitted to the data at each temperature. The resulting coefficients are listed in Figure 5.1 and the fits are shown in Figures 5.3 and 5.4. Also shown on these figures are the linear portion of the fits given by

$$S_N^{\text{lin}} = A_1 S_D \tag{5.17}$$

The measured temperature ratio $\mathcal{R}_m$ is given by

$$\mathcal{R}_m = A_1 + A_2 S_D + A_3 S_D^2 \tag{5.18}$$

but the real value of the diagnostic ratio is simply

$$\mathcal{R}_r = A_1 \tag{5.19}$$

The resulting temperature error is then

$$\Delta T = \frac{\mathcal{R}_m - \mathcal{R}_r}{\partial \mathcal{R}/\partial T} = \frac{A_2 S_D + A_3 S_D^2}{\partial R/\partial T} \tag{5.20}$$

Equation (5.20) may be related to laser fluence by substitution for S_D through equation (5.4a).

[2]Cann et. al. [3] give a $T^{-0.7}$ dependence.

5.2.5 Pressure Effects

Ideally, all O_2 LIF and N_2 Raman signals depend linearly on pressure. Consequently, the temperature diagnostic ratio $\mathcal{R}$ is independent of pressure. However, a weak pressure dependence may be introduced through two sources: collisional quenching and beam path absorption. Although the two sources were not studied separately during experimental studies, the worst-case error magnitude from each source may be estimated by asssuming that the entire pressure dependence comes from that source.

During calibration runs, data were taken at five different pressure levels between 1.4 atm (20 psia) and 6.1 atm (90 psia), and at eleven different temperature levels. The path length between the casing window and the measurement point was 3.6 cm. An equation of form

$$\mathcal{R} = \mathcal{R}_{\text{ref}} + C\,(P - P_{\text{ref}})\,, \tag{5.21}$$

with $P_{\text{ref}} = 3.77$ atm, was fitted to the data at each temperature level. The resulting $\mathcal{R}_{\text{ref}}$ and C values are listed in Table 5.2 and the fits are shown in Figures 5.5 and 5.6. The $\mathcal{R}_{\text{ref}}$ values are the "mean" temperature diagnostic ratios shown in Table 4.9.

Figure 5.7 plots $C/\mathcal{R}_{\text{ref}}$ as a function of temperature. This normalized quantity is fairly constant over temperature with an average value of -0.009.

5.2.5.1 Collisional Quenching

Once an O_2 molecule is promoted to the upper electronic state, it may be moved out of this state before fluorescing as a result of collisions with other molecules, and the fluorescence signal is reduced. Collisional quenching theory is discussed in Chapter 2.

Figure 5.7 compares the observed pressure dependence against the pressure dependence which is expected from the collisional quenching models derived from Cann et. al. [3,4] and Miles et. al. [10]. Although the pressure effects exhibit roughly the temperature dependence expected from collisional quenching models, the magnitude of the effect is not as strong as predicted by the two data sets.

Actually, the data presented by Cann et. al. is an empirical model for pressure broadening linewidths of absorption transitions. In this project, that data was extended to collision rate of upper electronic state by assuming that both upper and lower electronic states had the same collisional cross-section. The experimental data suggest that this is an inaccurate assumption; collisions are much less effective in redistribution molecules in the B upper electronic state than in the X ground electronic state.

The only other collisional quenching model in literature is that of Miles et. al. [10]. These authors state that a collisional quenching rate of 1.0×10^{11} s^{-1} at 500 K and 1 atm, which is five times the rate predicted by Cann data, was necessary to match their experimental LIF signal levels to their theoretical model. The data obtained during this project indicate that either the LIF model or the experimental data analysis used by Miles et. al. is inaccurate.

Based on the two data sets, a collision rate of 20% of the Cann data explains the observed pressure dependence. This is also plotted on Figure 5.7. Since Cann model is based on the total pressure, this suggests that only oxygen-oxygen collisions are effective in quenching the B electronic state. The collisional quenching rate at 300 K and 1 atm is 5.3×10^9 s^{-1}, and scales as $P/T^{0.7}$.

Assuming that the entire pressure error is to the collisional quenching, the temperature error resulting from pressure error is listed in Table 5.2. If the pressure is known, the pressure error may be eliminated by using a calibration curve obtained at the appropriate pressure. For example, Table 4.9 lists coefficients for five different pressure levels.

Although small, collisional quenching is not negligible as assumed by all theoretical oxygen LIF studies.

5.2.5.2 Beam Path Absorption

The other source for the pressure error is beam path absorption. Although most of the beam path is purged with nitrogen, the beam must transit a short path containing oxygen molecules between the casing window and the measurement volume. The oxygen molecules in this region will absorb photons from the beam. This will reduce the numerator and denumerator signals and, if the reduction in the two signals is not the same, change the temperature diagnostic ratio $\mathcal{R}$. This will result in an error in the temperature measurement.

The beam path absorption effects depend on the measurement volume temperature (T), beam path temperature (T_{path}), and the quantity $P_{\text{path}}X_{O_2}L_{\text{path}}$. In the calibration experiments used in this project, L_{path} was kept constant at 3.6 cm for all experiments, and the pressure was varied between 1.2 atm and 6.1 atm. Therefore, beam path effects, if any, appear as pressure effects.

Equation (5.21) can be written as

$$\mathcal{R} = \mathcal{R}_{\text{ref}} + C' \left[(P_{\text{path}}X_{O_2}L_{\text{path}}) - (P_{\text{path}}X_{O_2}L_{\text{path}})_{\text{ref}} \right] \tag{5.22}$$

where C' is related to C as follows:

$$C' = \frac{C}{X_{O_2}L_{\text{ref}}} \tag{5.23}$$

Figure 5.7 compares the observed pressure dependence to that predicted from the beam path absorption model of Chapter 2. The observed temperature dependence does not match the dependence predicted by beam path absorption effects. Futhermore, the magnitude of the pressure effects is significantly stronger than those predicted by the beam path absorption model. Therefore, the data presented in this section suggest that the collisional quenching, albeit at a lower rate than that predicted by either Cann or Miles data, is responsible for the pressure effects, and the beam path absorption effects are masked by the collisional quenching effects.

Nevertheless, assuming that the entire pressure dependence in $\mathcal{R}$ originates from beam path absorption, the temperature error ΔT resulting from an path length error ΔL is given by

$$\Delta T = \frac{C'PX_{O_2}}{\partial\mathcal{R}/\partial T}\Delta L \tag{5.24}$$

These temperature errors are also listed in Table 5.2 for $P_{\text{path}} = 3.77$ atm and $X_{O_2} = 0.2$.

Calibration of the technique for beam path effects is much more difficult than calibration for collisional quenching effects. Since the beam path effects depend not only on T and $PX_{O_2}L$, but also on T_{path}, each of these parameters must be independently varied. One possible method is the introduction of a cell whose temperature and pressure can be independently adjusted into the beam path. The effect of beam path pressure and temperature may then be determined by adjusting the pressure and temperature inside this cell.

5.2.6 Flow Rate Effects

Each pulse from the ArF laser generates photochemical products. In particular, ozone (O_3) may be detected by smell in the (unpurged) laser beam path. The ozone is probably produced by the $O + O_2 \rightarrow O_3$ reaction where the O atom is the predissociation product resulting from the ArF laser pulse.

Because this chemical reaction path is slow, it does not effect the measurements from a single pulse. On the other hand, since the recombination of the products to reform O_2 molecules is also slow, the products of a pulse may affect the measurements of subsequent pulses. Consequently, for a measurement volume of L and a laser repetition rate of f, the flow velocity must satisfy the following condition

$$u \gg Lf \tag{5.25}$$

so that the photochemical products of one pulse are flushed out of the measurement volume before the next pulse.

For $L = 1$ mm and $f = 100$ Hz, the flow rate should be $\gg 0.1$ cm/s. This should not pose any problem for turbomachinery flows where flow rates are of the order of 10^2 m/s.

Although the mean flow speed satisfies equation (5.25), the stagnant regions in the flow may pose a problem. For example, the regions just outside the boundary of a free jet may not have the necessary high flow rate. Fortunately, the LIF spectrum provides an indicator of low-flow conditions: a non-O_2 LIF peak appears at 207.7 nm (see Figure 5.8).

5.2.7 Temperature Variations

The LIF technique measures the temperature in a finite volume. Any temperature gradient across this volume will result in an error.

Let the temperature distribution across the measurement volume located in the region $-L/2 \geq x \geq L/2$ be given by $T(x)$. The numerator and denumerator signals will be

$$S_{D_m} = \int_{-L/2}^{L/2} S_D(T(x))dx \tag{5.26a}$$

$$S_{N_m} = \int_{-L/2}^{L/2} S_N(T(x))dx = \int_{-L/2}^{L/2} \mathcal{R}(T(x))S_D(T(x))dx \tag{5.26b}$$

The mean temperature in this region is given by

$$\bar{T} = \frac{1}{L}\int_{-L/2}^{L/2} T(x)dx \tag{5.27}$$

but the temperature measured by the LIF technique will be

$$T_m = \mathcal{R}^{-1}\left(\frac{S_{N_m}}{S_{D_m}}\right) \tag{5.28}$$

The resulting error in temperature is given by

$$\Delta T = T_m - \bar{T} \tag{5.29}$$

The equations presented in section 5.1 have been used to compute the temperature measurement error resulting from a linear variation in temperature across the measurement volume (see Figure 5.9) at three temperature levels. The results are shown in Figure 5.10. The temperature error is insensitive to the average temperature and may be approximated using the following formula:

$$\Delta T = 0.00064\delta T^2 \tag{5.30}$$

For $\delta T < 40\ K$, the temperature error due to spatial temperature variations is less than 1 K.

5.2.8 Calibration Uncertainty

The calibration uncertainty results from the uncertainty in the thermocouple measurements and temperature diagnostic ratios $\mathcal{R}$ used to calculate the model coefficients listed in Table 4.9. These uncertainties are listed in Table 5.3.

According to the values in this table, the precision of the calibration is determined by the uncertainty in $\mathcal{R}$. The uncertainty in $\mathcal{R}$ may always be reduced by integrating data from multiple shots as described in section 5.3.3. As the uncertainty in $\mathcal{R}$ is reduced, the calibration uncertainty will be determined by the uncertainty in the thermocouple measurements.

In addition, the function used for calibration only approximates the real function, and therefore, introduces an error. The magnitude of this error is also tabulated in Table 5.3. Except at 322.4 K, the calibration error is less than the calibration uncertainty.

5.3 Precision Improvement

The precision of the measurement technique is limited by quantum and detector noise. For a given thermal conditions (i. e. given T, P), there are three ways of improving measurement precision: increasing laser fluence, increasing signal collection, or integrating signals from multiple laser shots.

5.3.1 Laser Fluence

Increasing laser fluence (E'') does increase the signal precision. For detector noise dominated measurements, the improvement is linear with E''; for quantum noise dominated measurements, the improvement scales as $\sqrt{E''}$.

One upper limit on the laser fluence is the capability of the experimental apparatus. For this apparatus, with a maximum laser energy of 100 mJ and a transmission efficiency of 15%, the maximum fluence is approximately 1100 J/cm^2. However, note that this requires that the laser be operated at low repetition rates ($\leq$ 10 Hz).

However, increasing laser fluence also increases errors due to nonlinear phenomena, namely O_2^+ LIF at lower temperatures and saturation at higher temperatures. In fact, over most of the temperature and pressure range considered in this project, it is the nonlinear errors, rather than the performance of the experimental apparatus, which limit the laser fluence.

5.3.2 Collection Optics

Another method for improving technique precision is to increase the amount of signal collected. Once again, the precision improvement scales linearly with the signal level for detector-noise dominated measurements, and with the square root of the signal level for quantum-noise dominated measurements. Consequently, the experimental apparatus should be designed so that the maximum signal is collected.

As described in Chapter 3, the experimental apparatus for this project was indeed designed to collect the maximum LIF signal given the constraints imposed by the turbomachinery environment. Furthermore, the transmission efficiency of the optical equipment, such as the imaging lens, spectrometer and detector, are typical of the state-of-the-art components currently in the market. Since the amount of light collected is limited by the spectrometer f-number, using a larger imaging lens will not increase the signal level.

In conclusion, for this project, the technique precision may not be improved by redesigning the collection optics.

5.3.3 Multiple Shot Measurements

The third method for improving technique precision is to collect data from multiple laser shots. The LIF signals from the multiple shots are then summed, and this composite LIF signal is used in the data reduction method of Chapter 4.

The summation may be performed either physically on the detector ("on-detector integration") or numerically off the detector ("off-detector integration").

In on-detector integration, the detector is exposed for multiple laser shots. The LIF signal produced by these laser shots are collected on the detector photodiodes, and the photodiodes are read out only once after the last laser shot.

For a given laser repetition rate, the technique precision improves as N for readout noise dominated measurements, and $\sqrt{N}$ for thermal or quantum noise dominated measurements.

The digitization limit of the detector is 65535 counts per photodiode (16-bit). The number of shots for on-detector integration must be limited so that the reading per channel does not exceed this value. In addition, the laser gas life places an upper limit of 250,000 shots assuming that cryogenic purification is used.

Figure 5.11 compares theoretical behavior with experimental data at 426 K and 3.75 atm. The data in this experiment is dominated by quantum noise; therefore, the improvement

scales with $\sqrt{N}$ for $N < 5000$. The two anamolous points at $N = 5000$ and $10,000$ may be explained by the temperature fluctuations in the calibration test cell; the magnitude of the fluctuations is consistent with the fluctuations measured in the test cell using a high-speed thermocouple probe (see Appendix A).

There are two major disadvantages to on-detector integration. First, the effect of laser energy decrease with increasing number of shots cannot be monitored. For $N > 10^4$, the laser energy will be gradually decreasing during an experiment. Second, the chances of contamination by anomalous spectra is higher; furthermore, if there is an anomalous spectra, all data from the N shots is useless.

In off-detector integration, the detector is read out after every shot. The data from N shots is then digitally added on a computer. In this case, the improvement scales with $\sqrt{N}$ regardless of the dominant noise source. Consequently, on-detector integration always performs better than off-detector integration (see Figure 5.12). However, off-detector integration allows one to examine the laser energy decrease, and if there is contamination by anomalous spectra, it affects measurement from a single shot.

It is possible to combine the advantages of both on-detector and off-detector integration. For example, N laser shots may be integrated on the detector per spectrum, and then M such spectra may be digitally integrated. In this case, N should be high enough that the readout noise is negligible. From formulae given in section 5.2.3, readout noise is negligible compared to thermal noise for $X \gg 500$ ms. For a laser repetition rate of 100 Hz, this corresponds to $N \gg 50$ shots. For most of the experiments in this project, 500 shots were integrated on-detector per spectrum.

5.4 Optimum Precision and Accuracy

As described in the previous section, there is a direct trade-off between precision and accuracy through laser fluence. High laser fluences lead to high-precision, low-accuracy measurements, whereas low fluences lead to low-precision, high-accuracy measurements.

The optimum point may be chosen as that where the uncertainty σ_T is equal to the error $|\Delta T|$. This condition is demonstrated in Figure 5.13.

Accuracy depends only on the laser fluence; however, precision depends on laser fluence as well as the number of shots integrated. Consequently, the optimum laser fluence depends on the number of shots. Figures 5.14 through 5.16 and Table 5.4 shows the optimum laser fluences at three temperature as a function of number of shots. Note that as the number of shots increase, the optimum laser fluence decreases in order to keep the measurement error equal to the measurement uncertainty.

Figure 5.17 shows the resulting improvement in measurement precision. Nominally, the measurement precision improves with $\sqrt{N}$. However, because the laser fluence has to be reduced, the observed improvement scales with $\sqrt[3]{N}$.

Table 5.5 show how precision and accuracy depend on temperature. If the temperature level to be measured were to be known a priori (for example, it may have been estimated from a previous mesurement), the data in this table may be used to determine the optimum laser fluence and the resulting temperature precision and accuracy.

On the other hand, if the temperature were not known a priori, one would choose an average fluence. For 1, 1000 and 250000 shots, these fluences are 2000, 150 and 20 J/cm^2 respectively. The resulting temperature uncertainties are shown as functions of pressure and temperature in Figures 5.18 through 5.20, and the temperature errors are shown in Figures 5.21 through 5.23.

5.5 Correction for Nonlinear Phenomena

Theoretically, the temperature error due to nonlinear phenomena may be reduced or eliminated by simulataneously measuring the laser beam fluence and correcting for the nonlinear effects during the data reduction process. This section discusses the benefits and limitations of these measurements.

The fluence dependence of the laser diagnostic ratio may be written

$$\mathcal{R}_m = \mathcal{R} + k_1(T,P)E'' + k_2(T,P)\left(E''\right)^2 + \ldots \tag{5.31}$$

Figure 5.24 plots the temperature uncertainty resulting from measurements corrected for fluence at 428 K and 1 atm. The temperature error and uncertainty for uncorrected measurements, obtained from Figure 5.25, are also plotted. A relative fluence measurement and correction uncertainty of 20% (i. e. $\sigma_{E''}/E'' = 0.2$) has been assumed. Furthermore, since there is no measurement error, the uncertainty for the corrected measurements have been multiplied by 0.64, so that the probability of obtaining a measurement within $\pm\sigma$ of the true value is the same for corrected and uncorrected measurements.

As discussed above, the optimum fluence without the correction is the point given by the intersection of ΔT and σ_T lines for a given number of shots. For corrected measurements, the optimum fluence for a given number of shots is at the minimum uncertainty; these points are marked on Figure 5.24.

Figure 5.25 compares the measurement precision with and without fluence correction. The fluence correction reduces the uncertainty by a factor of approximately 1.8; the improvement with the increasing number of shots is the same for both corrected and uncorrected measurements.

However, implementing fluence measurement and correction technique presents several disadvantages. First, since k_1 and k_2 are functions of temperature, which is being measured, an iterative data reduction procedure is needed. Second, the 20% uncertainty assumed above includes the total uncertainty introduced by the fluence measurement and correction technique, including the uncertainties resulting from fluence measurements, the uncertainties in the model constants k_1 and k_2, and the data reduction procedure. Finally, because the laser noise affects the measurement through the higher-order terms, the fluence of every laser pulse must be measured and recorded separately.

In conclusion, although implementing a fluence measurement and correction technique improves the measurement precision by a factor of about 1.8 compared to the uncorrected measurements, this technique presents several disadvantages. Therefore, limiting the fluence and increasing the number of shots is an easier and more promising technique.

5.6 Practical Measurement Considerations

Assume that 1000 shots are used per measurement. At 200 Hz laser repetition rate, the maximum which can be reliably obtained from the particular laser used in this study, each point requires 5 s. If an automated positioning system is used, 5760 points, corresponding to almost an 18^3 grid, may be measured in an eight-hour day. This is reasonable for measurements in steady-state rigs.

In comparison, the LDA system in use on a turbomachinery rig at NASA Lewis Research Center acquires data from 1000 circumferential points in less than 1 minute [11, 12]. The optical temperature measurement technique, limited by the quantum efficiency and nonlinear processes, is almost 100 times slower than the optical velocity measurement technique, which is limited by seeding and data acquisition rates.

5.7 Laser Fluence Threshold

This is the first study which determines the limiting fluence E'' as a function of temperature. This section compares the limiting fluence levels of this study with values cited in two other studies.

Laufer et. al. [6,7] cite a O_2^+ LIF threshold of 1.8 J/cm^2, and Annen and Nelson [1] cite a threshold of 50 J/cm^2. As explained in Annen and Nelson, the value given by Laufer et. al. was incorrectly calculated, and the correct value is approximately 25 J/cm^2, which is consistent with the latter authors' result.

The conditions at which Annen and Nelson calculated the threshold fluence may be obtained from Kolczak [5], who used the same data. The temperature is 298 K (25°C), the pressure is 1.3 atm (1300 mbar) and 100 shots were integrated on the detector. From Table 5.4, the limiting fluence obtained by this study is 150 J/cm^2, which is three times the value given by Annen and Nelson.

Annen and Nelson's limiting fluence comes from a visual inspection of LIF spectrum; their threshold value is the fluence at which the O_2^+ features become visible. This study does a trade-off between measurement accuracy and measurement precision; the limiting fluence is the value at which the uncertainty equals the error. Consequently, this study tolerates a higher level of O_2^+ LIF signal than Annen and Nelson, and this observation explains why the laser fluence threshold cited here is higher than the value given by Annen and Nelson.

In conclusion, the laser fluence threshold cited here at 298 K is consistent with the value cited by Annen and Nelson, and is also consistent with the value cited by Laufer et. al. provided their data is corrected as explained in Annen and Nelson.

5.8 Summary

This chapter presents the first comprehensive and quantitative error analysis of O_2 LIF temperature measurement technique.

The technique precision is limited by quantum and detector noise, and the technique accuracy is limited by nonlinear phenomena, namely O_2^+ LIF at lower temperatures and

saturation at higher temperatures. Increasing laser fluence increases measurement precision due to increased signal levels, but also increases measurement error due to nonlinear errors. At the optimum conditions, the measurement precision and accuracy are equal. The optimum laser fluences and the resulting measurement precision and accuracies have been calculated.

The technique precision may be improved by integrating LIF signals from multiple shots. Because the laser fluence must be reduced to keep the accuracy equal to the precision, the improvement scales as $\sqrt[3]{N}$.

For measurements better than 1 K, 1000-shot measurements are adequate for temperatures above 400 K at 3.77 atm. At 300 K, sub-degree measurements require 250,000 shots.

This is the first study to determine the laser fluence threshold as a function of temperature and number of shots. The threshold value at 300 K is consistent with data given by other researchers.

Temperature error due to pressure effects, originating from either collisional quenching or beam path absorption, have been calculated. The pressure dependence have been shown to be inconsistent with and higher than that predicted by the beam path absorption model of Chapter 2. The pressure effects exhibit roughly the same temperature dependence predicted by collisional quenching model, although their magnitudes are significantly lower than those predicted by the Cann and Miles models.

Other error sources have also been analyzed. The error due to spatial variations in temperature across the measurement volume is less than 1 K for δT <40 K. For accurate measurement, the flow rate at the measurement volume should be $\gg Lf$. Measurements in stagnant regions may be identified by the presence of an additional non-O_2 LIF spectral feature at 207.7 nm.

The particular calibration given in Chapter 4 has been shown to be precise within 5 K for temperatures between 320 K and 531 K. The error introduced by the calibration function of equation 4.13 is within the calibration uncertainty at ten of eleven points. The calibration precision is consistent with the number of shots used per experiment.

References

[1] ANNEN, K., AND NELSON, D. Turbomachinery Tempearture Measurements Using an O_2 LIF Flowfield Diagnostic. Tech. Rep. ARI-RR-954, Aerodyne Research, Inc., 45 Manning Road, Billerica, MA 01821, September 1992.

[2] BEVINGTON, P. R., AND ROBINSON, D. K. *Data Reduction and Error Analysis for the Physical Sciences*, second ed. McGraw-Hill, Inc., New York, NY, 1992.

[3] CANN, M. W. P., NICHOLLS, R. W., EVANS, W. F. J., KOHL, J. L., ET AL. High Resolution Atmospheric Transmission Calculations Down to 28.7 km in the 200-243-nm Spectral Range. *Applied Optics 18*, 7 (April 1979), 964–977.

[4] CANN, M. W. P., SHIN, J. B., AND NICHOLS, R. W. Oxygen absorption in the spectral range 180-300 nm for temperatures to 3000K and pressures to 50 atm. *Canadian Journal of Physics 62* (1984), 1738–1751.

[5] KOLCZAK, F. Temperature Measurements in a Flow Using Laser Induced Fluorescence of Oxygen. Master's thesis, Massachusetts Insitititue of Technology, Cambridge, MA 02139, September 1992.

[6] LAUFER, G., FLETCHER, D., AND MCKENZIE, R. A Method for Measuring Temperatures and Densities in Hypersonic Wind Tunnel Air Flows Using Laser Induced O_2 Fluorescence. *AIAA Paper AIAA-90-0626* (1990).

[7] LAUFER, G., AND MCKENZIE, R. L. Temperature Measurements in Hypersonic Air Flows Using Laser-Induced O_2 Fluorescence. *AIAA Paper AIAA-88-4679-CP* (1988).

[8] LAUFER, G., MCKENZIE, R. L., AND HUO, W. M. Radiative Processes in Air Excited by an ArF Laser. *Optics Letters 13*, 2 (February 1988), 99–101.

[9] MARCUSE, D. *Principles of Quantum Electronics.* Academic Press, New York, NY, 1980.

[10] MILES, R. B., CONNORS, J. J., HOWARD, P. J., MARKOVITZ, E. C., AND ROTH, G. J. Proposed Single-Pulse Two-Dimensional Temperature and Density Measurements of Oxygen and Air. *Optics Letters 13*, 3 (March 1988), 195–197.

[11] POWELL, J. A., STRAZISAR, A. J., AND SEASHOLTZ, R. G. Efficient Laser Anemometer for Intra-Rotor Flow Mapping in Turbomachinery. *Journal of Engineering for Power 103* (April 1981), 424–429.

[12] STRAZISAR, A. J., AND POWELL, J. A. Laser Anemometer Measurements in a Transonic Axial Flow Compressor Rotor. *Journal of Engineering for Power 103* (April 1981), 430–437.

Table 5.1: Fitted Coefficients for Nonlinear Model (see equation (5.16))

T K	A_1	A_2	A_3
297.0	0.9394	1.44×10^{-3}	-3.59×10^{-7}
322.4	0.9820	1.30×10^{-3}	-9.74×10^{-7}
348.5	1.1232	9.72×10^{-4}	-5.27×10^{-7}
375.6	1.3319	5.38×10^{-4}	2.61×10^{-6}
401.7	1.6643	6.88×10^{-4}	-4.38×10^{-7}
427.7	2.0853	4.17×10^{-4}	3.24×10^{-7}
455.6	2.6103	-1.09×10^{-4}	4.59×10^{-7}
481.3	3.2346	-7.79×10^{-4}	1.48×10^{-6}
507.2	3.7019	-3.44×10^{-4}	3.05×10^{-7}

Table 5.2: Fitted Coefficients for Collisional Quenching Function (see equation (5.21))

			COLLISIONAL QUENCHING		BEAM PATH ABSORPTION	
T		$\mathcal{R}_{\text{ref}}$	C	$\Delta T/\Delta P$	C'	$\Delta T/\Delta L$ [a]
K	C		atm^{-1}	K atm^{-1}	cm^{-1} atm^{-1}	K cm^{-1}
301.1	27.9	0.860	−0.0086	−2.8	−0.012	−2.9
322.4	49.2	0.991	−0.0092	−2.1	−0.013	−2.2
348.4	75.2	1.092	−0.012	−1.8	−0.017	−1.9
374.9	101.7	1.320	−0.013	−1.3	−0.018	−1.4
400.8	127.6	1.642	−0.019	−1.4	−0.026	−1.4
425.8	152.6	2.015	−0.0083	−0.45	−0.012	−0.49
452.7	179.5	2.568	−0.030	−1.3	−0.041	−1.3
477.8	204.6	3.151	−0.039	−1.6	−0.054	−1.7
505.0	231.8	3.865	−0.040	−1.8	−0.056	−1.9
531.4	258.2	4.300	−0.034	−2.4	−0.047	−2.6
556.9	283.7	4.561	−0.032	−5.8	−0.044	−6.1

[a] $P_{\text{ref}} = 3.77$ atm, $X_{O_2} = 0.2$.

Table 5.3: Calibration Uncertainty and Error

TEMPERATURE DATA		SPECTRAL DATA		MODEL		CALIBRATION UNCERTAINTY	CALIBRATION ERROR	
$\bar{T}$	σ_T	$\bar{\mathcal{R}}$	$\sigma_{\mathcal{R}}$	$R(\bar{T})$	dR/dT	σ	T_{calc}	ΔT
K	K				K^{-1}	K	K	K
301.1	0.10	0.8604	0.0332	0.8821	0.00303	10.94	293.4	-7.7
322.4	0.18	0.9912	0.0189	0.9601	0.00436	4.35	329.1	-6.7
348.4	0.23	1.092	0.0152	1.101	0.00660	2.30	347.0	1.4
374.9	0.89	1.320	0.0165	1.316	0.00979	1.68	375.3	-0.4
400.8	1.10	1.642	0.0219	1.620	0.0139	1.58	402.4	-1.6
425.8	0.63	2.015	0.0287	2.023	0.0184	1.56	425.4	0.4
452.7	1.38	2.568	0.0358	2.581	0.0228	1.57	452.1	0.6
477.8	0.55	3.151	0.0803	3.184	0.0246	3.26	476.5	1.3
505.0	1.20	3.865	0.0509	3.827	0.0218	2.34	506.7	-1.7
531.4	1.67	4.300	0.0619	4.313	0.0144	4.31	530.5	0.9
556.9	0.84	4.561	0.0693	4.567	0.00553	12.53	555.9	1.0

Table 5.4: Optimum Laser Fluences at 3.77 atm for 297 K, 428 K and 507 K

	297.0 K		427.7 K		507.2 K	
	E''	$\sigma_T = \Delta T$	E''	$\sigma_T = \Delta T$	E''	$\sigma_T = \Delta T$
N	J/cm^2	K	J/cm^2	K	J/cm^2	K
1	750	72.2	1350	6.6	1770	4.2
10	330	32.5	650	2.9	670	2.1
100	150	14.9	310	1.3	300	1.0
1000	70	6.9	150	0.6	130	0.5
10000	30	3.0	70	0.3	60	0.2
100000	15	1.5	40	0.2	30	0.1
250000	15	0.9	25	0.1	25	0.1

Table 5.5: Optimum Laser Fluences at 3.77 atm for 1 shot, 1000 shots and 250,000 shots

	1 shots			1000 shots			250,000 shots		
T	E''	$\sigma_T = \Delta T$	LIMITING	E''	$\sigma_T = \Delta T$	LIMITING	E''	$\sigma_T = \Delta T$	LIMITING
K	J/cm^2	K	PROCESS	J/cm^2	K	PROCESS	J/cm^2	K	PROCESS
297.0	750	72	O_2^+ LIF	70	6.9	O_2^+ LIF	15	0.9	O_2^+ LIF
322.4	880	43	O_2^+ LIF	80	4.2	O_2^+ LIF	15	0.6	O_2^+ LIF
348.5	1060	25	O_2^+ LIF	100	2.4	O_2^+ LIF	20	0.3	O_2^+ LIF
375.6	970	17	O_2^+ LIF	130	1.4	O_2^+ LIF	25	0.2	O_2^+ LIF
401.7	1290	9.6	O_2^+ LIF	120	1.0	O_2^+ LIF	20	0.1	O_2^+ LIF
427.7	1350	6.6	O_2^+ LIF	150	0.6	O_2^+ LIF	25	0.1	O_2^+ LIF
455.6	2830	3.4	O_2^+ LIF	460	0.3	SAT	50	<0.1	SAT
481.3	2930	2.9	O_2^+ LIF	90	0.5	SAT	15	0.1	SAT
507.2	5620	2.3	O_2^+ LIF	130	0.5	SAT	25	0.1	SAT

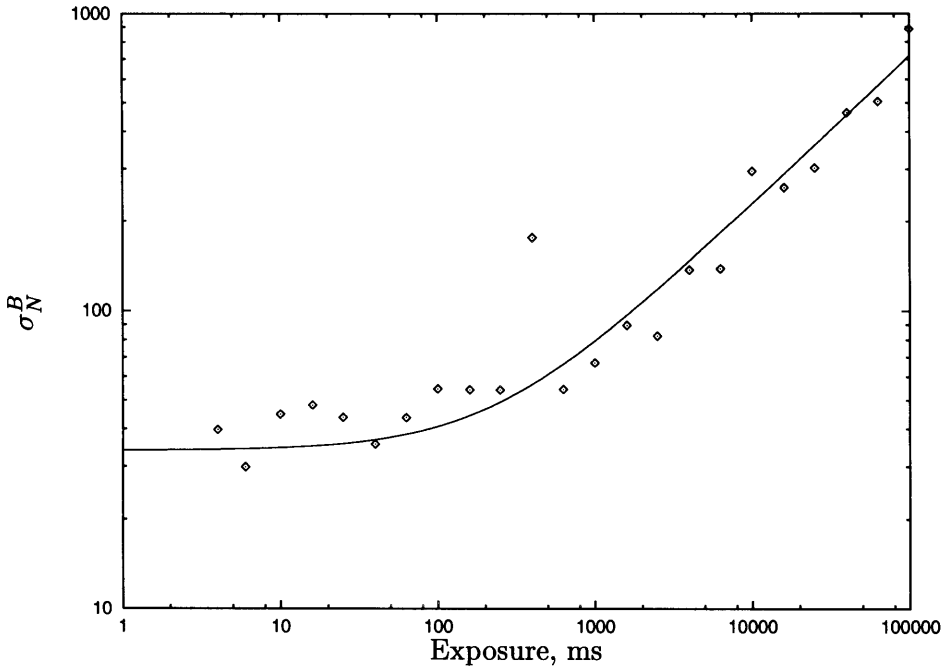

(a) Numerator Signal

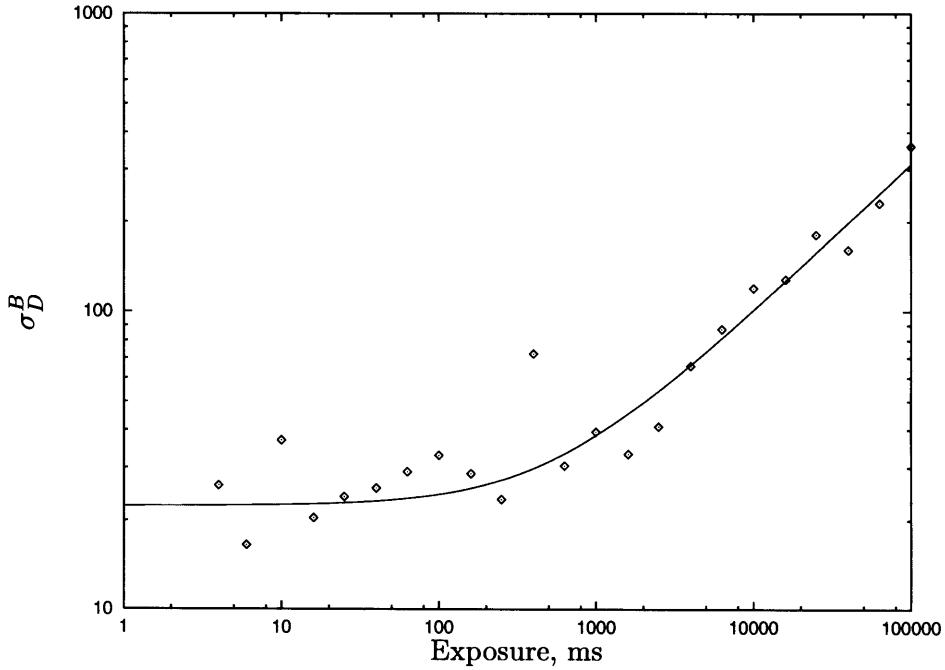

(b) Denumerator Signal

Figure 5.1: Thermal and Readout Noise

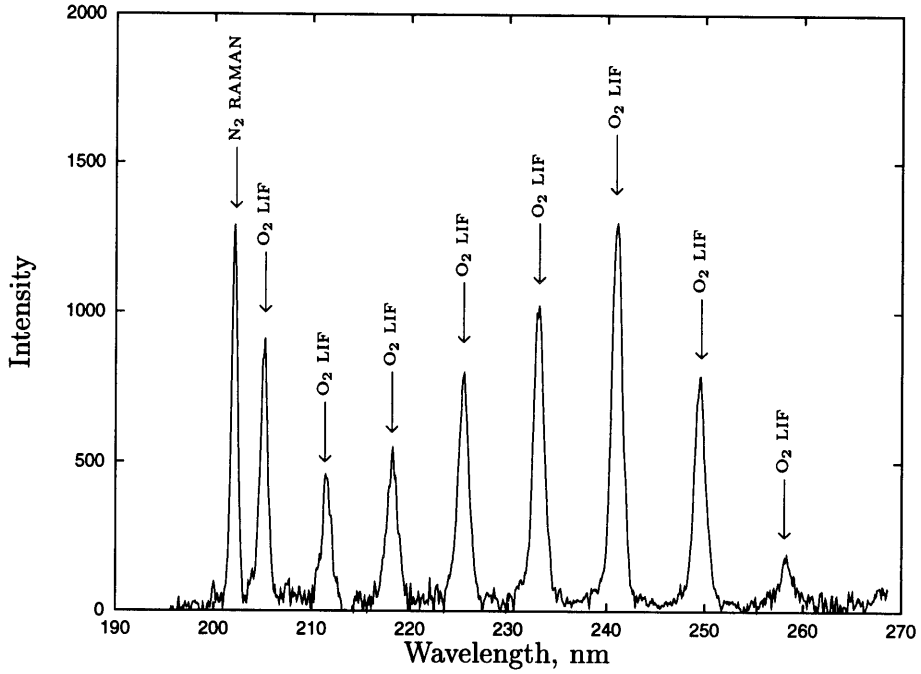

(a) Low Fluence Spectra at 301 K

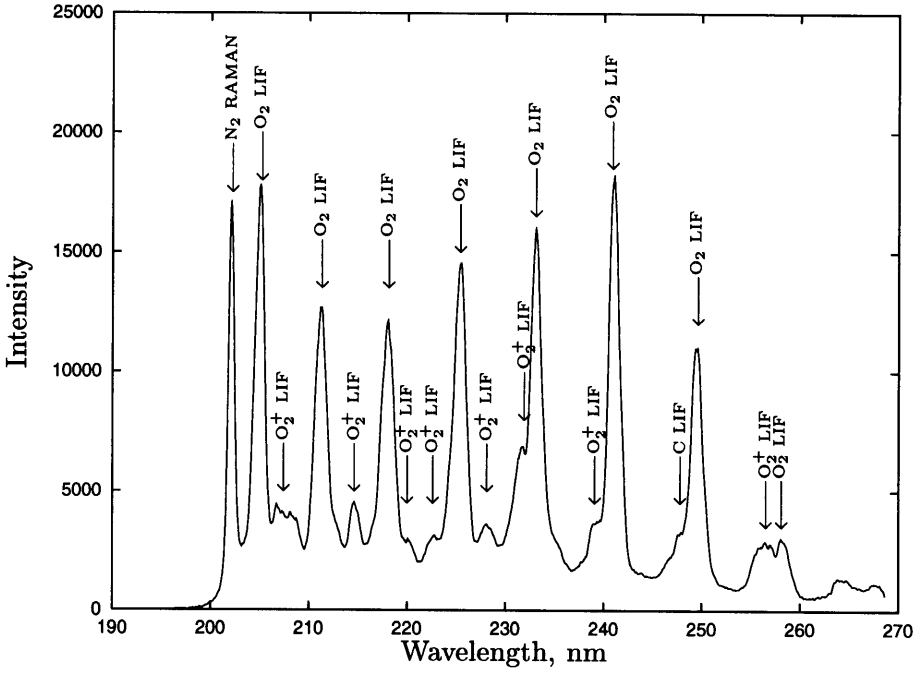

(b) High Fluence Spectrum at 301 K

Figure 5.2: Dependence of LIF Spectrum on Laser Fluence

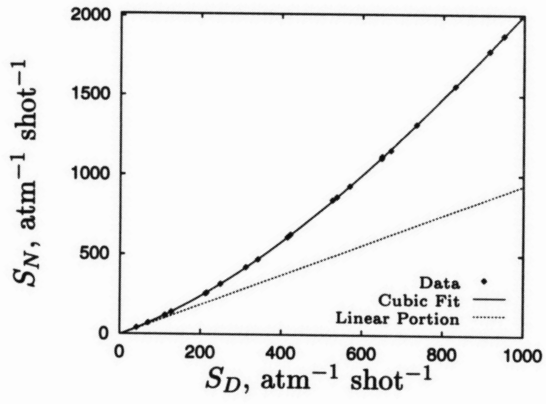

(a) 297 K (24 °C)

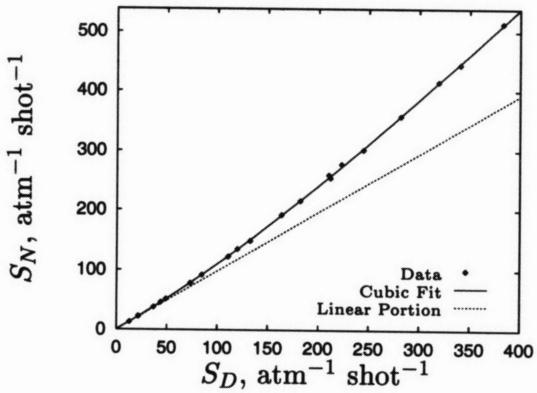

(b) 322 K (49 °C)

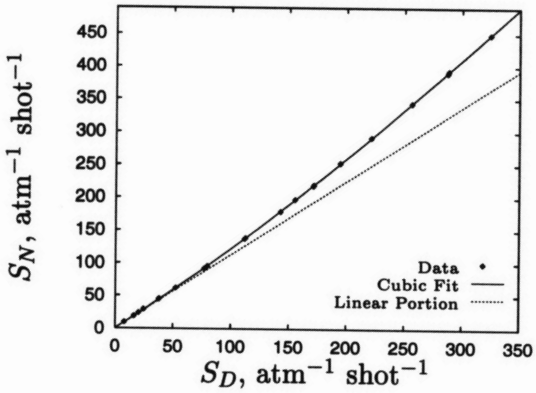

(c) 348 K (75 °C)

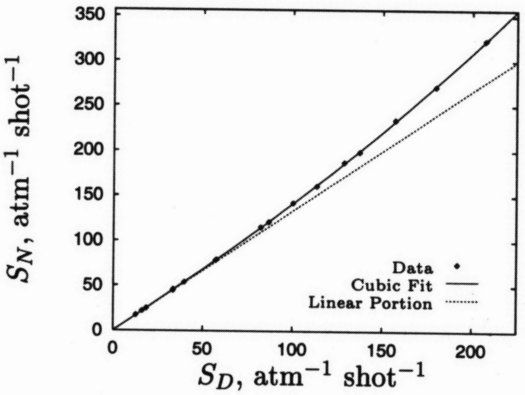

(d) 375 K (102 °C)

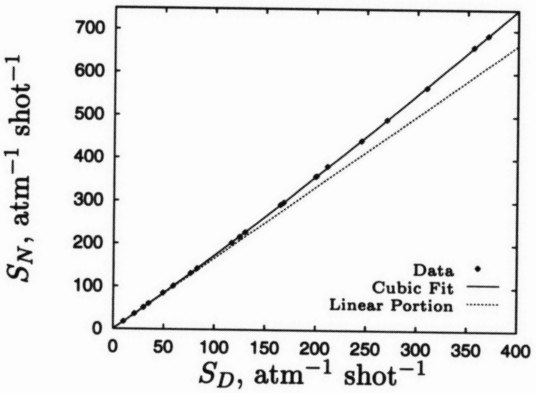

(e) 402 K (129 °C)

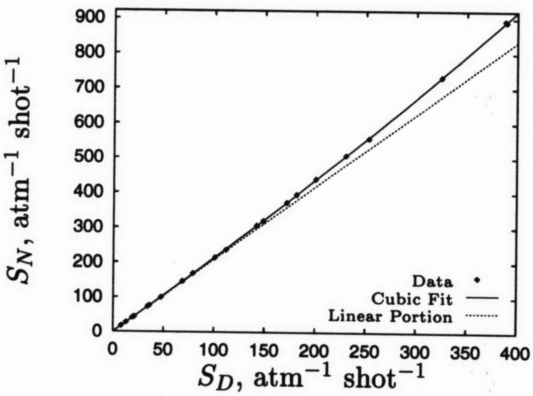

(f) 428 K (155 °C)

Figure 5.3: Nonlinear Signals for 297 K–428 K (24 °C–155 °C)

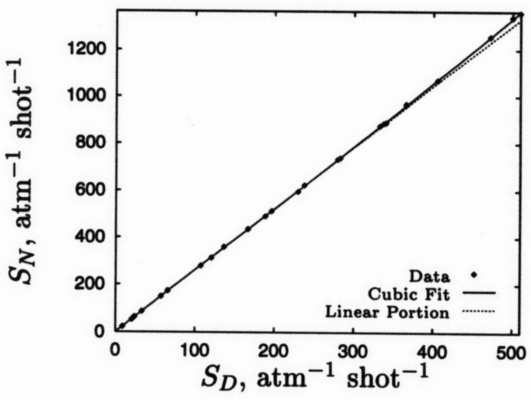

(a) 455 K (182 °C)

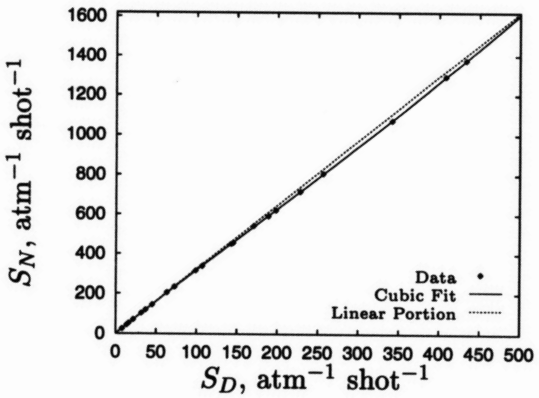

(b) 481 K (208 °C)

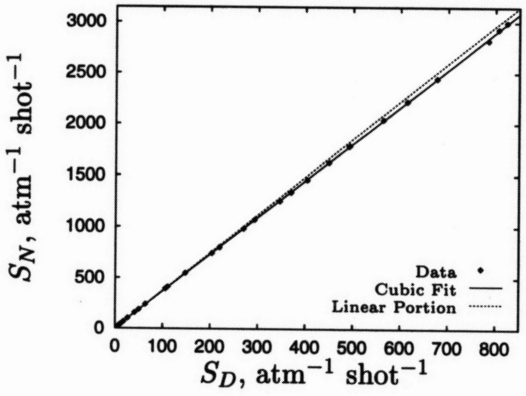

(c) 507 K (234 °C)

Figure 5.4: Nonlinear Signals for 455 K–507 K (182 °C–234 °C)

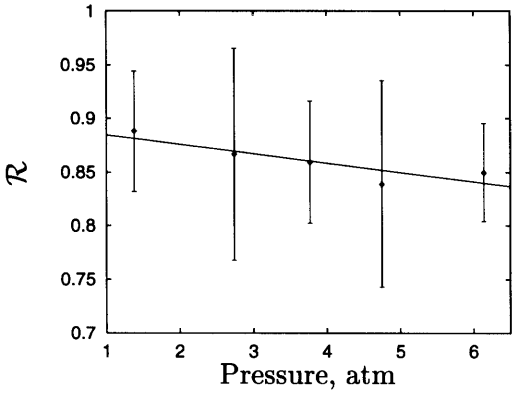

(a) 301 K (28 °C)

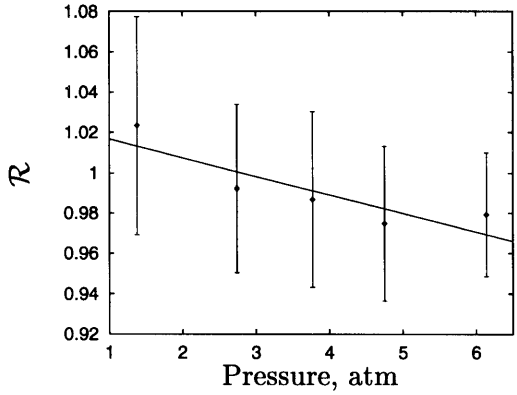

(b) 322 K (49 °C)

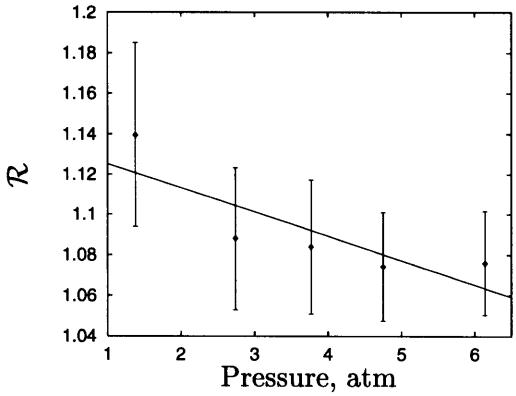

(c) 348 K (75 °C)

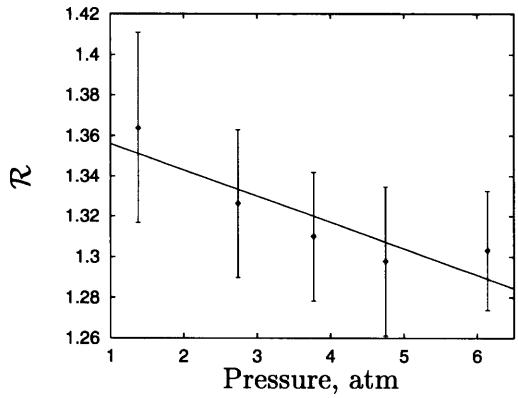

(d) 375 K (102 °C)

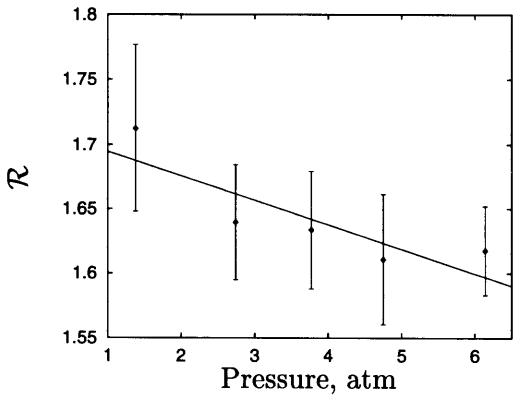

(e) 401 K (128 °C)

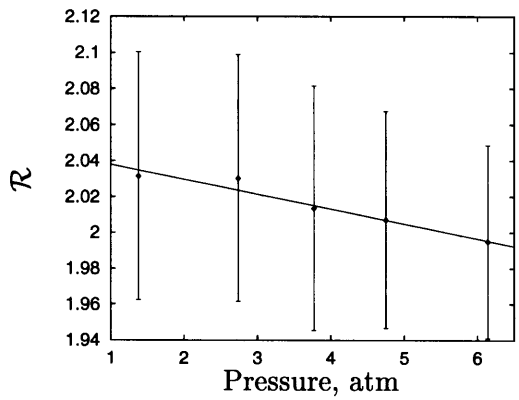

(f) 426 K (153 °C)

Figure 5.5: Pressure Effects for 301 K–426 K (28 °C–153 °C)

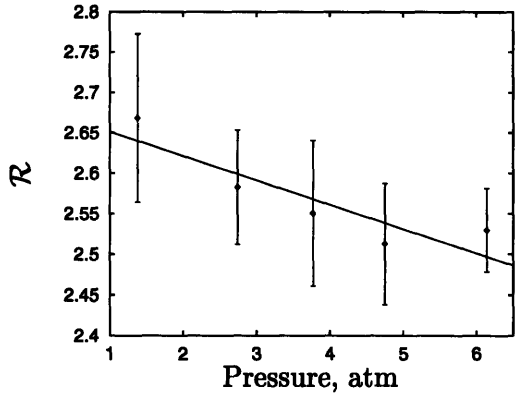

(a) 453 K (180 °C)

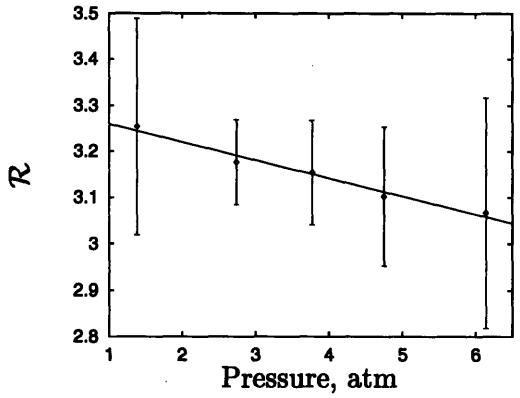

(b) 478 K (205 °C)

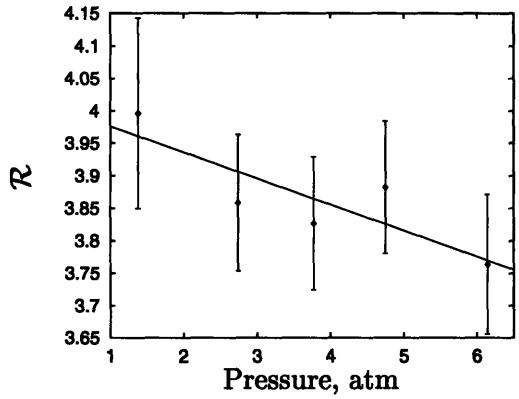

(c) 505 K (232 °C)

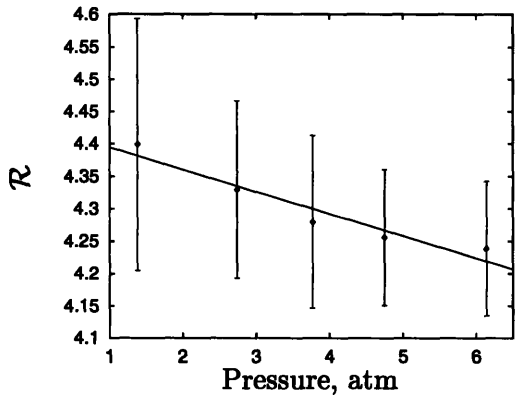

(d) 531 K (258 °C)

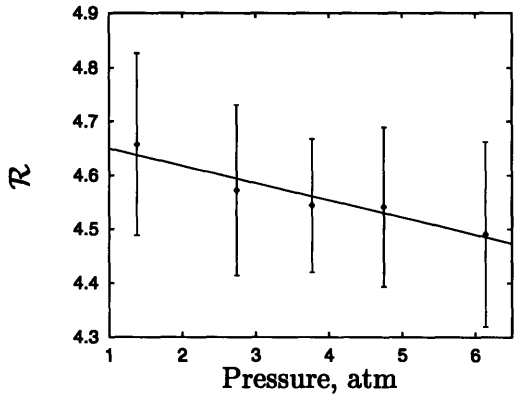

(e) 557 K (284 °C)

Figure 5.6: Pressure Effects for 453 K–557 K (180 °C–284 °C)

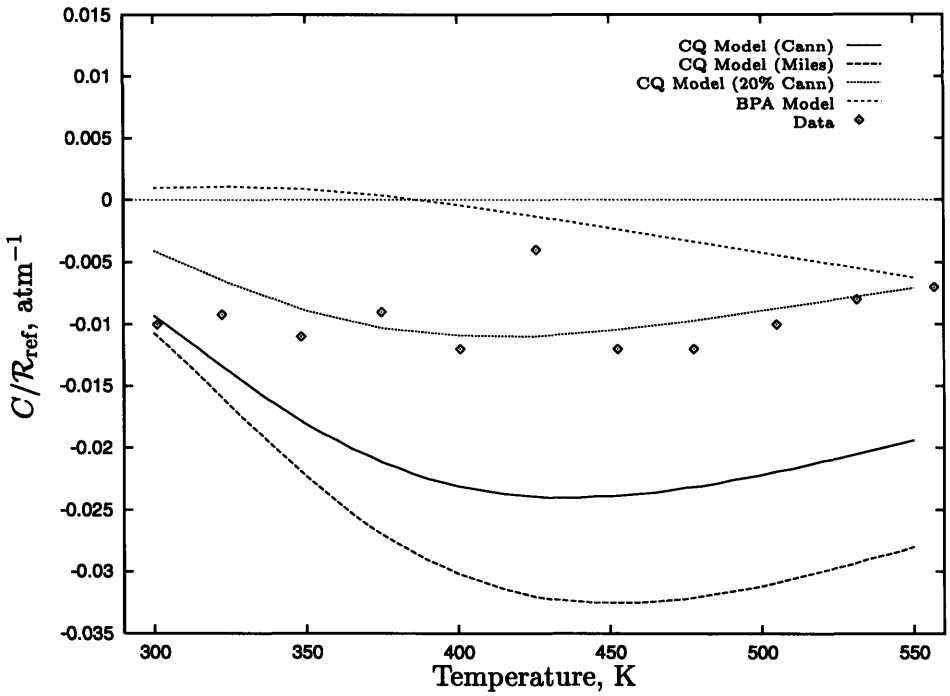

Figure 5.7: Comparison of Observed Pressure Dependence to Collisional Quenching and Beam Path Absorption Models

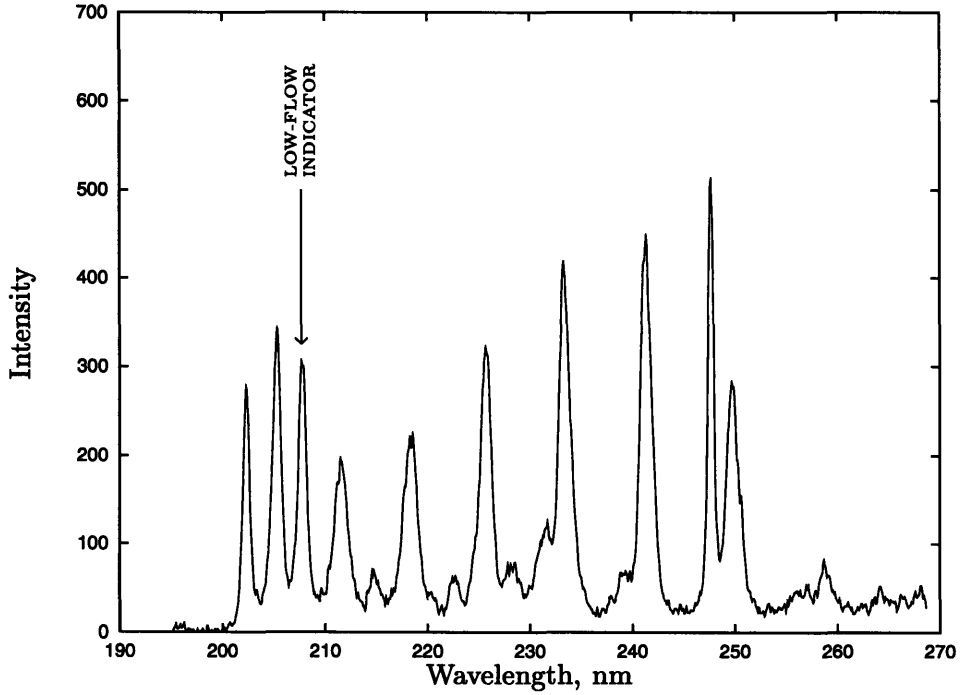

Figure 5.8: Spectral Indicator of Low-Flow Regions

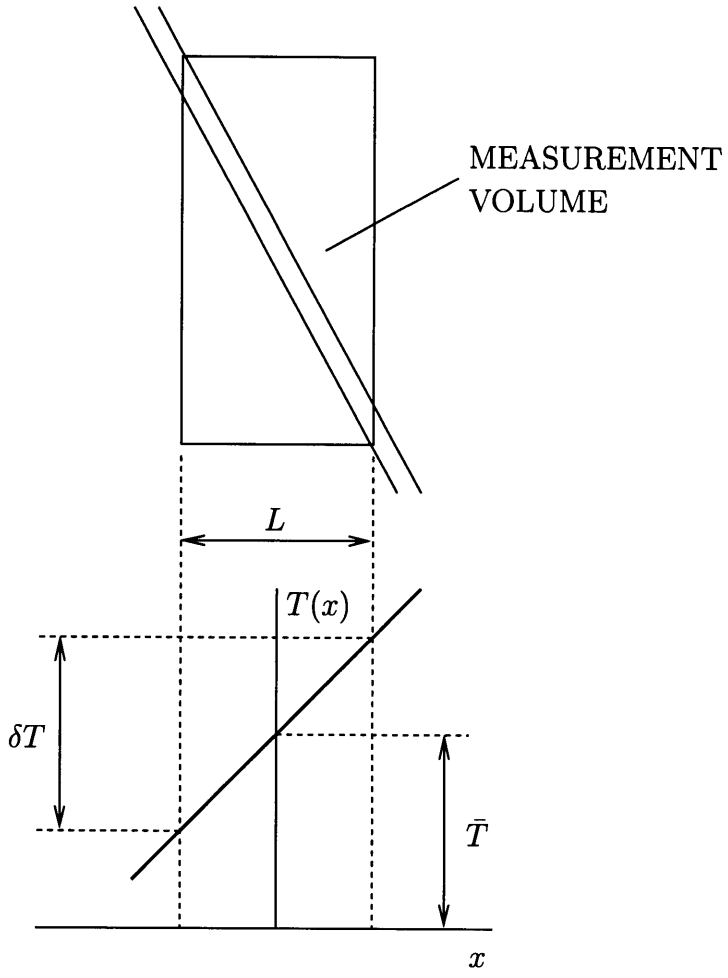

Figure 5.9: Temperature Variation Across Measurement Volume

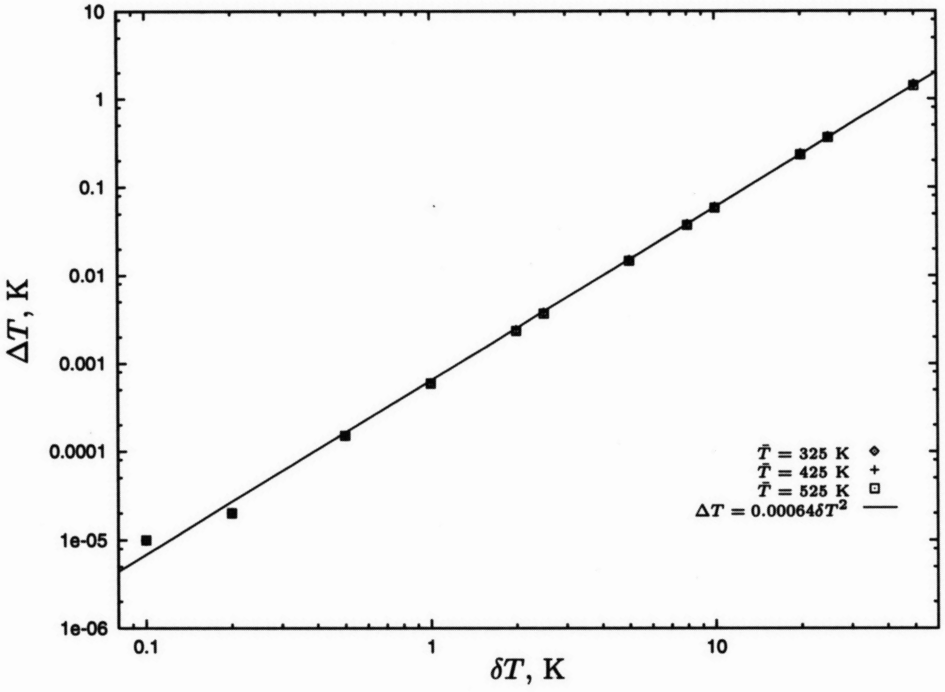

Figure 5.10: Temperature Error Resulting from Temperature Variation Across Measurement Volume

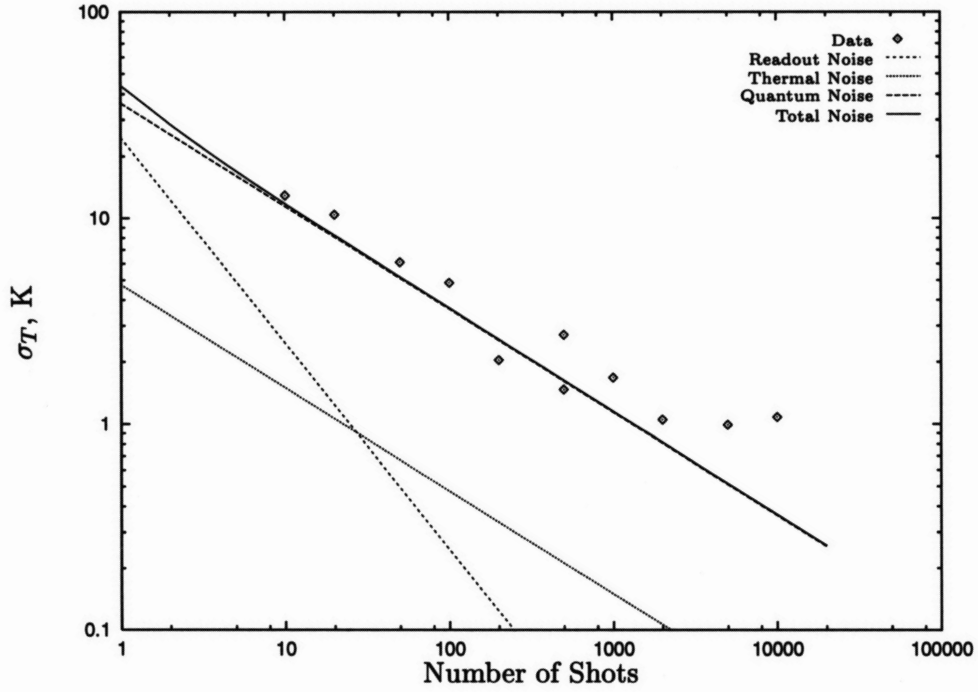

Figure 5.11: Measurement Uncertainty Improvement with On-Detector Integration at 426 K and 3.75 atm

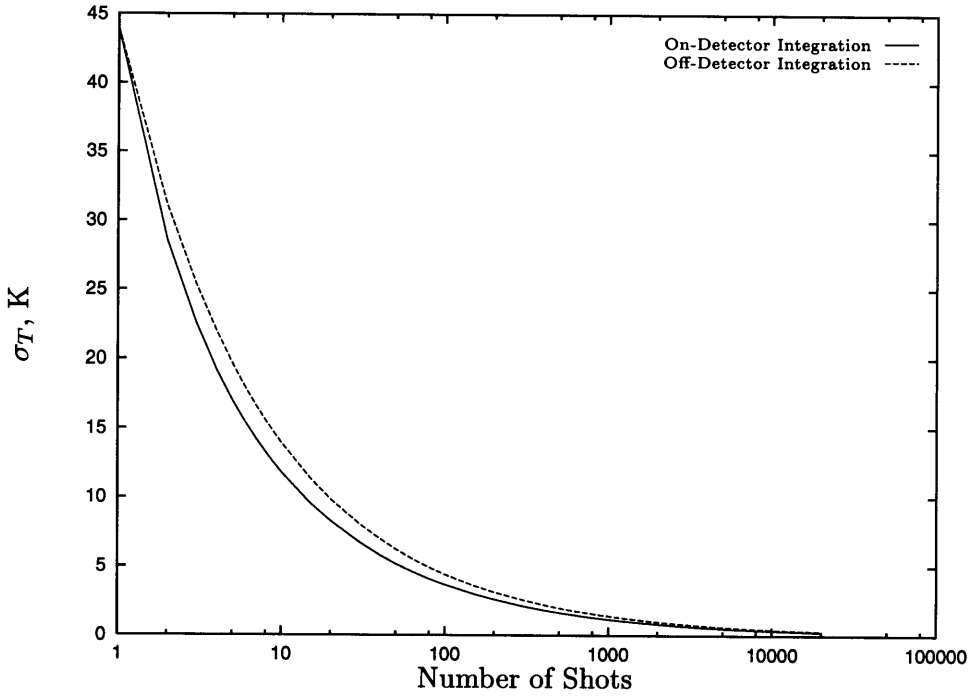

Figure 5.12: Comparison of On-Detector and Off-Detector Integration at 426 K and 3.75 atm

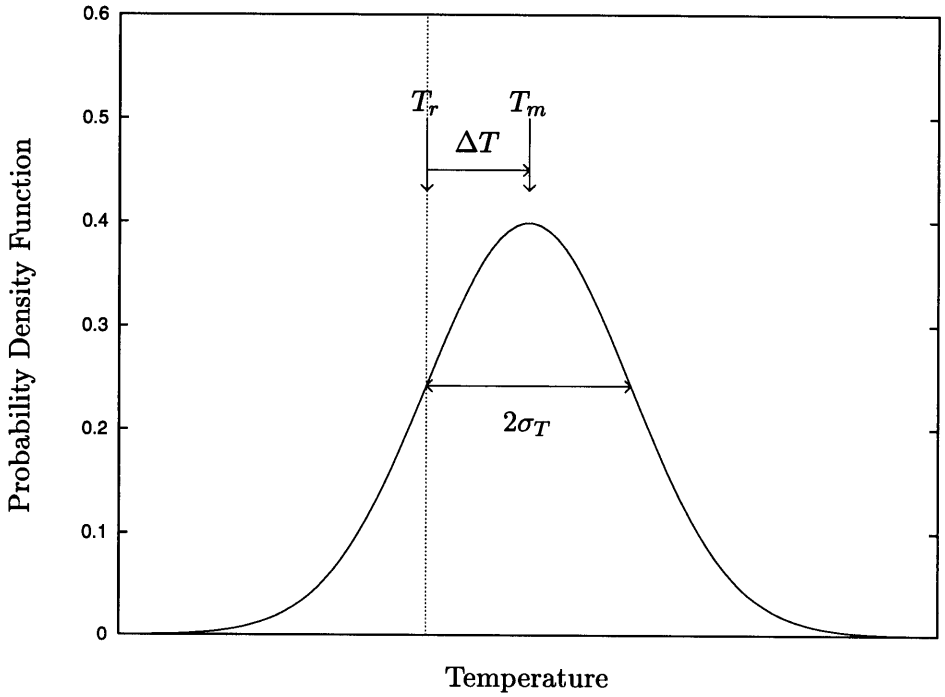

Figure 5.13: Measurement Error and Uncertainty

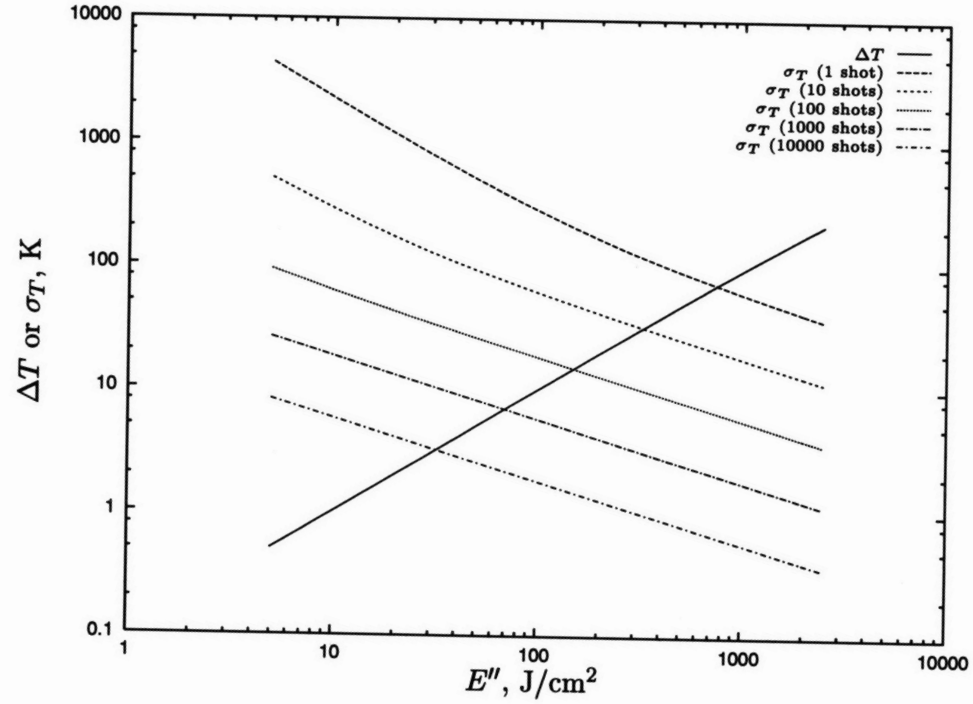

Figure 5.14: Measurement Error and Uncertainty at 297 K and 3.77 atm

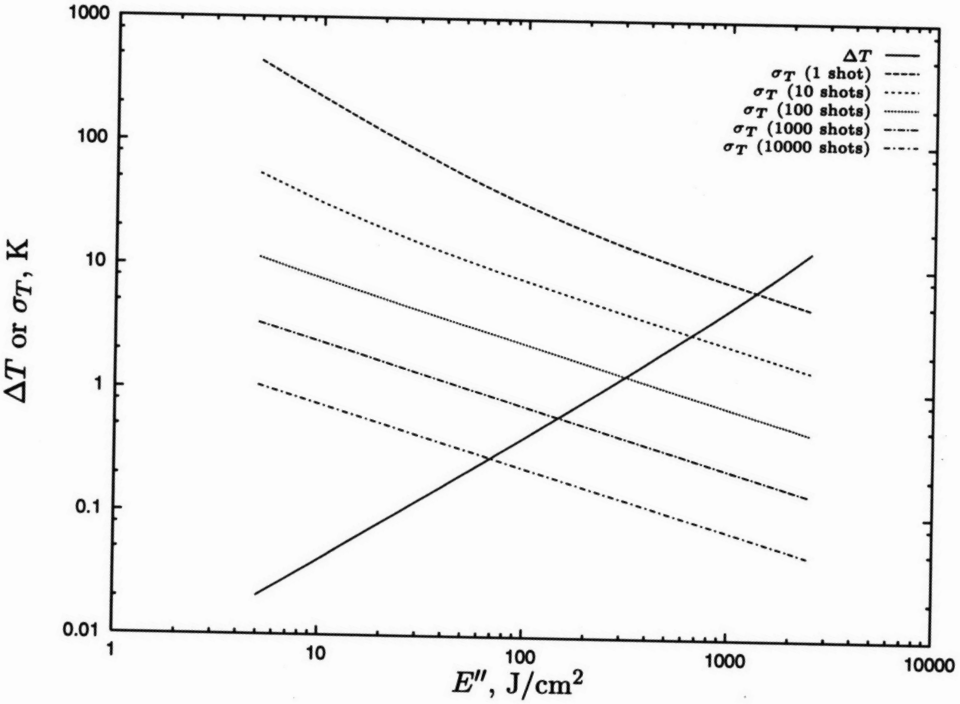

Figure 5.15: Measurement Error and Uncertainty at 428 K and 3.77 atm

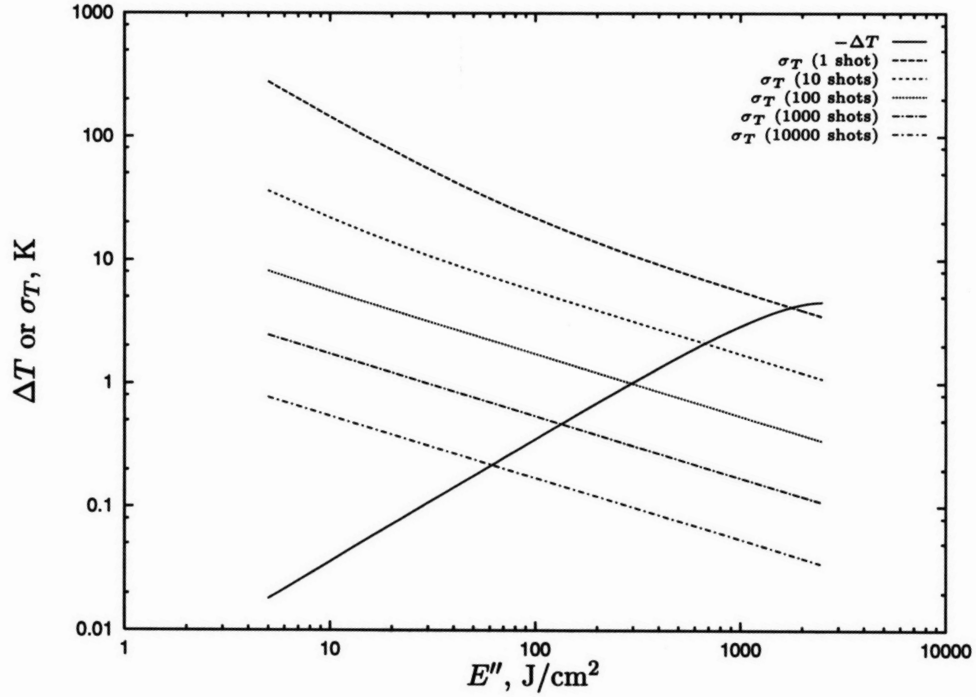

Figure 5.16: Measurement Error and Uncertainty at 507 K and 3.77 atm

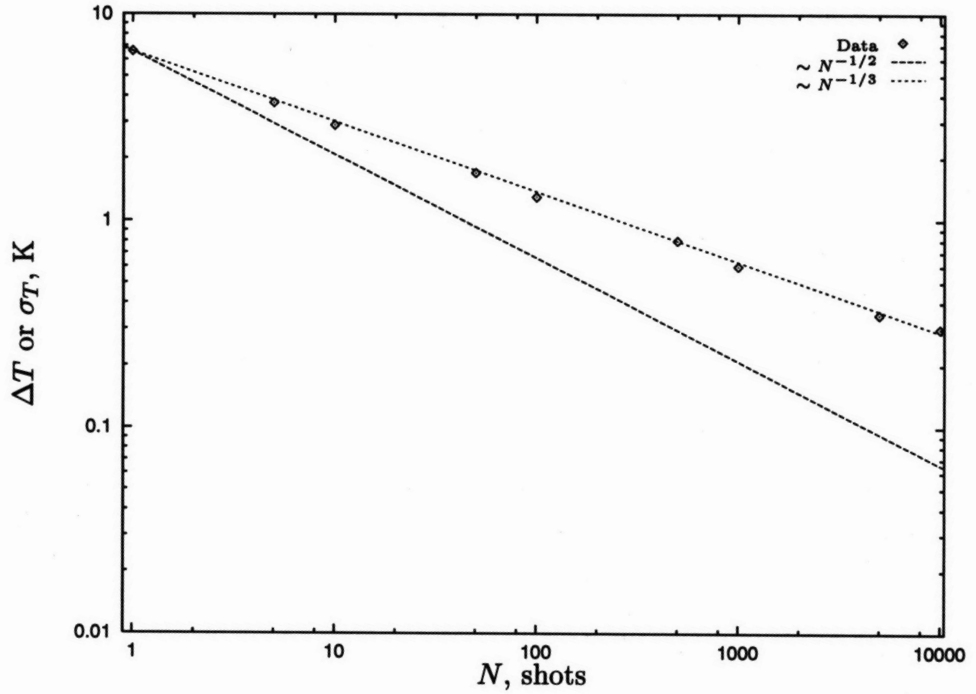

Figure 5.17: Improvement of Measurement Uncertainty with Number of Shots at 428 K and 3.77 atm

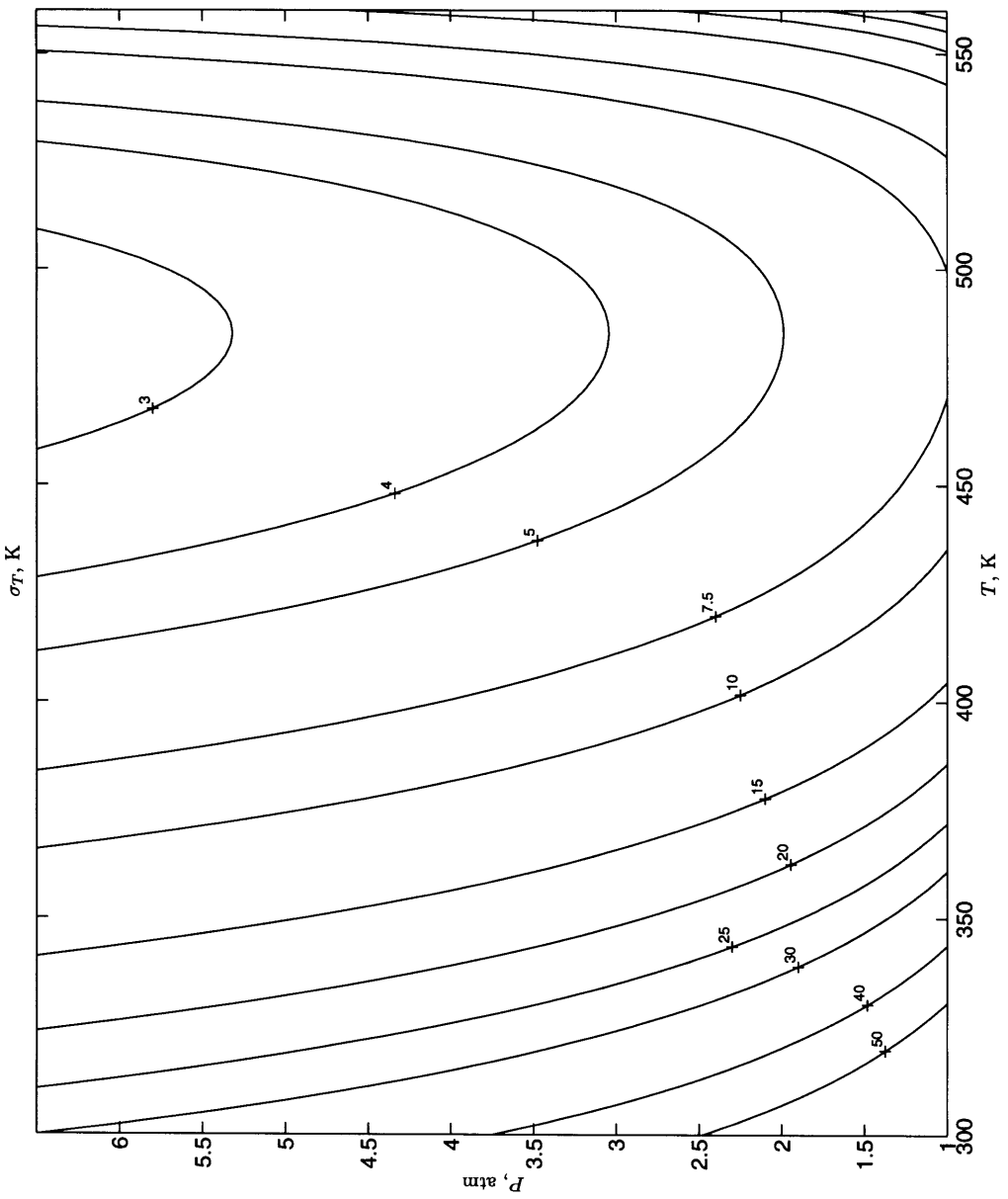

Figure 5.18: Measurement Precision due to a Single Shot Measurement with $E'' = 2000$ J/cm^2

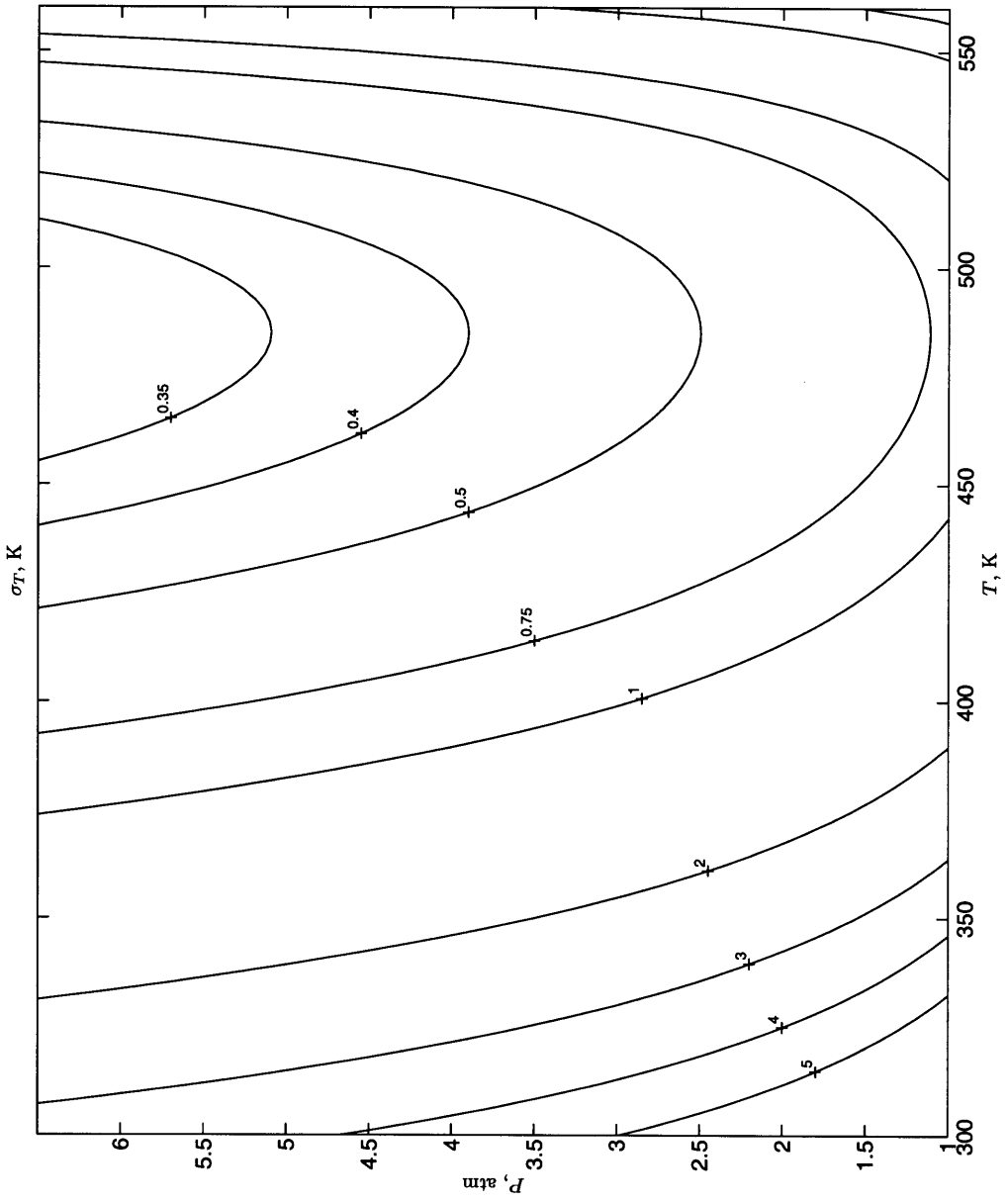

Figure 5.19: Measurement Precision due to a 1000-Shot Measurement with $E'' = 150$ J/cm^2

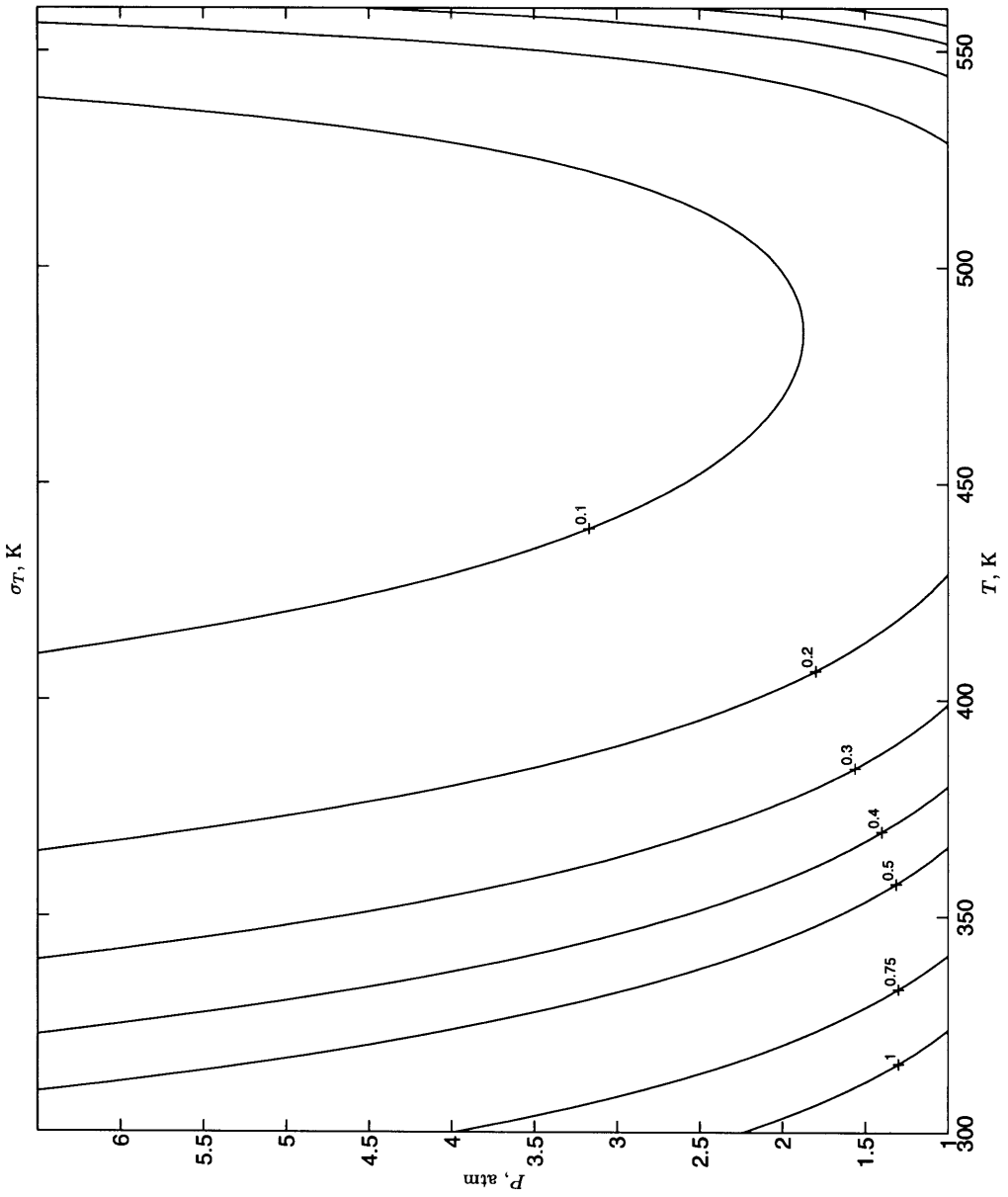

Figure 5.20: Measurement Precision due to a 250000-Shot Measurement with $E'' = 20$ J/cm^2

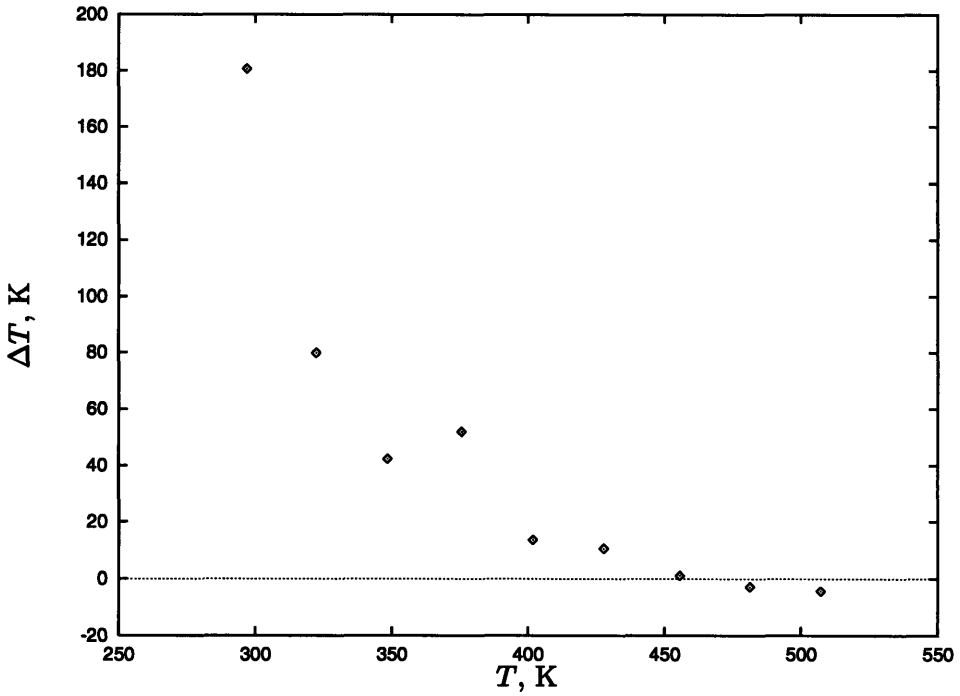

Figure 5.21: Measurement Error due to Nonlinear Phenomena at $E'' = 2000$ J/cm^2

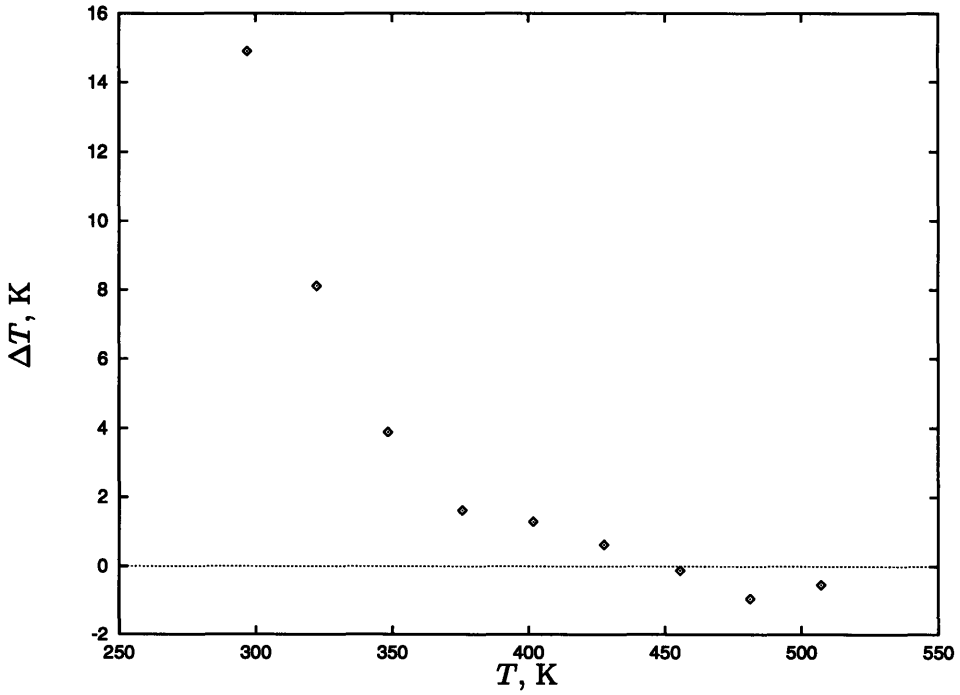

Figure 5.22: Measurement Error due to Nonlinear Phenomena at $E'' = 150$ J/cm^2

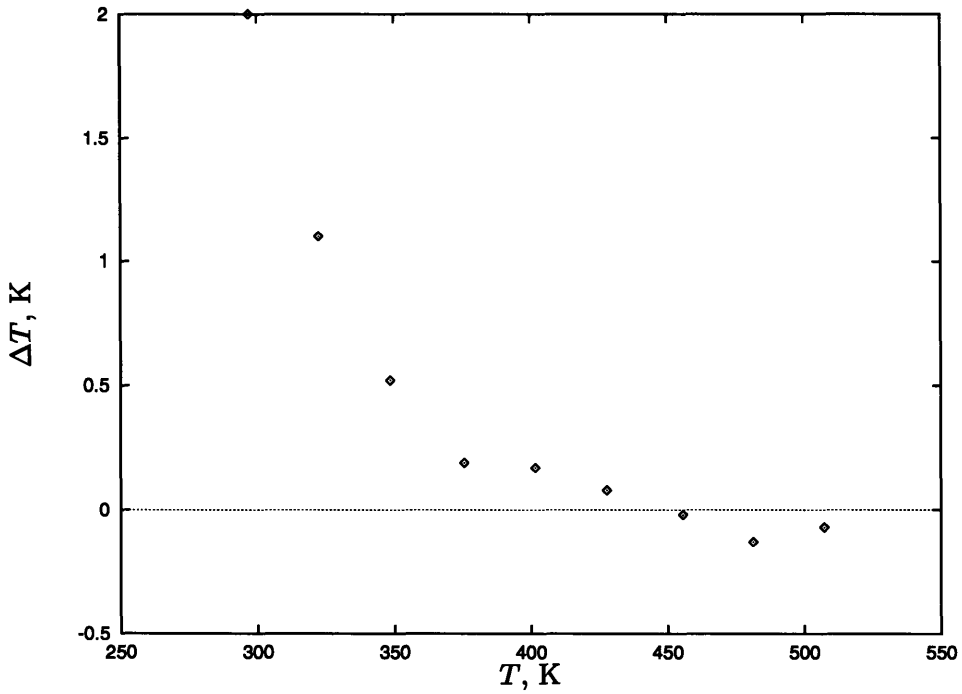

Figure 5.23: Measurement Error due to Nonlinear Phenomena at $E'' = 20$ J/cm^2

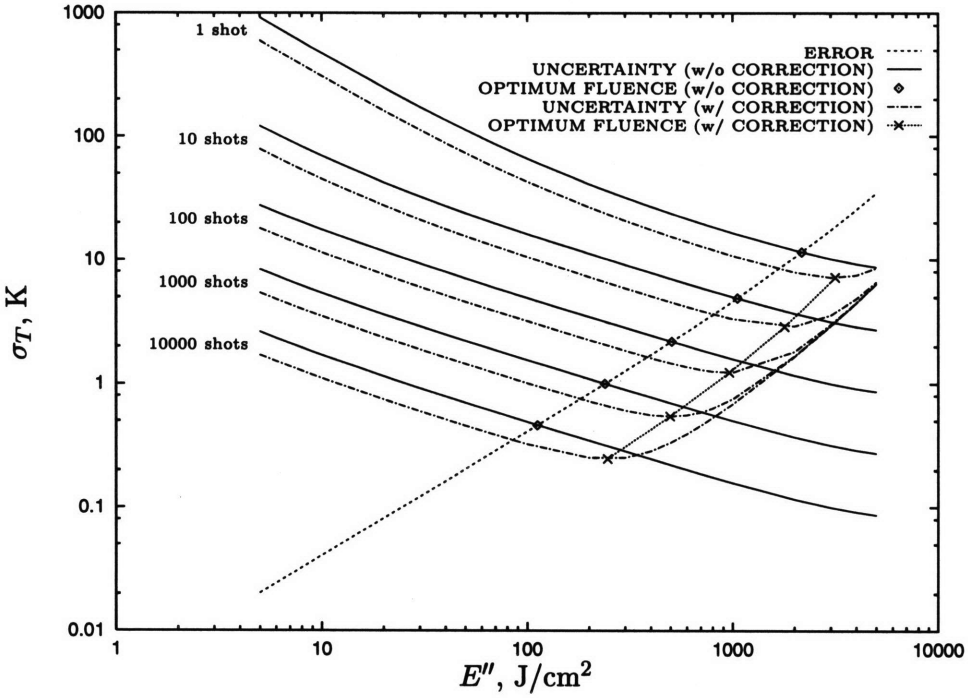

Figure 5.24: Measurement Error and Uncertainty at 428 K and 3.77 atm, with and without Correction for Nonlinear Processes

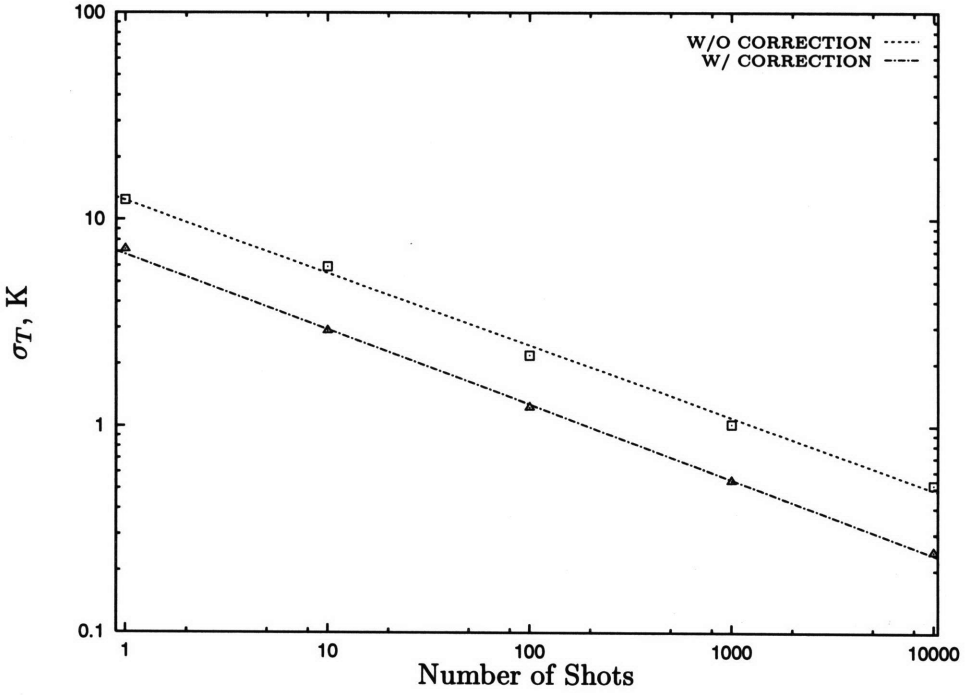

Figure 5.25: Improvement of Measurement Uncertainty with Number of Shots at 428 K and 3.77 atm, with and without Correction for Nonlinear Processes

Chapter 6
Temperature Measurements in High-Speed Flows

Internal flows in turbomachinery are transonic (i. e. Ma $\sim$ 1). Over the 300–550 K temperature range, the flow velocities are of the order of 10^2 m/s. The flow covers 1 mm, the desired spatial resolution, in 10^{-5} s. In order to achieve this spatial resolution, the LIF technique must respond to temperature changes much faster than this time; otherwise, the technique cannot be used for temperature measurements in high-speed turbomachinery.

This chapter considers the impact of vibrational relaxation time on the oxygen LIF temperature measurement technique. Section 6.1 presents spectral data from literature on the vibrational relaxation of oxygen. The measurement errors resulting from the finite relaxation time are described in Section 6.2. Section 6.3 presents experimental data taken on a free jet to support the discussion of the previous sections. The high-speed[1] flow data in literature is re-evaluated in light of the discussion here in Section 6.4. Finally, in Section 6.5, rotational measurement techniques, which avoids the problems with the finite relaxation time, are described and their limitations are pointed out.

6.1 Vibrational Relaxation

When a gas in thermal equilibrium undergoes a sudden change in temperature, it takes some time for the distribution of molecules among quantum states to adjust to the new equilibrium values. Although the rotational distribution adjusts relatively rapidly, vibrational adjustment takes longer. The characteristic time with which vibrational states adjust is known as the vibrational relaxation time.

6.1.1 Vibrational Relaxation Time

Billing and Kolesnick [2] present a theory for computing vibrational relaxation as a result of following reaction:

$$O_2(v) + O_2(v = 0) \rightarrow O(v - 1) + O(v = 0) \tag{6.1}$$

The relaxation time is a function of the vibrational level v. For $v = 1$ level, the relaxation time is approximately 15 ms at 300 K and 1 atm, and 1.3 ms at 500 K and 1 atm. The relaxation time for $v = 2$ level is about 4 times as fast; however, over 300–550 K temperature

[1]This chapter uses the term "high-speed" flows in describing the effect of vibrational relaxation on temperature measurement instead of "compressible flows." This is because the effect originates from the flow speed rather than the compressibility (internal-kinetic energy exchange), and vibrational relaxation may affect temeperature measurement even when compressibility effects are negligible. Compressible flows are, of course, high-speed.

range, the fluorescence signals originating from $v = 1$ level are much stronger than those from $v = 2$ level. Billing and Kolesnick's theoretical data for $v = 1$ agrees with experimental data in literature [10, 12, 13, 17, 18]. Relaxation time scales linearly with the reciprocal of pressure.

In air, 80% of collisions of an O_2 molecule is with a N_2 molecule. According to Parker [18], the main determinant of the vibrational relaxation time for diatomic molecules is the reduced mass of the pair of molecules colliding, with lighter molecules yielding faster relaxation times. If the empirical equation given by Millikan and White [17] is used to extend the data of Billing and Kolesnick to O_2–N_2 collisions, the vibrational relaxation time is found to be about 40% faster than O_2–O_2 collisions. On the other hand, Blackman [3], using high temperature data, suggests that O_2–N_2 collisions are approximately 40% as effective as O_2–O_2 collisions.

In conclusion, using the data of Billing and Kolesnick with the total gas pressure (as opposed to O_2 partial pressure) may be the best estimate of the vibrational relaxation time. The resulting values are probably valid within an order of magnitude. The following formula will be used for the vibrational relaxation time in this study:

$$\tau_v = \frac{15 \text{ ms atm}}{P} \left(\frac{300 \text{ K}}{T} \right)^{4.66} \tag{6.2}$$

6.1.2 Vibrational Temperature

In equilibrium, the distribution of molecules among quantum states is given by Boltzmann distribution, which may be written as follows [22]:

$$\begin{aligned} \frac{N_{(v,J)}}{N} &= \frac{g_{(v,J)} \exp\left(-\dfrac{hcF_{(v,J)}}{kT} \right)}{Q(T)} \\ &= \left[\frac{\exp\left(-\dfrac{hcF_v}{kT} \right)}{Q_v(T)} \right] \left[\frac{g_J \exp\left(-\dfrac{hcF_J}{kT} \right)}{Q_r(T)} \right] \end{aligned} \tag{6.3}$$

The first term in brackets is the fraction of molecules in the v vibrational level, and the second term in brackets is the fraction of molecules in the J rotational level. The second term adjusts to temperature changes almost instantaneously.

Vibrational temperature T_v may be defined as follows:

$$T_v \equiv \frac{k}{hcF_1} \ln\left(\frac{N}{N_{v=1}} \right) \tag{6.4}$$

In other words, the vibrational temperature of a system is the temperature in which a system in equilibrium would have the same vibrational distribution as the system.

Rotational temperature T_r may be similarly defined. However, because of the fast response time (typically 10^{-10} to 10^{-9} s [22]) of the rotational distribution, $T_r = T$. Also, in equilibrium, $T_v = T_r = T$.

The system response to change in temperature is given by

$$\frac{dN_{v=1}}{dt} = \frac{N^*_{v=1} - N_{v=1}}{\tau(T,P)} \tag{6.5}$$

where $N^*_{v=1}$ is the equilibrium population of the $v = 1$ vibrational level obtained from Boltzmann distribution.

In a flow, equation 6.5 becomes

$$\frac{DN_{v=1}}{Dt} = \frac{\partial N_{v=1}}{\partial t} + u_x\frac{\partial N_{v=1}}{\partial x} + u_y\frac{\partial N_{v=1}}{\partial y} + u_z\frac{\partial N_{v=1}}{\partial z} = \frac{N^*_{v=1} - N_{v=1}}{\tau(T,P)} \tag{6.6}$$

so the relaxation distance L is defined as

$$L = u\tau_v \tag{6.7}$$

Figure 6.1 plots the relaxation distance LP as a function of temperature T and Mach number Ma.

6.2 Temperature Error

Assume that a flow in equilibrium goes through a normal shock with a resulting step change in temperature (see Figure 6.2). The rotational distribution of the flow adjusts essentially immediately to the new temperature. However, the vibrational distribution does not change across the shock. Consequently, vibrational temperature T_v just downstream of the shock is equal to the upstream temperature.

Figure 6.3 shows the dependence of the temperature diagnostic ratio (spectral normalization) on both the actual temperature T_r and vibrational temperature T_v. A system in equilibrium would fall along the dashed $T_r = T_v$ line. For $T \gtrsim 300$ K, almost all of the temperature dependence originates from the vibrational distribution, and the LIF technique essentially measures vibrational temperature.

An example is useful in illustrating the impact of the vibrational relaxation time on temperature measurement accuracy. Assume that flow upstream of the normal shock has a Mach number of 1.5, static temperature of 379 K and static pressure of 2.44 atm. Downstream of the shock, the Mach number is 0.684, the static temperature is 500 K and static pressure is 6.0 atm [19]. The flow speed is 307 m/s. From equation (6.2), the characteristic time is 0.23 ms. Just downstream of the shock, the LIF technique measures the vibrational temperature, which is equal to the upstream gas temperature, so the temperature error is 121 K. After 7.1 cm, the distance the flow covers in 0.23 ms, the temperature error is reduced to 36% of the original value or to 44 K. The distance it takes for the temperature error to be reduced to 1.2 K, or 1% of the original value, is 33 cm. This is an enormous distance considering that the blade chord in a typical aeroengine turbine or compressor is a few centimeters.

The actual and vibrational temperatures are plotted in Figure 6.4 using two different scales. The finer scale indicates the desired spatial resolution. Clearly, the long vibrational relaxation time of oxygen prevents us from achieving the specified spatial resolution of 1 mm.

Furthermore, the conditions for the example were chosen so that the temperature and pressure range were at the high end of the specifications of Chapter 1, yielding the fastest response. For example, at 500 K and 1 atm, the 33 cm distance for 1% temperature error is increased to 2.0 m; at 300 K and 6 atm, the same distance[2] becomes 2.7 m. In short, the oxygen LIF technique cannot be used to achieve spatial resolution of 1 mm under such conditions.

Figure 6.1 may be used to determine the applicability of the technique to the high-speed flows. Even if the real vibrational relaxation time is faster by one or even two orders of magnitude, the technique will still not achieve the desired spatial resolution of 1 mm over the temperature and pressure range of interest.

The non-dimensional parameter which indicates when the technique can be used is given by

$$\frac{L_r}{u\tau_v} \gg 1 \tag{6.8}$$

where L_r is the desired resolution.

Figure 6.5 shows the dependence of N_2 Raman normalization as a function of gas temperature and vibrational temperature. Once again, for $T \gtrsim 300$ K, most of the temperature sensitivity originates from the vibrational levels, and this normalization cannot measure temperature accurately either.

For temperatures below 250 K, however, the temperature sensitivity originates completely from the rotational distribution. This is because the upper vibrational levels ($v \geq 1$) are not filled. Consequently, there are no LIF signals originating from vibrational levels and the vibrational relaxation time does not impact the measurements.

6.3 Experimental Data

Experiments were run on the free jet facility in the MIT Gas Turbine Laboratory to demonstrate this behavior. A schematic of the facility is shown in Figure 6.6. The jet issued from a contoured, converging nozzle with a diameter of 10 mm to ambient air.

Figure 6.7 shows the flow structures expected from the jet for three major flow regimes. For $P_t/P \leq 1.89$, the nozzle is unchoked, and the nozzle exit pressure is equal to the ambient pressure. For $P_t/P > 1.89$, the nozzle becomes choked. Consequently, the nozzle exit pressure is higher than the ambient pressure and the jet adjusts to the ambient pressure through a series of expansion and compression waves. If the pressure ratio is increased further ($P_t/P \gtrsim 3.5$), the compression waves, instead of meeting at the jet axis, are connected by a normal shock, called a "Mach disk." For all three regimes, viscous mixing regions are

[2]This calculation assumes that the Mach number downstream of the shock remains 0.684, so the flow velocity at 300 K is 240 m/s.

indicated; in all cases, the LIF measurements are performed in the inviscid core along the centerline near the nozzle exit. Detailed discussions of the structure of the free jet may be found in Adamson and Nicholls [1], and in Dash et. al. [6,7].

In the first experiment, the jet stagnation pressure was 5.5 atm and the jet stagnation temperature was 330 K. A computational code[3] was used to predict the pressure, temperature and Mach number distributions along the jet axis. The results are shown in Figure 6.8. Note the sudden drop in Mach number between 15 mm and 20 mm due to the Mach disk.

The transit time of oxygen molecules through the nozzle and across the measured portion of the jet is small compared to the vibrational relaxation time. Therefore, the vibrational temperature of oxygen remains "frozen" at approximately the stagnation temperature. The resulting temperature diagnostic ratio $\mathcal{R}$ which would be measured by the oxygen LIF temperature is shown in Figure 6.9.

Figure 6.10 compares the measured temperature diagnostic ratio with that obtained from Figure 6.9. The profile of the measured ratio matches the theoretical value. Although the measured ratios are slightly lower than the theoretical value, this deviation is reasonable considering the approximations made in computing the theoretical dependence of Figure 6.9[4].

Figure 6.11 shows the observed signal level during the measurements. For a given laser energy, the signal level is proportional to pressure. Note the sharp increase in signal level across the Mach disk between 15–20 mm[5].

In another experiment, the temperature was measured at $x = 5$ mm using the oxygen LIF technique. The pressure ratio of the jet was varied from 1.24, corresponding to an isentropic Mach number of 0.56, to 4.31, corresponding to an isentropic Mach number of 1.52. Because the air supplied to the free jet was heated with a constant power heater, the stagnation temperature of the free jet decreased from 412 K to 342 K with increasing pressure ratio.

The measured temperature, normalized by the stagnation temperature, is plotted as a function of jet pressure ratio in Figure 6.12. The nondimensionalized temperature dependence obtained from computational model is shown as COMPUTATIONAL. The other two curves are obtained from Figure 6.3 and the calibration equation of Chapter 4. In both cases, the temperature diagnostic ratio $\mathcal{R}$ is computed from the map of Figure 6.3 and the measured temperature is then determined using the calibration equation. For the EQUILIBRIUM curve, the vibrational temperature is assumed equal to the static gas temperature obtained from the computational model; for the VIB. FROZEN curve, the vibrational temperature is assumed equal to the measured stagnation pressure.

For temperatures above 300 K, the O_2 LIF measurement does not pick up the decrease in the nondimensionalized temperature predicted by both the computational model and the equilibrium model. The discrepancy between the measured temperatures and the vibrationally frozen curves may be the result of several approximations. First, as discussed

[3]For details of this code, see Bryanston-Cross and Epstein [4, pp. 255–259]. This paper refers to this code as the "Giles" code after its author.

[4]The technique was not calibrated as a function of vibrational and rotational temperatures.

[5]The localized increase in signal level between 23–25 mm is probably due to laser energy variations. The absolute signal levels were not normalized for laser energy.

above, the technique was calibrated only for equilibrium conditions, and any extension to the nonequilibrium conditions could not be verified by experimental measurements. Second, the vibrational temperature may not be equal to the stagnation temperature as assumed. As the pressure ratio increases, the flow speed in the nozzle increases (for subsonic flows, $P_t/P < 1.89$), resulting in a decrease in the residence time, and the gas temperature in the nozzle decreases, resulting in a significant increase in the vibrational relaxation time (note the $\tau \sim T^{-4.66}$ dependence in equation 6.2). Consequently, as the pressure ratio increases, the actual vibrational temperature may change from a value close to the actual static temperature (equilibrium conditions) to a value close to the stagnation temperature (vibrationally frozen flow). This is very similar to the behavior shown in Figure 6.12. Finally, since the free jet is not thermally insulated, heat loss to the environment may contribute to the discrepany. As the pressure ratio of the jet increases, the stagnation temperature of the jet, which drives the heat loss, decreases and the mass flow increases. Consequently, the effects of heat loss become less important with increasing pressure ratio and the measured temperature approaches the vibrationally frozen temperature as shown in Figure 6.12.

Since the technique was neither designed nor calibrated for gas temperatures below 300 K, the measured temperature is not valid for this temperature range. As Figure 6.12 shows, even at equilibrium conditions, the technique does not measure the true gas temperature; this discrepancy results from the $\mathcal{R}(T)$ curve not being monotonic for temperatures below 300 K. This behavior is also apparent in Figure 6.3 along the $T = T_v$ equilibrium line.

Unfortunately, the heater size in the GTL free jet facility limits the experiments which may be performed to verify the vibrational temperature behavior. The nozzle size is determined by the spatial resolution of the experimental apparatus; the nozzle diameter should be larger than the 1-mm resolution, hence the 1-cm nozzle used in these experiments. For a given pressure ratio, the heater size now limits the stagnation temperature. For example, in order to produce a Mach disk, the pressure ratio of the jet must exceed 3.5. At this pressure ratio, the stagnation temperature of the jet is 350 K and the temperature just ahead of the Mach disk is 190 K. Ideally, this temperature should be 300 K, the lower end of the calibration range. The required stagnation temperature is then 553 K. Assuming a heater inlet temperature of 300 K and neglecting heat loss to the environment, the heater power must then be increased by a factor of 5.

In conclusion, the experimental data presented in this section supports the conclusion that the finite vibrational life of oxygen does not allow accurate temperature measurements in high-speed flows.

6.4 Evaluation of Literature Data

Although Grinstead and Laufer [11] briefly pointed out the possible problem with oxygen LIF temperature measurements caused by the long vibrational relaxation time of oxygen molecules in a conference paper, this fact is not widely appreciated in the engineering community[6]. For example, papers by Smith, Price and Williams [20,21], published a few years

[6]In their paper, Grinstead and Laufer [11] state "vibrational nonequilibrium distributions in O_2 may persist up to 50 μs and 5 mm downstream of the point where it was induced," citing a study by Miles et.

after Grinstead and Laufer, state that a two-line oxygen LIF temperature measurement, where the two transitions originate from $v'' = 0$ and $v'' = 1$ levels respectively, as a promising method for temperature measurement in supersonic and hypersonic flows in the 300–500 K temperature range.

Although no paper, with the one exception mentioned above, discuss the impact of vibrational relaxation time on the oxygen LIF temperature measurement technique, two studies do indeed present data from high-speed flows. This section evaluates these studies in light of the discussion of this chapter.

In a 1991 paper, Fletcher and McKenzie [8, 9] use the oxygen LIF technique with N_2 Raman normalization on a Mach 2 flow boundary layer. The stagnation temperature is 290 K and the static freestream gas temperature at the measurement location is 157 K. As these researchers use a narrowband laser to excite a single transition from the $v'' = 0$ vibrational level, their LIF signals do not contain any signal from higher vibrational levels. Consequently, these researchers avoid the problems with the slow vibrational relaxation times.

In an earlier 1987 paper, Cohen et. al. [5] publish planar oxygen LIF (O_2 PLIF) data taken on a slightly underexpanded supersonic free jet. These researchers state that their results are consistent with theoretical calculations. A critical examination of their results, however, demonstrates that their results are in fact inconsistent with the theoretical calculations.

Figure 6.13 is the fluorescence signal along the axis of of jet obtained from this paper. The nozzle (orifice) diameter is 1.65 mm, and the imaged region is 6 mm long. The jet pressure ratio was 2.5, and the stagnation temperature was 1050 K. Figure 6.14 shows the results of the computational calculations for this geometry and flow conditions.

In their paper, Cohen et. al. simply compare the relative magnitudes of the first peak to the first valley, and conclude that these values "compare favorably" with theoretical predictions. They attribute the first peak to the high T, high P and low Ma feature and the first valley to the low T, low P and high Ma feature.

However, comparison of Figure 6.13 with Figure 6.14 indicates that this is in error. The highest temperature and pressure is at the nozzle exit; the theoretical model would expect the highest signal to be in this region. However, in Figure 6.13, the nozzle exit has the lowest signal. In fact, comparison of the two figures reveal that the peaks and valleys are reversed. This observation suggests that the analysis of Cohen et. al. based on this anomalous data is suspect. Unfortunately, due to the limited amount of data given in this paper, the source of this anomaly cannot be determined.

On the other hand, a 1989 study by Miles et. al. [15, 16], although not a temperature measurement experiment, supports the conclusion that the long vibrational lifetime of the oxygen molecules will affect temperatures measured by the oxygen LIF technique. In this study, the authors use "oxygen flow tagging" to study velocity profiles in a supersonic free

al. [14] to support their point. Examination of that study indicates that the vibrationally excited molecules are easily detectable at 50μs and 5 mm downstream, but these are not the limiting time or distance. In fact, Miles et. al. clearly state that the accuracy of the measurement will increase if the time and distance between production and detection is increased.

jet. The researchers tag the flow by promoting oxygen molecules to the $v = 1$ vibrational level. Downstream, these tagged molecules are probed by an ArF laser. The time and distance between tagging and probing yields the velocity measurement. The long vibrational lifetime of oxygen, which poses a problem for temperature measurement, makes this technique possible.

6.5 Rotational Measurement Technique

Because of the long relaxation time, any technique which relies on the vibrational distribution of the oxygen molecules cannot be used in high-speed flows. However, techniques which rely on the rotational distribution may be used since the rotational relaxation time is 10^{-10} to 10^{-9} s, corresponding to a relaxation distance of 10^{-5} to 10^{-4} mm at a flow speed of 100 m/s. This section discusses these techniques and their limitations.

Spectral normalization, discussed in Chapter 2, relies on the vibrational distribution of oxygen molecules, and may not be used in high-speed flows. The only alternative is N_2 Raman normalization.

In rotational temperature measurement, a perfect narrowband laser (locking efficiency equal to unity) is tuned to a rotational transition originating from the $v'' = 0$ ground vibrational level. For low temperatures ($T \ll \Theta_v$, $\Theta_v = 2270$ K is the characteristic temperature for vibration for O_2 [22]), the population of this ground vibrational level is independent of vibrational temperature. Consequently, the technique measures the rotational temperature, which is equal to the static temperature.

Figure 6.15 shows the spectral absorption coefficient for transitions originating from $v'' = 0$–2 vibrational levels in the tuning range of the ArF laser. The rotational transitions from the $v'' = 0$ level are labeled. In addition, the spectral distribution of a narrowband ArF laser is shown in this figure.

In order to avoid contamination by signals which are sensitive to vibrational temperature, the chosen $v'' = 0$ transition must not overlap any rotational transitions originating from $v'' = 1$ and 2 excited vibrational levels. Examination of Figure 6.15 indicates that only two $v'' = 0$ transitions, namely $P(15)$ and $P(19)$, satisfy this requirement.

The theoretical temperature measurement uncertainty resulting from using each of these two rotational transitions are plotted in Figure 6.16 and are compared to the uncertainty of broadband measurements obtained from Figure 2.8. The peak in the $P(15)$ curve results from the "null" temperature where the technique is not sensitive to temperature (i. e. $d\mathcal{R}/dT = 0$); it also indicates that the $\mathcal{R}(T)$ curve is not monotonic.

At 425 K, the temperature uncertainty of the better rotational technique, namely $P(19)$, is about ten times higher than the uncertainty of the better broadband technique, namely spectral normalization. Therefore, to achieve the same precision as the broadband technique, the number of shots must be increased by a factor of 100.

In addition, an accurate temperature measurement using rotational technique requires stable, repeatable laser locking efficiency equal to unity. As discussed in Chapter 2, any change in the locking efficiency results in an error in the measured temperature. Furthermore, any decrease from a locking efficiency of unity will result in contamination by signals

which are sensitive to vibrational temperature; as a result, the measured temperature will depend on not only the static temperature but also the vibrational temperature. Commericially available ArF lasers do not meet these requirements; consequently, narrowband temperature measurements are not feasible.

6.6 Summary

For high-speed flows, the accuracy of the oxygen LIF temperature measurement technique is limited by the long vibrational relaxation time of oxygen molecules since the technique measures the vibrational temperature. For temperature and pressure ranges of interest, the distance required for the temperature error to be reduced to 1% of the temperature rise across a shock ranges from 30 cm to 3 m. A spatial resolution of 1 mm is impossible with this technique.

Measurements on a supersonic free jet support the conclusions of this chapter. The literature data involving high-speed flows can be either explained in terms of temperature ranges or shown to be erroneous.

For temperatures below 250 K, the oxygen LIF technique does not excite any signals from higher vibrational levels and may be used in high-speed flows. Although rotational temperature measurements with narrowband lasers theoretically avoid the problem of long vibrational relaxation time, they are not feasible with current commericial ArF lasers, whose locking efficiencies have neither the level nor the stability required for such measurements.

References

[1] ADAMSON, JR., T. C., AND NICHOLLS, J. A. On the Structure of Jets From Highly Underexpanded Nozzles into Still Air. *Journal of the Aero/Space Sciences 26* (January 1959), 16–24.

[2] BILLING, G. D., AND KOLESNICK, R. E. Vibrational Relaxation of Oxygen. State to State Rate Constants. *Chemical Physics Letters 200*, 4 (December 1992), 382–386.

[3] BLACKMAN, V. Vibrational relaxation in oxygen and nitrogen. *Journal of Fluid Mechanics 1* (1956), 61–85.

[4] BRYANSTON-CROSS, P. J., AND EPSTEIN, A. The Application of Sub-Micron Partical Visualization for PIV (Particle Image Velocimetry) at Transonic and Supersonic Speeds. *Progress in Aerospace Sciences 27* (1990), 237–265.

[5] COHEN, L. M., LEE, M. P., PAUL, P. H., AND HANSON, R. K. Two-Dimensional Imaging Measurements in Supersonic Flows Using Laser-Induced Fluorescence of Oxygen. *AIAA Paper AIAA-87-1527* (1987).

[6] DASH, S. M., AND WOLF, D. E. Interactive Phenomena in Supersonic Jet Mixing Problems, Part I: Phenomenology and Numerical Modeling Techniques. *AIAA Journal 22*, 7 (July 1984), 905–913.

[7] DASH, S. M., AND WOLF, D. E. Interactive Phenomena in Supersonic Jet Mixing Problems, Part II: Numerical Studies. *AIAA Journal 22*, 10 (October 1984), 1395–1404.

[8] FLETCHER, D., AND MCKENZIE, R. Measurements of Density, Temperature, and Their Fluctuations in Turbulent, Supersonic Flow Using UV Laser Spectroscopy. *Sixth International Symposium on Applications of Laser Techniques to Fluid Mechanics* (July 1992).

[9] FLETCHER, D., AND MCKENZIE, R. Single-Pulse Measurement of Density and Temperature in a Turbulent, Supersonic Flow Using UV Laser Spectroscopy. *Optics Letters 17*, 22 (November 1992), 1614–1616.

[10] FREY, R., LUKASIK, J., AND DUCUING, J. Tunable Raman Excitation and Vibrational Relaxation in Diatomic Molecules. *Chemical Physics Letters 14*, 4 (June 1972), 514–517.

[11] GRINSTEAD, J. H., AND LAUFER, G. Requirements for Temperature Measurements in Nonequilibrium Flows Using Laser-Induced O_2 Fluorescence. In *International Congress on Instrumentation in Aerospace Simulation Facilities (ICIASF)* (1991), pp. 262–269.

[12] HANSEN, C. F., AND PEARSON, W. E. Three-Dimensional Model of Collision-Induced Vibrational Transitions in Homonuclear Diatomic Molecules. *Journal of Chemical Physics 53*, 9 (November 1970), 3557–3567.

[13] HOLMES, R., SMITH, F. A., AND TEMPEST, W. Vibrational Relaxation in Oxygen. *Proceedings of the Physical Society 81* (1963), 311–319.

[14] MILES, R., COHEN, C., CONNORS, J., HOWARD, P., HUANG, S., ET AL. Velocity Measurements by Vibrational Tagging and Fluorescence Probing of Oxygen. *Optics Letters 12*, 11 (November 1987), 861–863.

[15] MILES, R. B., CONNORS, J., MARKOVITZ, E., HOWARD, P., AND ROTH, G. Instantaneous Supersonic Velocity Profiles in An Underexpanded Sonic Air Jet by Oxygen Flow Tagging. *Physics of Fluids: A. Fluid Dynamics 1*, 2 (February 1989), 389–393.

[16] MILES, R. B., CONNORS, J. J., MARKOVITZ, E. C., HOWARD, P. J., AND ROTH, G. J. Instantaneous Profiles and Turbulence Statistics of Supersonic Free Shear Layers by Raman Excitation plus Laser-Induced Electronic Fluorescence (RELIEF) Velocity Tagging of Oxygen. *Experiments in Fluids 8* (1989), 17–27.

[17] MILLIKAN, R. C., AND WHITE, D. R. Systematics of Vibrational Relaxation. *Journal of Chemical Physics 39*, 12 (December 1963), 3209–3213.

[18] PARKER, J. G. Effect of Several Light Molecules on the Vibrational Relaxation Time of Oxygen. *Journal of Chemical Physics 34*, 5 (May 1961), 1763–1772.

[19] SHAPIRO, A. H. *The Dynamics and Thermodynamics of Compressible Fluid Flow*, vol. I. John Wiley & Sons, New York, NY, 1953.

[20] SMITH, M., PRICE, L., AND WILLIAMS, W. Laser-Induced Fluorescence Diagnostics Using a Two-Line Excitation Method. *AIAA Journal 31*, 3 (March 1993), 478–482.

[21] SMITH, M. S., PRICE, L. L., AND WILLIAMS, W. D. Laser-Induced Fluorescence Diagnostics Using a Two-Line Excitation Method. *AIAA Paper AIAA-92-0512* (1992).

[22] VINCENTI, W. G., AND KRUGER, JR., C. H. *Introduction to Physical Gas Dynamics.* Robert E. Krieger Publishing Company, Malabar, FL, 1965.

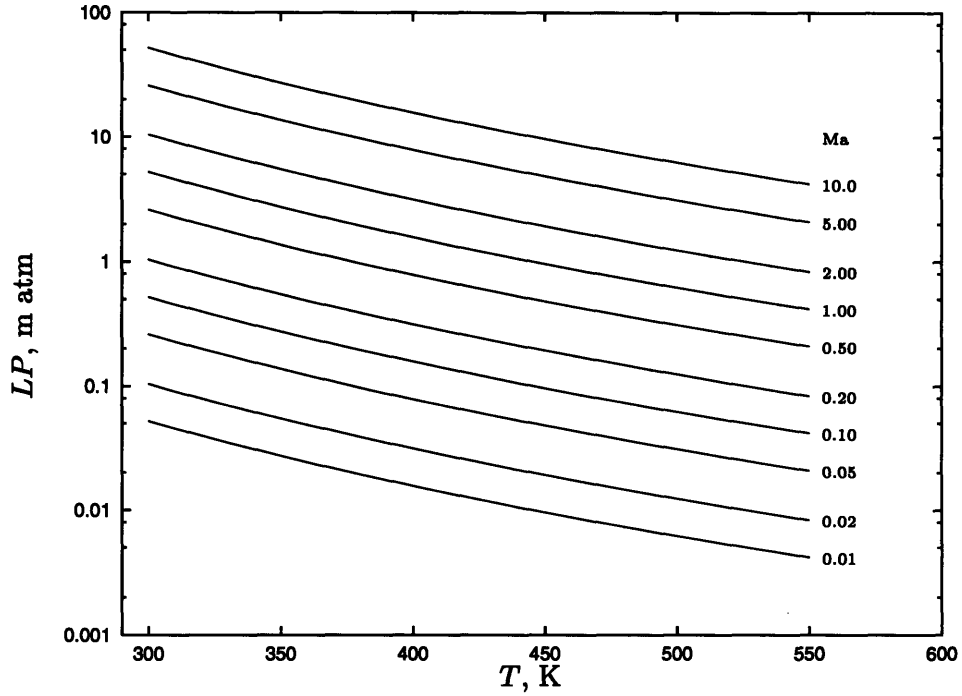

Figure 6.1: Dependence of Relaxation Distance on Temperature and Mach Number

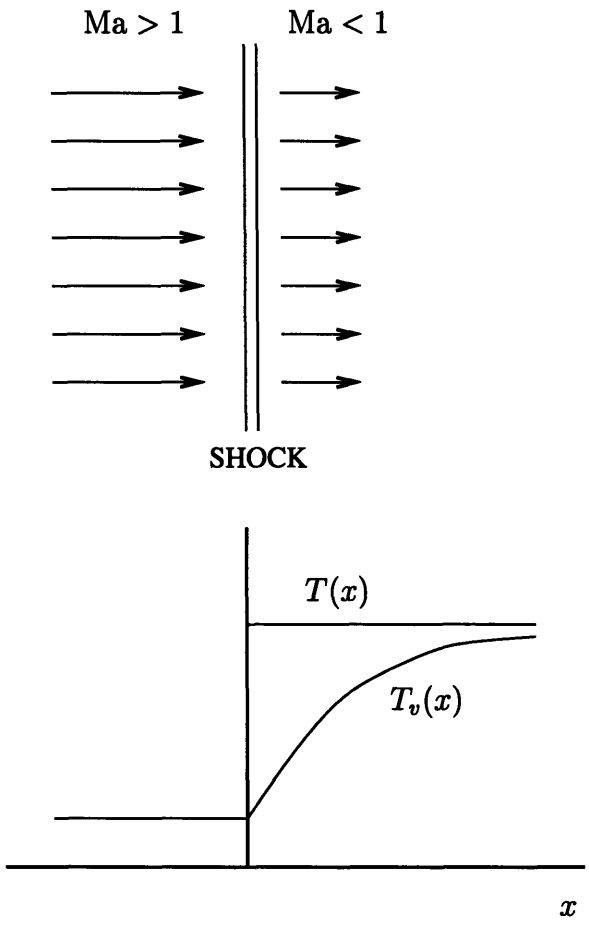

Figure 6.2: Flow Through a Normal Shock and Resulting Temperature Error

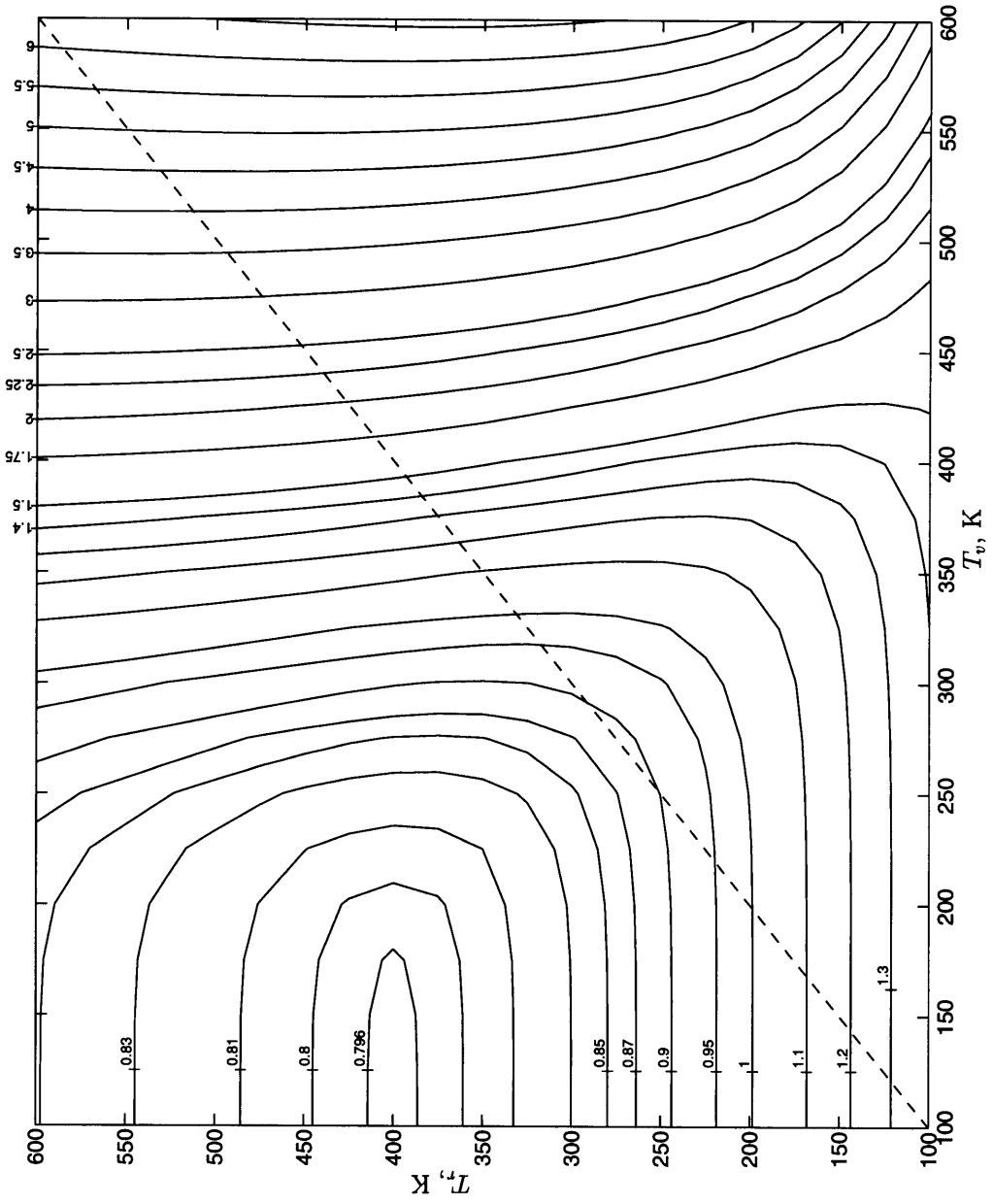

Figure 6.3: Dependence of Temperature Diagnostic Ratio $\mathcal{R}$ (Spectral Normalization) on Gas Temperature and Vibrational Temperature

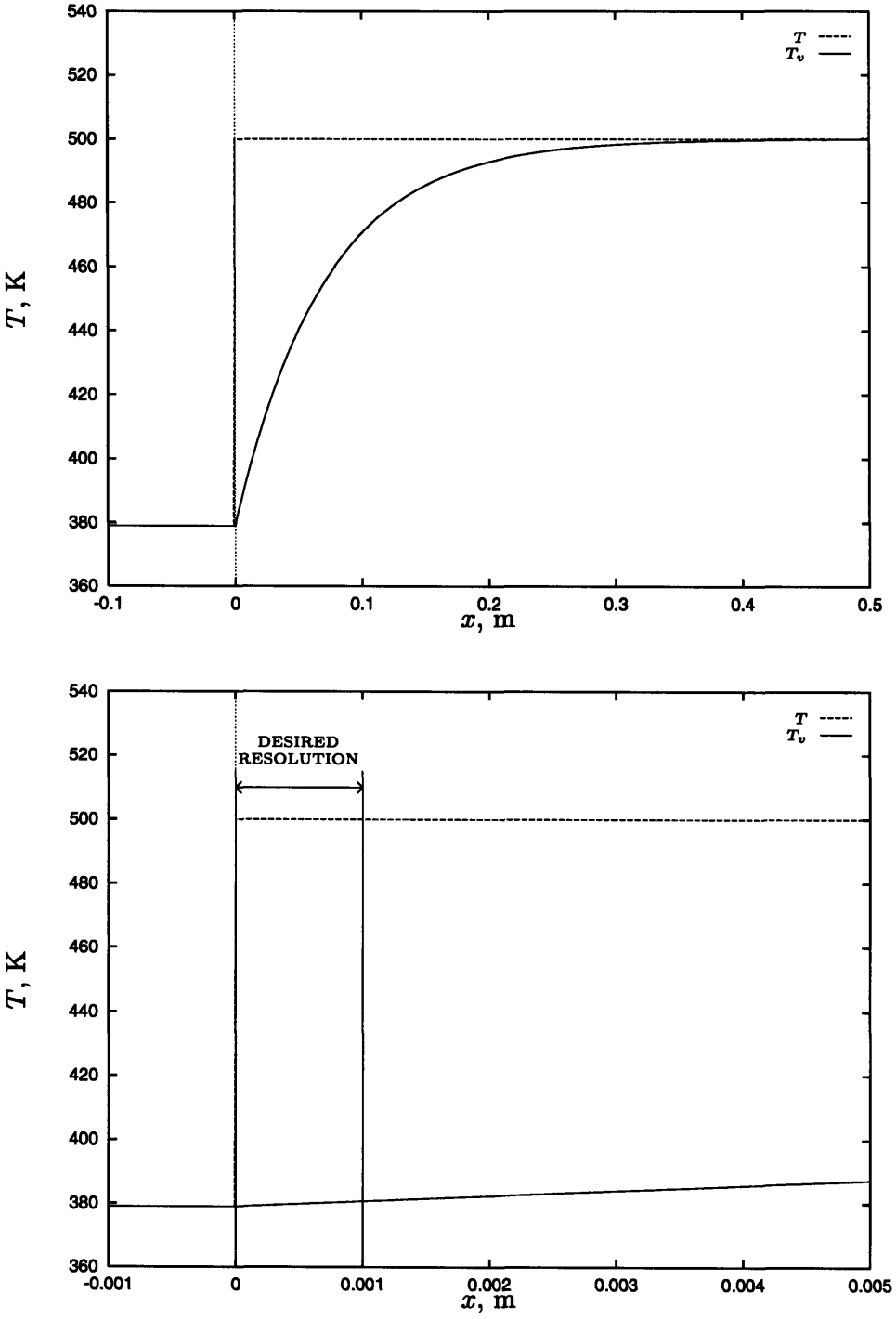

Figure 6.4: Actual and Vibrational Temperature Downstream of a Normal Shock

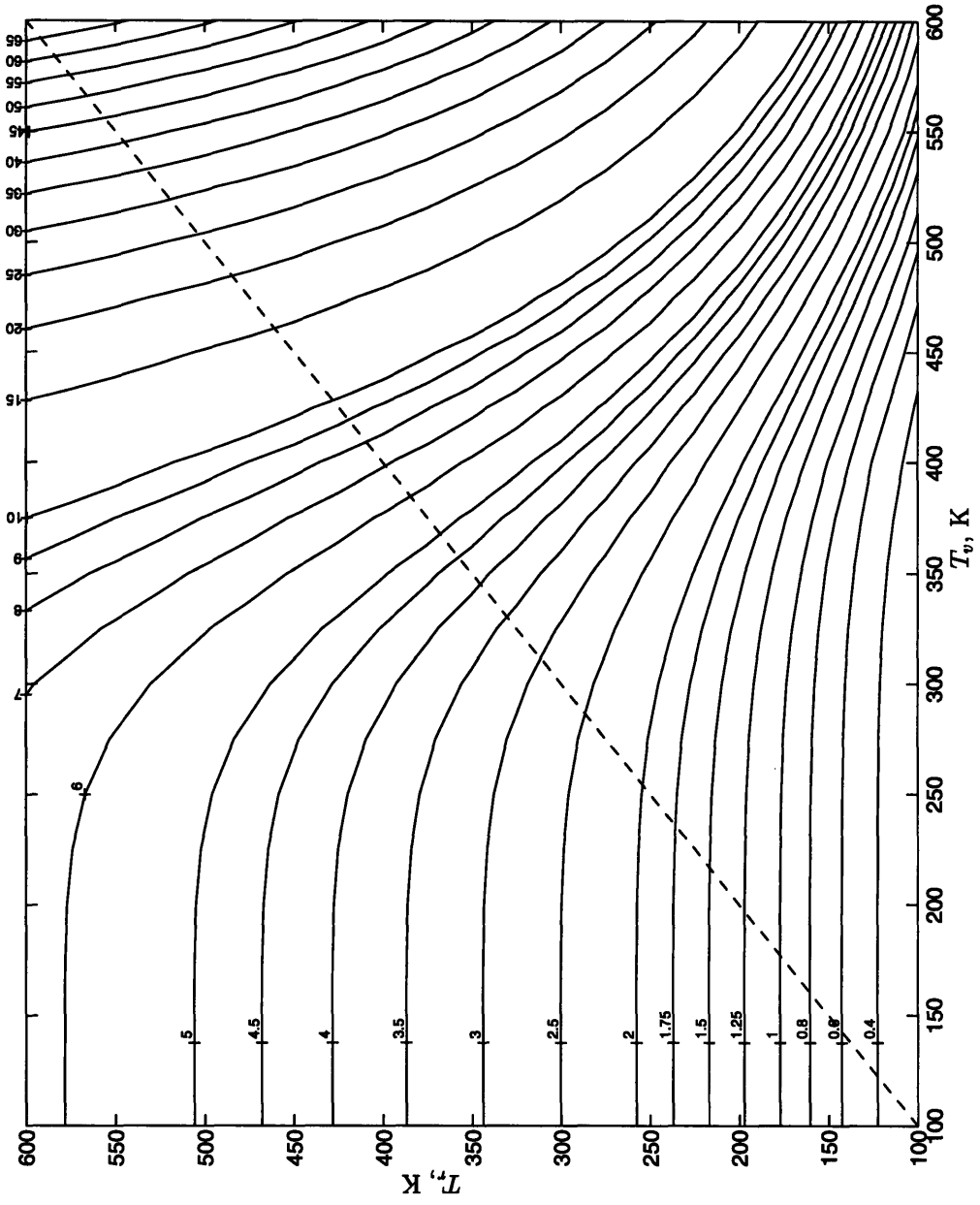

Figure 6.5: Dependence of Temperature Diagnostic Ratio $\mathcal{R}$ (N_2 Raman Normalization) on Gas Temperature and Vibrational Temperature

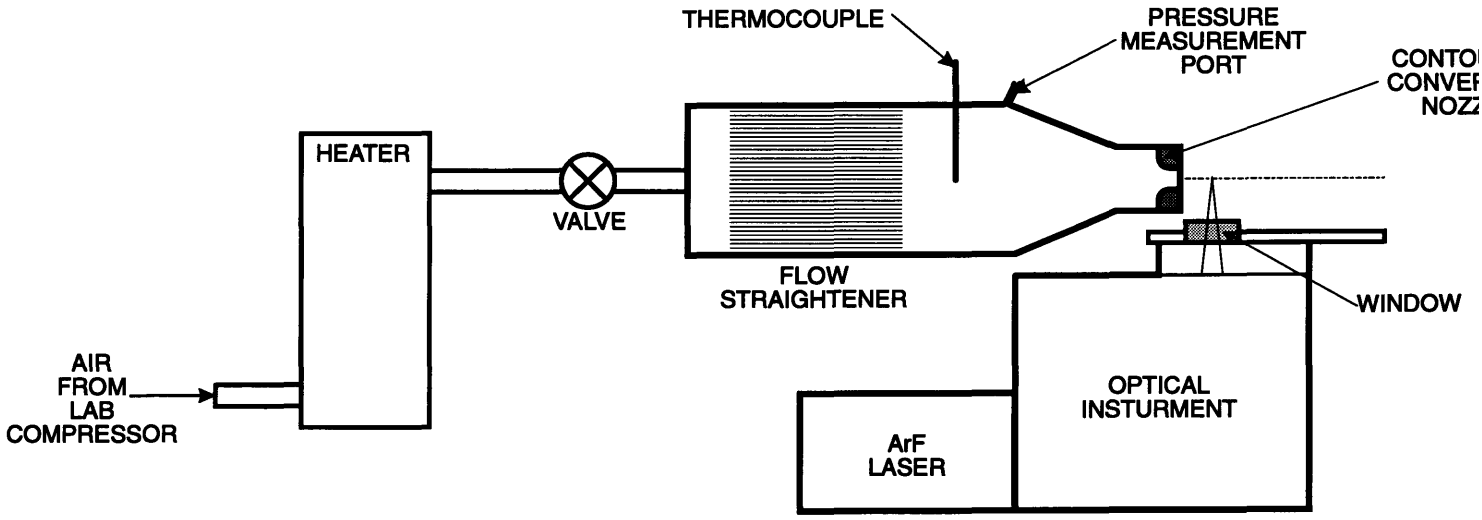

Figure 6.6: Schematic of the Free Jet Facility

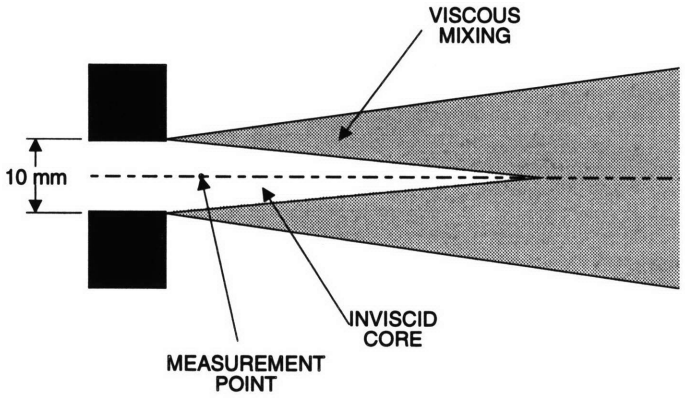

(a) $P_t/P < 1.89$ (Subsonic)

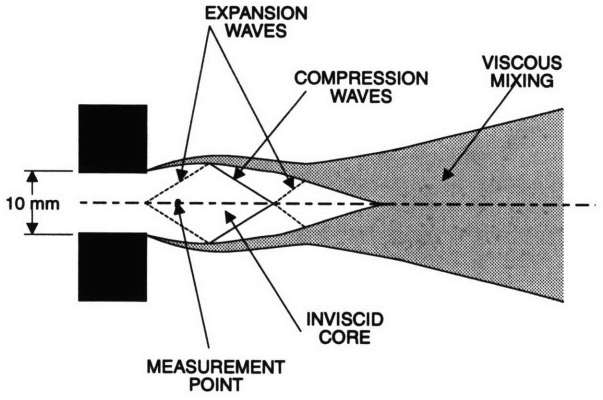

(b) $1.89 < P_t/P \lesssim 3.5$ (Supersonic)

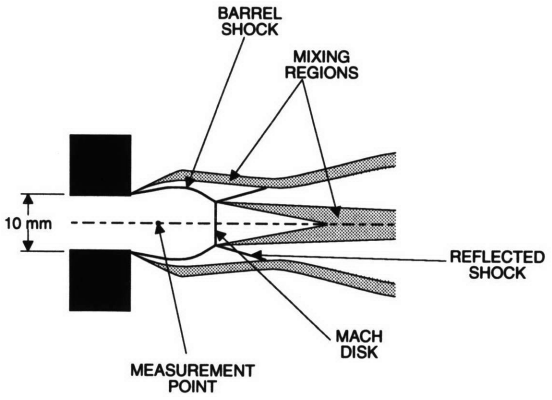

(c) $P_t/P \gtrsim 3.5$ (Supersonic)

Figure 6.7: Free Jet Structure

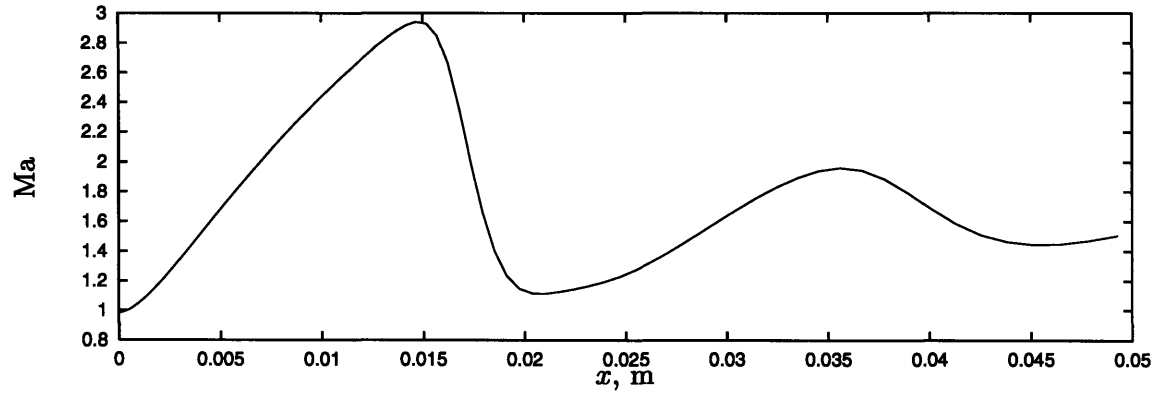

(a) Mach Number

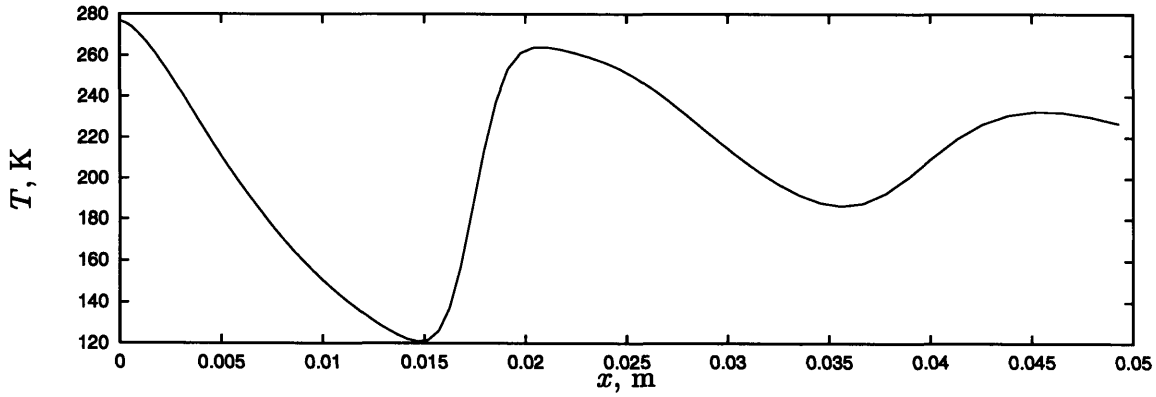

(b) Temperature

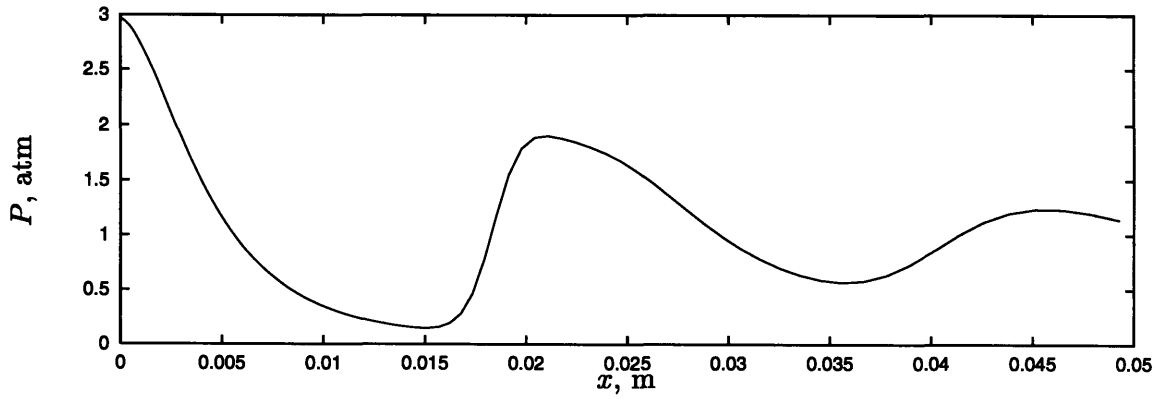

(c) Pressure

Figure 6.8: Computational Profiles for the Free Jet for $P_t/P = 5.5$

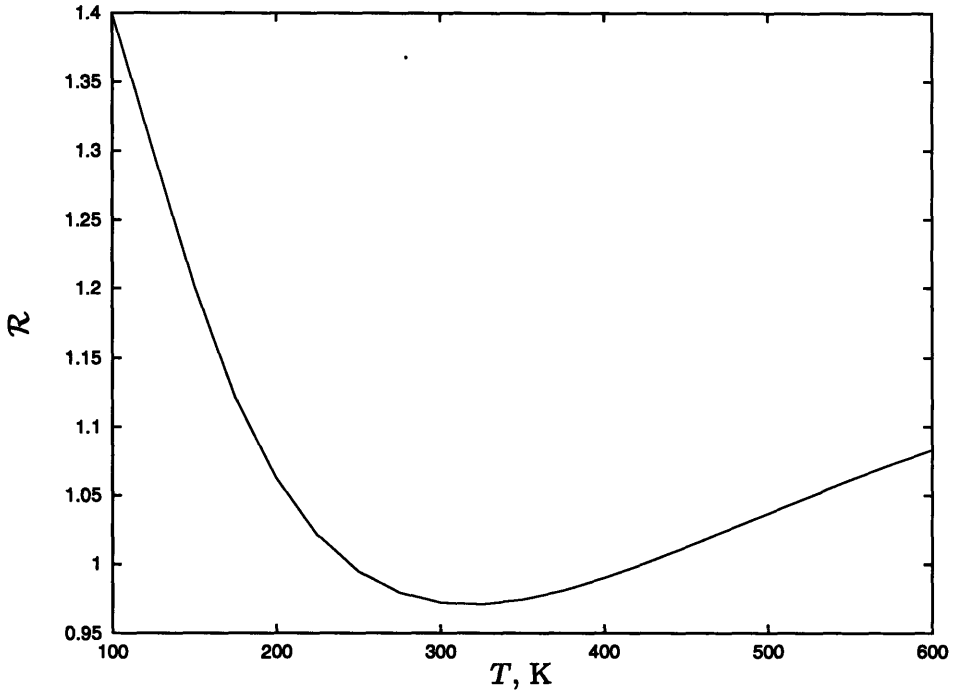

Figure 6.9: Temperature Diagnostic Ratio at Vibrational Temeprature of 325 K

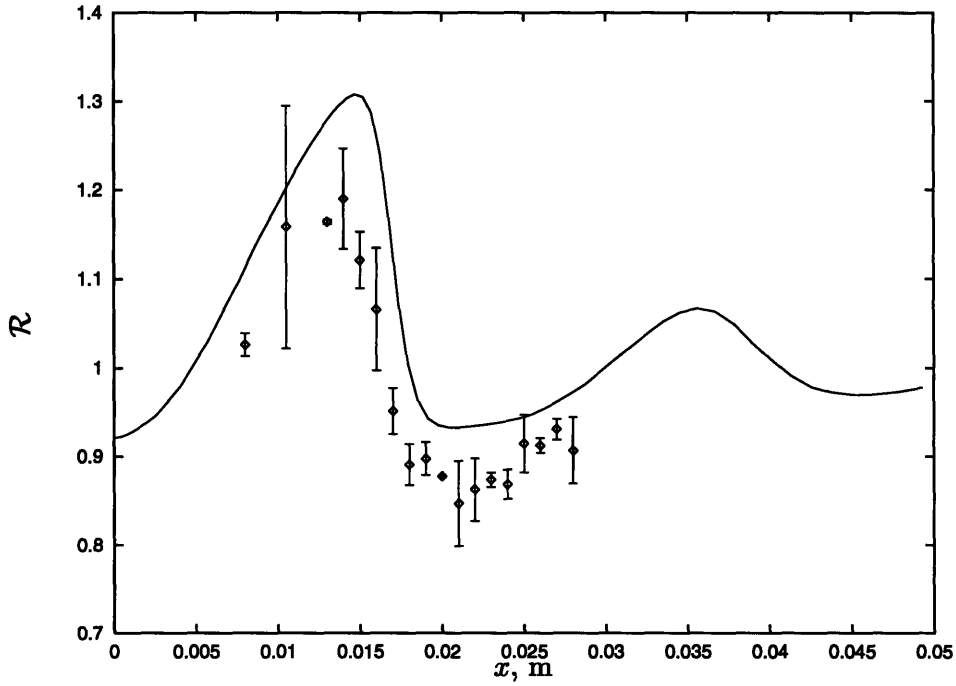

Figure 6.10: Measured and Expected Temperature Diagnostic Ratio along the Jet Axis Assuming a Frozen Vibrational Temperature of 325 K

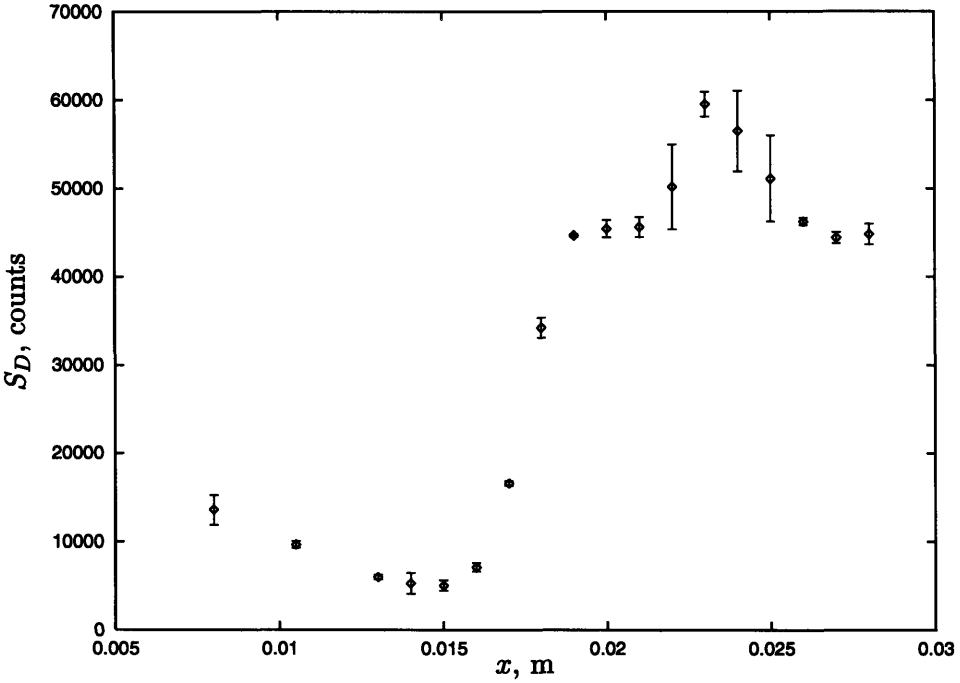

Figure 6.11: Fluorescence Signal Level along the Jet Axis

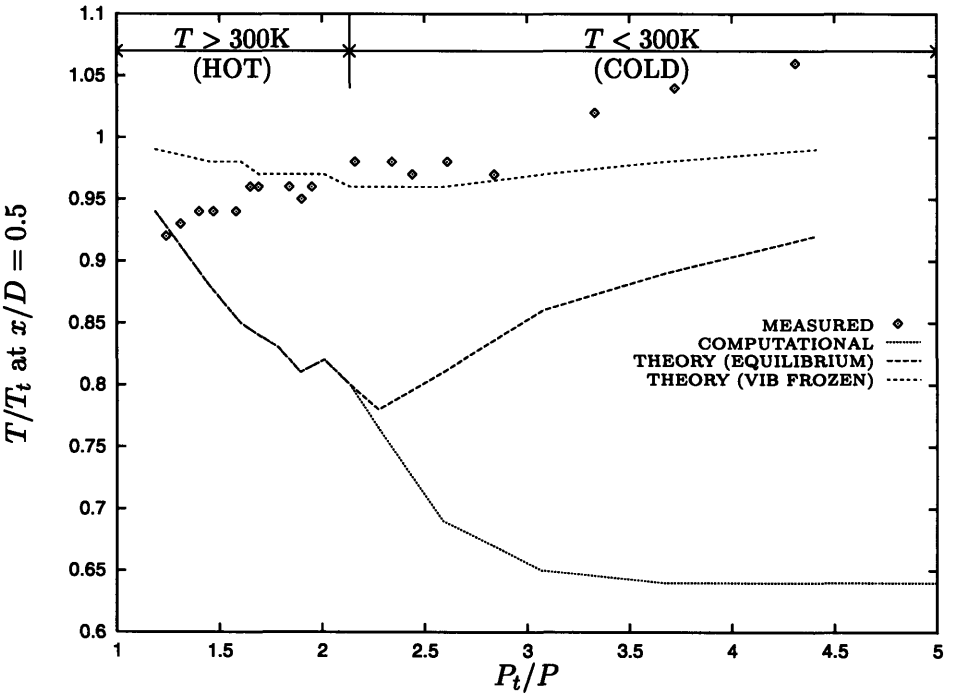

Figure 6.12: Measured and Expected Gas Temperature at $x = 5$ mm as a Function of Jet Pressure Ratio

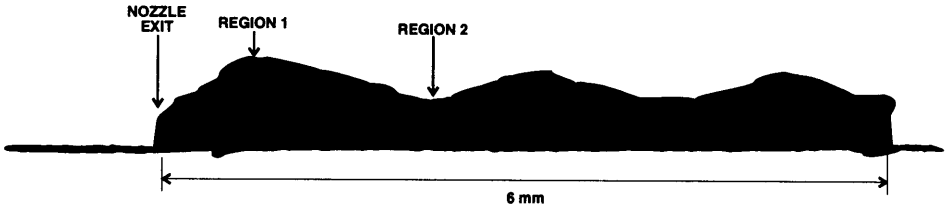

Figure 6.13: Fluorescence Signal Along Free Jet Axis for $P_t/P = 2.5$ [5]

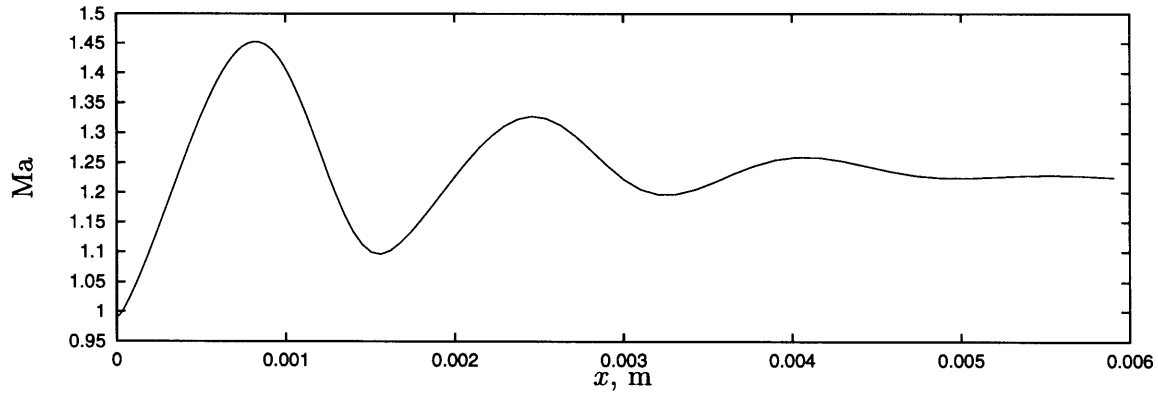

(a) Mach Number

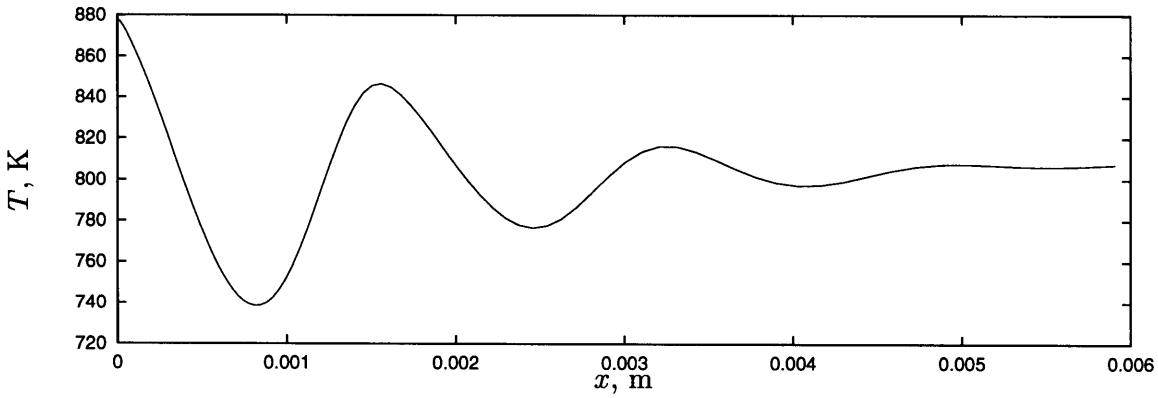

(b) Temperature

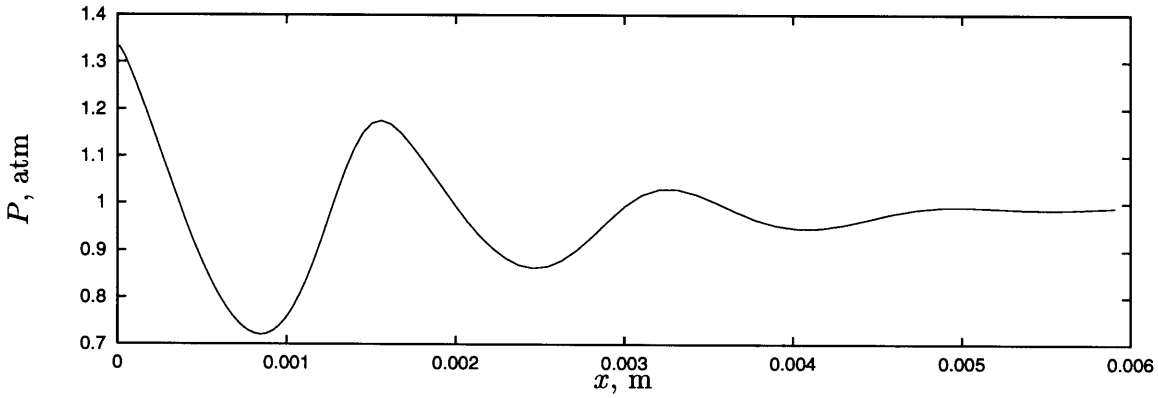

(c) Pressure

Figure 6.14: Computational Profiles for the Free Jet for $P_t/P = 2.5$, $T_t = 1050$ K

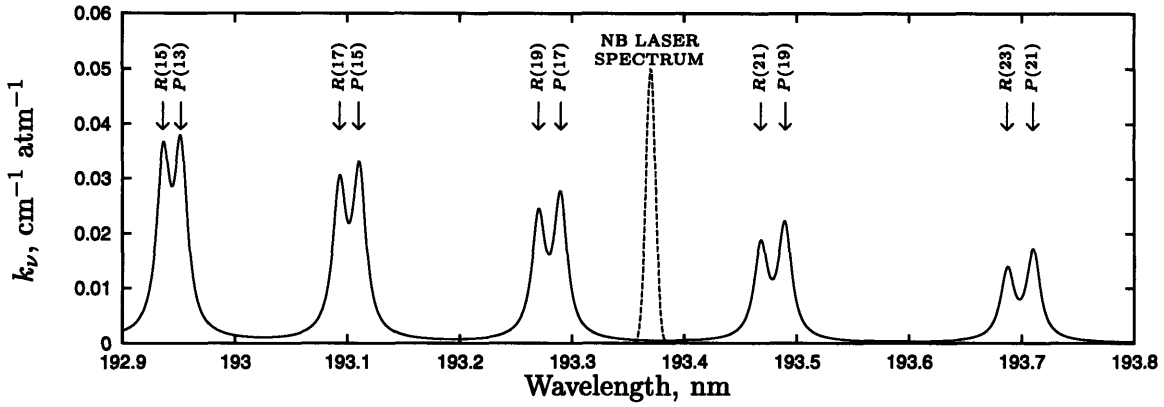

(a) $v'' = 0$ Transitions

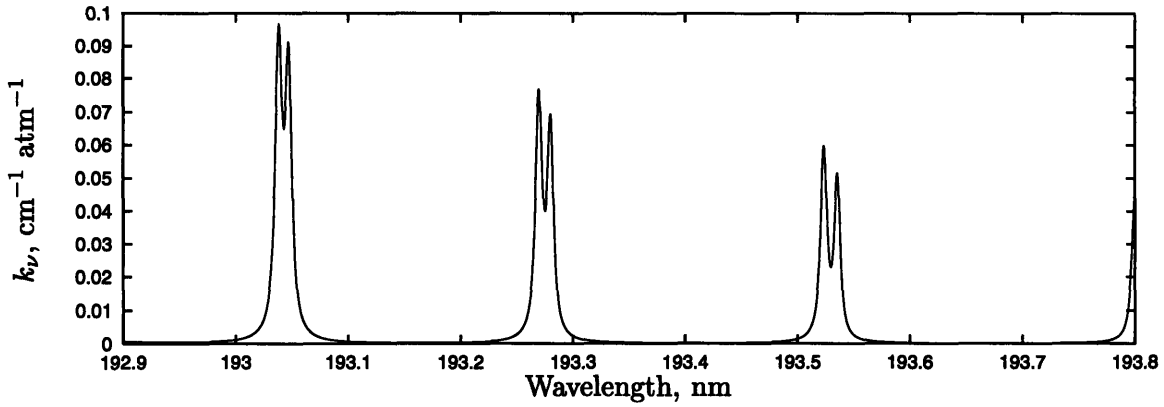

(b) $v'' = 1$ Transitions

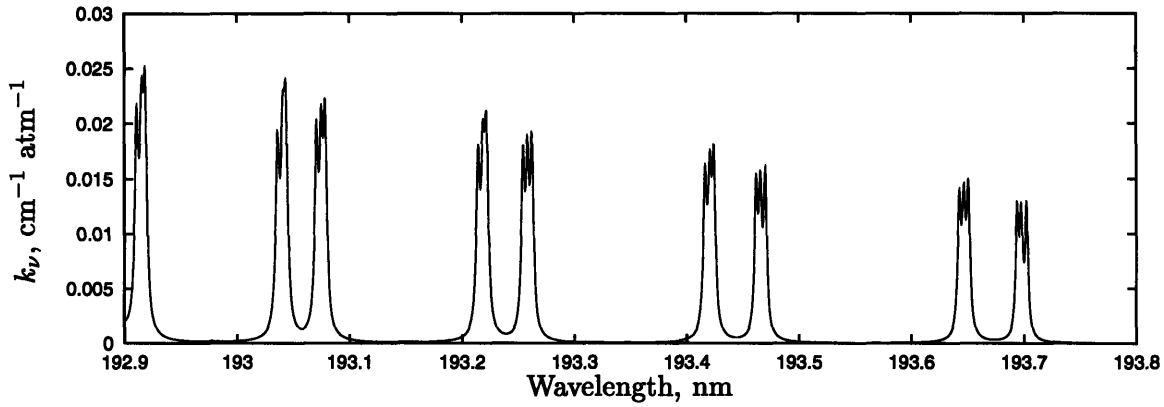

(c) $v'' = 2$ Transitions

k_ν: Spectral absorption coefficient

Figure 6.15: Rotational Transitions Originating from Vibrational Levels $v'' = 0$–2

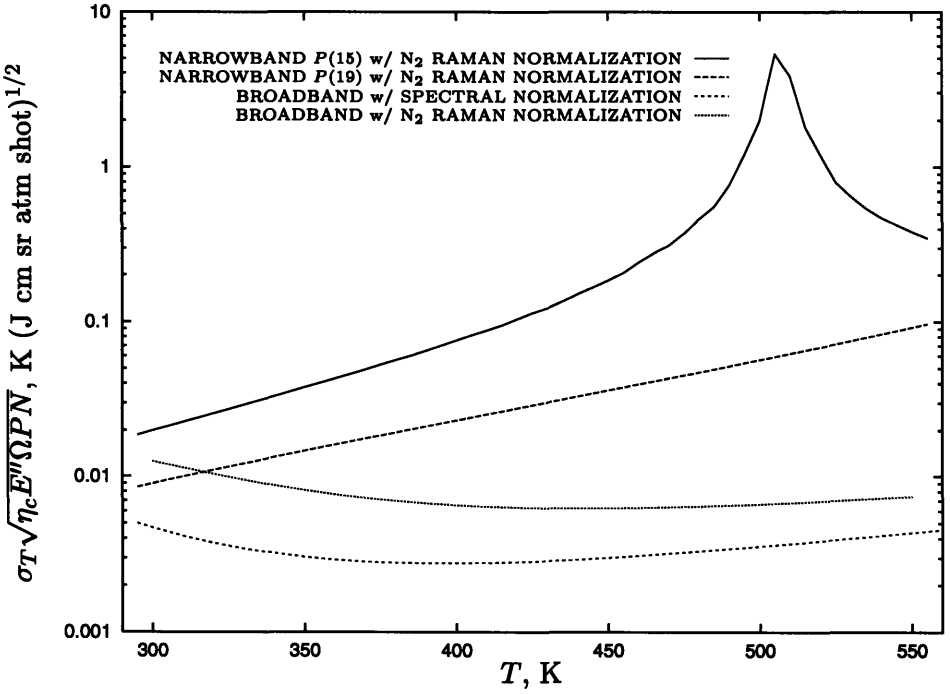

Figure 6.16: Theoretical Temperature Measurement Uncertainty for Narrowband Rotational Measurements Compared to Broadband Measurements

Chapter 7
Summary and Conclusions

This study investigated the feasiblity of using the oxygen LIF temperature measurement technique for engineering temperature measurements in general and turbomachinery intrarotor temperature measurements in particular. This chapter summarizes the investigation results and outlines the major conclusions.

7.1 Summary

The performance of the oxygen LIF temperature measurement technique was experimentally investigated for low-speed and high-speed flows.

A spectral model of the LIF process was constructed in order to assist in the design of the experimental apparatus and the evaluation of experimental data. This model was used in the identification of the optimum measurement and normalization methods and the preliminary investigation of possible error sources.

The experimental apparatus was designed for the turbomachinery environment. The dimensions of the Blowdown Turbine Facility at the MIT Gas Turbine Laboratory were used as representative of the turbomachinery research rigs. The limited optical access offered by the turbomachinery environment necessitated the use of a side-scatter configuration and a spectral filter to eliminate reflected light. Performance of the apparatus components were measured.

The temperature was determined by dividing the LIF signal into regions, summing the regional signals into numerator and denumerator signals, and forming a temperature diagnostic ratio. The assignment of regional signals to numerator and denumerator signals were optimized for maximum temperature precision using experimental data.

A complete error analysis was performed for low-speed flows in a controlled-temperature, controlled-pressure calibration apparatus. The following noise and error sources were investigated: quantum noise, laser noise, detector noise (thermal and readout noise), O_2^+ LIF signals, saturation, collisional quenching, beam path absorption, flow rate effects, temperature variations, and calibration apparatus. The trade-off between precision and accuracy was quantified and the optimum laser fluences were determined at different temperatures. Improvement of measurement precision with signal integration (multiple-shot measurements) was investigated, and its limitations outlined.

The impact of vibrational relaxation time on temperature measurements in high-speed flow was examined. The dependence of relaxation time on temperature, pressure and collision partners were discussed using spectral data from literature. The impact of the relaxation time on temperature measurement error was then examined, and supported by

experimental data taken on a supersonic free jet. High-speed flow data from literature was re-examined in light of the previous discussion. Finally, alternative measurement methods were described and their limitations outlined.

7.2 Conclusions

The major conclusions of this thesis are outline below with references to the appropriate chapter.

- For temperatures above 300 K, the oxygen LIF temperature measurement technique cannot be used in most high-speed flows because of the long vibrational lifetime of oxygen molecules. The oxygen LIF technique can be used if

$$\frac{L_r}{u\tau} \gg 1 \tag{7.1}$$

  where L_r is the desired spatial resolution, u is the flow speed, and τ is the vibrational relaxation time.

  Below 250 K, the technique does not rely on vibrational dependence and may be used for any high-speed flow. (See Chapter 6)

- The optimum laser fluence is determined by a trade-off between precision, limited by quantum noise, and accuracy, limited by nonlinear phenomena (O_2^+ LIF and saturation). Higher laser fluences lead to better precision but worse accuracy; lower laser fluences lead to better accuracy but worse precision. The optimum laser fluence is a function of temperature and number of laser shots. (See Chapter 5)

- Measurement precision may be increased by integrating LIF signals from multiple laser shots. As the number of laser shots increases, the optimum laser fluence decreases. Consequently, the precision improvement scales as $N^{1/3}$ instead of $N^{1/2}$ predicted by statistics. (See Chapter 5)

- Collisional quenching, although small, is not negligible. This study obtained a collisional quenching rate of 5.3×10^9 s^{-1} at 1 atm and 300 K. Neglection of collisional quenching, as done by almost all oxygen LIF studies, will result in an error of up to 3 K/atm over the 300–530 K temperature range. (See Chapter 5)

- The configuration of the experimental apparatus and the performance of the apparatus components do impact the performance of the measurement technique. For example, elimination of reflected light requires the use of a spectral filter, which significantly reduces O_2 and N_2 Raman signals, making Raman normalization unattractive. Similarly, narrowband measurements, which have high temperature sensitivity, may not be used because available ArF lasers do not have the necessary locking efficiency stability or level. (See Chapters 3 and 6)

In summary, the oxygen LIF temperature measurement technique does not appear to be useful for high speed flows. For low-speed flows and for high-speed flows below 250 K,

it is a feasible technique although its precision is much lower than advertised because of nonlinear phenomena. For high-speed flows above 250 K, the technique fails to yield any reasonable spatial resolution owing to the long vibrational relaxation time of oxygen.

The major contributions of this thesis include the following:

1. The first detailed analysis of the feasibility of laser induced fluorescence of oxygen (O_2 LIF) for engineering temperature measurements.
2. The first detailed, quantitative discussion of the impact of vibrational relaxation time of oxygen on the temperature measurements in high-speed flows.
3. The first quantitative and experimental description of the trade-off between measurement precision and accuracy.
4. The first experimental determination of the collisional quenching rate for O_2 LIF temperature measurement technique.

Appendix A
Calibration Apparatus

A controlled-environment calibration apparatus was used in the technique calibration and low-speed flow error analysis experiments. This appendix describes the calibration apparatus and presents data on the temperature variation and stability in the apparatus.

A.1 General Description

Figure A.1 presents a schematic of the calibration apparatus.

The air into the calibration apparatus is supplied by the laboratory compressor at approximately 8 atm (absolute). After passing through a flow-regulating valve and a variable-area flow meter, the air is heated to the desired temperature in a 6.4-kW heater. The air then flows through the test cell, which is described below. At the outlet of the test cell, a regulating valve is used to control the pressure in the test cell. The air is then dumped to the ambient atmosphere through an exhaust duct and exhaust fan.

A digital process controller with PID control is used to maintain the test cell temperature at the user-specified level.

The test cell is designed for a flow rate of 5 m/s, a temperature range of 300–600 K and a pressure range of 1.3–6.5 atm. The heater is sized with a margin of 100% in order to ensure rapid heat up. Pressures below 1.3 atm are not possible because of the pressure drops in the pressure control valve and exhaust duct.

Figure A.2 shows a cross-section of the test cell, which is shown photographically in Figure A.3. Figure A.4 presents a close-up of the measurement section.

The main part of the test cell is a six-arm, stainless steel, flanged union pipe. The heated air enters the test cell from the bottom. After passing through several honeycomb flow straighteners and perforated plates designed to reduce any temperature and velocity gradients, the flow enters the measurement section. Here the experimental apparatus is used to optically measure the gas temperature, which is also monitored with three conventional temperature probes. The flow exits the test cell through the top.

The test cell is wrapped in high-temperature insulation to minimize heat loss to the environment.

A.2 Instrumentation

The measurement section temperature is monitored with two thermocouples and one RTD.

One thermocouple is a K-type, high-speed probe, and serves as the main reference temperature measurement. The other thermocouple, also K-type but with slower response, is used to control the test cell temperature. The RTD is used as an independent check to the main thermocouple.

The high-speed thermocouple and the RTD probe are mounted on a linear slide and may be moved across the cell to measure the spatial variations in temperature.

The three temperature probes, along with temperature probes from other parts of the calibration apparatus, are monitored using a Helios I Data Acqusition Front End, manufactured by Fluke Corporation. The front end is controlled by an IBM PC/AT using Labtech Notebook software. The digitized data is stored on the same computer.

The pressure is monitored using a Setra 0-100 psia digital pressure gage. The pressure port is on one of the six arms of the measurement section.

A.3 Performance

Figures A.5 and A.6 show the variation of the temperature across the test cell at 153 °C and 284°C, respectively. The data was taken by moving the high-speed thermocouple probe across the test cell using the linear slide. Except for $x > 20$ mm, the temperature is constant to within ±1 °C in both cases. The decrease for $x > 20$ mm may be attributed to the thermocouple entering the stagnant region in one of the test cell arms.

Figures A.7 and A.8 give temperature fluctuations at 150°C and 275°C respectively. These data were recorded using a high-speed thermocouple amplifier and a digital oscilloscope. Digital signal processing with notch filters were used to remove signals at 60 Hz and its multiples, which were attributed to RF interference from the heaters.

The main temperature fluctuaions have a period of approximately 400 s and an amplitude of 1.0–1.2°C. These fluctuations may be traced to compressor cycling. Because the air flow used by the calibration apparatus is relatively small, the compressor cycles on and off, resulting in a cycling in the supply pressure. This supply pressure variations in turn result in fluctuations in the mass flow through and the heat load on the heater. Consequently, the measurement point temperature fluctuates. The temperature controller cannot reduce the fluctuations any further because of the finite response time of the heater.

The pressure fluctuations due to compressor cycleing is approximately ±1%. A pressure regulator could not be used because of the low supply pressure (approximately 8 atm) compared to the pressure requirement (up to 6.5 atm). From data of Chapter 5, a ±1% variation at 3.5 atm corresponds to a temperature uncertainty (due to collisional quenching) of less than ±0.1 K, so the pressure fluctuations are negligible compared to the temperature fluctuations.

In summary, the calibration test cell provides a constant-temperature environment to within ±1 K to ±1.5 K.

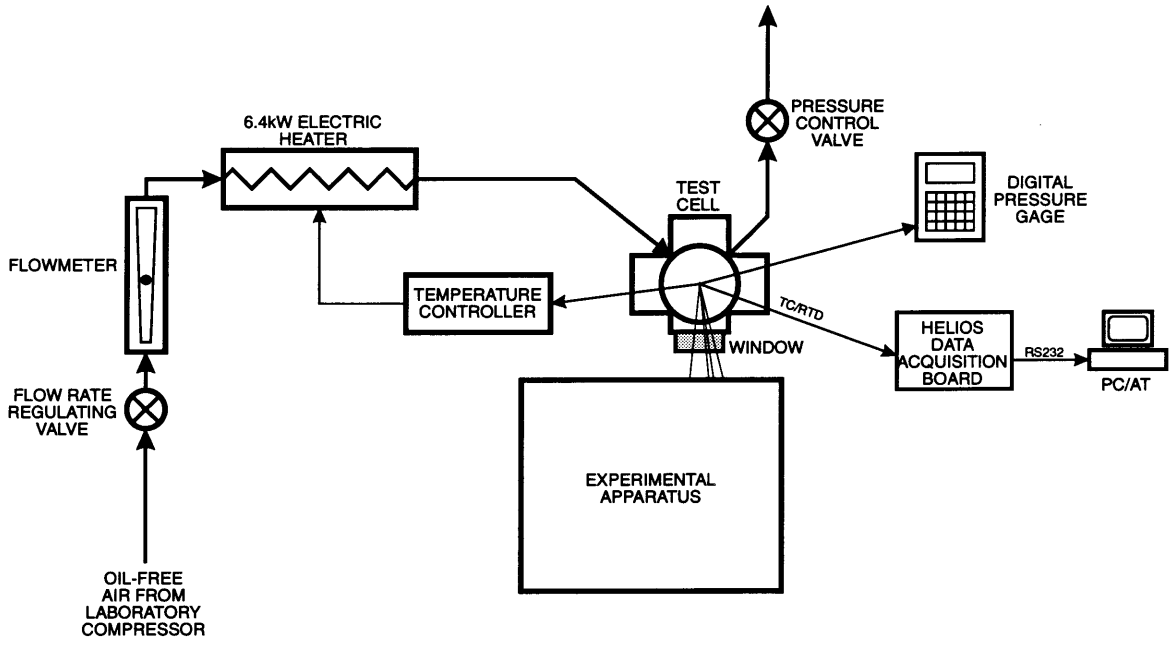

Figure A.1: Calibration Apparatus Schematic

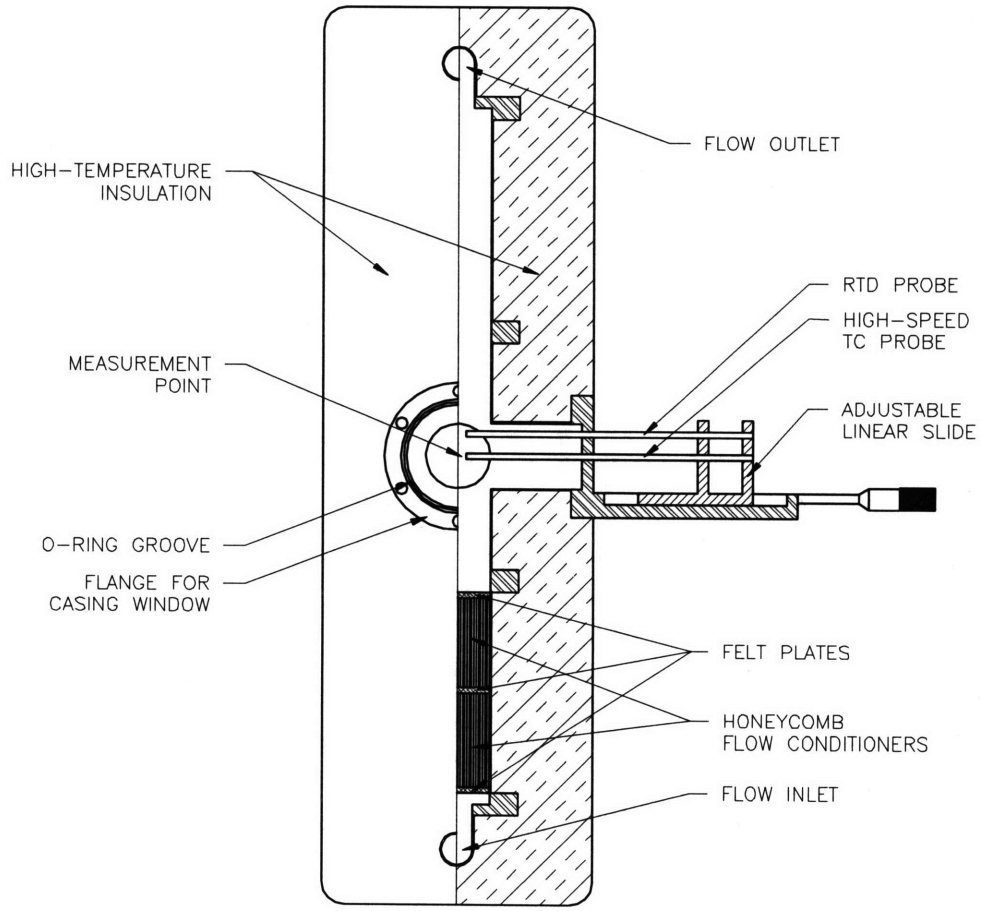

Figure A.2: Test Cell and Temperature Probes

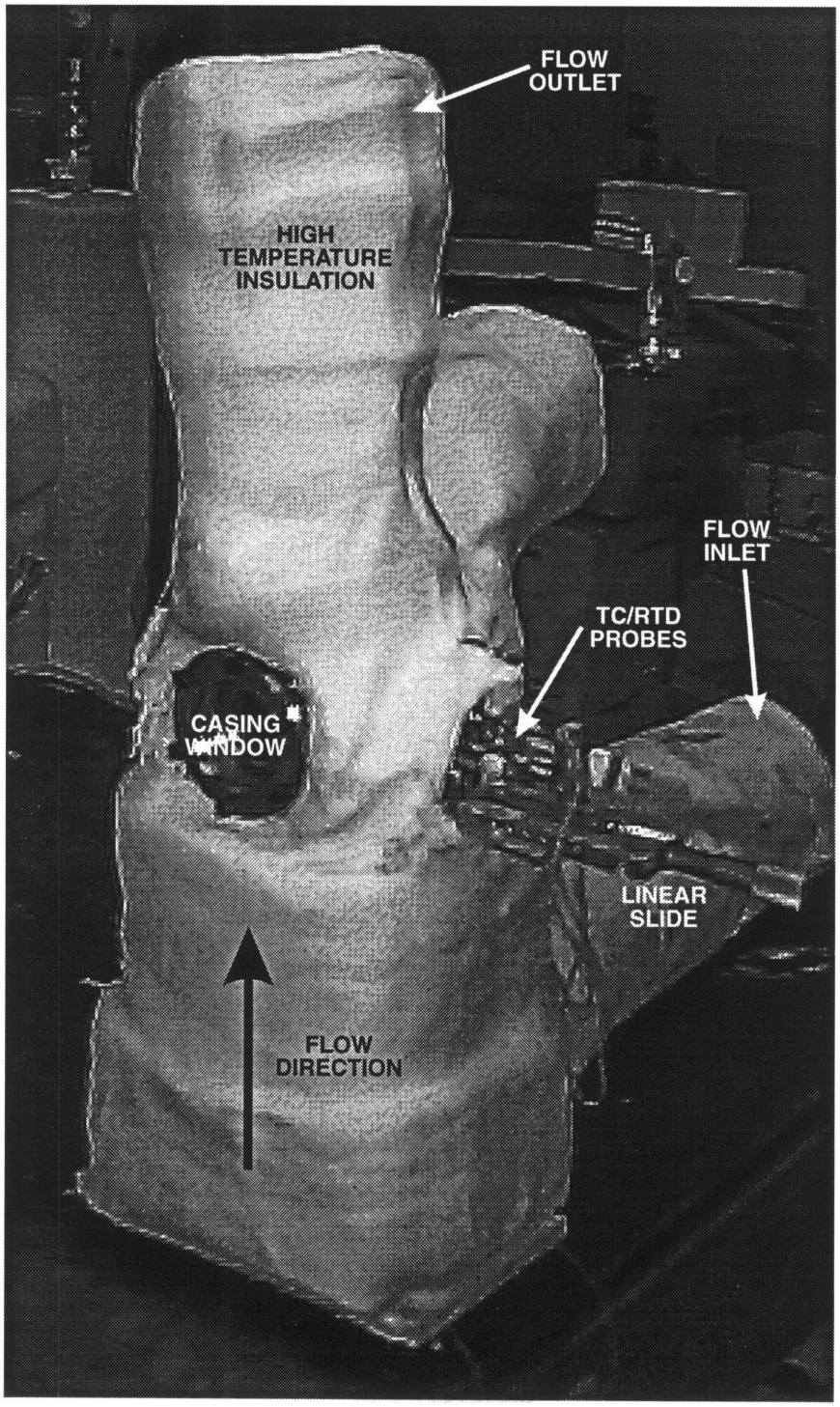

Figure A.3: Test Cell

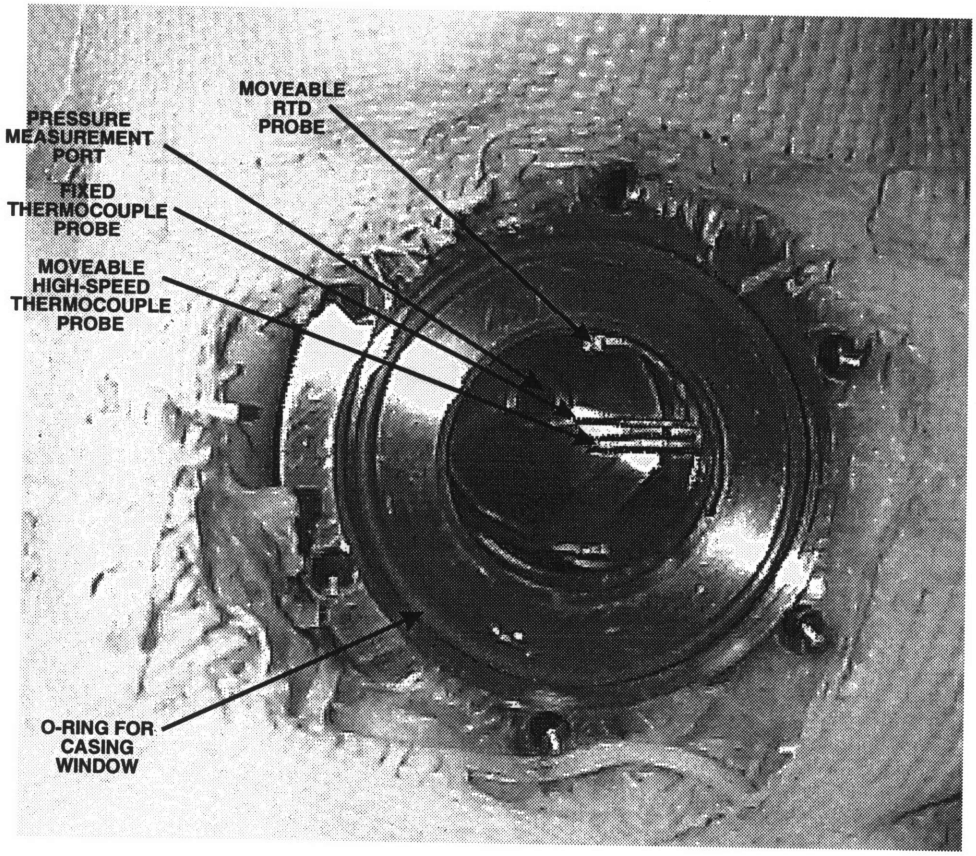

Figure A.4: Measurement Section with Temperature Probes

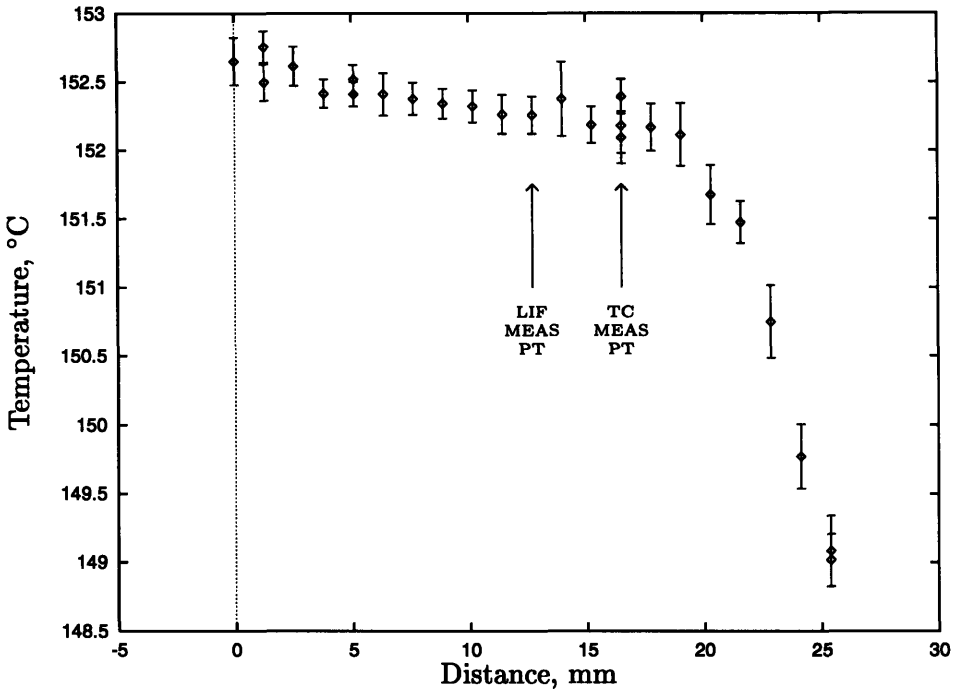

Figure A.5: Spatial Variation of Temperature across Measurement Volume at 153°C

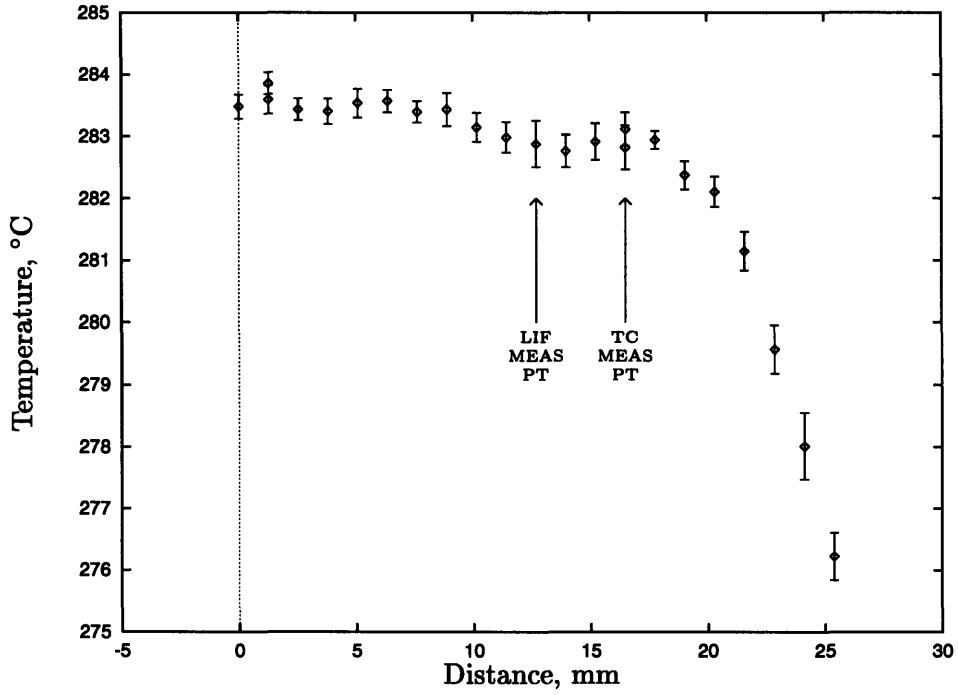

Figure A.6: Spatial Variation of Temperature across Measurement Volume at 283°C

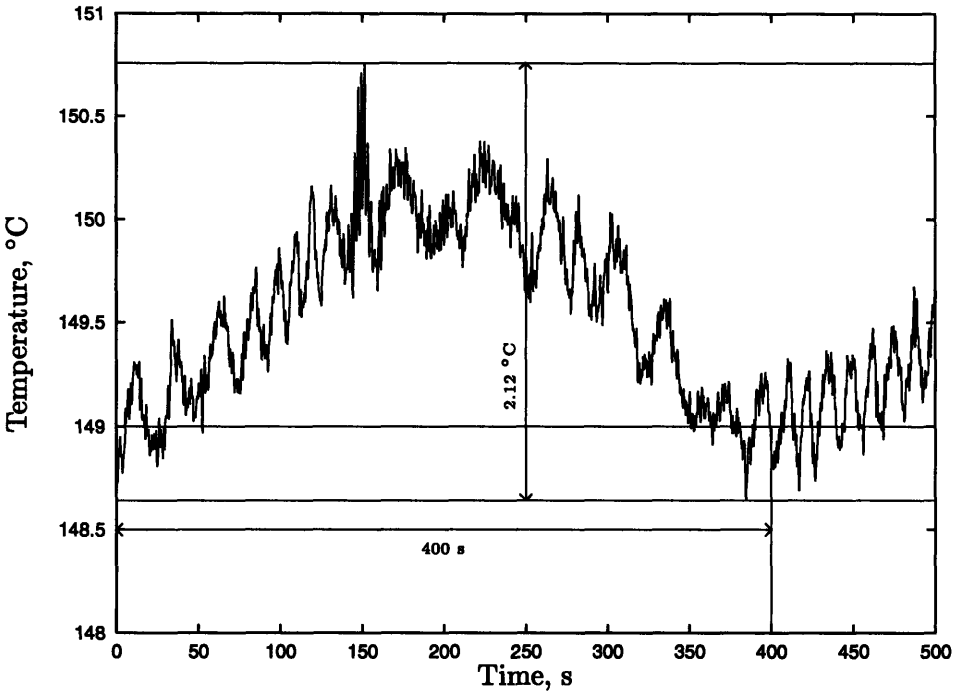

Figure A.7: Temperature Fluctuations in Measurement Volume at 150°C, recorded with High-Speed Instrumentation

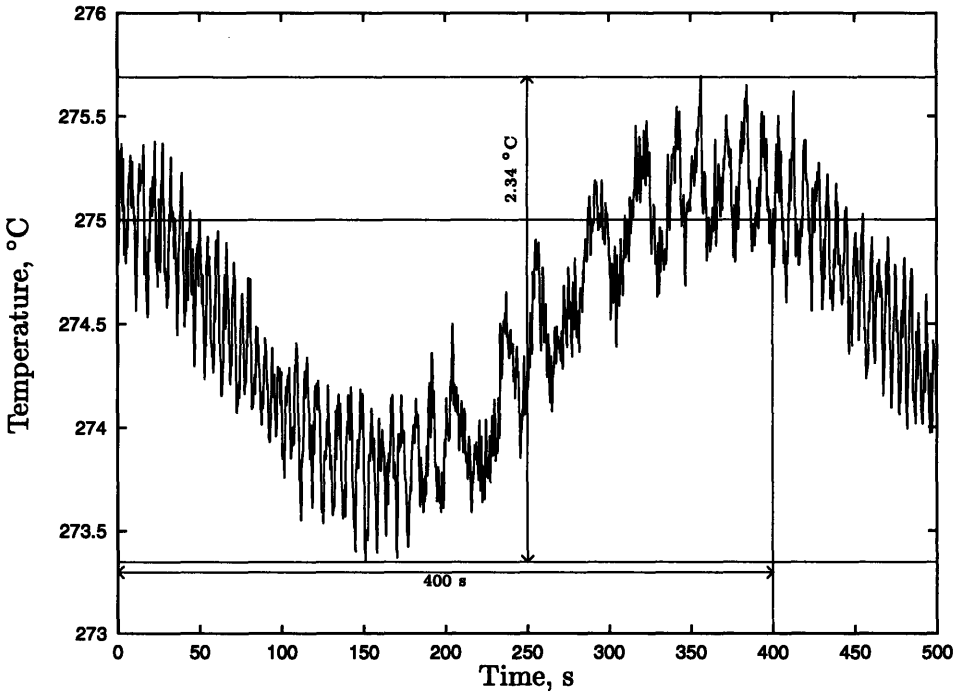

Figure A.8: Temperature Fluctuations in Measurement Volume at 275°C, recorded with High-Speed Instrumentation